공학박사학위논문

Computational procedure for structural analysis of DNA nanostructures using connectivity information between DNA bases

DNA 염기 사이의 연결 정보를 이용한 DNA 나노구조물의 전산구조해석

2023년 8월

서울대학교 대학원

기계항공공학부

이 재 경

Computational procedure for structural analysis of DNA nanostructures using connectivity information between DNA bases

DNA 염기 사이의 연결 정보를 이용한 DNA 나노구조물의 전산구조해석

지도교수 김 도 년

이 논문을 공학박사 학위논문으로 제출함

2023 년 4 월

서울대학교 대학원

기계항공공학부

이 재 경

이재경의 공학박사 학위논문을 인준함

2023 년 6 월

위 원 장 : 윤 병 동 (인)

부위원장 : 김 도 년 (인)

위 원 : 양 진 규 (인)

위 원 : 신 용 대 (인)

위 원 : 전 형 민 (인)

Abstract

Computational procedure for structural analysis of DNA nanostructures using connectivity information between DNA bases

Jae Gyung Lee
Department of Mechanicl and Aerospace Engineering
The Graduate School
Seoul National University

DNA has been employed as an engineered material to construct DNA nanostructures with specific shapes and functions in the field of DNA nanotechnology, rather than solely serving as genetic material. Structured DNA assemblies have primarily been designed on a well defined three-dimensional lattice, utilizing self-assembly which relies on base complementarity, a major characteristic of DNA, for the convenience of aligning and connecting DNA helices. However, this design strategy involves the arbitrary division of a three-dimensional DNA nanostructure into one or several substructures, followed by arranging and connecting them on a prepositioned lattice. This design procedure can result in artificially stretched bonds connecting bases in the designed initial configuration or incorrect classification of DNA structural motifs due to misalignment of DNA strands. As a consequence, computational structural analysis starting from the lattice-based configuration may face computational

difficulties such as nonconvergence or predicting an inappropriate final equilibrium shape.

In this study, we present a computational procedure for designing a DNA nanostructure based on the connectivity between DNA bases and accurately predicting its final equilibrium shape. We begin by understanding DNA structural motifs through the examination of their sequence-dependent geometric and mechanical properties using all-atom molecular dynamics simulations. Next, we roughly classify the structural motifs and generate a distributed configuration (DSTBCONF) based on the connectivity between bases. We then perform coarse-grained Brownian dynamics modeling and simulation on the DSTBCONF to generate a defined configuration (DEFCONF) with a more detailed classification of structural motifs. Finally, we develop a finite element model that incorporates intrinsic structural properties corresponding to the base sequences of the detailedly classified structural motifs, as well as considers the electrostatic repulsion between negatively charged DNA helices. Through finite element analysis with the numerical procedure, we successfully predict the final equilibrium shapes of various-shaped DNA nanostructures. Additionally, we analyze the mechanical and dynamic properties through normal mode analysis. It is expected that this proposed comprehensive computational procedure will significantly expedite the design-analysis-validation process of structured nucleic acid assemblies.

Keywords: DNA nanotechnology, Computational analysis, Multiscale modeling, Molecular dynamics simulation, Brownian dynamics, Finite element analysis

Student Number: 2016-27382

Acknowledgments

I am thankful to God, my heavenly Father, for bestowing upon me a marvelous opportunity to study at Seoul National University (SNU) and forge valuable connections. Your unwavering guidance consistently steers me and my family towards the correct direction. May your name be always honored and respected.

To begin with, I would like to convey my sincerest appreciation to my supervisor, Prof. Do-Nyun Kim, for his outstanding guidance and profound insights throughout my doctoral research. His exceptional mentorship and valuable perspectives greatly contributed to my academic development. Specifically, his teachings on the importance and excellence of integrating theory and computational simulation with experimental outcomes, as well as his passion and dedication to engineering-related research, have significantly influenced my growth as a researcher on the right path. Furthermore, his personal advice has assisted me in leading a wise and purposeful life.

I am also immensely grateful to my committee members, Prof. Byeng Dong Youn, Prof. Jinkyu Yang, Prof. Yongdae Shin, and Prof. Hyungmin Jun, for their valuable comments and suggestions on my doctoral thesis. Despite their busy personal schedules, they generously provided guidance not only on the research conducted during my doctoral course but also practical advice to enhance the overall completeness of the thesis.

I would also like to express my gratitude to my fellow colleagues at the Simulation-driven Structure Design Laboratory whom I have had the pleasure of meeting. This includes individuals such as Dr. Kyungho Yoon, Dr. Young-Joo Kim, Dr. Chanseok Lee, Dr. Jae Young Lee, Dr. Jaehyun Kim, Dr. Namkyu Kim, Dr. Giseok Yun, Dr. Yunhyoung Nam, Dr. Jaehoon Kim, Dr. Youngkyung Do, Dr. Heeyuen Koh, Dr. Manoj Kumar Dhadwal, (soon-to-be Dr.) Jeong Min Hur, (soon-to-be Dr.) Hyeonho Cho, Jeehwan Lee, Kyung Soo Kim, Jaekyung Lim, Dong-Sik Seo, Kyounghwa Jeon, Seungkwan Lee, Seong Woo Lee, Kwang Je Lee, Taehwi

Kim, Junho Park, Heonyoung Lee, Taeyeon Kim, Kyusoon Jung, Hyun-Suk Lee, Hongseok Kim, Miyoung Lee, Sungho Joo, Jinu Jeong, Myoungseok Kim, Nohong Kwak, Sunjae Park, Jiwon Kang, Jinho Lee, Jun Mo Kim, Iksu Jeong, Kwangseok Lee, Duhwan Kang, Donghyeon Lee, Yanggyun Kim, Taeyoung Ryu, Seoungwoo Lee, Jozsef Adam Sebestyen, and Chien Truong-Quoc. During my academic journey and research period, engaging in countless discussions on various subjects with them has been instrumental in my development as a researcher. Notably, the extensive conversations I had with my colleagues in the DNA research team, particularly centered around comprehending the interpretation of multiscale simulations and experimental results for DNA origami structures, have proven to be an invaluable asset in advancing my research undertakings.

I am deeply appreciative of the meaningful friendships I established with individuals from the Department of Mechanical and Aerospace Engineering at SNU, SNU freshman gatherings, various clubs, high school-university associations, scholarship societies, and other social interactions. Their support and encouragement have been invaluable during my time in graduate school, providing solace during moments of concern and inspiring me to regain my strength.

I am eternally grateful to my beloved family. A heartfelt thank you goes out to my father, Youngjoo Lee, my mother, Youngmi Kim, and my younger brother, Gyubeen Lee. They have showered me with boundless love, unwavering support, constant encouragement, and heartfelt prayers throughout every endeavor I pursued. Their steadfast support has been a constant presence in my life, nurturing my growth not only during my doctoral course but also throughout the long journey from elementary school, middle school, high school, university, and graduate school. Also, special thanks to my father-in-law, Minhyo Koh, and mother-in-law, Junguk Lim. They have been a source of unwavering support and prayers during my doctoral studies.

My beloved daughter, Yebin, fills my heart with boundless joy and happiness, consistently uplifting my spirits with her radiant smile. She is a precious gift, and her very existence is a blessing. Her loving nature brings me immeasurable happiness

that words cannot describe, surpassing any worldly treasure. I want to express my infinite love and profound gratitude to my daughter, whose mere being, whether I lay my eyes on her or ponder her, casts a luminous glow on everything around me.

Lastly, I would like to convey *my utmost and most valuable appreciation to my wife, Minjung*. She has consistently stood beside me, supporting my personal growth as an individual, a husband, and a father, through unwavering love, unconditional support, self-sacrifice, and constant encouragement. As my devoted partner, she shares love with me, co-parents our daughter, stands as my companion in life, and serves as a mentor-mentee, providing invaluable guidance and motivation. I sincerely extend my infinite gratitude and love for her, recognizing her as the most treasured and irreplaceable presence in my life.

Contents

List of Figures

models of ten helices and 16 helices are generated to investigate the sequence-dependent properties of the regular and stacked nick motifs, respectively. Each DNA helix is assigned a specific name that reflects its structural motif and the base sequences it comprises. Examples of these designations include regular (AA/TT) and stacked nick (AA/TnT).

Figure 2-2. A variety of DNA bundle structures. The first design invloves constructing four all-atom models of 6-helix-bundle DNA structures with varying sequences, resulting in a total of 13 bundle structures. Through the utilization of all-atom molecular dynamics simulations, the sequence-dependent properties of structural motifs such as junction nick, double junction, single junction, and open nick are investigated. Each bundle structure is uniquely designated with names like 6-helix-bundle-1.1, 6-helix-bundle-1.2, 6-helix-bundle-1.3, 6-helix-bundle-1.4, 6-helix-bundle-2, 6-helix-bundle-3, 6-helix-bundle-4, 6-helix-bundle-5, 6-helix-bundle-6, 6-helix-bundle-7, 6-helix-bundle-8, 6-helix-bundle-9, and 6-helix-bundle-10.

Figure 2-3. Root-mean-squared deviations of DNA helices and DNA bundle structures. Throughout the 300 [ns] molecular dynamics simulations, the root-mean-squared deviations are 0.56 ± 0.16 [nm] for DNA helices and 1.00 ± 0.30 [nm] for DNA bundle structures. The analysis of geometric and mechanical properties of DNA structural motifs is carried out using the simulation trajectories from the last 150 [ns].

Figure 2-4. Sequence-dependent geometric properties of DNA structural motifs. Prticularly significant are the values of $R_{x,1}$ and $R_{x,2}$ in the stacked motifs (regular, stacked nick, and junction nick), as well as T_x and $R_{z,1}$ in the crossover motifs (double junction, single junction, and open nick).

Figure 2-5. Sequence-dependent primary mechanical rigidities of DNA structural motifs. The primary mechanical rigidities encompass the stretching

repulsive forces on these vertices, we determine the positions of the substructures (Step 4). Subsequently, we rotate the substructures to minimize the sum of squared lengths of stretched bonds between them, thereby determining the positions of all base-pair nodes necessary for structural analysis (Step 5).

Figure 3-5. Determining the positions of base-pair nodes when given only the connectivity between bases. Here, dsDNAs and the structural motifs connecting them are represented as vertices and edges, respectively. The entire network is divided into several subnetworks by analyzing the connectivity between vertices. Attractive and repulsive forces are applied to both the subnetworks and the vertices within each subnetwork, resulting in their even spatial distribution in three-dimensional space (Steps 1 and 2). Then, the subnetworks are rigidly rotated to minimize the sum of squared edge lengths between vertices in different subnetworks (Step 3). We determine the positions of all dsDNAs by exeerting attractive and repulsive forces on them (Step 4). Consequently, the positions of all base-pairs, which are necessary for structural analysis, are determined by rotating the dsDNAs so that the sum of squared lengths of structural motifs between base-pairs in different dsDNAs becomes minimum (Step 5).

Figure 3-6. Determining the orientations of base-pairs when given only the connectivity between bases. Structural motifs, such as regular which is each compoenent of dsDNA and N-way junction, possess specific geometric characteristics. By leveraging these characteristics, we obtain the orientations of all base-pair nodes, which are essential for structural analysis.

Figure 4-1. Additional DNA structural motifs. DNA nanostructures exhibit additional structural motifs, specifically stacked nick and open nick, derived from the detailed classification of nick. Additionally, the structural motifs include junction nick, double junction, and single

indicate regular, bulge, nick, ssDNA, and junction, respectively. (B) The DSTBCONF when the positions and orientations of base-pairs as well as the connectivity between bases are initially provided. (C) The DSTBCONF when only the connectivity between bases is provided. (D) Correlation between substructures in Figure 6-4B and subnetworks in Figure 6-4C with the Pearson correlation coefficient of 0.97. (E) The final equilibrium shape predicted by finite element structural analysis. (F) Divergence of structural analysis from its lattice-based configuration.

Figure 6-5. Structural analysis of DNA wireframe structures. (A) Predicted final equilibrium shapes of two-dimensional wireframes. (B) Predicted final equilibrium shapes of three-dimensional wireframes.

Figure 6-6. Structural analysis of DNA wireframes with nonstraight wireframe edges. (A) Predicted final equilibrium shapes of tetrahedron, octahedron, and icosahedron wireframes with straight or bent edges. (B) TEM images of octahedron wireframes with straight, inwardly bent, and outwardly bent edges.

Figure 6-7. Structural analysis of topologically closed circular structures. (A) DSTBCONFs with respect to the number of substructures when the positions and orientations of base-pairs as well as the connectivity between bases are provided. (B) Computational time required in structural analysis with respect to the number of substructures. Green, yellow, and orange indicate the computational time required for partitioning the structure into substructures, generating the DSTBCONF, and performing structural analysis. The computation is implemented using MATLAB version R2019a (MathWorks) on a single PC (Intel Xeon CPU E5-2660 v4 @ 2.00 GHz). (C) A DSTBCONF generated when only the connectivity between bases is provided. (D) Predicted final equilibrium shapes of ten circular structures.

List of Tables

1. Introduction

1.1. Background and objectives

Deoxyribonucleic acid (DNA) serves not only as genetic material but also as a valuable engineering substance for designing and manufacturing artificial structures in the field of DNA nanotechnology[1,2]. DNA self-assembly, which relies on the complementary base-pairing rule of DNA, enables its use as a programmable material for constructing structural DNA assemblies with precise shapes and functions[3-15]. Furthermore, a variety of computational design approaches and strategies have been developed to facilitate and enhance the design and manufacturing procedures of DNA nanostructures[16-30].

It is well known that DNA exhibits a twist of approximately 240 [˚] per 7 base-pairs or 270 [˚] per 8 base-pairs, resulting in an overall rotation of about two turns per 21 base-pairs. This fundamental geometric characteristic of DNA plays a significant role in the design of DNA nanostructures, which are commonly structured as honeycomb-pleated or square-pleated DNA helices[5,19]. As a result, DNA nanostructures have been predominantly designed on a well defined three-dimensional honeycomb or square lattice due to the convenience of arranging and cross-linking DNA helices[19] (Figure 1-1).

Despite its convenience, the lattice-based design procedure often imposes several limitations on computational structural analysis. In this approach, DNA bases are forcibly and constrainedly located on positioned lattices, resulting in an unnatural configuration that deviates from the final equilibrium shape. For example, when designing a three-dimensional wireframe structure on a lattice surface, it is usually partitioned into substructures corresponding to wireframe edges. These substructures are then positioned in parallel on the lattice surface and interconnected using artificially stretched bonds between bases that traverse through them. When conducting structural analysis based on the lattice design, shortening the lengths of the stretched bonds causes the wireframe edges to overlap, resulting in a failure of

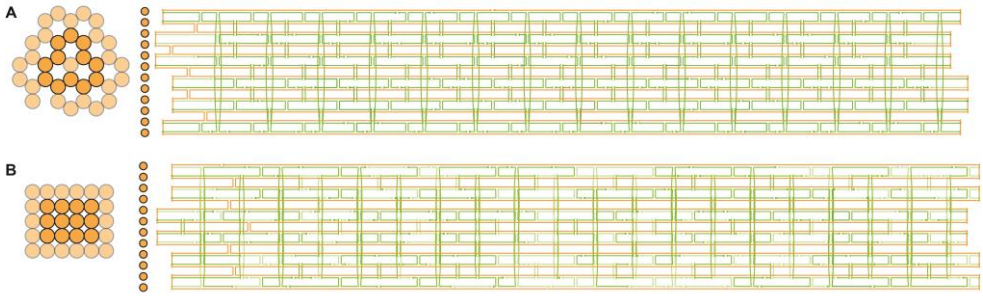

Figure 1-1. Designs of DNA nanostructures on a well defined three-dimensional lattice. (A) Design on a honeycomb lattice. (B) Design on a square lattice.

convergence (Figure 1-2A). For a topologically closed circular structure, the design procedure entails arbitrarily cutting and flattening the structure onto the lattice surface, followed by connecting the ends using artificially stretched bonds to form a closed circular shape. During structural analysis from the lattice design, these stretched bonds introduce instability to the structure, such as structural buckling, ultimately resulting in nonconvergence in the structural analysis (Figure 1-2B). Furthermore, the lattice-based approach may erroneously define DNA structural motifs, especially those that exhibit diverse conformations. Among DNA structural motifs, Holliday junction and nick are representative examples of such structural motifs with various conformational states. Holliday junctions in an ionic solution containing metallic cations exist in two stacked isomers (referred to as isomer1 or isomer2), and nicks can adopt either stacked nick or open nick conformations. The specific conformation of these structural motifs inherently depends on their surrounding environment (Figure 1-2C). However, the lattice-based design imposes a single geometry for each of these DNA structural motifs, disregarding their inherent two conformational states. For instance, all Holliday junctions in the lattice design are defined as isomer1 since the design procedure mandates the horizontal arrangement of DNA strands within each helix, irrespective of the specific environment surrounding the junction motifs. This design-based definition of DNA

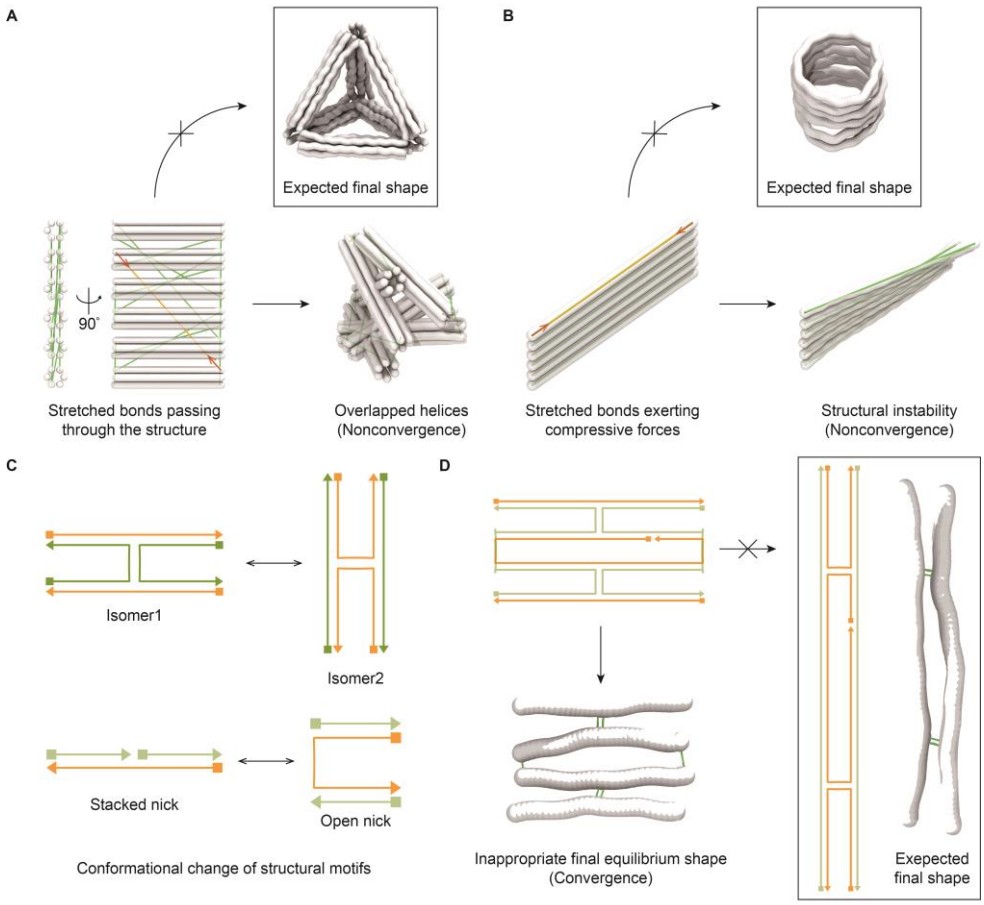

Figure 1-2. Structural analysis from lattice-based designs incorrectly predicting final equilibrium shapes. (A) Tetrahedron wireframe structure. Stretched bonds between bases passing through the on-lattice configuration cause nonconvergence in structural analysis, resulting in overlapping DNA helices. (B) Topologically closed circular structure. Stretched bonds between both ends exert compressive forces on the structure, leading to structural instability such as buckling. (C) Structural motifs with conformational change. Holliday junctions and nicks have two stacked isomers and can adopt either a stacked or open conformation, respectively. The conformation of these structural motifs is determined by their surroundings. (D) Tile structure with inappropriate shape prediction. Two Holliday junctions in the structure prefer to be isomer2, as shown in Figure 1-2C, but the conventional analysis procedure defines them as isomer1 based on the lattice-based configuration.

structural motifs can lead to nonconvergence or an inappropriate final equilibrium shape during the structural analysis of DNA nanostructures, including Holliday junctions that physically have isomer2 states (Figure 1-2D).

In order to address the computational difficulties associated with the interplay of design and analysis in structural DNA assemblies, we propose a design method that relies on the connectivity information between DNA bases instead of the conventional lattice-based approach. Our computational procedure involves generating a DEFCONF in three-dimensional space, where both conditions are satisfied: 1) the constituent components are evenly distributed, and 2) the DNA structural motifs are clearly defined. This DEFCONF is then transformed into a continuum-level finite element model that incorporates the sequence-dependent geometric and mechanical properties of DNA structural motifs, obtained from all-atom molecular dynamics simulations. Subsequently, multiscale structural analysis, combining finite element analysis with atom-level properties, is conducted to predict the final equilibrium shape. We rigorously validate our computational procedure by analyzing a diverse set of DNA nanostructures with different shapes.

1.2. Research outline

Chapter 1 presents a comprehensive overview of the computational procedure involved in generating a DEFCONF and conducting multiscale structural analysis of a DNA nanostructure. This procedure utilizes the connectivity information between DNA bases. The chapter briefly discusses the procedure for generating a DSTBCONF, which involves determining the positions and orientations of base-pairs. Additionally, it covers the classification of DNA structural motifs that compose the DNA nanostructure. In the DEFCONF, each DNA structural motif connects two bsae-pairs and is represented using a finite element beam model. The model's geometric and mechanical properties are derived from all-atom molecular dynamics simulations. The final equilibrium shape of the structure is predicted by performing finite element structural analysis.

Chapter 2 focuses on the examination of the geometric and mechanical properties of various DNA structural motifs through all-atom molecular dynamics simulation. We construct all-atom models for different DNA helices and DNA bundle structures composed of six helices. These structures exhibit diverse base sequences and shapes. Molecular dynamics simulations are conducted to investigate the sequence-dependent geometric and mechanical properties of DNA structural motifs, such as regular, stacked nick, junction nick, double junction, single junction, and open nick. The results obtained from these simulations serve as the foundation for subsequent modeling approaches presented in Chapters 4 and 5. Consequently, this study aims to achieve a precise prediction of the final equilibrium shape at an atomic scale.

Chapter 3 provides a detailed explanation of the technical procedure involved in generating the DSTBCONF using connectivity information between bases. First, we establish the connectivity between base-pairs by analyzing the initially provided connectivity between bases. Subsequently, it roughly classifies structural motifs such as dsDNA (a cluster of regulars), bulge, nick, ssDNA, and junction by analyzing both the connectivity between bases and the connectivity between base-pairs. The procedure for determining the positions and orientations of base-pairs encompasses

two cases: one where both the positions and orientations of base-pairs and the connectivity between bases are given, and another where only the connectivity between bases is given. As a result, the base-pairs whose positions and orientations are determined exhibit the DSTBCONF in three-dimensional space.

Chapter 4 describes the detailed classification procedure of DNA structural motifs. We specifically focus on two motifs: nick and junction, which are categorized in Chapter 3. These motifs possess multiple conformational states that necessitate detailed classification. Firstly, the nick motif is further classified into stacked nick and open nick, depending on the stacking status of the two base-pairs within the motif. Detailed classification of the junction motif considers whether it comprises four arms or not, leading to its division into 4-way junction and non-4-way junction. Within the 4-way junction category, detailed classification is performed to differentiate between 4-way double junction and 4-way single junction, depending on whether the structural motif is formed by four or five DNA strands, respectively. Moreover, the 4-way double junction and the 4-way single junction are further classified as two double junctions and two junction nicks, and one single junction and two junction nicks, respectively. Notably, the 4-way double junction displays two distinct conformational states, isomer1 and isomer2, which are influenced by the surrounding environment. The detailed classification of these structural motifs is accomplished through coarse-grained Brownian dynamics modeling and simulation of the DSTBCONF. As a result of this procedure, all structural motifs are successfully classified in detail, leading to the generation of the DEFCONF.

Chapter 5 elucidates the finite element modeling approach to describe the DEFCONF as a finite element model. The model includes structural beam elements representing strucutural motifs that connect two base-pairs. Each structural element has specific intrinsic properties derived from Chapter 2, which consider its types and base sequences. Additionally, electrostatic truss elements are introduced to effectively model the electrostatic repulsion between DNA helices. Consequently, the finite element analysis with a nonlinear solution method is conducted to predict the final equilibrium shape.

Chapter 6 highlights the findings of the finite element structural analysis carried out on the DEFCONFs. Through the structural analysis of previously reported DNA nanostructures with diverse shapes, we verify that the predicted final equilibrium shapes exhibit a close resemblance to the observed equilibrium shapes in experimental investigations. Additionally, we corroborate that the local properties of the structural motifs within the equilibrated structures are in accordance with those obtained from all-atom molecular dynamics simulations. This successful correspondence serves to validate and demonstrate the suitability and effectiveness of the proposed computational procedure for conducting structural analysis.

Chapter 7 evaluates the overall rigidity and dynamic characteristics of DNA nanostructures. Through the application of normal mode analysis, we meticulously analyze the bending persistence lengths of DNA nanotubes and the fluctuation of structured DNA assemblies. The obtained results align consistently with previously reported findings and atom-level simulation results. This confirmation reinforces the applicability and utility of the proposed computational procedure, demonstrating its effectiveness not only in predicting the final equilibrium shape but also in analyzing the mechanical and dynamic properties of DNA nanostructures.

1.3. Overview of the computational analysis procedure

Before performing structural analysis on DNA nanostructures based on the connectivity between DNA bases, it is important to establish a comprehensive understanding of the diverse structural motifs that constitute structured DNA assemblies. These motifs, such as regular, stacked nick, junction nick, double junction, single junction, open nick, and others, possess unique properties that depend on the base sequences within each motif. To gain a thorough comprehension of the geometric and mechanical properties of the regular motif, which consists of 10 base sequence combinations, as well as other motifs, each encompassing 16 base sequence combinations, we construct all-atom models of 26 DNA helices and 13 DNA bundle structures with varying shapes and base sequences. Subsequently, these structures undergo all-atom molecular dynamics simulations, followed by the analysis of sequence-dependent properties using the 3DNA definition[31,32] and quasi-harmonic approximation[33]. By investigating the sequence-dependent geometric and mechanical properties, we can seamlessly incorporate these structural motifs into subsequent modeling procedures (Figure 1-3).

The connectivity between DNA bases in DNA nanostructures is represented by an M-by-5 matrix, where M corresponds to the number of bases. Each column of the matrix signifies the unique identifier of the current base, the identifier of the base in the 5'-direction, the identifier of the base in the 3'-direction, the identifier of the complementary base, and the base sequence of the current base, respectively. Utilizing this connectivity information, we establish the connectivity between base-pairs. Through an analysis of both the connectivity between bases and the connectivity between base-pairs, we roughly classify the structural motifs that connect these base-pairs. Initially, the structural motif is categorized as either regular or bulge, based on whether two base-pairs are connected by two DNA strands. The regular motif signifies a direct connection between two bases within a base-pair and two bases in the subsequent base-pair. Conversely, the bulge motif involves a direct connection between one base in a base-pair and another base in the following base-pair, with additional bases intervening between the two base-pairs. A cluster of regul-

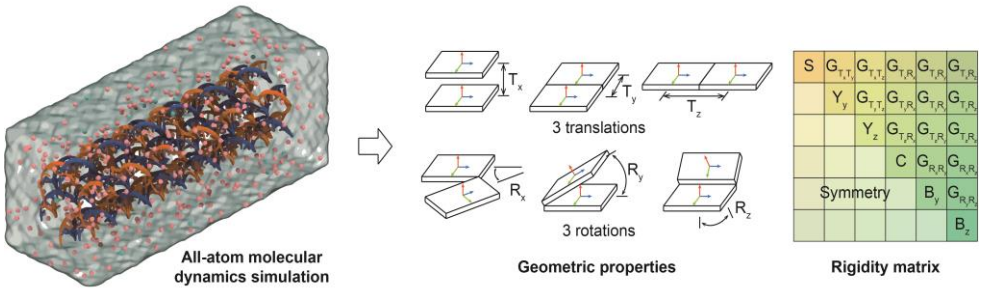

Figure 1-3. Geometric properties and mechanical rigidities of DNA structural motifs. Geometric and mechanical properties of structural motifs are obtained through all-atom molecular dynamics simulations. The geometric properties of each structural motif include the translational relationships (T_x, T_y, and T_z) and the rotational ones (R_x, R_y, and R_z) between two base-pairs connected by the motif. Its mechanical properties encompass stretching (S), shearing (Y_y and Y_z), twisting (C), bending (B_y and B_z), and coupling (G) rigidities.

ar motifs is identified as dsDNA. Furthermore, if two base-pairs are connected by three DNA strands, the motif is categorized as either ssDNA (with additional bases present between the base-pairs) or nick (with no intervening bases). Finally, the structural motif composed of N base-pairs connected by DNA strands, where N is greater than or equal to three, is referred to as N-way junction (Figure 1-4).

When provided with the positions and orientations of base-pairs, as well as the connectivity between bases, we differentiate adjacent base-pairs from nonadjacent ones. Adjacent base-pairs refer to those that are either stacked or connected via a Holliday junction, while nonadjacent base-pairs encompass all other cases. Subsequently, we identify each cluster of adjacent base-pairs as a component. If both ends of the component are connected by stretched bonds, forming a topologically closed loop, it is further partitioned into four components. On the other hand, if we only have the connectivity information between bases, each dsDNA is defined as a component, and the orientations of base-pairs are determined based on the geometric properties of the corresponding dsDNA. Components undergo attractive and repulsi-

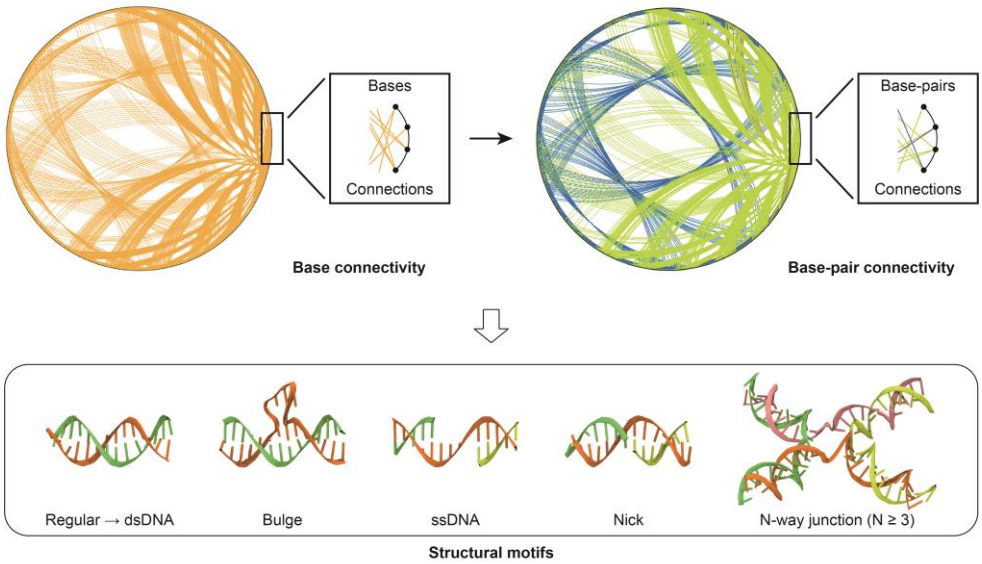

Figure 1-4. Rough classification of DNA structural motifs. Starting from the initially provided connectivity between bases, we derive the connectivity between base-pairs. By analyzing both the connectivity between bases and the connectivity between base-pairs, we roughly classify the structural motifs.

ve forces depending on their connectivity, leading to their distribution in three-dimensional space, thereby determining the positions of all base-pairs. Additionally, their orientations are calculated by considering the rotational transformation relationship between components before and after distribution, as well as the geometric characteristics of DNA origami nanostructures. As a result of this procedure, we establish the DSTBCONF of DNA nanostructures (Figure 1-5).

To ensure a seamless structural analysis of DNA nanostructures, it is necessary to classify the nick and junction motifs in detail among the roughly classified DNA structural motifs. The nick motif exhibits two conformational states: stacked and open. Depending on whether the base-pairs connected by the motif are stacked or not, the nick motif is further classified as stacked nick or open nick. As for the junction motif, it is initially categorized as 4-way junction or non-4-way junction ba-

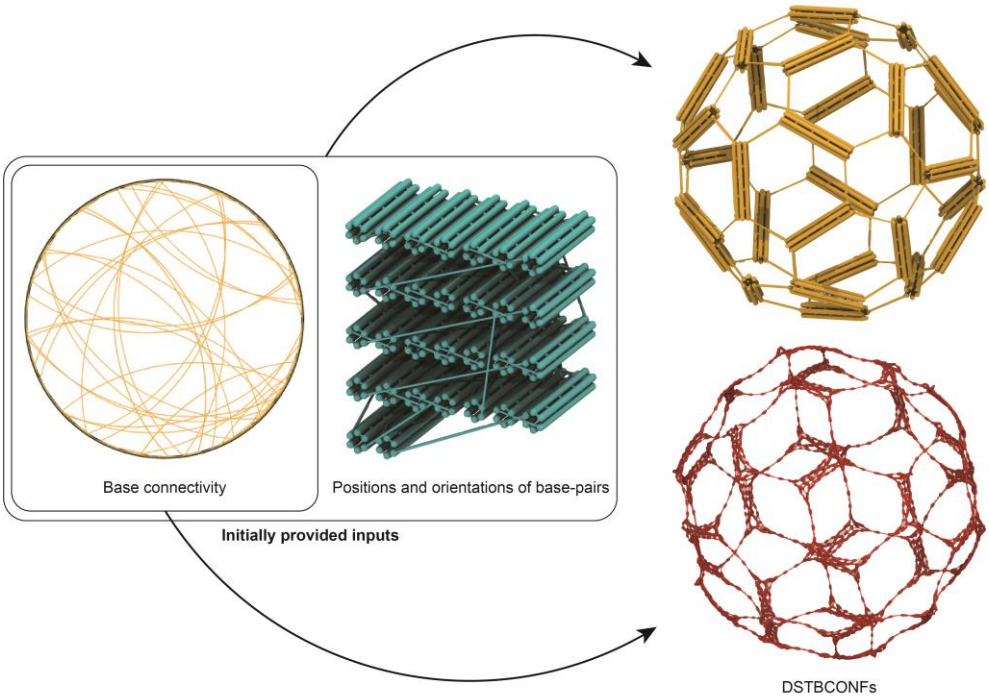

Figure 1-5. Generation of a DSTBCONF. A cluster of adjacent base-pairs is deemed a component when both the positions and orientations of base-pairs and the connectivity between bases are given. However, if only the base connectivity is provided, each dsDNA among DNA structural motifs is regarded as a component. By exerting attractive and repulsive forces on the components while considering their connectivity, they are positioned in three-dimensional space, resulting in the generation of the DSTBCONF.

sed on the number of arms it possesses (four or not). The 4-way junction is then subdivided into two categories: 4-way double junction or 4-way single junction, depending on whether it is composed of four or five DNA strands, respectively. The 4-way double junction, also known as the Holliday junction, exhibits two isomeric states (isomer1 and isomer2) and is further classified as two junction nicks and two double junctions. On the other hand, the 4-way single junction possesses a single geometry and is further classified as two junction nicks and one single junction. Det-

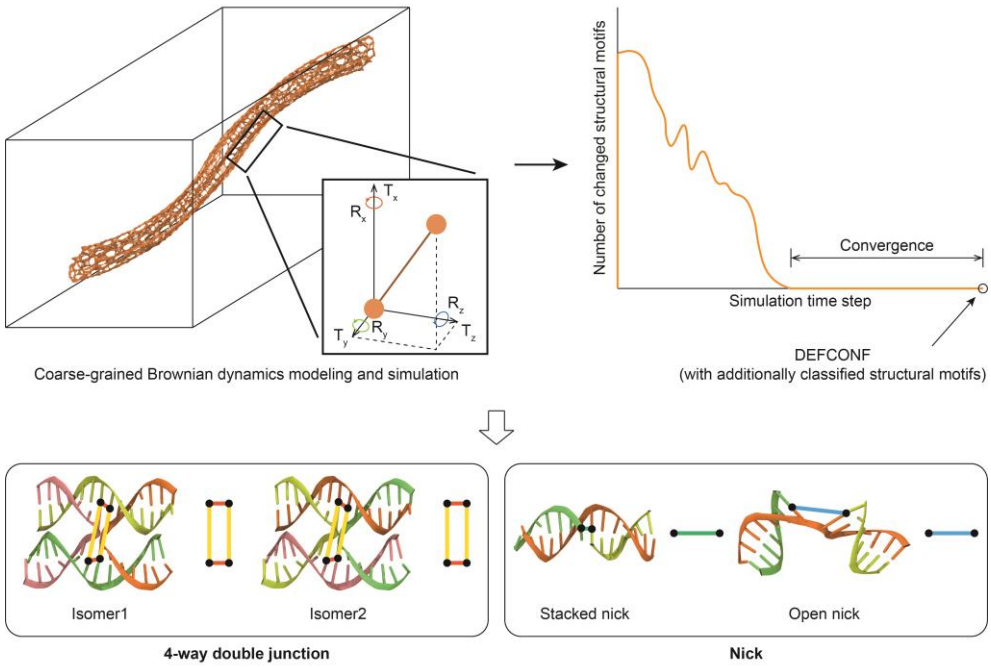

Figure 1-6. Detailed classification of DNA structural motifs. Through coarse-grained Brownian dynamics modeling and simulation of the DSTBCONF, detailed classification of structural motifs is performed. The simulation particularly focuses on determining the equilibrated conformations of the 4-way double junction and nick motifs, each having two distinct conformational states. Here, the junction nick, double junction, stacked nick, and open nick motifs are represented by orange, yellow, green, and blue lines, respectively.

ailed classification of the nick and 4-way double junction motifs is particularly important due to their two distinct conformations, which are physically determined by their surrounding environment, regardless of the initially set configurations.

For the detailed classification proceudre, a coarse-grained Brownian dynamics modeling and simulation approach is utilized with the DSTBCONF. The geometric and mechanical properties of all structural motifs in the modeling and simulation are determined using findings obtained from all-atom molecular dynamics simulations of various DNA helices and DNA bundle structures. As the simulation progresses,

additional structural motifs are naturally identified, leading to the generation of the DEFCONF that encompasses the positions and orientations of all base-pairs, as well as the classification of all structural motifs (Figure 1-6).

In order to predict the final equilibrium shapes of DNA nanostructures, we convert the DEFCONF into a finite element model. Each structural motif is represented as an elastic beam element. The geometric and mechanical properties of the structural beam elements are obtained from all-atom molecular dynamics simulations, which capture the base sequences and the classified structural motifs. Additionally, we incorporate elastic truss elements to account for the electrostatic repulsions between negatively charged DNA helices in an ionic solution. The generation of electrostatic elements is based on the Debye-Hückel theory, and they are constructed when the distance between the corresponding base-pairs falls below a specific cutoff distance. By assembling the local stiffness matrices of all structural and electrostatic elements, we obtain the global stiffness matrix. Subsequently, the final equilibrium shapes of DNA nanostructures are predicted using a nonlinear solution procedure in the finite element structural analysis (Figure 1-7A). Furthermore, we examine the overall bending persistence lengths of DNA nanotubes with various shapes and the fluctuation of base-pairs within DNA nanostructures, using normal mode analysis (Figure 1-7B). Through these analyses, we demonstrate the feasibility and effectiveness of the proposed computational procedure for the structural analysis of DNA nanostructures. Mathematical notations used in this study are described in Appendix A.1.

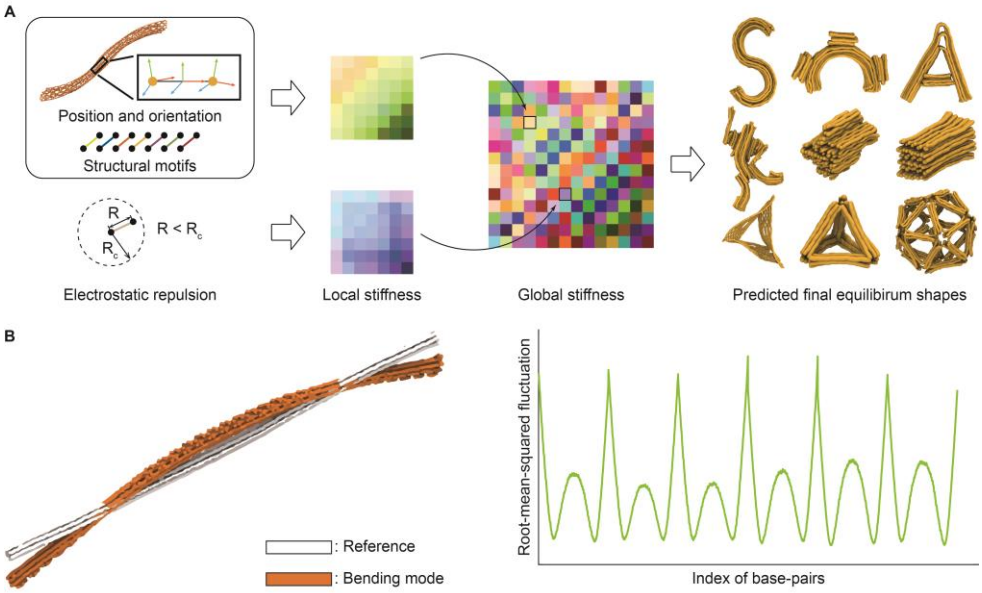

Figure 1-7. Finite element structural analysis. (A) Predicting the final equilibrium shapes of DNA nanostructures. The structural motifs and the electrostatic repulsion between DNA helics are modeled using elastic beam and truss elements, respectively. The local stiffness matrices are assembled into the global stiffness matrix. The finite element analysis with the nonlinear solution procedure predicts the final equilibrium shapes of DNA nanostructures. (B) Analyzing the mechanical and dynamic properties. Using normal mode analysis, the bending peristence lengths of DNA nanotubes and the fluctuation of base-pairs constituting DNA nanostructures are investigated.

2. Investigating properties of DNA structural motifs

2.1. Abstract

We utilize all-atom molecular dynamics simulations to investigate the sequence-dependent geometric properties and mechanical rigidities of various DNA structural motifs that connect two base-pairs within DNA nanostructures. The structural motifs under investigation encompass regular, stacked nick, junction nick, double junction, single junction, and open nick. In order to comprehend the structural properties of these motifs, we construct all-atom models of 26 DNA helices and 13 DNA 6-helix-bundle structures. Subsequently, we conduct all-atom molecular dynamics simulations on the DNA helices and DNA bundle structures to investigate the properties of the regular and stacked nick motifs, as well as other structural motifs, respectively. The examination of geometric properties involves the analysis of three translational and three rotational relationships between the base-pairs. Additionally, we assess six primary mechanical rigidities and 15 coupling coefficients under the quasi-harmonic approximation to analyze the mechanical properties. This study not only establishes a comprehensive database documenting the sequence-dependent properties of DNA structural motifs but also highlights the possibility of coarse-grained modeling or finite element modeling with atom-level accuracy.

2.2. Generation of DNA structure atomic models

In order to analyze the geometric properties and mechanical rigidities of DNA structural motifs constituting DNA nanostructures, we generate all-atom models for 26 DNA helices and 13 DNA bundle structures. Each DNA helix consists of 42 base-pairs, with the central two base-pairs having base sequences of MN/PQ or MN/PnQ. These sequences represent combinations in the 5'-to-3' direction, including AA/TT, AC/GT, AG/CT, AT/AT, CA/TG, CC/GG, CG/CG, GA/TC, GC/GC, TA/TA, AA/TnT, AC/GnT, AG/CnT, AT/AnT, CA/TnG, CC/GnG, CG/CnG, CT/AnG, GA/TnC, GC/GnC, GG/CnC, GT/AnC, TA/TnA, TC/GnA, TG/CnA, and TT/AnA. Here, A, C, G, and T denote adenine, cytosine, guanine, and thymine, respectively, and n indicates the presence of a nick (Figure 2-1 and Table 2-1). All DNA bundle structures are composed of six helices and include a total of 456 junction nicks, 368 double junctions, 44 single junctions, and 49 open nicks. Both the junction nick and open nick motifs have 16 base sequence combinations, including AA/TnT, AC/GnT, AG/CnT, AT/AnT, CA/TnG, CC/GnG, CG/CnG, CT/AnG, GA/TnC, GC/GnC, GG/CnC, GT/AnC, TA/TnA, TC/GnA, TG/CnA, and TT/AnA, which are similar to the stacked nick motif. Also, the double junction and single junction motifs have 16 sequence combinations denoted as MN||PQ and MN|PQ, respectively, such as AA||TT, AC||GT, AG||CT, AT||AT, CA||TG, CC||GG, CG||CG, CT||AG, GA||TC, GC||GC, GG||CC, GT||AC, TA||TA, TC||GA, TG||CA, and TT||AA, as well as AA|TT, AC|GT, AG|CT, AT|AT, CA|TG, CC|GG, CG|CG, CT|AG, GA|TC, GC|GC, GG|CC, GT|AC, TA|TA, TC|GA, TG|CA, and TT|AA (Figure 2-2 and Table 2-2). The base sequences of DNA strands in all DNA bundle structures are detailedly and comprehensively represented in Table A-1 (in Appendix A.2).

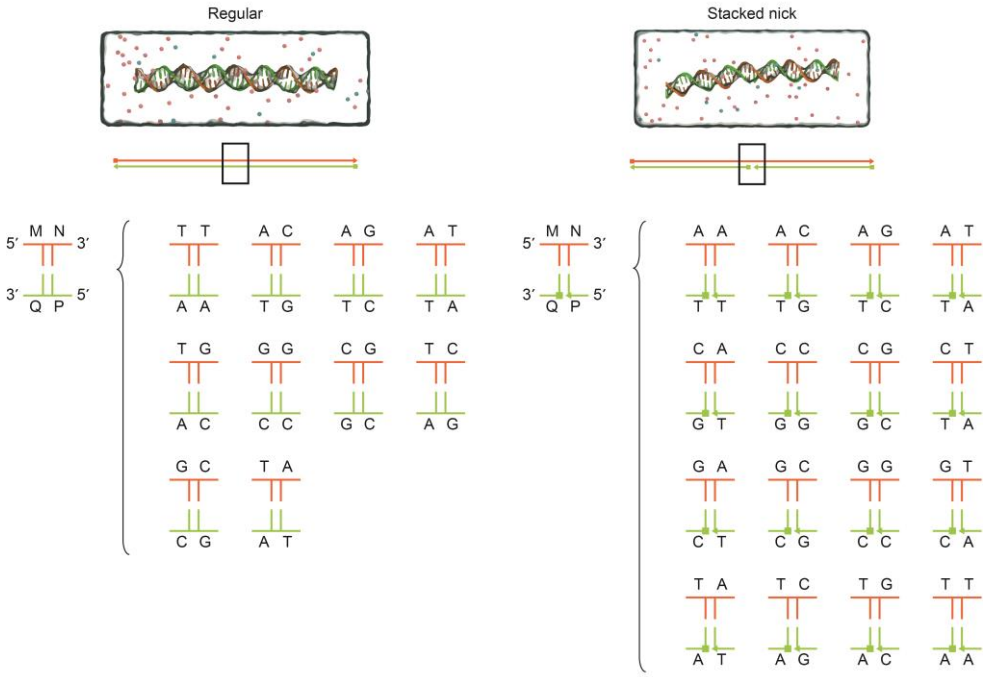

Figure 2-1. A schematic illustration representing the DNA helices. All-atom models of ten helices and 16 helices are generated to investigate the sequence-dependent properties of the regular and stacked nick motifs, respectively. Each DNA helix is assigned a specific name that reflects its structural motif and the base sequences it comprises. Examples of these designations include regular (AA/TT) and stacked nick (AA/TnT).

Table 2-1. Base sequences of DNA helices analyzed using all-atom molecular dynamics simulations. All DNA helices are comprised of two complementary DNA strands. The first strand is characterized by the sequence of 5'-$(CTGA)_5$-MN-$(AGTC)_5$-3'. The base sequences of the second strand in the regular and stacked nick helices are 5'-$(GACT)_5$-PQ-$(TCAG)_5$-3' and 5'-$(GACT)_5$-PnQ-$(TCAG)_5$-3', respectively. Here n indicates the presence of a nick.

Structural motifs	Sequence	M	N	P	Q
Regular	AA/TT	T	T	A	A
	AC/GT	A	C	G	T
	AG/CT	A	G	C	T
	AT/AT	A	T	A	T
	CA/TG	T	G	C	A
	CC/GG	G	G	C	C
	CG/CG	C	G	C	G
	GA/TC	T	C	G	A
	GC/GC	G	C	G	C
	TA/TA	T	A	T	A
Stacked nick	AA/TnT	A	A	T	T
	AC/GnT	A	C	G	T
	AG/CnT	A	G	C	T
	AT/AnT	A	T	A	T
	CA/TnG	C	A	T	G
	CC/GnG	C	C	G	G
	CG/CnG	C	G	C	G
	CT/AnG	C	T	A	G
	GA/TnC	G	A	T	C
	GC/GnC	G	C	G	C
	GG/CnC	G	G	C	C
	GT/AnC	G	T	A	C
	TA/TnA	T	A	T	A
	TC/GnA	T	C	G	A
	TG/CnA	T	G	C	A
	TT/AnA	T	T	A	A

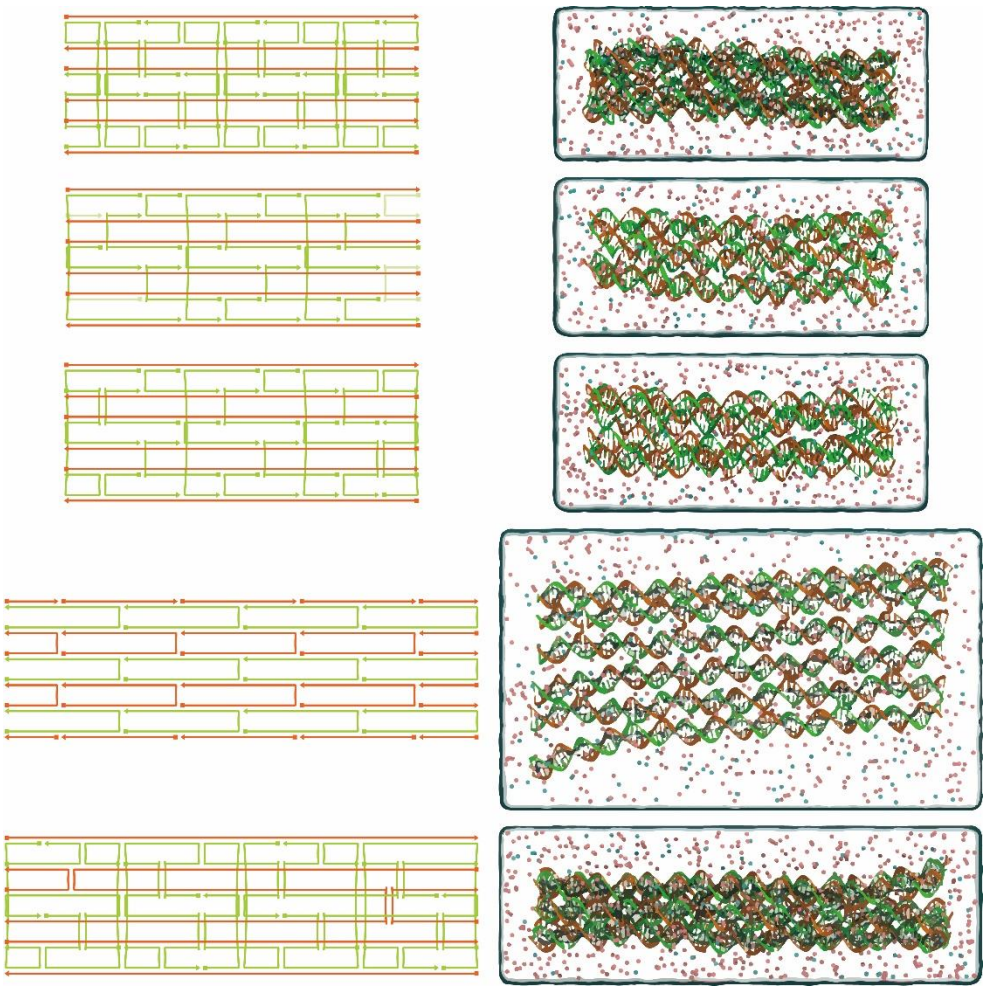

Figure 2-2. A variety of DNA bundle structures. The first design invloves constructing four all-atom models of 6-helix-bundle DNA structures with varying sequences, resulting in a total of 13 bundle structures. Through the utilization of all-atom molecular dynamics simulations, the sequence-dependent properties of structural motifs such as junction nick, double junction, single junction, and open nick are investigated. Each bundle structure is uniquely designated with names like 6-helix-bundle-1.1, 6-helix-bundle-1.2, 6-helix-bundle-1.3, 6-helix-bundle-1.4, 6-helix-bundle-2, 6-helix-bundle-3, 6-helix-bundle-4, 6-helix-bundle-5, 6-helix-bundle-6, 6-helix-bundle-7, 6-helix-bundle-8, 6-helix-bundle-9, and 6-helix-bundle-10.

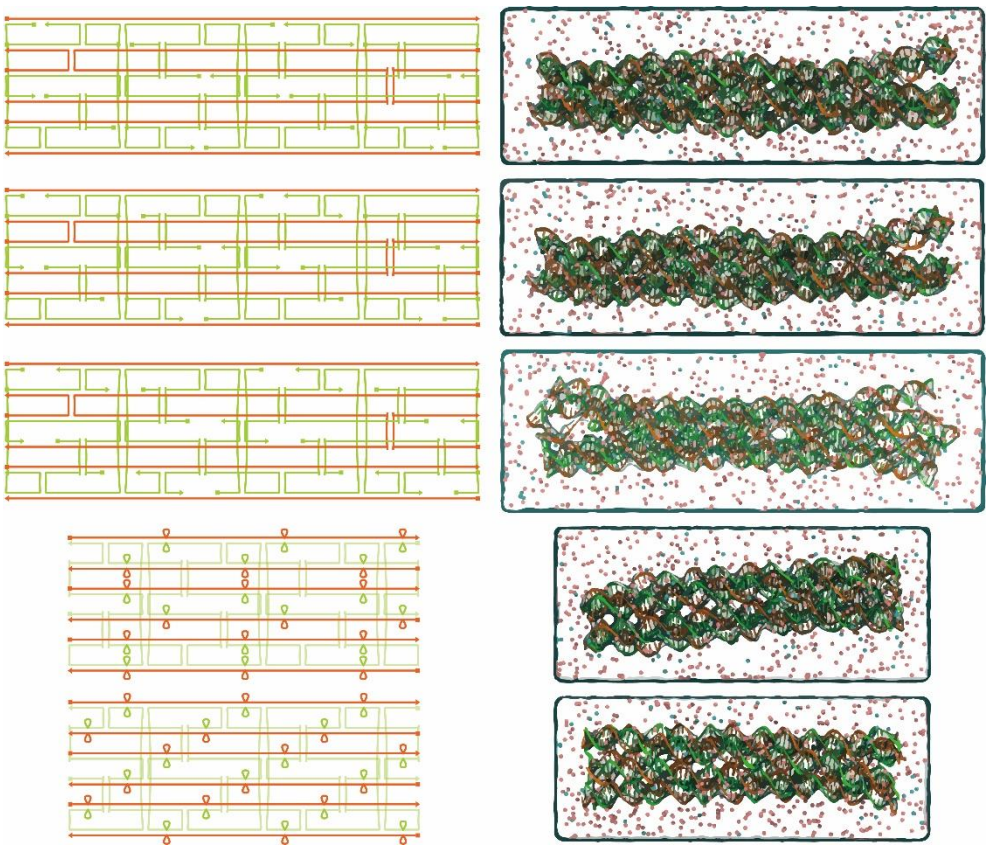

Figure 2-2 (Continued)

Table 2-2. The number of structural motifs belonging to DNA bundle structures.

Models	Structural motifs			
	Double junction	Single junction	Junction nick	Open nick
6-helix-bundle-1.1	32	0	32	4
6-helix-bundle-1.2	32	0	32	4
6-helix-bundle-1.3	32	0	32	4
6-helix-bundle-1.4	32	0	32	4
6-helix-bundle-2	0	15	30	2
6-helix-bundle-3	8	12	32	4
6-helix-bundle-4	0	17	34	3
6-helix-bundle-5	42	0	42	4
6-helix-bundle-6	42	0	42	4
6-helix-bundle-7	42	0	42	4
6-helix-bundle-8	42	0	42	4
6-helix-bundle-9	32	0	32	4
6-helix-bundle-10	32	0	32	4

2.3. All-atom molecular dynamics simulations

We perform all-atom molecular dynamics simulations on a comprehensive set comprising the 26 DNA helices and the 13 DNA bundle structures, using the NAMD program[34] with the AMBER BSC1 force-field[35]. The AMBER BSC1 force-field is selected since it well aligns with experimental findings on various DNA nanostructures[35,36]. Each DNA atomic structure is explicitly solvated using the TIP3P water box[37], and ionized with $MgCl_2$ to neutralize the negative charge of nucleotides. Periodic boundary conditions are applied with the 15 [Å] padding distance between the DNA structure and the cell boundary. Information regarding the box dimension and the number of water and ion molecules for every simulation set is tabulated in Table A-2 (in Appendix A.3). The short-range electrostatic and van der Walls potentials are employed with a cutoff distance of 12 [Å]. For efficient computation of long-range electrostatic interactions, the Particle Mesh Ewald method[38] is used with a grid spacing of 1 [Å]. We perform static energy minimization over 20000 steps, employing a time step of 2 [fs]. Following a pre-equilibrium procedure lasting 10 [ns], we obtain trajectories spanning 300 [ns] under the isobaric-isothermal ensemble, with a pressure of 1 [bar] and a temperature of 300 [K]. The Nosé–Hoover Langevin piston scheme[39] and Langevin thermostat[34] are employed for pressure and temperature control, respectively. Structural properties of DNA structural motifs are analyzed based on the last 150 [ns] of trajectories, focusing on converged states exhibiting equilibrated root-mean-squared deviation values (Figure 2-3).

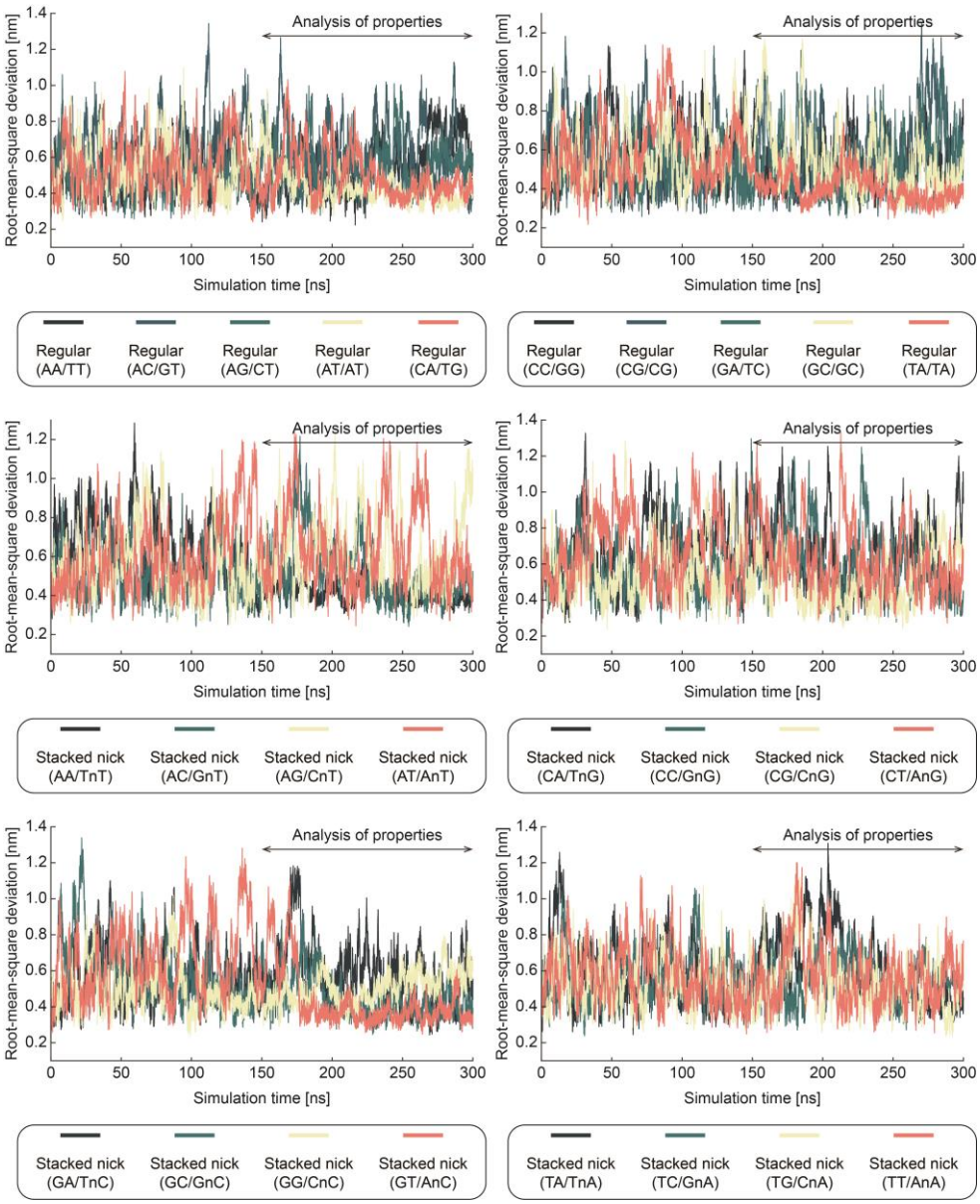

Figure 2-3. Root-mean-squared deviations of DNA helices and DNA bundle structures. Throughout the 300 [ns] molecular dynamics simulations, the root-mean-squared deviations are 0.56 ± 0.16 [nm] for DNA helices and 1.00 ± 0.30 [nm] for DNA bundle structures. The analysis of geometric and mechanical properties of DNA structural motifs is carried out using the simulation trajectories from the last 150 [ns].

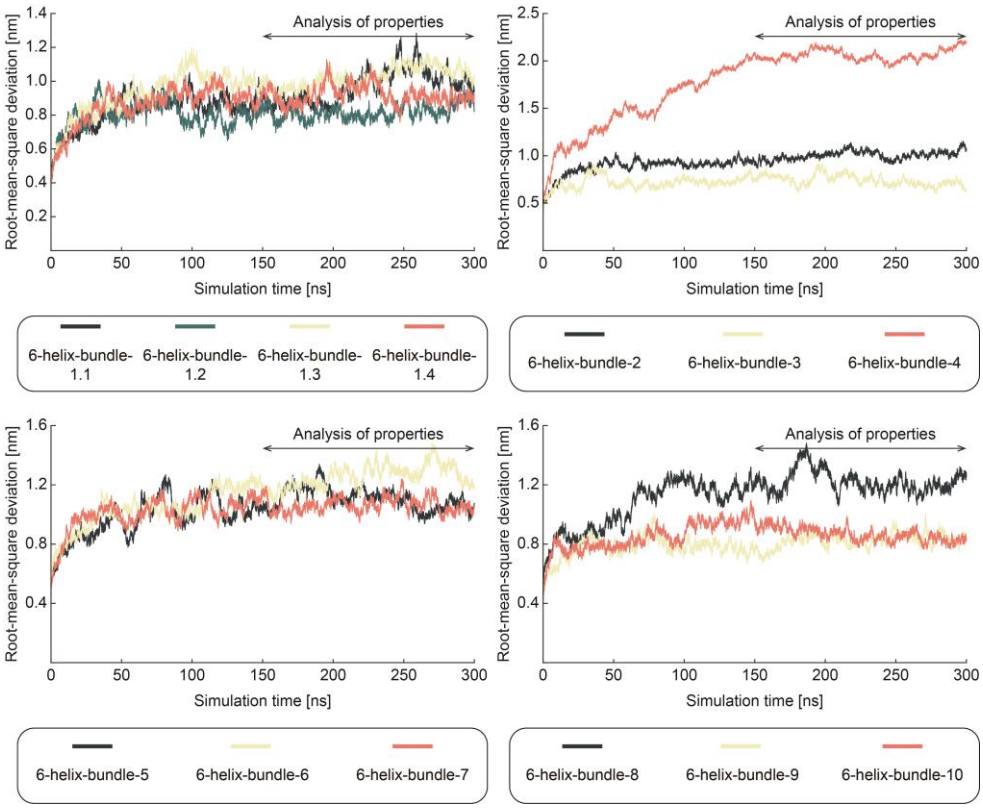

Figure 2-3 (Continued)

2.4. Analysis of properties of DNA structural motifs

In order to analyze the geometric and mechanical properties of DNA structural motifs, we begin by defining the base-pairs that compose the DNA helices and DNA bundle structures used in the molecular dynamics simulations as nodes. For each base-pair node, we establish the respective position and triad orientation vectors for each base-pair node, as well as the triad orientation vectors of the element representing the structural motif. By employing the 3DNA definition[31,32], we obtain the position vector ($\vec{O}_k$) and original triad vectors ($\vec{e}_{x,k}$, $\vec{e}_{y,k}$, and $\vec{e}_{z,k}$) for the *k*th base-pair node. In this study, utilizing this information, we newly define the triad orientation vectors ($\vec{m}_{x,k}$, $\vec{m}_{y,k}$, and $\vec{m}_{z,k}$) of the *k*th node among the interconnected base-pairs, which exhibit structural motifs like the regular, stacked nick, or junction nick motifs, which are expressed as equations (2-1), (2-2), and (2-3). Here, k is set to be 1 or 2.

$$\vec{m}_{x,k} = \vec{e}_{z,k} \tag{2-1}$$

$$\vec{m}_{y,k} = \vec{e}_{y,k} \tag{2-2}$$

$$\vec{m}_{z,k} = -\vec{e}_{x,k} \tag{2-3}$$

On the other hand, the *k*th base-pair in two base-pairs connected via the double junction, single junction, or open nick motifs has the triad vectors calculated as

$$\vec{m}_{y,k} = -\vec{e}_{x,k} \tag{2-4}$$

$$\vec{m}_{z,k} = \vec{e}_{z,k}{}^{out} \tag{2-5}$$

$$\vec{m}_{x,k} = \vec{m}_{y,k} \times \vec{m}_{z,k} \tag{2-6}$$

where $\vec{e}_{z,k}{}^{out}$ is the normal vector of the *k*th node, defined by 3DNA[31,32], pointing outward of the helix. After determining the nodal triad vectors, the hinge axis ($\vec{h}$) and bending angle (Γ) between the nodes are calculated as equations (2-7) and (2-8).

$$\vec{h} = [h_x \quad h_y \quad h_z]^T = \frac{\vec{m}_{x,1} \times \vec{m}_{x,2}}{\|\vec{m}_{x,1} \times \vec{m}_{x,2}\|} \tag{2-7}$$

$$\Gamma = \cos^{-1}(\vec{m}_{x,1} \cdot \vec{m}_{x,2}) \tag{2-8}$$

Considering a rotation vector ($\vec{u} = [u_x \quad u_y \quad u_z]^T$) and a rotation angle ($\theta$), the corresponding rotation matrix (**R**) is expressed as

$$\mathbf{R}(\vec{u}|\theta) = \begin{bmatrix} c_\theta + (1-c_\theta){u_x}^2 & (1-c_\theta)u_x u_y - s_\theta u_z & (1-c_\theta)u_x u_z + s_\theta u_y \\ (1-c_\theta)u_x u_y + s_\theta u_z & c_\theta + (1-c_\theta){u_y}^2 & (1-c_\theta)u_y u_z - s_\theta u_x \\ (1-c_\theta)u_x u_z - s_\theta u_y & (1-c_\theta)u_y u_z + s_\theta u_x & c_\theta + (1-c_\theta){u_z}^2 \end{bmatrix} \tag{2-9}$$

where c_θ and s_θ are $\cos\theta$ and $\sin\theta$, respectively. Then, the aligned nodal orientation matrix ($\mathbf{B}_k$) of the *k*th node is calculated as equation (2-10).

$$\mathbf{B}_k = \mathbf{R}\left(\vec{h}\middle|(-1)^{k+1}\frac{\Gamma}{2}\right)[\vec{m}_{x,k} \quad \vec{m}_{y,k} \quad \vec{m}_{z,k}] \tag{2-10}$$

The triad orientation matrix ($\bar{\mathbf{R}}$) of the element is determined by using two aligned nodal orientation matrices as equations (2-11) and (2-12).

$$\boldsymbol{\mathcal{B}} = [\vec{\mathscr{b}}_x \quad \vec{\mathscr{b}}_y \quad \vec{\mathscr{b}}_z] = \mathbf{B}_1 + \mathbf{B}_2 \tag{2-11}$$

$$\bar{\mathbf{R}} = [\vec{r}_x \quad \vec{r}_y \quad \vec{r}_z] = \left[\frac{\vec{\mathscr{b}}_x}{\|\vec{\mathscr{b}}_x\|} \quad \frac{\vec{\mathscr{b}}_y}{\|\vec{\mathscr{b}}_y\|} \quad \frac{\vec{\mathscr{b}}_z}{\|\vec{\mathscr{b}}_z\|}\right] \tag{2-12}$$

By utilizing equations (2-13) to (2-16), the orientation matirx of the the double

junction, single junction, or open nick motifs is refined to $\bar{\boldsymbol{\mathcal{R}}}$, considring the significant difference in direction between $\vec{\mathrm{m}}_{\mathrm{x}}$ and the connecting vector between the two nodes, in contrast to the regular, stacked nick, and junction nick motifs.

$$\vec{r}_{\mathrm{x}} = \frac{\vec{\mathrm{O}}_2 - \vec{\mathrm{O}}_1}{\left\|\vec{\mathrm{O}}_2 - \vec{\mathrm{O}}_1\right\|} \tag{2-13}$$

$$\vec{r}_{\mathrm{z}} = \frac{\vec{r}_{\mathrm{x}} \times \left(\vec{\mathrm{m}}_{\mathrm{y},1} + \vec{\mathrm{m}}_{\mathrm{y},2}\right)}{\left\|\vec{r}_{\mathrm{x}} \times \left(\vec{\mathrm{m}}_{\mathrm{y},1} + \vec{\mathrm{m}}_{\mathrm{y},2}\right)\right\|} \tag{2-14}$$

$$\vec{r}_{\mathrm{y}} = \vec{r}_{\mathrm{z}} \times \vec{r}_{\mathrm{x}} \tag{2-15}$$

$$\bar{\boldsymbol{\mathcal{R}}} = \begin{bmatrix} \vec{r}_{\mathrm{x}} & \vec{r}_{\mathrm{y}} & \vec{r}_{\mathrm{z}} \end{bmatrix} \tag{2-16}$$

Included in the geometric properties are the translational and rotational relations. The translational relations ($\mathrm{T_x}$, $\mathrm{T_y}$, and $\mathrm{T_z}$) between two nodes are calculated as equation (2-17).

$$\begin{bmatrix} \mathrm{T_x} & \mathrm{T_y} & \mathrm{T_z} \end{bmatrix} = \left(\vec{\mathrm{O}}_2 - \vec{\mathrm{O}}_1\right)^{\mathrm{T}} \bar{\mathbf{R}} \tag{2-17}$$

Also, the rotational relations ($\mathrm{R_{x,k}}$, $\mathrm{R_{y,k}}$, and $\mathrm{R_{z,k}}$) between the *k*th node and the element are analyzed as

$$\begin{bmatrix} \mathrm{R_{x,k}} & \mathrm{R_{y,k}} & \mathrm{R_{z,k}} \end{bmatrix} = \begin{bmatrix} -\mathrm{C}_{\mathrm{k}}^{(2,3)} & \mathrm{C}_{\mathrm{k}}^{(1,3)} & -\mathrm{C}_{\mathrm{k}}^{(1,2)} \end{bmatrix} \tag{2-18}$$

where $\mathrm{C}_{\mathrm{k}}^{(\mathrm{i,j})}$ represents the component at the *i*th row and the *j*th column of the matrix $\mathbf{C}_{\mathrm{k}}$, which is defined as equation (2-19).

$$\mathbf{C}_k = \frac{\cos^{-1}\left(\frac{\mathrm{tr}(\mathbf{R}_k) - 1}{2}\right)}{2\sin\left(\cos^{-1}\left(\frac{\mathrm{tr}(\mathbf{R}_k) - 1}{2}\right)\right)}\left(\mathbf{R}_k - \mathbf{R}_k{}^{\mathrm{T}}\right) \tag{2-19}$$

Here, $\mathbf{R}_k$ indicates the matrix representing the rotational relation between the *k*th node and the element, which is determined as

$$\mathbf{R}_k = \mathbf{A}^{\mathrm{T}}\left[\vec{\mathrm{m}}_{x,k} \quad \vec{\mathrm{m}}_{y,k} \quad \vec{\mathrm{m}}_{z,k}\right] \tag{2-20}$$

where $\mathbf{A}$ is $\bar{\mathbf{R}}$ for the regular, stacked nick, and junction nick motifs, or $\bar{\boldsymbol{\mathcal{R}}}$ for the double junction, single junction, and open nick motifs. The rotational relations ($\mathrm{R_x}$, $\mathrm{R_y}$, and $\mathrm{R_z}$) between two nodes are calculated as equation (2-21).

$$[\mathrm{R_x} \quad \mathrm{R_y} \quad \mathrm{R_z}] = [\mathrm{R}_{x,2} - \mathrm{R}_{x,1} \quad \mathrm{R}_{y,2} - \mathrm{R}_{y,1} \quad \mathrm{R}_{z,2} - \mathrm{R}_{z,1}] \tag{2-21}$$

To obtain the mechanical properties of structural motifs, we construct the covariance matrix (**H**) with the geometric properties between two nodes based on the quasi-harmonic approximation[33] as

$$\mathbf{H} = \langle(\vec{\mathrm{s}} - \langle\vec{\mathrm{s}}\rangle) \otimes (\vec{\mathrm{s}} - \langle\vec{\mathrm{s}}\rangle)\rangle \tag{2-22}$$

where $\vec{\mathrm{s}}$ is the parameter vector and $\langle\vec{\mathrm{s}}\rangle$ is the ensemble average of $\vec{\mathrm{s}}$, which are expressed as equations (2-23) and (2-24), respectively.

$$\vec{\mathrm{s}} = [\mathrm{T_x} \quad \mathrm{T_y} \quad \mathrm{T_z} \quad \mathrm{R_x} \quad \mathrm{R_y} \quad \mathrm{R_z}]^{\mathrm{T}} \tag{2-23}$$

$$\langle\vec{\mathrm{s}}\rangle = [\langle\mathrm{T_x}\rangle \quad \langle\mathrm{T_y}\rangle \quad \langle\mathrm{T_z}\rangle \quad \langle\mathrm{R_x}\rangle \quad \langle\mathrm{R_y}\rangle \quad \langle\mathrm{R_z}\rangle]^{\mathrm{T}} \tag{2-24}$$

Then, the stiffness matrix (**K**) of structural motifs is derived as

$$\mathbf{K} = k_B T_a \mathbf{H}^{-1} \tag{2-25}$$

where k_B and T_a are the Boltzmann's constant and the absolute temperature, respectively. The mechanical rigidity matrix (**L**) is calculated as

$$\mathbf{L} = \begin{bmatrix} S & G_{T_xT_y} & G_{T_xT_z} & G_{T_xR_x} & G_{T_xR_y} & G_{T_xR_z} \\ G_{T_xT_y} & Y_y & G_{T_yT_z} & G_{T_yR_x} & G_{T_yR_y} & G_{T_yR_z} \\ G_{T_xT_z} & G_{T_yT_z} & Y_z & G_{T_zR_x} & G_{T_zR_y} & G_{T_zR_z} \\ G_{T_xR_x} & G_{T_yR_x} & G_{T_zR_x} & C & G_{R_xR_y} & G_{R_xR_z} \\ G_{T_xR_y} & G_{T_yR_y} & G_{T_zR_y} & G_{R_xR_y} & B_y & G_{R_yR_z} \\ G_{T_xR_z} & G_{T_yR_z} & G_{T_zR_z} & G_{R_xR_z} & G_{R_yR_z} & B_z \end{bmatrix} = \mathbf{K}\|\vec{O}_2 - \vec{O}_1\| \tag{2-26}$$

where S, Y_y, Y_z, C, B_y, B_z, and $G_{s_1s_2}$ represent the stretching rigidity of T_x, the shearing rigidities of T_y and T_z, the twisting rigidity of R_x, the bending rigidity of R_y and R_z, and the coupling coefficients of two geometric parameters s_1 and s_2, respectively. Here, $G_{s_1s_2}$ is also expressed as $G(s_1, s_2)$. The equivalent isotropic shearing (Y) and bending (B) rigidities are calculated by using the harmonic average of Y_y and Y_z, and B_y and B_z, respectively, as equations (2-27) and (2-28).

$$Y = \frac{2Y_yY_z}{Y_y + Y_z} \tag{2-27}$$

$$B = \frac{2B_yB_z}{B_y + B_z} \tag{2-28}$$

2.5. Geometric properties of structural motifs

We first investigate the sequence-dependent geometric properties of stacked motifs which include regular, stacked nick, and junction nick. For the regular motif, the values of T_x, T_y, T_z, $R_{x,1}$, $R_{x,2}$, $R_{y,1}$, $R_{y,2}$, $R_{z,1}$, and $R_{z,2}$ between two base-pairs are measured as 0.34 ± 0.03 [nm], -0.05 ± 0.07 [nm], -0.04 ± 0.08 [nm], -17.46 ± 2.95 [°], 17.46 ± 2.94 [°], -1.58 ± 3.25 [°], 1.34 ± 3.25 [°], 0.53 ± 2.44 [°], and -0.94 ± 2.46 [°], respectively. Detailed values for each sequence of the regular motif are represented in Table A-3 (in Appendix A.4). In the case of the stacked nick motif, the geometric properties include T_x (0.33 ± 0.03 [nm]), T_y (-0.07 ± 0.08 [nm]), T_z (0.00 ± 0.09 [nm]), $R_{x,1}$ (-16.03 ± 4.89 [°]), $R_{x,2}$ (16.03 ± 4.88 [°]), $R_{y,1}$ (-1.24 ± 3.34 [°]), $R_{y,2}$ (1.26 ± 3.35 [°]), $R_{z,1}$ (-0.28 ± 2.59 [°]), and $R_{z,2}$ (0.02 ± 2.58 [°]), calculated on average across base sequences. Similarly, for the junction nick motif, the geometric properties consist of averaged values for T_x (0.31 ± 0.08 [nm]), T_y (-0.07 ± 0.10 [nm]), T_z (-0.03 ± 0.19 [nm]), $R_{x,1}$ (-14.52 ± 6.46 [°]), $R_{x,2}$ (14.51 ± 6.39 [°]), $R_{y,1}$ (-1.39 ± 4.51 [°]), $R_{y,2}$ (1.34 ± 4.61 [°]), $R_{z,1}$ (0.09 ± 5.06 [°]), and $R_{z,2}$ (-0.37 ± 4.93 [°]). Detailed values for each sequence of the stacked nick and junction nick motifs are represented in Table A-4 and Table A-5 (in Appendix A.4), respectively.

Geometric parameters (shift, slide, rise, tilt, roll, and twist) of two stacked base-pairs are defined using 3DNA[31,32]. Here, these parameters can be calculated as $-T_z$, T_y, T_x, $R_{z,1} - R_{z,2}$, $R_{y,2} - R_{y,1}$, and $R_{x,2} - R_{x,1}$, respectively. Our comprehensive analysis, based on the all-atom molecular dynamics simulations, reveals the following 3DNA geometric parameters for the regular, stacked nick, and junction nick motifs: shift of 0.04 ± 0.08 [nm], 0.00 ± 0.09 [nm], and 0.03 ± 0.19 [nm]; slide of -0.05 ± 0.07 [nm], -0.07 ± 0.08 [nm], and -0.07 ± 0.10 [nm]; rise of 0.34 ± 0.03 [nm], 0.33 ± 0.03 [nm], and 0.31 ± 0.08 [nm]; tilt of 1.50 ± 4.82 [°], -0.32 ± 5.10 [°], and 0.49 ± 9.83 [°]; roll of 2.95 ± 6.45 [°], 2.49 ± 6.64 [°], and 2.69 ± 8.56 [°]; and twist of 34.93 ± 5.89 [°], 32.08 ± 9.75 [°], and 29.05 ± 12.87 [°]. These findings align with previously reported values[29,33]. Detailed 3DNA parameters for each sequence are represented in Tables A-6, A-7, and A-8 (in Appendix A.4).

In addition, we investigate the sequence-dependent geometric properties of crossover motifs such as double junction, single junction, and open nick. Unlike the stacked motifs, the determination of triad orientation vectors in these cases follows a different approach. Specifically, the geometric properties of the double junction and single junction motifs include T_x of 1.81 ± 0.15 [nm] and 1.79 ± 0.13 [nm], T_y of 0.43 ± 0.24 [nm] and 0.51 ± 0.14 [nm], T_z of 0.17 ± 0.25 [nm] and 0.18 ± 0.19 [nm], $R_{x,1}$ of -2.15 ± 9.22 [º] and -0.13 ± 7.47 [º], $R_{x,2}$ of 3.62 ± 8.71 [º] and 2.01 ± 6.99 [º], $R_{y,1}$ of 6.83 ± 10.95 [º] and 7.04 ± 8.70 [º], $R_{y,2}$ of 4.08 ± 11.13 [º] and 5.00 ± 7.63 [º], $R_{z,1}$ of -28.37 ± 18.54 [º] and -41.29 ± 17.72 [º], and $R_{z,2}$ of 2.04 ± 15.28 [º] and 9.56 ± 13.64 [º], respectively. Also, the open nick motif exhibit the geometric properties with T_x of 1.54 ± 0.45 [nm], T_y of 0.26 ± 0.46 [nm], T_z of 0.10 ± 0.36 [nm], $R_{x,1}$ of 1.02 ± 16.12 [º], $R_{x,2}$ of 1.89 ± 17.98 [º], $R_{y,1}$ of 15.93 ± 26.67 [º], $R_{y,2}$ of -4.19 ± 20.27 [º], $R_{z,1}$ of -24.93 ± 32.54 [º], and $R_{z,2}$ of 8.00 ± 20.64 [º], based on the average across base sequences. Detailed sequence-dependent geometric properties for the double junction, single junction, and open nick motifs are represented in Tables A-9, A-10, and A-11 (in Appendix A.4). Figure 2-4 provides an overview of the overall sequence-dependent geometric properties of all DNA structural motifs.

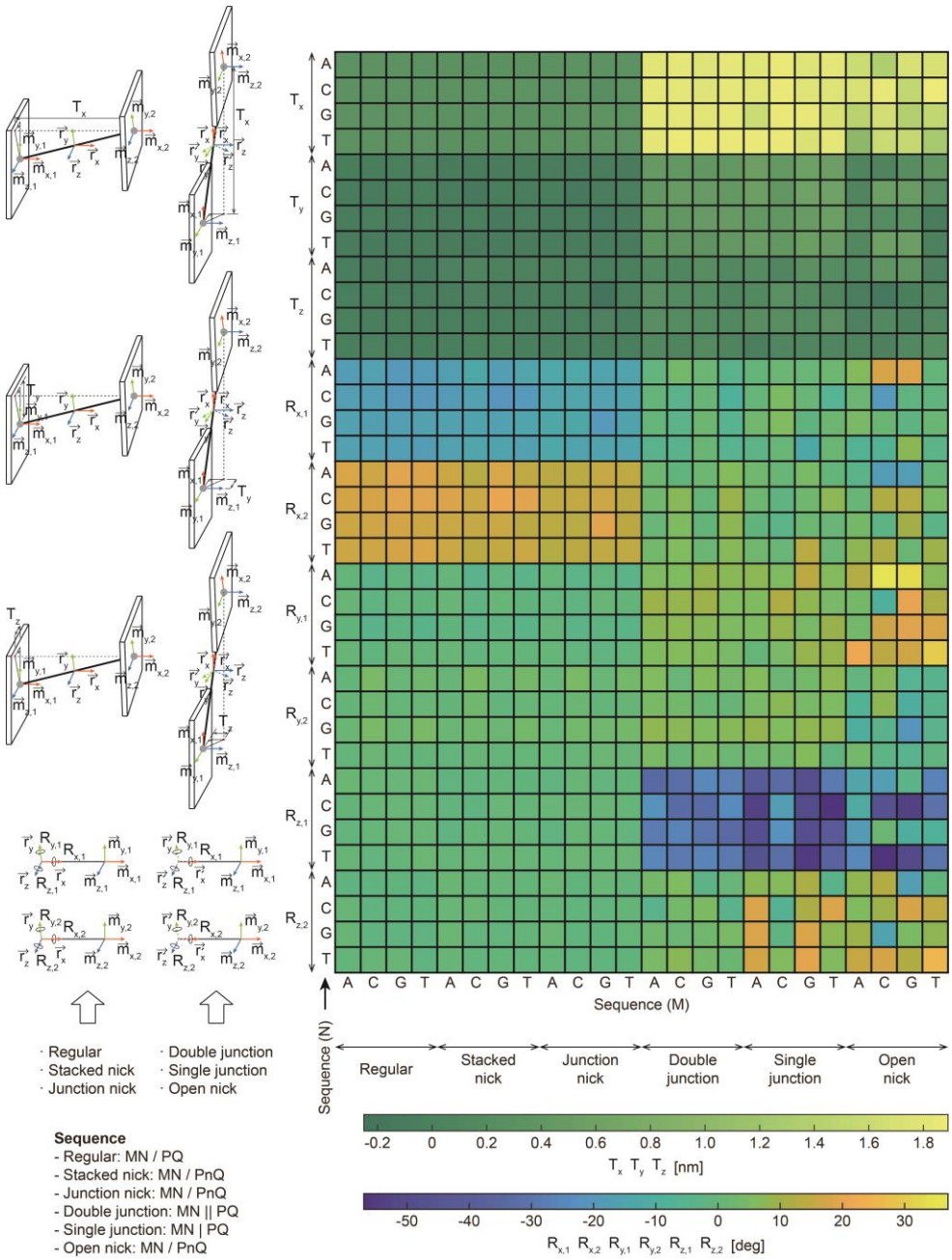

Figure 2-4. Sequence-dependent geometric properties of DNA structural motifs. Prticularly significant are the values of $R_{x,1}$ and $R_{x,2}$ in the stacked motifs (regular, stacked nick, and junction nick), as well as T_x and $R_{z,1}$ in the crossover motifs (double junction, single junction, and open nick).

2.6. Mechanical rigidities of structural motifs

The sequence-dependent mechanical properties of DNA structural motifs are calculated from the geometric properties analyzed above. These mechanical properties encompass a total of 21 rigidities, including stretching rigidity (S), shearing rigidities (Y_y and Y_z), twisting rigidity (C), bending rigidities (B_y and B_z), and 15 coupling coefficients (G).

For the regular motif, the six primary mechanical rigidities are as folllows: S (2211.02 ± 484.91 [pN]), Y_y (658.85 ± 159.20 [pN]), Y_z (400.60 ± 88.03 [pN]), C (283.43 ± 77.74 [pN·nm^2]), B_y (197.82 ± 40.16 [pN·nm^2]), and B_z (311.64 ± 63.50 [pN·nm^2]). Additionally, the equivalent isotropic shearing rigidity (Y) and bending rigidity (B) of the regular motif are measured to be 489.81 ± 97.34 [pN] and 240.16 ± 44.28 [pN·nm^2], respectively. In the case of the stacked nick and junction nick motifs, the mechanical rigidities include S (2044.49 ± 438.33 [pN] and 2052.96 ± 642.56 [pN]), Y_y (430.42 ± 123.54 [pN] and 742.85 ± 332.76 [pN]), Y_z (343.71 ± 97.62 [pN] and 466.21 ± 174.72 [pN]), Y (373.47 ± 98.42 [pN] and 533.38 ± 172.59 [pN]), C (129.43 ± 40.72 [pN·nm^2] and 233.29 ± 100.92 [pN·nm^2]), B_y (180.25 ± 39.27 [pN·nm^2] and 201.59 ± 66.64 [pN·nm^2]), B_z (271.49 ± 58.30 [pN·nm^2] and 268.49 ± 81.83 [pN·nm^2]), and B (214.26 ± 40.58 [pN·nm^2] and 222.31 ± 57.13 [pN·nm^2]), respectively, averaged over the base sequences. These findings are consistent with previously reported values[33].

Furthermore, the results reaffirm the previously reported fact[33] that the twisting rigidity experiences a significant reduction of approximately 54.33 [%] on average when the regular motif transforms into the stacked nick motif. Also, the findings indicate that shearing and bending towards the groove (Y_z and B_y) exhibit greater flexibility compared to those towards the backbone (Y_y and B_z), which confirms an established observation[33].

Moreover, the investigation of the mechanical properties of the DNA helix reveals a negatively correlation between twist and stretch, which has been extensively studied in both experimental and computational investigations[33,40-44]. The coupling coefficient ($G(T_x, R_x)$) for the regular and stacked nick motifs has

values of -200.10 ± 44.99 [pN·nm] and -145.07 ± 37.23 [pN·nm], respectively. Also, the structural motifs exhibit a negative twist-slide coupling ($G(T_y, R_x)$), with values of -142.06 ± 55.47 [pN·nm] and -82.20 ± 40.46 [pN·nm], respectively. This implies that DNA undergoes elongation while the inter-strand distance corresponding to slide decreases when it is over-twisted. More detailed sequence-dependent mechanical rigidities for the regular, stacked nick, and junction nick motifs are represented in Tables A-12, A-13, and A-14 (in Appendix A.5), respectively, which align with the reference values[29,33].

The mechanical rigidities of the double junction and single junction motifs are as follows: for the double junction, S is 3668.64 ± 1991.87 [pN], Y_y of 1368.53 ± 533.71 [pN], Y_z is 625.03 ± 230.69 [pN], C is 413.78 ± 105.96 [pN·nm^2], B_y is 401.52 ± 133.65 [pN·nm^2], and B_z is 521.13 ± 333.06 [pN·nm^2], and for the single junction, S is 2365.95 ± 1431.28 [pN], Y_y is 1542.85 ± 505.73 [pN], Y_z is 532.10 ± 277.35 [pN], C is 333.05 ± 80.85 [pN·nm^2], B_y is 289.25 ± 102.38 [pN·nm^2], and B_z is 306.26 ± 160.42 [pN·nm^2]. On average, the double junction exhibits higher values for Y and B, with Y being 811.43 ± 263.29 [pN] and B being 420.33 ± 160.79 [pN·nm^2], whereas the single junction has Y of 755.30 ± 266.15 [pN] and B of 281.19 ± 94.45 [pN·nm^2]. As previously reported[29], it is confirmed that the double junction is more rigid than the single junction. Furthermore, the results indicate that both shearing and bending in the direction of the helix (Y_z and B_y) are more flexible compared to those in the direction perpendicular to the helix (Y_y and B_z). The double junction and single junction motifs have a positively correlated coupling of helix-directed shear and twist ($G(T_z, R_x)$) with values of 125.83 ± 72.70 [pN·nm] and 84.32 ± 53.90 [pN·nm], respectivley, indicating that the helix-directed distance in the junction decreases when it becomes over-twisted.

The open nick motif exhibits a similar configuration to the single junction but demonstrates significantly lower rigidity. When transitioning from the single junction to the open nick, the six primary rigidities (S, Y_y, Y_z, C, B_y, and B_z) experience reduction ratios of approximately 77.78 [%], 75.75 [%], 65.28 [%], 58.02 [%], 53.33 [%], and 58.48 [%], respectively. Detailed information on the sequence-

dependent mechanical rigidities of the double junction, single junction, and open nick motifs is represented in Tables A-15, A-16, and A-17 (in Appendix A.5), respectively. The overall mechanical properties of all DNA structural motifs are described in Figures 2-5 and 2-6.

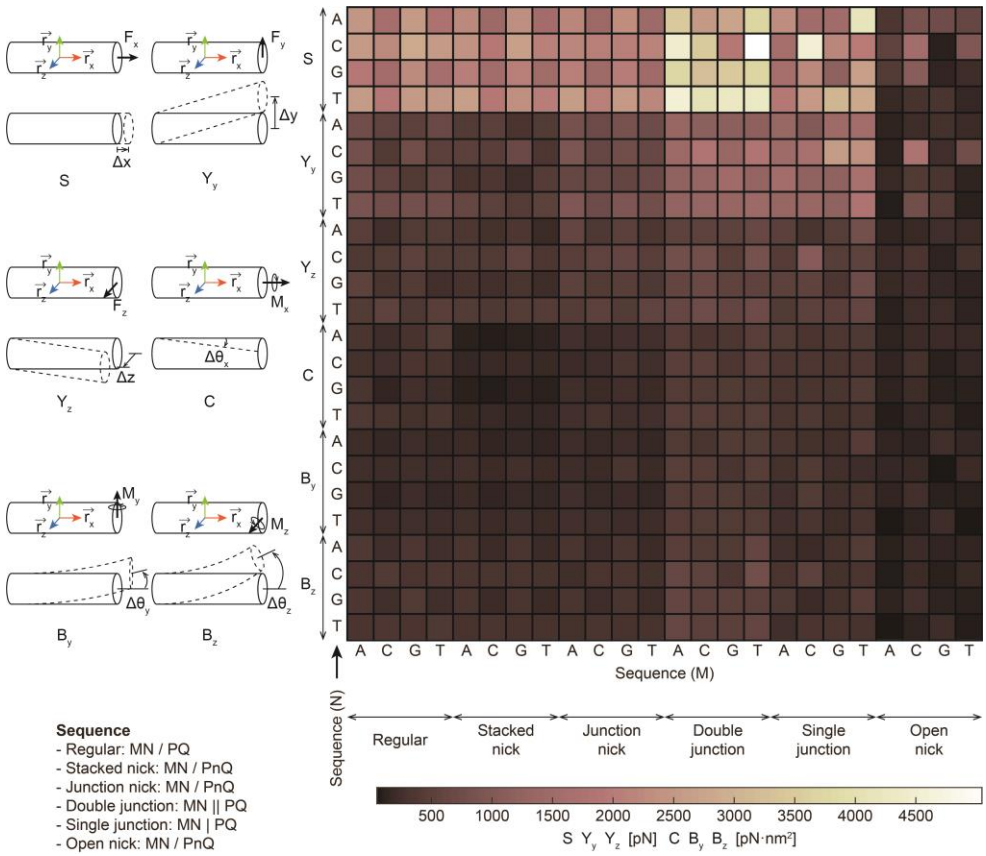

Figure 2-5. Sequence-dependent primary mechanical rigidities of DNA structural motifs. The primary mechanical rigidities encompass the stretching rigidity (S), shearing rigidities (Y_y and Y_z), twisting rigidity (C), and bending rigidities (B_y and B_z).

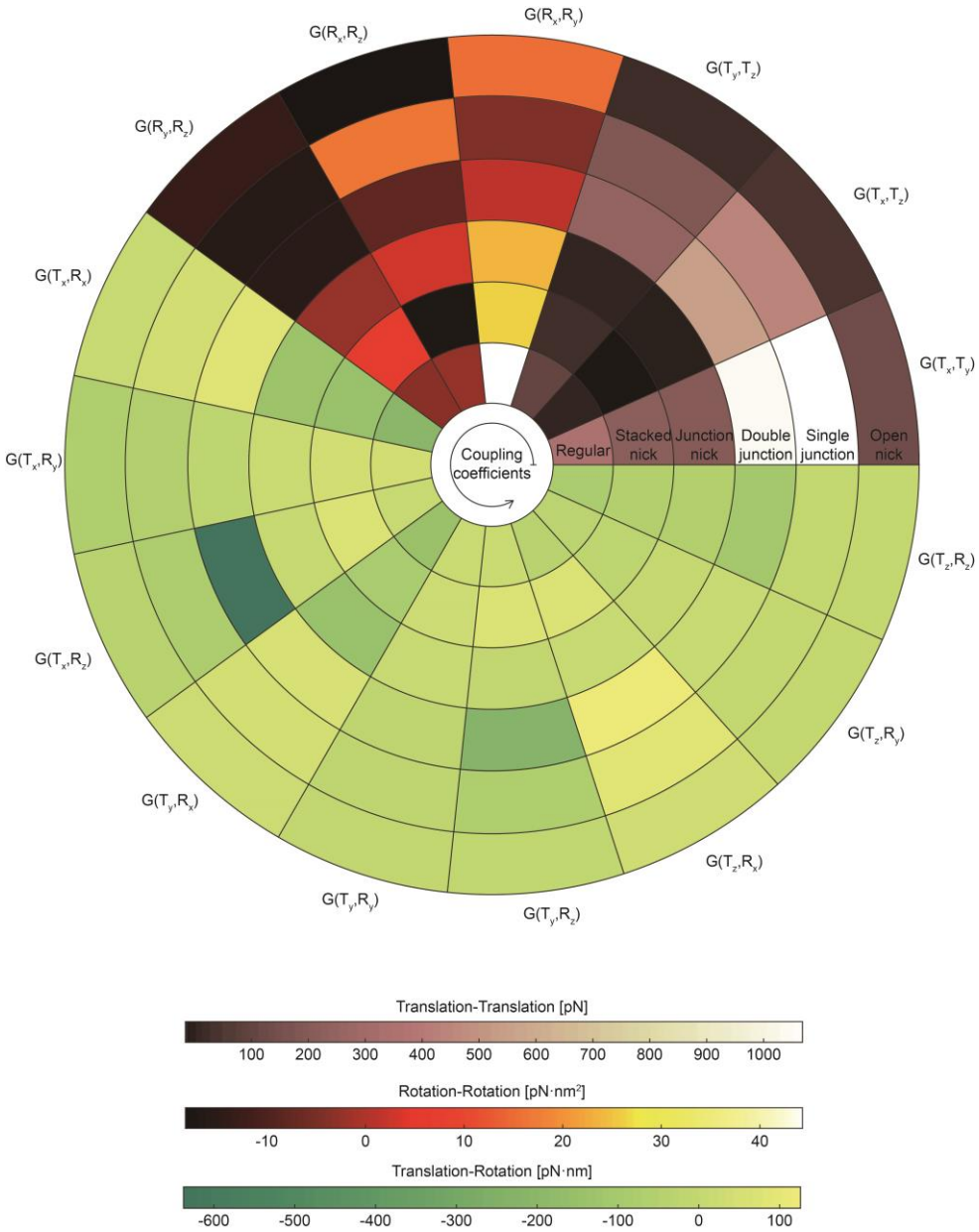

Figure 2-6. Coupling coefficients of DNA structural motifs. The coupling coefficients, totaling 21 for each structural motif, encompass three translation-translation ($G(T_x, T_y)$, $G(T_x, T_z)$, and $G(T_y, T_z)$), three rotation-rotation ($G(R_x, R_y)$, $G(R_x, R_z)$, and $G(R_y, R_z)$), and nine translation-rotation ($G(T_x, R_x)$, $G(T_x, R_y)$, $G(T_x, R_z)$, $G(T_y, R_x)$, $G(T_y, R_y)$, $G(T_y, R_z)$, $G(T_z, R_x)$, $G(T_z, R_y)$, and $G(T_z, R_z)$,) coefficients, which are thoroughly investigated.

3. Generating a DSTBCONF

3.1. Abstract

DNA structural motifs in structured DNA assemblies are roughly classified based on the connectivity between bases. The classification procedure begins by defining two complementary bases as a base-pair and determining the connectivity between base-pairs. Through a comprehensive analysis of both the connectivity between bases and the connectivity between base-pairs, we identify various structural motifs, including regular (representing each component of dsDNA), bulge, ssDNA, nick, and junction. To establish a DSTBCONF, we introduce a force-based placement procedure. This procedure entails positioning vertices in three-dimensional space by applying attractive and repulsive forces to vertices, considering their relative positions and connectivity. When provided with the positions and orientations of base-pairs, as well as the connectivity between bases, we define a cluster of adjacent base-pairs as a substructure. Additionally, a substructure is further divided into four substructures if stretched bonds connecting its ends exist. The substructures and the connections between them are represented as vertices and edges, respectively. By applying the force-based placement procedure, the vertices are spatially distributed. The substructures are rotated to minimize the sum of squared lengths of connections between them, resulting in the establishment of the DSTBCONF. In contrast, when we only have information about the connectivity between bases, dsDNAs and the connections between them are represented as vertices and edges, respectively. The entire network, comprising vertices and edges, is divided into several subnetworks. The subnetworks and the connections between them are represented as unified-vertices and unified-edges, respectively. The force-based placement procedure is applied to both the unified-vertices and the vertices within each subnetwork. The subnetworks are rotated to minimize the sum of squared lengths of connections between them. By applying the force-based placement procedure to all vertices, they are spatially distributed. Finally, the dsDNAs are rotated to minimize the sum of squared lengths of connections

between them, leading to the generation of the DSTBCONF.

3.2. Connectivity between bases

We utilize the connectivity between DNA bases to identify DNA structural motifs within DNA nanostructures. The base connectivity is determined by the topology of all bases in DNA nanostructures and is represented by an N-by-5 matrix, where N is the number of bases. Each column of the matrix contains the unique identifier of a current base, the identifier of its neighboring base in the 5'-direction, the identifier of its neighboring base in the 3'-direction, the identifier of its complementary base, and its base sequence, respectively. The unique identifier of each base, described in the first column, must be the natural number and must be written sequentially from 1. If the current base is not connected to another base in the 5'-direction or the 3'-direction, the second or third column in the matrix contains -1, respectively. Similarly, if the current base is in a single-stranded DNA and has no complementary base, the fourth column contains -1. The sequence of the current base is one of the four bases (adenine, cytosine, guanine, and thymine), which are abbreviated as DA, DC, DG, and DT, respectively, in the fifth column. To adhere to the DNA complementary rule, sequences of complementary bases must be either DA and DT or DC and DG. Two complementary bases are paired together to form a base-pair. The connectivity between base-pairs is constructed based on the connectivity between the individual bases (Figure 3-1). The connectivity between bases of the lattice-based design in Figure 3-1 is detaildly explained in Figure A-1 (in Appendix A.6).

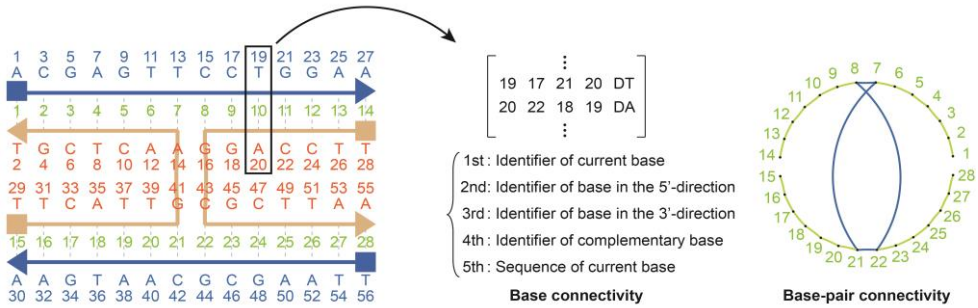

Figure 3-1. Connectivity between DNA bases. The base connectivity indicates the topology of DNA bases that constitute a DNA nanostructure. The connectivity between base-pairs is determined based on the initially set base connectivity.

3.3. Rough classification of DNA structural motifs

By analyzing both the connectivity between bases and the connectivity between base-pairs, we can roughly classify DNA structural motifs in DNA nanostructures. Each motif represesents a connection between two base-pairs. These structural motifs include regular, bulge, ssDNA, nick, and junction, which are determined by the number of DNA strands constituting the motifs, the number of base-pairs connected to each other, and the type of connection. If two base-pairs are connected by two DNA strands, we classify the structural motif as either regular or bulge. A structural motif is considered regular if two bases in a base-pair are directly connected to two bases in the next base-pair. If a cluster of regulars is connected only by regulars without other structural motifs, it is classifed as dsDNA. On the other hand, the structural motif is classified as bulge if one base in a base-pair is directly connected to one base in the next base-pair, and the remaining bases in the base-pairs are connected with several bases between them. When two base-pairs are connected by three DNA strands, the structural motif is calssified as either ssDNA or nick, depending on the presence or absence of additional bases between the base-pairs. If several bases between the base-pairs are present, the structural motif is classified as ssDNA; otherwise, it is classified as nick. Finally, if three or more base-pairs are connected by three or more DNA strands, we classify each structural motif connecting two base-pairs as a junction. Using this classification procedure, DNA structural motifs in DNA nanostructures can be rougly determined based on the connectivity between bases and that between base-pairs (Figure 3-2 and Table 3-1).

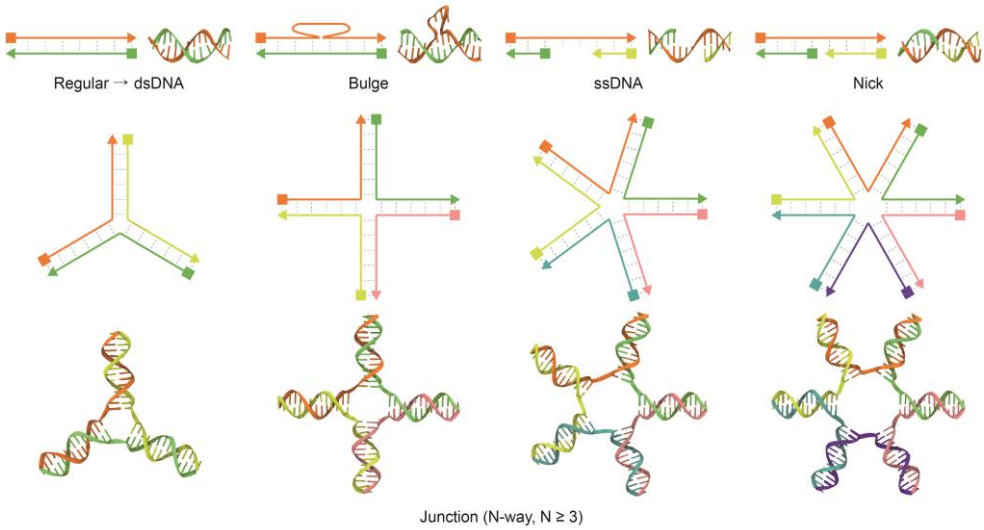

Figure 3-2. Rough classification of DNA structural motifs. Structural motifs within a DNA nanostructure are categorized as dsDNA (a cluster of regulars), bulge, ssDNA, nick, and junction by analyzing the connectivity between bases and the connectivity between base-pairs.

Table 3-1. Criteria for rough classification of DNA structural motifs. It is based on the number of DNA strands in the motifs and the presence or absence of additional bases unrelated to two corresponding base-pairs.

Structural motifs	Number of DNA strands	Additional bases
Regular	2	Absence
Bulge		Presence
ssDNA	3	Presence
Nick		Absence
N-way junction	3 or more	Not considered

3.4. Generation of distributed vertices

For successful structural analysis, it is crucial to construct a DSTBCONF that specifies the positions and orientations of nodes comprising the structure. In order to generate well distributed base-pair nodes constituting a DNA nanostructure based on the connectivity between its bases, we introduce a force-based placement procedure utilizing the following approach[45]. This method evenly distributes vertices in three-dimensional space by defining the vertices and edges connecting them according to

$$\mathbf{V} = [V_1 \quad V_2 \quad \cdots \quad V_{N_v}] \tag{3-1}$$

$$\mathbf{E} \subseteq \{\{x, y\} \mid x, y \in \mathbf{V} \ \& \ x \neq y\} \tag{3-2}$$

where $\mathbf{V}$ and $\mathbf{E}$ are a set of vertices and edges, respectively, and N_v denotes the number of vertices. Attractive (F_a) and repulsive (F_r) forces are applied between the vertices, which are defined as

$$F_a(d) = \frac{d^2}{c} \tag{3-3}$$

$$F_r(d) = \frac{c^2}{d} \tag{3-4}$$

where d and c represent the distance between two vertices and the optimal distance between them, respectively. Here, c is set to be

$$c = \left(\frac{V_c}{N_v}\right)^{1/3} \tag{3-5}$$

where V_c indicates the volume of a virtual cuboid that encloses all vertices. The attractive force is exerted on a pair of vertices connected by an edge, causing the

distance between them to become the optimal distance c. On the other hand, the repulsive force is applied among all vertices to prevent them from being in close proximity to each other, particulary for those without edges. The position vector ($\vec{v}_i$) of the *i*th vertex (V_i) is incrementally updated by

$$\vec{v}_i^{\,\text{updated}} = \vec{v}_i - \sum_j \frac{\vec{v}_i - \vec{v}_j^{\,e}}{\|\vec{v}_i - \vec{v}_j^{\,e}\|} F_a\left(\|\vec{v}_i - \vec{v}_j^{\,e}\|\right) + \sum_{k \neq i} \frac{\vec{v}_i - \vec{v}_k}{\|\vec{v}_i - \vec{v}_k\|} F_r\left(\|\vec{v}_i - \vec{v}_k\|\right) \tag{3-6}$$

where $\vec{v}^{e}$ denotes the original position vector of vertices connected to the *i*th vertex. The computation terminates once the alterations in the root-mean-squared deviation of vertex coordinates are less than 0.01 for the last five incremental steps. Through this procedure, we can obtain well distributed vertices in three-dimensional space (Figure 3-3).

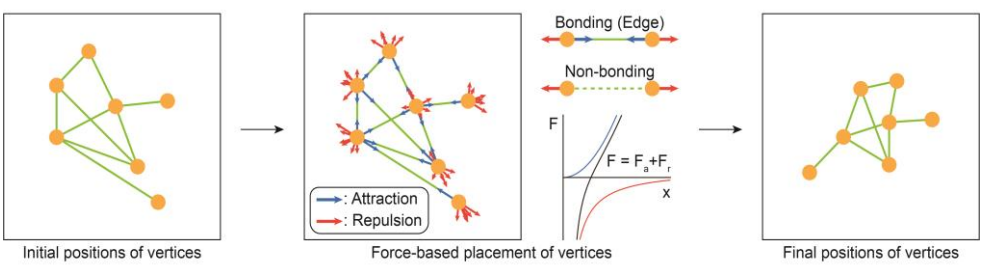

Figure 3-3. Force-based placement of vertices. The attractive force is exerted between two vertices that are connected by an edge, while the repulsive force is applied to all vertices, regardless of whether they are connected by an edge. The simultaneous application of these attractive and repulsive forces on vertices leads to the even distribution of vertices in three-dimensional space.

3.5. Determining positions of base-pairs

The procedure for determining the positions of base-pair nodes that constitute a DNA nanostructure in three-dimensional space for structural analysis is performed under two conditions: 1) when the positions and orientations of the base-pair nodes in a lattice-based design, as well as the connectivity between bases, are provided, and 2) when only the connectivity between bases is provided.

When the positions and orientations of the base-pair nodes, as well as the connectivity between bases, are provided, we examine the connectivity between the nodes on a three-dimensional lattice. Two base-pair nodes are considered adjacent when they are stacked in a DNA helix or connected by crossover strands spanning two neighboring helices. All other base-pair nodes are designated as nonadjacent nodes. This approach allows us to easily identify clusters of adjacent nodes, each of which is considered a substructure, as they are separated by nonadjacent ones. Moreover, a substructure is further partitioned into N substructures if both ends of the substructure are connected by stretched bonds, forming a topologically closed loop. This subdivision of each circular substructure overcomes the computational difficulty of properly analyzing its ring-shaped equilibrium shape, starting from the initially straight one designed on the lattice with highly stretched bonds. We set N as 4 to ensure computational efficiency[30].

To achieve convergence to the equilibrium shape and prevent nonconvergence in structural analysis, it is essential to position the substructures in three-dimensional space in a manner that avoids overlap or intertwining with the stretched bonds between them during computational calculations. We propose a placement procedure for the substructures that involves two successive steps: 1) translating the substructures to spatially well distributed positions, and 2) rotating them to minimize the sum of squared lengths of connections between them.

In the first step, we describe the substructures and their connections using vertices and edges, respectively. For each substructure, a vertex is positioned at the center of its corresponding substructure, which is computed as the mean position of all its base-pair nodes. When two substructures are connected by stretched bonds,

we construct an edge between their corresponding vertices. We then obtain the position matrix ($\mathbf{p}_0$) that encompasses the position vectors of well distributed vertices using the procedure outlined in Section 3.4. In order to ensure that all substructres do not overlap, the position matrix ($\mathbf{p}$) of all vertices is calculated as

$$\mathbf{p} = \frac{\mathrm{b}}{\mathrm{L}_{\mathrm{m}}^{\mathrm{e}}}\mathbf{p}_0 \tag{3-7}$$

where b is set to be 1.2 times the diagonal length of a virtual cuboid enclosing the largest substructures, and $\mathrm{L}_{\mathrm{m}}^{\mathrm{e}}$ represents the smallest length value among all edges.

After obtaining the spatially well distributed vertices, the second step involves calculating the orientations of the substructures. Each substructure is rigidly rotated around its fixed center position, which corresponds to the position of the corresponding vertex obtained in the first step. We determine the three-dimensional rotation angle of each substructure to minimize the sum of squared lengths of all stretched bonds between substructures. This procedure ensures that substructures and stretched bonds do not overlap or intertwine during computational calculations for structural analysis.

The position vectors of all base-pair nodes within a substructure are determined by transforming between the initially provided configuration and the generated configuration. When a substructure has the rotation angle vector $\vec{\theta} = [\theta_1 \quad \theta_2 \quad \theta_3]^{\mathrm{T}}$, all nodes in the substructure have the same rotation matrix ($\mathbf{R}_{\mathrm{Sub}}$) determined as

$$\mathbf{R}_{\mathrm{Sub}} = \begin{bmatrix} c_3c_2 & c_3s_2s_1 - s_3c_1 & c_3s_2c_1 + s_3s_1 \\ s_3c_2 & s_3s_2s_1 + c_3c_1 & s_3s_2c_1 - c_3s_1 \\ -s_2 & c_2s_1 & c_2c_1 \end{bmatrix} \tag{3-8}$$

and the same translation vector ($\vec{\mathrm{D}}_{\mathrm{Sub}}$) defined as

$$\vec{\mathrm{D}}_{\mathrm{Sub}} = \vec{\mathrm{V}} - \mathbf{R}_{\mathrm{Sub}}\vec{\mathrm{V}}_0 \tag{3-9}$$

where c_i and s_i each corresponds to $\cos\theta_i$ and $\sin\theta_i$, and $\vec{V}_0$ and $\vec{V}$ represent the position vectors for the center of the substructure in its initially provided and generated configurations, respectively. Then, the position vector ($\vec{p}_k$) of the *k*th node constituting the substructure in the generated configuration is calculated using

$$\vec{p}_k = \mathbf{R}_{Sub}\vec{p}_{0,k} + \vec{D}_{Sub} \tag{3-10}$$

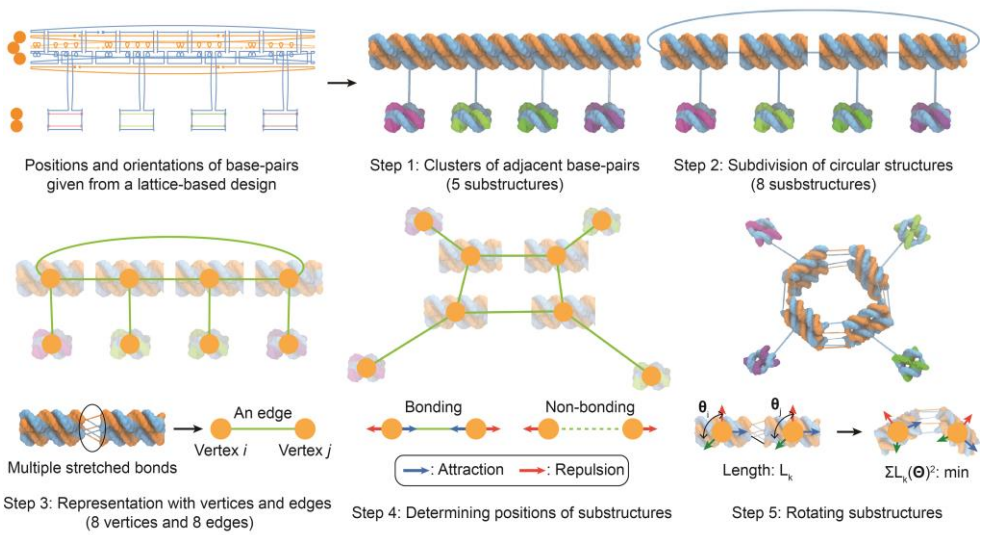

Figure 3-4. Determining the positions of base-pair nodes based on the provided configuration in the lattice-based design as well as the connectivity between bases. The lattice-based design is divided into several substructures by analyzing the adjacency of base-pairs and the presence or absence of stretched bonds connecting the ends (Steps 1 and 2). These substructures and stretched bonds are then represented as vertices and edges, respectively (Step 3). By applying attractive and repulsive forces on these vertices, we determine the positions of the substructures (Step 4). Subsequently, we rotate the substructures to minimize the sum of squared lengths of stretched bonds between them, thereby determining the positions of all base-pair nodes necessary for structural analysis (Step 5).

where $\vec{p}_{0,k}$ is the position vector of the *k*th node in the initially provided configuration (Figure 3-4).

On the other hand, if only the connectivity between bases is provided, we define each dsDNA (a cluster of regulars) as a substructre and describe it as a vertex among DNA structural motifs roughly categorized through the classification procedure (described in Section 3.3). Additionally, each structural motif connecting dsDNAs is represented by an edge. This procedure allows us to configure the connectivity between bases as a network composed of vertices and edges.

We divide this network into several subnetworks to achieve an effective spatial distribution of vertices in three-dimensional space. In the network, the subnetwork connection matrix ($\mathbf{C}$) is defined as

$$C_{ij} = \frac{N^c{}_{ij}}{N^c{}_{total}} \tag{3-11}$$

where C_{ij} represents the component in the *i*th row and *j*th column of $\mathbf{C}$, $N^c{}_{ij}$ denotes the number of connections between the *i*th and *j*th subnetworks, and $N^c{}_{total}$ indicates the toal number of connections in the network. Then, the modularity (Q) is introduced to effectively divide the network into several subnetworks, which is calculated as

$$Q = \sum_i [C_{ii} - p_i{}^2] \tag{3-12}$$

where p_i indicates the proportion of connections in the *i*th subnetwork, which is described by equation (3-13).

$$p_i = \sum_i C_{ij} \tag{3-13}$$

The modularity measures the degree to which vertices in the network are clustered

together. A high modularity indicates that the network is divided into subnetworks consisting of densely connected vertices, with relatively fewer connections between the subnetworks. When partitioning the network into subnetworks, the modularity change between two neighboring subnetworks *i* and *j* is calculated using equation (3-14).

$$\Delta Q_{ij} = 2\left(C_{ij} - p_i p_j\right) \tag{3-14}$$

Also, to ensure equal treatment of each subnetwork, we introduce the normalization of ΔQ, which is calculated using equation (3-15).

$$\Delta \mathcal{Q}_{ij} = \frac{\Delta Q_{ij}}{p_i} \tag{3-15}$$

Initially, each vertex in the network is treated as a separate subnetwork, and then we identify the highest $\Delta \mathcal{Q}_{ij}$. If ΔQ_{ij} is positive, the *i*th and *j*th subnetworks can be merged into a single subnetwork. This iterative procedure continues until the entire network is encompassed within a single subnetwork. Consequently, we partition the network into several subnetworks with the relatively highest modularity.

We follow a five-step procedure to determine the positions of all base-pair nodes in the network and subnetworks. First, we define each subnetwork, which is a cluster of vertices, and the connections between two subnetworks as a unified-vertex and a unified-edge, respectively. The spatial distribution of unified-vertices is achieved using both the procedure described in Section 3.4 and equation (3-7) with b and L_m^e set to three times the number of vertices in the subnetwork with the most vertices and the minimum value of lenghs among all unified-edges, respectively. In the next step, vertices within each subnetwork are located using both the procedure described in Section 3.4 and equation (3-7) with b and L_m^e set to 0.408 times the number of base-pair nodes in the subnetwork and the mean value of lengths of all edges

connecting vertices, respectively. This ensures that dsDNAs (represented as vertices) within the subnetwork do not overlap. The thired step involves determining the orientations of subnetworks. Each subnetwork is treated as a rigid body located at its center. The subnetworks are then roatated around their center positions to minimize the sum of squared lengths of edges connecting subnetworks. When the rotation vector of the *i*th subnetwork is $\vec{\varphi} = [\varphi_1 \quad \varphi_2 \quad \varphi_3]^T$, its rotation matrix ($\mathbf{R}_i^s$) is obtained using equation (3-8) with c_i and s_i representing $\cos\varphi_i$ and $\sin\varphi_i$, respectively. Also, its translation vector ($\vec{D}_i^s$) is calculated using equation (3-16). Here, $\vec{p}_i^s$ denotes the mean position vector of all vertices in the *i*th subnetwork.

$$\vec{D}_i^s = \vec{p}_i^s - \mathbf{R}_i^s \vec{p}_i^s \tag{3-16}$$

Then, the position vector ($\vec{p}_{i,k}^v$) of the kth vertex in the ith subnetwork is calculated as

$$\vec{p}_{i,k}^v = \mathbf{R}_i^s \vec{p}_{i,k,0}^v + \vec{D}_i^s \tag{3-17}$$

where $\vec{p}_{i,k,0}^v$ indicates the position vector of the *k*th vertex in the *i*th subnetwork before rotating subnetworks. In the fourth step, to adjust the distances between vertices, we again apply both the procedure described in Section 3.4 and equation (3-7) with b and L_m^e set to be 1.2 times the diagonal length of a virtual cuboid enclosing the longest dsDNAs, and the smallest length value among all edges between vertices, respectively, to all vertices, resulting in determining the positions of all dsDNAs. Finally, we determine the orientations of all dsDNAs and the positions of all base-pair nodes in dsDNAs. The position vector ($\vec{p}_{i,k,0}^n$) of the *k*th base-pair node ($1 \le k \le N_i$) in the *i*th dsDNA, having N_i nodes is initially set as

$$\vec{p}_{i,k,0}^n = \vec{p}_i^v - \begin{bmatrix} 0.17 \times (N_i - 2k + 1) \\ 0 \\ 0 \end{bmatrix} \tag{3-18}$$

where $\vec{p}_i^v$ is the position vector of the *i*th vertex. Then, each dsDNA, including the base-pair nodes, is rigidly rotated at the corresponding vertex so that the sum of squared lengths of structural motifs connecting two nodes belonging to different dsDNAs becomes minimum. If the *i*th dsDNA has a rotation vector of $\vec{\theta} = [\theta_1 \quad \theta_2 \quad \theta_3]^T$, all base-pair nodes in the dsDNA have the rotation matrix ($\mathbf{R}_i^v$) calculated using equation (3-8) with c_i and s_i representing $\cos\theta_i$ and $\sin\theta_i$, and the translation vector ($\vec{D}_i^v$) determined as equation (3-19).

$$\vec{D}_i^v = \vec{p}_i^v - \mathbf{R}_i^v \vec{p}_i^v \tag{3-19}$$

The position vector ($\vec{p}_{i,k}^n$) of the *k*th node constituting the positioned *i*th dsDNA is then calculated using equation (3-20).

$$\vec{p}_{i,k}^n = \mathbf{R}_i^v \vec{p}_{i,k,0}^n + \vec{D}_i^v \tag{3-20}$$

As a result, we determine the positions of all well distributed base-pairs in three-dimensional space, which are necessary for structural analysis (Figure 3-5).

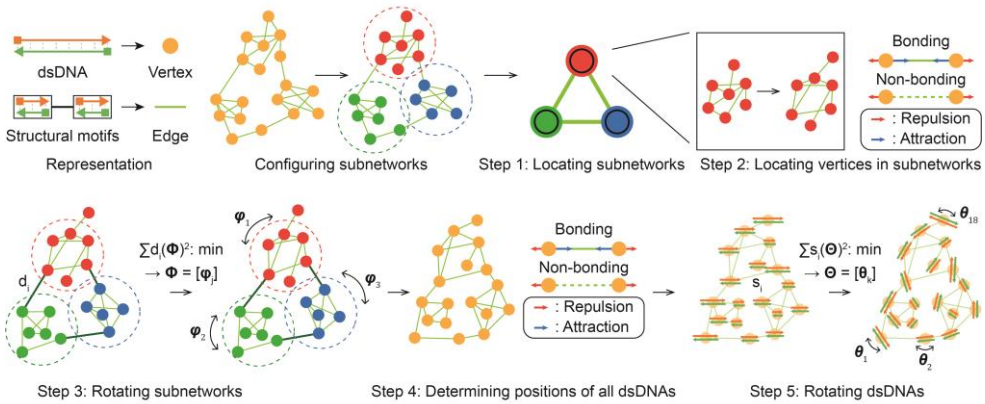

Figure 3-5. Determining the positions of base-pair nodes when given only the connectivity between bases. Here, dsDNAs and the structural motifs connecting them are represented as vertices and edges, respectively. The entire network is divided into several subnetworks by analyzing the connectivity between vertices. Attractive and repulsive forces are applied to both the subnetworks and the vertices within each subnetwork, resulting in their even spatial distribution in three-dimensional space (Steps 1 and 2). Then, the subnetworks are rigidly rotated to minimize the sum of squared edge lengths between vertices in different subnetworks (Step 3). We determine the positions of all dsDNAs by exeerting attractive and repulsive forces on them (Step 4). Consequently, the positions of all base-pairs, which are necessary for structural analysis, are determined by rotating the dsDNAs so that the sum of squared lengths of structural motifs between base-pairs in different dsDNAs becomes minimum (Step 5).

3.6. Determining orientations of base-pairs

When the initial configuration, including the positions and orientatioms of base-pairs, as well as the connectivity between bases, is provided, the orientations of all base-pair nodes in the substructure can be calculated using the substrucutre's transformation relation. When the substructure has the rotation matrix ($\mathbf{R}_{\mathrm{Sub}}$), determined as equation (3-8), the orientation matrix ($\mathbf{T}_{\mathrm{k}}$) of the kth node constituting the substructure in the determined configuration is calculated using

$$\mathbf{T}_{\mathrm{k}} = \mathbf{R}_{\mathrm{Sub}}\mathbf{T}_{\mathrm{k,0}} \tag{3-21}$$

where $\mathbf{T}_{\mathrm{k,0}}$ represents its orientation matrix in the initially provided configuration.

On the other hand, when given only the connectivity between bases, we determine the orientations of base-pair nodes considering the following characteristics of DNA nanostructures. A base-pair has the origin ($\vec{\mathrm{O}}$) and triad vectors ($\vec{\mathrm{e}}_{\mathrm{x}}$, $\vec{\mathrm{e}}_{\mathrm{y}}$, and $\vec{\mathrm{e}}_{\mathrm{z}}$) defined by 3DNA[31,32]. The vectors $\vec{\mathrm{e}}_{\mathrm{x}}$ and $\vec{\mathrm{e}}_{\mathrm{z}}$ represent the minor-major groove vector connecting from the minor groove to the major groove and the normal vector, respectively. The vector $\vec{\mathrm{e}}_{\mathrm{y}}$ is obtained by the calculating the cross product of the vectors $\vec{\mathrm{e}}_{\mathrm{z}}$ and $\vec{\mathrm{e}}_{\mathrm{x}}$. It is known that two stacked base-pairs in the regular motif have geometric properties of approximately shift and slide of 0 [nm], rise of 0.34 [nm], tilt and roll of 0 [°], and twist of 34.29 [°], as verified in Section 2.5. In addition, base-pairs in an N-way junction have the following two characteristics: 1) The vectors $\vec{\mathrm{e}}_{\mathrm{x}}$ of all base-pairs constituting the junction point in same general direction, as described by equation (3-22), and 2) The vector of $-\vec{\mathrm{e}}_{\mathrm{x}} \times \vec{\mathrm{e}}_{\mathrm{z}}{}^{\mathrm{out}}$ of a base-pair in the junction, along with the junction vectors ($\vec{\mathrm{J}}_1$ and $\vec{\mathrm{J}}_2$) associated with the base-pair, also point in the same general dirction, as described by equation (3-23). Here, $\vec{\mathrm{e}}_{\mathrm{z}}{}^{\mathrm{out}}$ represents the outward-pointing normal vector of the helix. The two junction vectors ($\vec{\mathrm{J}}_{1,\mathrm{i}}$ and $\vec{\mathrm{J}}_{2,\mathrm{i}}$) of the *i*th base-pair are defined by equation (3-24) when indicies of the base-pairs constituting the N-way junction are sequentially designated as 1, 2, $\cdots$, and N, following the direction in

which DNA strands are oriented. Using the geometric characteristics, the orientations of all base-pair nodes are determined (Figure 3-6). Consequently, the DSTBCONF containing the positions and orientations of all base-pairs is generated.

$$\vec{e}_{x,i} \cdot \vec{e}_{x,j} > 0 \tag{3-22}$$

$$\left(-\vec{e}_{x,i} \times \vec{e}_{z,i}{}^{out}\right) \cdot \vec{J}_{k,i} > 0 \tag{3-23}$$

$$\vec{J}_{k,i} = \frac{\vec{O}_{\{(i+k-2)\%N\}+1} - \vec{O}_{\{(i+k-3)\%N\}+1}}{\left\|\vec{O}_{\{(i+k-2)\%N\}+1} - \vec{O}_{\{(i+k-3)\%N\}+1}\right\|} \tag{3-24}$$

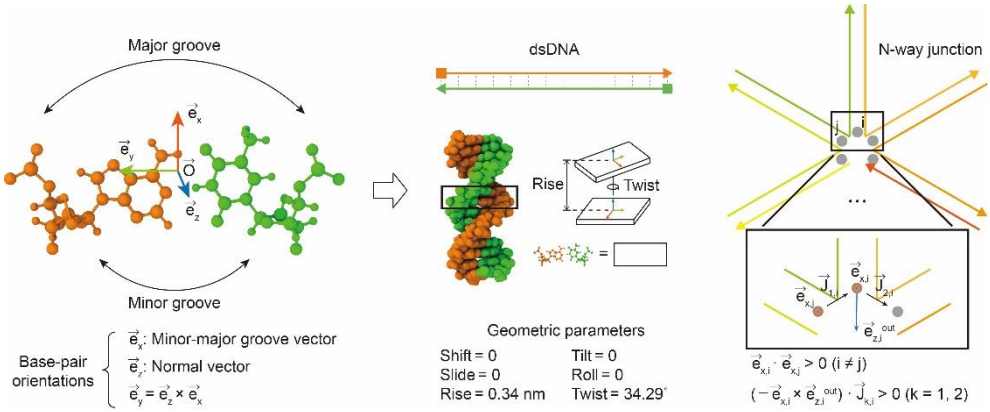

Figure 3-6. Determining the orientations of base-pairs when given only the connectivity between bases. Structural motifs, such as regular which is each compoenent of dsDNA and N-way junction, possess specific geometric characteristics. By leveraging these characteristics, we obtain the orientations of all base-pair nodes, which are essential for structural analysis.

4. Detailed classification of DNA structural motifs

4.1. Abstract

To obtain a more comprehensive understanding of DNA structural motifs within DNA nanostructures, a detailed classification is essential, particularly for the nick and junction motifs. The nick motif can exist in two conformations: stacked nick and open nick, determined by whether the two connected base-pairs are stacked or not. The 4-way junction motif is classified as either 4-way double junction or 4-way single junction, depending on the number of DNA strands it comprises. The 4-way double junction, which has two isomers, is further divided into two junction nicks and two double junctions. On the other hand, the 4-way single junction has only one geometry composed of two junction nicks and one single junction. To accurately classify the DNA structural motifs, a coarse-grained Brownian dynamics modeling of the DSTBCONF (generated in Chapter 3) is conducted. Throughout the simulation, the geometries of all structural motifs, including nicks and 4-way double junctions, are analyzed at each time step, leading to the detailed classification of the structural motifs. Structural motifs that remain unchanged during 10000 simulation time steps are considered well defined. This iterative procedure ultimately generates a DEFCONF with clearly defined structural motifs.

4.2. Additional DNA structural motifs

In Chapter 3, we propose a rough classification procedure for DNA structural motifs based on both the connectiviy between bases and the connectivity between base-pairs. This enables us to identify the types and numbers of structural motifs present in DNA nanostructures, including regular (each component of dsDNA), bulge, ssDNA, nick, and N-way junction. However, in Chapter 2, we identify additional structural motifs that constitute DNA nanostructures, such as stacked nick, junction nick, double junction, single junction, and open nick. Therefore, a detailed classification of DNA structural motifs is necessary for structural analysis.

The structural motif that connects two base-pairs through three DNA strands without any intervening bases is defined as nick. The nick motif in DNA nanostructures can be categorized into two fomrs, stacked nick and open nick, depending on whether the two base-pairs are stacked together or not. The stacked nick is commonly found within a helix, while the open nick functions as a crossover motif that connects different helices.

An indispensable DNA structural motif in building DNA nanostructures is 4-way junction, commonely known as a Holliday junction. For the 4-way junction, two broad classes of conformational isomers, namely open and stacked, can be exhibited depending on the salt conecentration in a solution. The open 4-way junction exhibits an arm-to-arm angle of approximately 90 [°] and no central base stacking, whereas the stacked 4-way junction is composed of two quasi-continuous helices with paired helical arms. The stacked 4-way junction is commonly discovered in a positively charged solution with metal ions, while the open 4-way junction is found in a solution with very low conectration of such ions[46]. Since DNA nanostructures are typically synthesized in a solution with enough cations to reduce the electrostatic repulsion between negatively charged DNA backbones, we assume that every 4-way junction has the stacked conformation in this study.

The classification of the stacked 4-way junction is determined by the number of DNA strands within it. Specifically, the 4-way junction consisting of four strands is defined as 4-way double junction, while one with five strands is identified as 4-way

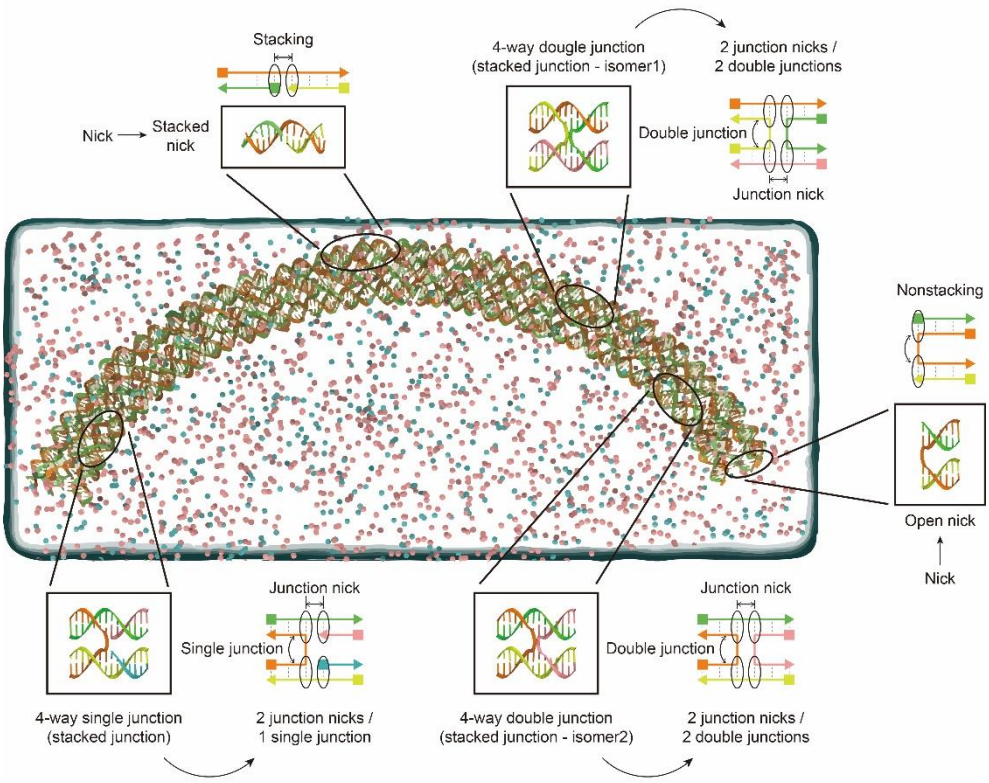

Figure 4-1. Additional DNA structural motifs. DNA nanostructures exhibit additional structural motifs, specifically stacked nick and open nick, derived from the detailed classification of nick. Additionally, the structural motifs include junction nick, double junction, and single junction, derived from the detailed classficiation of 4-way double junction and 4-way single junction.

single junction. It is important to classify the 4-way double junction accurately as it has two isomers: the first and third DNA strands form double junctions, while the second and fourth strands form junction nicks, and vice versa when we designate the four DNA strands in the 4-way double junction by their sequential indices from first to fourth. On the other hand, the 4-way single junction falls under the classification of one singe junction and two junction nicks, withouut any isomers. Figure 4-1 and Table 4-1 illustrate the detailed classification of structural motifs, including nick and 4-way junction. In summary, among the DNA structural motifs defined in Chapter 3,

nick is determined as either stacked nick or open nick, while junction is categorized as non-4-way junction, junction nick, double junction, or single junction.

Table 4-1. Additional DNA structural motifs.

<table>
<tr><th>Structural motifs roughly classified in Chapter 3</th><th colspan="3">Additional classification of structraul motifs</th></tr>
<tr><td>Regular</td><td colspan="3">Regular</td></tr>
<tr><td>Bulge</td><td colspan="3">Bulge</td></tr>
<tr><td>ssDNA</td><td colspan="3">ssDNA</td></tr>
<tr><td rowspan="2">Nick</td><td colspan="3">Stacked nick</td></tr>
<tr><td colspan="3">Open nick</td></tr>
<tr><td rowspan="5">N-way junction</td><td rowspan="4">4-way junction</td><td rowspan="2">4-way double junction</td><td>Double junction</td></tr>
<tr><td>Junction nick</td></tr>
<tr><td rowspan="2">4-way single junction</td><td>Single junction</td></tr>
<tr><td>Junction nick</td></tr>
<tr><td colspan="3">Non-4-way junction</td></tr>
</table>

4.3. Coarse-grained Brownian dynamics modeling

In order to perform the detailed classification of DNA structural motifs, we employ coarse-grained Brownian dynamics modeling on the DSTBCONF discussed in Chapter 3. To enhance computational efficiency, we simplify the representation of each dsDNA in the configuration by using a two-node-beam element. These two nodes correspond to the first and *N*th base-pairs of the dsDNA, where N represents the number of base-pairs in the dsDNA. Additionally, a two-node-beam element is utilized to describe each structural motif that connects two base-pair nodes in different dsDNAs.

The triad vectors ($\vec{m}_{x,k}$, $\vec{m}_{y,k}$, and $\vec{m}_{z,k}$) of the *k*th node, where k is either 1 or 2 in structural motifs such as dsDNA, stacked nick, and junction nick, are defined as

$$\vec{m}_{x,k} = \vec{e}_{z,k} \tag{4-1}$$

$$\vec{m}_{y,k} = \vec{e}_{y,k} \tag{4-2}$$

$$\vec{m}_{z,k} = -\vec{e}_{x,k} \tag{4-3}$$

where $\vec{e}_{x,k}$, $\vec{e}_{y,k}$, and $\vec{e}_{z,k}$ represent the triad vectors of the *k*th base-pair as defined by 3DNA[31,32]. Structurual motifs such as double junction, single junction, non-4-way junction, and open nick consist of the *k*th node with triad vectors defined as

$$\vec{m}_{y,k} = -\vec{e}_{x,k} \tag{4-4}$$

$$\vec{m}_{z,k} = \vec{e}_{z,k}{}^{out} \tag{4-5}$$

$$\vec{m}_{x,k} = \vec{m}_{y,k} \times \vec{m}_{z,k} \tag{4-6}$$

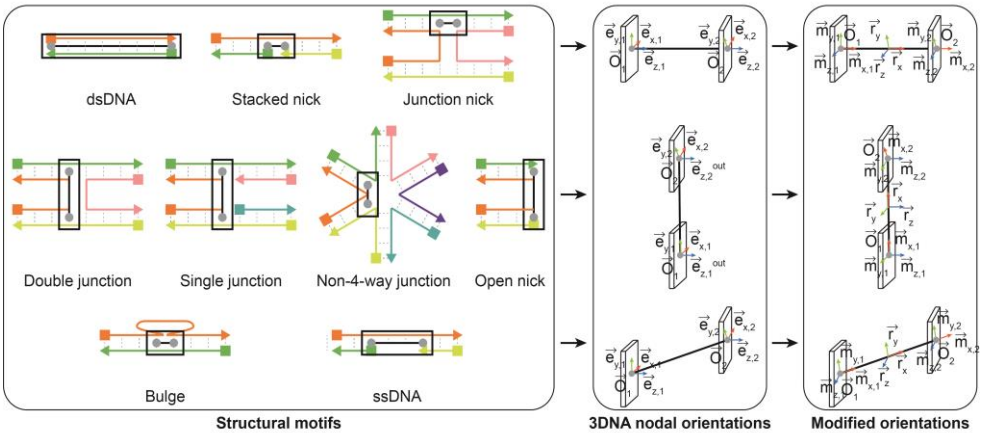

Figure 4-2. Coarse-grained Brownian dynamics modeling. Triad vectors of nodes and elements are determined based on the types of structural motifs.

where $\vec{e}_{z,k}{}^{out}$ denotes the normal vector of the *k*th base-pair, pointing outward of the helix. The triad vectors of the *k*th node in bulge or ssDNA are calculated as

$$\vec{m}_{x,k} = \frac{\vec{O}_2 - \vec{O}_1}{\|\vec{O}_2 - \vec{O}_1\|} \tag{4-7}$$

$$\vec{m}_{y,k} = \frac{(\vec{e}_{y,1} + \vec{e}_{y,2}) - \{(\vec{e}_{y,1} + \vec{e}_{y,2}) \cdot \vec{m}_{x,k}\}\vec{m}_{x,k}}{\|(\vec{e}_{y,1} + \vec{e}_{y,2}) - \{(\vec{e}_{y,1} + \vec{e}_{y,2}) \cdot \vec{m}_{x,k}\}\vec{m}_{x,k}\|} \tag{4-8}$$

$$\vec{m}_{z,k} = \vec{m}_{x,k} \times \vec{m}_{y,k} \tag{4-9}$$

where $\vec{O}_k$ indicates the origin vector of the *k*th base-pair defined by 3DNA[31,32]. The orientations ($\vec{r}_x$, $\vec{r}_y$, and $\vec{r}_z$) of each element describing the structural motif are defined using equations (4-10) to (4-12) (Figure 4-2).

$$\vec{r}_x = \frac{\vec{O}_2 - \vec{O}_1}{\|\vec{O}_2 - \vec{O}_1\|} \tag{4-10}$$

$$\vec{r}_z = \frac{\vec{r}_x \times (\vec{m}_{y,1} + \vec{m}_{y,2})}{\|\vec{r}_x \times (\vec{m}_{y,1} + \vec{m}_{y,2})\|} \tag{4-11}$$

$$\vec{r}_y = \vec{r}_z \times \vec{r}_x \tag{4-12}$$

The rotation matrix ($\mathbf{R}_k$) and rotaion angle vector ($\vec{\phi}_k$) between the *k*th node and the corresponding element are calculated as

$$\mathbf{R}_k = \begin{bmatrix}\vec{r}_x & \vec{r}_y & \vec{r}_z\end{bmatrix}^T \begin{bmatrix}\vec{m}_{x,k} & \vec{m}_{y,k} & \vec{m}_{z,k}\end{bmatrix} \tag{4-13}$$

$$\vec{\phi}_k = [\phi_{x,k} \quad \phi_{y,k} \quad \phi_{z,k}]^T = \begin{bmatrix}-C_k^{(2,3)} & C_k^{(1,3)} & -C_k^{(1,2)}\end{bmatrix}^T \tag{4-14}$$

where $C_k^{(i,j)}$ represents the component at the *i*th row and the *j*th column of the matrix $\mathbf{C}_k$, which is defined by equation (2-19). Then, the displacement vector ($\vec{U}_e$) of the element is described as

$$\vec{U}_e = \begin{bmatrix}L - L_0 & \left(\vec{\phi}_1 - \vec{\phi}_{0,1}\right)^T & \left(\vec{\phi}_2 - \vec{\phi}_{0,2}\right)^T\end{bmatrix}^T \tag{4-15}$$

where L and L_0 indicate the current length between two base-pair nodes, calculated as

$$L = \left\|\vec{O}_2 - \vec{O}_1\right\| \tag{4-16}$$

and the equilibrated length between them, respectively, and $\vec{\phi}_{0,k}$ refers to the equilibrated rotation angle vector of the *k*th vector, defined by equation (4-17).

$$\vec{\phi}_{0,k} = [R_{x,k,0} \quad R_{y,k,0} \quad R_{z,k,0}]^T \tag{4-17}$$

Here, $R_{x,k,0}$, $R_{y,k,0}$, and $R_{z,k,0}$ denote the angles that specify the equilibrated

rotation of the *k*th node around the x, y, and z axes, respectively. The external global force vector ($\vec{F}_e$) applied to the two nodes is calculated as

$$\begin{bmatrix} \vec{F}_1 \\ \vec{M}_1 \\ \vec{F}_2 \\ \vec{M}_2 \end{bmatrix} = \mathbf{B}_T \mathbf{K}_e \vec{U}_e \tag{4-18}$$

where $\vec{F}_k$ and $\vec{M}_k$ represent the force and moment vectors applied to the *k*th node, respectively, and $\mathbf{B}_T$ is the global transformation matrix described by equation (4-19).

$$\mathbf{B}_T = -(\mathbf{B}_{T1}\mathbf{B}_{T2})^T \tag{4-19}$$

Here, $\mathbf{B}_{T1}$ is the first transformation matrix defined as

$$\mathbf{B}_{T1} = \begin{bmatrix} 1 & 0 & 0 & 0 & 0 & 0 & 0 \\ 0 & B_{T1}^{(2,2)} & B_{T1}^{(2,3)} & B_{T1}^{(2,4)} & 0 & 0 & 0 \\ 0 & B_{T1}^{(3,2)} & B_{T1}^{(3,3)} & B_{T1}^{(3,4)} & 0 & 0 & 0 \\ 0 & B_{T1}^{(4,2)} & B_{T1}^{(4,3)} & B_{T1}^{(4,4)} & 0 & 0 & 0 \\ 0 & 0 & 0 & 0 & B_{T1}^{(5,5)} & B_{T1}^{(5,6)} & B_{T1}^{(5,7)} \\ 0 & 0 & 0 & 0 & B_{T1}^{(6,5)} & B_{T1}^{(6,6)} & B_{T1}^{(6,7)} \\ 0 & 0 & 0 & 0 & B_{T1}^{(7,5)} & B_{T1}^{(7,6)} & B_{T1}^{(7,7)} \end{bmatrix} \tag{4-20}$$

and each component of $\mathbf{B}_{T1}$ is determined as

$$B_{T1}^{(3k-1,3k-1)} = \frac{\vec{\phi}_k}{2}\cot\frac{\|\vec{\phi}_k\|}{2} + \left(1 - \frac{\vec{\phi}_k}{2}\cot\frac{\|\vec{\phi}_k\|}{2}\right)\frac{{\phi_{x,k}}^2}{\|\vec{\phi}_k\|^2} \tag{4-21}$$

$$B_{T1}^{(3k-1,3k)} = \left(1 - \frac{\vec{\phi}_k}{2}\cot\frac{\|\vec{\phi}_k\|}{2}\right)\frac{\phi_{x,k}\phi_{y,k}}{\|\vec{\phi}_k\|^2} + \frac{\phi_{z,k}}{2} \tag{4-22}$$

$$B_{T1}^{(3k-1,3k+1)} = \left(1 - \frac{\vec{\phi}_k}{2}\cot\frac{\|\vec{\phi}_k\|}{2}\right)\frac{\phi_{x,k}\phi_{z,k}}{\|\vec{\phi}_k\|^2} - \frac{\phi_{y,k}}{2} \tag{4-23}$$

$$B_{T1}^{(3k,3k-1)} = \left(1 - \frac{\vec{\phi}_k}{2}\cot\frac{\|\vec{\phi}_k\|}{2}\right)\frac{\phi_{x,k}\phi_{y,k}}{\|\vec{\phi}_k\|^2} - \frac{\phi_{z,k}}{2} \tag{4-24}$$

$$B_{T1}^{(3k,3k)} = \frac{\vec{\phi}_k}{2}\cot\frac{\|\vec{\phi}_k\|}{2} + \left(1 - \frac{\vec{\phi}_k}{2}\cot\frac{\|\vec{\phi}_k\|}{2}\right)\frac{{\phi_{y,k}}^2}{\|\vec{\phi}_k\|^2} \tag{4-25}$$

$$B_{T1}^{(3k,3k+1)} = \left(1 - \frac{\vec{\phi}_k}{2}\cot\frac{\|\vec{\phi}_k\|}{2}\right)\frac{\phi_{y,k}\phi_{z,k}}{\|\vec{\phi}_k\|^2} + \frac{\phi_{x,k}}{2} \tag{4-26}$$

$$B_{T1}^{(3k+1,3k-1)} = \left(1 - \frac{\vec{\phi}_k}{2}\cot\frac{\|\vec{\phi}_k\|}{2}\right)\frac{\phi_{x,k}\phi_{z,k}}{\|\vec{\phi}_k\|^2} + \frac{\phi_{y,k}}{2} \tag{4-27}$$

$$B_{T1}^{(3k+1,3k)} = \left(1 - \frac{\vec{\phi}_k}{2}\cot\frac{\|\vec{\phi}_k\|}{2}\right)\frac{\phi_{y,k}\phi_{z,k}}{\|\vec{\phi}_k\|^2} - \frac{\phi_{x,k}}{2} \tag{4-28}$$

$$B_{T1}^{(3k+1,3k+1)} = \frac{\vec{\phi}_k}{2}\cot\frac{\|\vec{\phi}_k\|}{2} + \left(1 - \frac{\vec{\phi}_k}{2}\cot\frac{\|\vec{\phi}_k\|}{2}\right)\frac{{\phi_{z,k}}^2}{\|\vec{\phi}_k\|^2} \tag{4-29}$$

where k is 1 or 2. The matrix $\mathbf{B}_{T2}$ is defined as

$$\mathbf{B}_{T2} = \begin{bmatrix} -\vec{r}_x{}^T & \mathbf{O}_{1\times3} & \vec{r}_x{}^T & \mathbf{O}_{1\times3} \\ -\mathbf{A}_1\mathbf{R}_r{}^T & (\mathbf{I}_3 + \mathbf{A}_2)\mathbf{R}_r{}^T & \mathbf{A}_1\mathbf{R}_r{}^T & \mathbf{A}_3\mathbf{R}_r{}^T \\ -\mathbf{A}_1\mathbf{R}_r{}^T & \mathbf{A}_2\mathbf{R}_r{}^T & \mathbf{A}_1\mathbf{R}_r{}^T & (\mathbf{I}_3 + \mathbf{A}_3)\mathbf{R}_r{}^T \end{bmatrix} \tag{4-30}$$

where $\mathbf{O}_{1\times3}$ and $\mathbf{I}_3$ are an 1-by-3 zero matrix and a 3-by-3 identity matrix, respectively. Here, $\mathbf{A}_1$, $\mathbf{A}_2$, $\mathbf{A}_3$, and $\mathbf{R}_r$ are defined as

$$\mathbf{A}_1 = \begin{bmatrix} 0 & 0 & -\frac{s_0}{L} \\ 0 & 0 & -\frac{1}{L} \\ 0 & \frac{1}{L} & 0 \end{bmatrix} \tag{4-31}$$

$$\mathbf{A}_2 = \begin{bmatrix} -\frac{s_{2,1}}{2} & \frac{s_{1,1}}{2} & 0 \\ 0 & 0 & 0 \\ 0 & 0 & 0 \end{bmatrix} \tag{4-32}$$

$$\mathbf{A}_3 = \begin{bmatrix} -\frac{s_{2,2}}{2} & \frac{s_{1,2}}{2} & 0 \\ 0 & 0 & 0 \\ 0 & 0 & 0 \end{bmatrix} \tag{4-33}$$

$$\mathbf{R}_r = \begin{bmatrix} \vec{r}_x & \vec{r}_y & \vec{r}_z \end{bmatrix} \tag{4-34}$$

where s_0, $s_{1,k}$, and $s_{2,k}$ are calculated using equations (4-35) to (4-37), respectively.

$$s_0 = \frac{\vec{r}_x \cdot \left(\vec{m}_{y,1} + \vec{m}_{y,2}\right)}{\vec{r}_y \cdot \left(\vec{m}_{y,1} + \vec{m}_{y,2}\right)} \tag{4-35}$$

$$s_{1,k} = \frac{2\vec{r}_x \cdot \vec{m}_{x,k}}{\vec{r}_y \cdot \left(\vec{m}_{y,1} + \vec{m}_{y,2}\right)} \tag{4-36}$$

$$s_{2,k} = \frac{2\vec{r}_y \cdot \vec{m}_{x,k}}{\vec{r}_y \cdot \left(\vec{m}_{y,1} + \vec{m}_{y,2}\right)} \tag{4-37}$$

The local stiffness matrix ($\mathbf{K}_e$) of the element is defined here as

$$\mathbf{K}_e = \begin{bmatrix} \frac{S}{L} & 0 & 0 & 0 & 0 & 0 & 0 \\ 0 & \frac{C}{L} & 0 & 0 & -\frac{C}{L} & 0 & 0 \\ 0 & 0 & \frac{B}{L} + \frac{23YL}{60} & 0 & 0 & \frac{13YL}{60} - \frac{B}{L} & 0 \\ 0 & 0 & 0 & \frac{B}{L} + \frac{23YL}{60} & 0 & 0 & \frac{13YL}{60} - \frac{B}{L} \\ 0 & -\frac{C}{L} & 0 & 0 & \frac{C}{L} & 0 & 0 \\ 0 & 0 & \frac{13YL}{60} - \frac{B}{L} & 0 & 0 & \frac{B}{L} + \frac{23YL}{60} & 0 \\ 0 & 0 & 0 & \frac{13YL}{60} - \frac{B}{L} & 0 & 0 & \frac{B}{L} + \frac{23YL}{60} \end{bmatrix} \tag{4-38}$$

where S, C, Y, and B indicate the stretching, twisting, equivalent isotropic shearing and bending rigidities, respectively. The detailed geometric and mechanical

properties of DNA structural motifs are represented in Tables 4-2 and 4-3, which are set based on the result of molecular dynamics simulations performed in Chapter 2.

Table 4-2. Values of geometric properties of DNA structural motifs used in the coarse-grained Brownian dynamics modeling. They are set based on the results of all-atom molecular dynamics simulations.

Structural motifs	T_x [nm]	T_y [nm]	T_z [nm]
dsDNA with N base-pairs	0.34×(N-1)	0.00	0.00
Stacked nick	0.33	-0.07	0.00
Junction nick	0.31	-0.07	-0.03
Double junction	1.81	0.43	0.17
Single junction	1.79	0.51	0.18
Open nick	1.54	0.26	0.10
Non-4-way junction	1.80	0.00	0.00
Bulge	1.00	0.00	0.00
ssDNA	1.00	0.00	0.00

Structural motifs	$R_{x,1,0}$ [°]	$R_{x,2,0}$ [°]
dsDNA with N base-pairs	[-17.46×(N-1)]%360	[17.46×(N-1)]%360
Stacked nick	-16.03	16.03
Junction nick	-14.52	14.51
Double junction	-2.15	3.62
Single junction	-0.13	2.01
Open nick	1.02	1.89
Non-4-way junction	0.00	0.00
Bulge	0.00	0.00
ssDNA	0.00	0.00

Structural motifs	$R_{y,1,0}$ [°]	$R_{y,2,0}$ [°]	$R_{z,1,0}$ [°]	$R_{z,2,0}$ [°]
dsDNA with N base-pairs	0.00	0.00	0.00	0.00
Stacked nick	-1.24	1.26	-0.28	0.02
Junction nick	-1.39	1.34	0.09	-0.37
Double junction	6.83	4.08	-28.37	2.04
Single junction	7.04	5.00	-41.29	9.56
Open nick	15.93	-4.19	-24.93	8.00

Table 4-2 (Continued)

Structural motifs	$R_{y,1,0}$ [°]	$R_{y,2,0}$ [°]	$R_{z,1,0}$ [°]	$R_{z,2,0}$ [°]
Non-4-way junction	0.00	0.00	-30.00	5.00
Bulge	0.00	0.00	0.00	0.00
ssDNA	0.00	0.00	0.00	0.00

Table 4-3. Values of mechanical rigidities of DNA structural motifs in the coarse-grained Brownian dynamics modeling. They are also set based on the results of all-atom molecular dynamics simulations.

Structural motifs	S [pN]	Y [pN]	C [pN·nm^2]	B [pN·nm^2]
dsDNA with N base-pairs	2211.02	489.81	283.43	240.16
Stacked nick	2044.49	373.47	129.43	214.26
Junction nick	2025.96	533.38	233.29	222.31
Double junction	3668.64	811.43	413.78	420.33
Single junction	2365.95	755.30	333.05	281.19
Open nick	525.75	219.71	139.80	124.80
Non-4-way junction	2500.00	780.00	350.00	300.00
Bulge	700.00	10.00	10.00	5.00
ssDNA	700.00	10.00	10.00	5.00

The positions of the six degrees of freedom (three translations represented by $\vec{X}_i$ and three rotations represented by $\vec{\Theta}_i$) of the *i*th node in the coarse-grained Brownian dynamics simulation are governed by

$$\vec{X}_i(t+\Delta t) = \vec{X}_i(t) + \frac{\vec{F}_i(t)}{\zeta_t}\Delta t + \vec{R}_N\sqrt{2D_t\Delta t} \tag{4-39}$$

$$\vec{\Theta}_i(t+\Delta t) = \vec{\Theta}_i(t) + \frac{\vec{M}_i(t)}{\zeta_r}\Delta t + \vec{R}_N\sqrt{2D_r\Delta t} \tag{4-40}$$

where $\vec{F}_i(t)$ and $\vec{M}_i(t)$ indicate the force and moment vectors applied to the *i*th node at time t, respectively. The translational (ζ_t) and rotational (ζ_r) drag coefficients of the node are set to be 6.41×10^{-7} [pN·s/nm] and 9.90×10^{-6} [pN·nm·s], respectively[47-49]. $\vec{R}_N$ is a 3-by-1 vector composed of normally distributed random numbers with a mean of 0 and a standard deviation of 1. D_t and D_r are the translational and rotational diffusion coefficients of the node, respectively, defined as

$$D_{t,i} = \frac{k_B T_a}{\zeta_t} \tag{4-41}$$

$$D_{r,i} = \frac{k_B T_a}{\zeta_r} \tag{4-42}$$

where k_B is Boltzmann's constant (1.38×10^{-2} [pN·nm/K]), and T_a is the absolute temperature set to be 300 [K]. Here, the simulation time step (Δt) is set to be 1 [ps].

As the coarse-grained Brownian dynamics simulation progresses on the DSTBCONF, specific structural motifs such as 4-way double junction and nick are distinguished as either isomer1 or isomer2, and either stacked nick or open nick, respectively. This distinction is performed by analyzing the geometric characteristics at each simulation time step.

For the 4-way double junction, the bending angles of the *k*th strand (represented as θ_k where k is a natural number from 1 to 4) are analyzed. Specifically, the angles

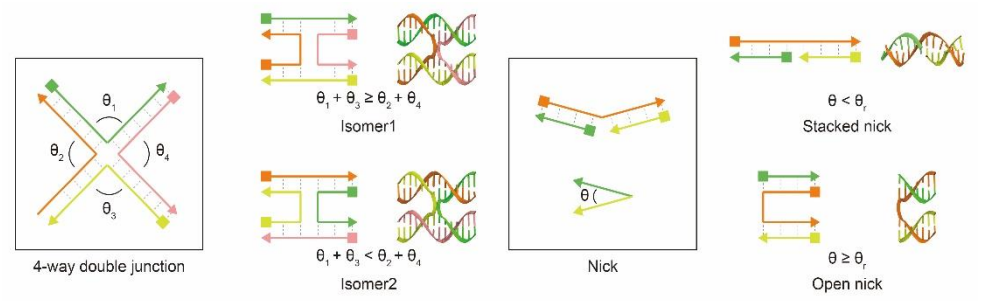

Figure 4-3. Detailed clssification of 4-way double junction and nick through the coarse-grained Brownian dynamics simulation. The structural motifs, including the 4-way double junction and nick motifs, are classified in detail by analyzing the geometric characteristic at each simulation time step. Structural motifs are considered well defined if their definition does not change during 10000 simulation time steps.

of $\theta_1 + \theta_3$ and $\theta_2 + \theta_4$ are considered. The geometric condition where $\theta_1 + \theta_3$ is equal to or larger than $\theta_2 + \theta_4$ classifies it as isomer1 with junction nicks on strands 1 and 3, and double junctions on strands 2 and 4. Conversely, when $\theta_1 + \theta_3$ is smaller than $\theta_2 + \theta_4$, it becoms isomer2 with junction nicks on strands 2 and 4, and double junctions on strands 1 and 3.

The additional nick motifs are determined by analyzing the angle between the normal vectors of two base-pairs connected by it. These normal vectors are set to point in a direction similar to that of the unbroken DNA strand. Based on this analysis, when the angle is smaller or equal to the reference angle (θ_r), the structural motif is identified as stacked nick. Conversely, when the angle is larger than θ_r, it is classified as open nick. Here, θ_r is set to be 45 [°] (Figure 4-3).

The detailed classification of DNA structrual motifs based on the geometric conditions is an ongoing process during the coarse-grained Brownian dynamics simulation. When all structural motifs remain unchanged for 10000 simulation time steps, they are considered well defined. At this point, we define the configuration with both the positions and orientations of nodes and elements, and the well classifed

structural motifs, as a DEFCONF.

5. Finite element modeling

5.1. Abstract

To perform the structural analysis, we build a finite element model of the DEFCONF (generated in Chapter 4), which includes the positions and orientations of base-pairs and the well defined structural motifs. We consider each base-pair and each structural motif between two base-pairs as a node and a two-node-beam element, respectively, with three translational and three rotational degrees of freedom. Additionally, we construct finite element truss elements with only three translational degrees of freedom to model electrostatic repulsions between negatively charged base-pair nodes. To achieve atomic level accuracy, the structural elements incorporate sequence-dependent geometric and mechanical properties obtained from all-atom molecular dynamics simulations. The local stiffness matrices of the structural and electrostatic elements are then assembled to construct a global stiffness matrix. Consequently, we conduct finite element structural analysis, in conjunction with the nonlinear solution method from the DEFCONF, to predict the final equilibrium shapes.

5.2. Two-node beam element

To describe each structural motif connecting two base-pairs, we construct a finite element beam model with two nodes. Depending on the types of structural motifs, we define nodal triad vectors differently, as outlined in Chapters 2 and 4. If the triad vectors of the *k*th base-pair, defined as $\vec{e}_{x,k}$, $\vec{e}_{y,k}$, and $\vec{e}_{z,k}$, are obtained using 3DNA[31,32], then the nodal triad vectors ($\vec{m}_{x,k}$, $\vec{m}_{y,k}$, and $\vec{m}_{z,k}$) for structural motifs connecting stacked base-pairs (regular, stacked nick, and junction nick), crossover motifs (double junction, single junction, non-4-way junction, and open nick), and other structural motifs (bulge and ssDNA) are determined using equations (4-1) to (4-3), (4-4) to (4-6), and (4-7) to (4-9), respectively. The triad vectors ($\vec{r}_x$, $\vec{r}_y$, and $\vec{r}_z$) of each element representing regular, stacked nick, and junction nick, bulge, and ssDNA are defined as

$$\begin{bmatrix}\vec{r}_x & \vec{r}_y & \vec{r}_z\end{bmatrix} = \mathbf{M}_1\left(\mathbf{M}_1{}^{\mathrm{T}}\mathbf{M}_2\right)^{\frac{1}{2}} = \mathbf{M}_2\left(\mathbf{M}_2{}^{\mathrm{T}}\mathbf{M}_1\right)^{\frac{1}{2}} \tag{5-1}$$

where $\mathbf{M}_k$ is the nodal orientaion matrix of the *k*th node, as defined in equation (5-2). Here, k is set to be 1 or 2.

$$\mathbf{M}_k = \begin{bmatrix}\vec{m}_{x,k} & \vec{m}_{y,k} & \vec{m}_{z,k}\end{bmatrix} \tag{5-2}$$

The beam element describing crossover motifs has the triad vectors calculated as

$$\vec{r}_x = \frac{\vec{O}_2 - \vec{O}_1}{\left\|\vec{O}_2 - \vec{O}_1\right\|} \tag{5-3}$$

$$\vec{r}_z = \frac{\vec{r}_x \times \left(\vec{m}_{y,1} + \vec{m}_{y,2}\right)}{\left\|\vec{r}_x \times \left(\vec{m}_{y,1} + \vec{m}_{y,2}\right)\right\|} \tag{5-4}$$

$$\vec{r}_y = \vec{r}_z \times \vec{r}_x \tag{5-5}$$

where $\vec{O}_k$ is the origin vector of the kth node defined as 3DNA[31,32].

At each incremental step during the structural analysis, the origin vector of the *k*th node and the triad vectors of the element are changed from $\vec{O}_k$ to $\vec{\mathcal{O}}_k$ and from $\vec{r}_x$, $\vec{r}_y$, and $\vec{r}_z$ to $\vec{\mathcal{r}}_x$, $\vec{\mathcal{r}}_y$, and $\vec{\mathcal{r}}_z$, respectively. These changes are described by equations (5-6), (5-7), and (5-8).

$$\vec{\mathcal{r}}_x = \frac{\vec{\mathcal{O}}_2 - \vec{\mathcal{O}}_1}{\|\vec{\mathcal{O}}_2 - \vec{\mathcal{O}}_1\|} \tag{5-6}$$

$$\vec{\mathcal{r}}_z = \frac{\vec{\mathcal{r}}_x \times (\vec{m}_{y,1} + \vec{m}_{y,2})}{\|\vec{\mathcal{r}}_x \times (\vec{m}_{y,1} + \vec{m}_{y,2})\|} \tag{5-7}$$

$$\vec{\mathcal{r}}_y = \vec{\mathcal{r}}_z \times \vec{\mathcal{r}}_x \tag{5-8}$$

Then, the rotation matrix ($\mathbf{R}_k$) and the rotaion angle vector ($\vec{\phi}_k$) between the *k*th node and the element are calculated using equations (5-9) and (4-14), respectively.

$$\mathbf{R}_k = \begin{bmatrix} \vec{\mathcal{r}}_x & \vec{\mathcal{r}}_y & \vec{\mathcal{r}}_z \end{bmatrix}^T \begin{bmatrix} \vec{m}_{x,k} & \vec{m}_{y,k} & \vec{m}_{z,k} \end{bmatrix} \tag{5-9}$$

The displacement vector ($\vec{U}_e$) of the element is described as

$$\vec{U}_e = \begin{bmatrix} \mathcal{L} - L_0 & (\vec{\phi}_1 - \vec{\phi}_{0,1})^T & (\vec{\phi}_2 - \vec{\phi}_{0,2})^T \end{bmatrix}^T \tag{5-10}$$

where $\mathcal{L}$ and L_0 are the current length between the nodes, calculated as

$$\mathcal{L} = \|\vec{\mathcal{O}}_2 - \vec{\mathcal{O}}_1\| \tag{5-11}$$

and the equilibrated length between them, respectively, and $\vec{\phi}_{0,k}$ is the equilibrated rotation angle vector of the *k*th vector, defined by equation (4-17). The global internal

force ($\vec{\mathrm{F}}_1$ and $\vec{\mathrm{F}}_2$) and moment ($\vec{\mathrm{M}}_1$ and $\vec{\mathrm{M}}_2$) vectors applied to the two nodes are calculated as

$$\begin{bmatrix} \vec{\mathrm{F}}_1 \\ \vec{\mathrm{M}}_1 \\ \vec{\mathrm{F}}_2 \\ \vec{\mathrm{M}}_2 \end{bmatrix} = \boldsymbol{\mathcal{B}}_{\mathrm{T}} \vec{\mathrm{F}}_{\mathrm{e}} \tag{5-12}$$

where $\boldsymbol{\mathcal{B}}_{\mathrm{T}}$ and $\vec{\mathrm{F}}_{\mathrm{e}}$ are the global transformation matrix and the local force vector, respectively, each of which is described by equations (5-13) and (5-14).

$$\boldsymbol{\mathcal{B}}_{\mathrm{T}} = (\mathbf{B}_{\mathrm{T1}} \boldsymbol{\mathcal{B}}_{\mathrm{T2}})^{\mathrm{T}} \tag{5-13}$$

$$\vec{\mathrm{F}}_{\mathrm{e}} = \mathbf{K}_{\mathrm{e}} \vec{\mathrm{U}}_{\mathrm{e}} \tag{5-14}$$

Here, $\mathbf{B}_{\mathrm{T1}}$ and $\boldsymbol{\mathcal{B}}_{\mathrm{T2}}$ are the local transformation matrices defined by equations (4-20) and (5-15), respectively.

$$\boldsymbol{\mathcal{B}}_{\mathrm{T2}} = \begin{bmatrix} -\vec{r}_{\mathrm{x}}{}^{\mathrm{T}} & \mathbf{O}_{1\times 3} & \vec{r}_{\mathrm{x}}{}^{\mathrm{T}} & \mathbf{O}_{1\times 3} \\ -\boldsymbol{\mathcal{A}}_1 \boldsymbol{\mathcal{R}}_{\mathrm{r}}{}^{\mathrm{T}} & (\mathbf{I}_3 + \boldsymbol{\mathcal{A}}_2)\boldsymbol{\mathcal{R}}_{\mathrm{r}}{}^{\mathrm{T}} & \boldsymbol{\mathcal{A}}_1 \boldsymbol{\mathcal{R}}_{\mathrm{r}}{}^{\mathrm{T}} & \boldsymbol{\mathcal{A}}_3 \boldsymbol{\mathcal{R}}_{\mathrm{r}}{}^{\mathrm{T}} \\ -\boldsymbol{\mathcal{A}}_1 \boldsymbol{\mathcal{R}}_{\mathrm{r}}{}^{\mathrm{T}} & \boldsymbol{\mathcal{A}}_2 \boldsymbol{\mathcal{R}}_{\mathrm{r}}{}^{\mathrm{T}} & \boldsymbol{\mathcal{A}}_1 \boldsymbol{\mathcal{R}}_{\mathrm{r}}{}^{\mathrm{T}} & (\mathbf{I}_3 + \boldsymbol{\mathcal{A}}_3)\boldsymbol{\mathcal{R}}_{\mathrm{r}}{}^{\mathrm{T}} \end{bmatrix} \tag{5-15}$$

The matrices $\mathbf{O}_{1\times 3}$ and $\mathbf{I}_3$ are an 1-by-3 zero matrix and a 3-by-3 identity matrix, respectively, and $\boldsymbol{\mathcal{A}}_1$, $\boldsymbol{\mathcal{A}}_2$, $\boldsymbol{\mathcal{A}}_3$, and $\boldsymbol{\mathcal{R}}_{\mathrm{r}}$ are defined as

$$\boldsymbol{\mathcal{A}}_1 = \begin{bmatrix} 0 & 0 & -\dfrac{\mathcal{S}_0}{\mathcal{L}} \\ 0 & 0 & -\dfrac{1}{\mathcal{L}} \\ 0 & \dfrac{1}{\mathcal{L}} & 0 \end{bmatrix} \tag{5-16}$$

$$\boldsymbol{\mathcal{A}}_2 = \begin{bmatrix} -\frac{\mathcal{s}_{2,1}}{2} & \frac{\mathcal{s}_{1,1}}{2} & 0 \\ 0 & 0 & 0 \\ 0 & 0 & 0 \end{bmatrix} \tag{5-17}$$

$$\boldsymbol{\mathcal{A}}_3 = \begin{bmatrix} -\frac{\mathcal{s}_{2,2}}{2} & \frac{\mathcal{s}_{1,2}}{2} & 0 \\ 0 & 0 & 0 \\ 0 & 0 & 0 \end{bmatrix} \tag{5-18}$$

$$\boldsymbol{\mathcal{R}}_{\mathrm{r}} = \begin{bmatrix} \vec{\mathcal{r}}_{\mathrm{x}} & \vec{\mathcal{r}}_{\mathrm{y}} & \vec{\mathcal{r}}_{\mathrm{z}} \end{bmatrix} \tag{5-19}$$

where $\mathcal{s}_0$, $\mathcal{s}_{1,\mathrm{k}}$, and $\mathcal{s}_{2,\mathrm{k}}$ are calculated using equations (5-20), (5-21), and (5-22), respectively, and k has a value of 1 or 2.

$$\mathcal{s}_0 = \frac{\vec{\mathcal{r}}_{\mathrm{x}} \cdot \left(\vec{\mathrm{m}}_{\mathrm{y},1} + \vec{\mathrm{m}}_{\mathrm{y},2}\right)}{\vec{\mathcal{r}}_{\mathrm{y}} \cdot \left(\vec{\mathrm{m}}_{\mathrm{y},1} + \vec{\mathrm{m}}_{\mathrm{y},2}\right)} \tag{5-20}$$

$$\mathcal{s}_{1,\mathrm{k}} = \frac{2\vec{\mathcal{r}}_{\mathrm{y}} \cdot \vec{\mathrm{m}}_{\mathrm{x,k}}}{\vec{\mathcal{r}}_{\mathrm{y}} \cdot \left(\vec{\mathrm{m}}_{\mathrm{y},1} + \vec{\mathrm{m}}_{\mathrm{y},2}\right)} \tag{5-21}$$

$$\mathcal{s}_{2,\mathrm{k}} = \frac{2\vec{\mathcal{r}}_{\mathrm{y}} \cdot \vec{\mathrm{m}}_{\mathrm{x,k}}}{\vec{\mathcal{r}}_{\mathrm{y}} \cdot \left(\vec{\mathrm{m}}_{\mathrm{y},1} + \vec{\mathrm{m}}_{\mathrm{y},2}\right)} \tag{5-22}$$

The local stiffness matrix ($\mathbf{K}_{\mathrm{e}}$) of the element with six degrees of freedom is defined here as

$$\mathbf{K}_{\mathrm{e}} = \begin{bmatrix} \mathrm{K}_{\mathrm{e}}^{(1,1)} & \mathrm{K}_{\mathrm{e}}^{(1,2)} & \mathrm{K}_{\mathrm{e}}^{(1,3)} & \mathrm{K}_{\mathrm{e}}^{(1,4)} & \mathrm{K}_{\mathrm{e}}^{(1,5)} & \mathrm{K}_{\mathrm{e}}^{(1,6)} & \mathrm{K}_{\mathrm{e}}^{(1,7)} \\ \mathrm{K}_{\mathrm{e}}^{(2,1)} & \mathrm{K}_{\mathrm{e}}^{(2,2)} & \mathrm{K}_{\mathrm{e}}^{(2,3)} & \mathrm{K}_{\mathrm{e}}^{(2,4)} & \mathrm{K}_{\mathrm{e}}^{(2,5)} & \mathrm{K}_{\mathrm{e}}^{(2,6)} & \mathrm{K}_{\mathrm{e}}^{(2,7)} \\ \mathrm{K}_{\mathrm{e}}^{(3,1)} & \mathrm{K}_{\mathrm{e}}^{(3,2)} & \mathrm{K}_{\mathrm{e}}^{(3,3)} & \mathrm{K}_{\mathrm{e}}^{(3,4)} & \mathrm{K}_{\mathrm{e}}^{(3,5)} & \mathrm{K}_{\mathrm{e}}^{(3,6)} & \mathrm{K}_{\mathrm{e}}^{(3,7)} \\ \mathrm{K}_{\mathrm{e}}^{(4,1)} & \mathrm{K}_{\mathrm{e}}^{(4,2)} & \mathrm{K}_{\mathrm{e}}^{(4,3)} & \mathrm{K}_{\mathrm{e}}^{(4,4)} & \mathrm{K}_{\mathrm{e}}^{(4,5)} & \mathrm{K}_{\mathrm{e}}^{(4,6)} & \mathrm{K}_{\mathrm{e}}^{(4,7)} \\ \mathrm{K}_{\mathrm{e}}^{(5,1)} & \mathrm{K}_{\mathrm{e}}^{(5,2)} & \mathrm{K}_{\mathrm{e}}^{(5,3)} & \mathrm{K}_{\mathrm{e}}^{(5,4)} & \mathrm{K}_{\mathrm{e}}^{(5,5)} & \mathrm{K}_{\mathrm{e}}^{(5,6)} & \mathrm{K}_{\mathrm{e}}^{(5,7)} \\ \mathrm{K}_{\mathrm{e}}^{(6,1)} & \mathrm{K}_{\mathrm{e}}^{(6,2)} & \mathrm{K}_{\mathrm{e}}^{(6,3)} & \mathrm{K}_{\mathrm{e}}^{(6,4)} & \mathrm{K}_{\mathrm{e}}^{(6,5)} & \mathrm{K}_{\mathrm{e}}^{(6,6)} & \mathrm{K}_{\mathrm{e}}^{(6,7)} \\ \mathrm{K}_{\mathrm{e}}^{(7,1)} & \mathrm{K}_{\mathrm{e}}^{(7,2)} & \mathrm{K}_{\mathrm{e}}^{(7,3)} & \mathrm{K}_{\mathrm{e}}^{(7,4)} & \mathrm{K}_{\mathrm{e}}^{(7,5)} & \mathrm{K}_{\mathrm{e}}^{(7,6)} & \mathrm{K}_{\mathrm{e}}^{(7,7)} \end{bmatrix} \tag{5-23}$$

where each component of $\mathbf{K}_{\mathrm{e}}$ is calculated using equations (5-24) to (5-42).

$$K_e^{(1,1)} = \frac{S}{L} \tag{5-24}$$

$$K_e^{(1,2)} = K_e^{(2,1)} = -\frac{G_{T_zR_x}}{2L} \tag{5-25}$$

$$K_e^{(1,3)} = K_e^{(3,1)} = -\frac{G_{T_xT_z}}{24} - \frac{G_{T_zR_y}}{2L} \tag{5-26}$$

$$K_e^{(1,4)} = K_e^{(4,1)} = \frac{G_{T_yT_z}}{24} - \frac{G_{T_zR_z}}{2L} \tag{5-27}$$

$$K_e^{(1,5)} = K_e^{(5,1)} = \frac{G_{T_zR_x}}{2L} \tag{5-28}$$

$$K_e^{(1,6)} = K_e^{(6,1)} = \frac{G_{T_xT_z}}{24} + \frac{G_{T_zR_y}}{2L} \tag{5-29}$$

$$K_e^{(1,7)} = K_e^{(7,1)} = -\frac{G_{T_yT_z}}{24} + \frac{G_{T_zR_z}}{2L} \tag{5-30}$$

$$K_e^{(2,2)} = K_e^{(5,5)} = \frac{C}{L} \tag{5-31}$$

$$K_e^{(2,3)} = K_e^{(3,2)} = K_e^{(5,6)} = K_e^{(6,5)} = \frac{G_{T_xR_x}}{12} + \frac{G_{R_xR_y}}{L} \tag{5-32}$$

$$K_e^{(2,4)} = K_e^{(4,2)} = K_e^{(5,7)} = K_e^{(7,5)} = -\frac{G_{T_yR_x}}{12} + \frac{G_{R_xR_z}}{L} \tag{5-33}$$

$$K_e^{(2,5)} = K_e^{(5,2)} = -\frac{C}{L} \tag{5-34}$$

$$K_e^{(2,6)} = K_e^{(6,2)} = K_e^{(3,5)} = K_e^{(5,3)} = -\frac{G_{T_xR_x}}{12} - \frac{G_{R_xR_y}}{L} \tag{5-35}$$

$$K_e^{(2,7)} = K_e^{(7,2)} = K_e^{(4,5)} = K_e^{(5,4)} = \frac{G_{T_yR_x}}{12} - \frac{G_{R_xR_z}}{L} \tag{5-36}$$

$$K_e^{(3,3)} = K_e^{(6,6)} = \frac{G_{T_xR_y}}{6} + \frac{23Y_zL}{60} + \frac{B_y}{L} \tag{5-37}$$

$$K_e^{(3,4)} = K_e^{(4,3)} = K_e^{(6,7)} = K_e^{(7,6)} = \frac{G_{T_xR_z}}{12} - \frac{G_{T_yR_y}}{12} - \frac{G_{T_xT_y}L}{144} + \frac{G_{R_yR_z}}{L} \tag{5-38}$$

$$K_e^{(3,6)} = K_e^{(6,3)} = -\frac{G_{T_xR_y}}{6} + \frac{13Y_zL}{60} - \frac{B_y}{L} \tag{5-39}$$

$$K_e^{(3,7)} = K_e^{(7,3)} = K_e^{(4,6)} = K_e^{(6,4)} = -\frac{G_{T_xR_z}}{12} + \frac{G_{T_yR_y}}{12} + \frac{G_{T_xT_y}L}{144} - \frac{G_{R_yR_z}}{L} \quad (5\text{-}40)$$

$$K_e^{(4,4)} = K_e^{(7,7)} = -\frac{G_{T_yR_z}}{6} + \frac{23Y_yL}{60} + \frac{B_z}{L} \quad (5\text{-}41)$$

$$K_e^{(4,7)} = K_e^{(7,4)} = \frac{G_{T_yR_z}}{6} + \frac{13Y_yL}{60} - \frac{B_z}{L} \quad (5\text{-}42)$$

Here, L is the length between the two nodes, calculated using equation (4-16). Using $\mathcal{L}$ instead of L is permissible, but the insignificance in the difference between the two values leads to the calculation of $\mathbf{K}_e$ using L in this study. S, Y_y, Y_z, C, B_y, and B_z represent the stretching rigidity, shearing rigidities along the y- and z- axes, twisting rigidity, and bending rigidities about the y- and z- axes, respectively. The coupling rigidity of two geometric parameters s_1 and s_2 is denoted as $G_{s_1s_2}$.

The geometric and mechanical properties of the elements representing regular, stacked nick, junction nick, double junction, single junction, and open nick among structural motifs have sequence-dependent values obtained from all-atom molecular dynamics simulations in Chapter 2. These values are detailed in Tables A-3 to A-5, and A-9 to A-17 (in Appendices A.4 and A.5). Conversly, bulge and non-4-way junction are set to have sequence-independent properties as listed in Table 5-1.

The global stiffness matrix ($\mathbf{K}_g$) of the structural elements is derived by assembling the local stiffness matrices using equation (5-43).

$$\mathbf{K}_g = \boldsymbol{\mathcal{B}}_T \mathbf{K}_e \boldsymbol{\mathcal{B}}_T{}^T + \boldsymbol{\mathcal{B}}_{T2}{}^T \mathbf{K}_1 \boldsymbol{\mathcal{B}}_{T2} + \mathbf{K}_2 \quad (5\text{-}43)$$

Here, $\mathbf{K}_1$ is calculated as

$$\mathbf{K}_1 = \begin{bmatrix} 0 & 0 & 0 & 0 & 0 & 0 & 0 \\ 0 & c_1^{(1,1)} & c_1^{(1,2)} & c_1^{(1,3)} & 0 & 0 & 0 \\ 0 & c_1^{(2,1)} & c_1^{(2,2)} & c_1^{(2,3)} & 0 & 0 & 0 \\ 0 & c_1^{(3,1)} & c_1^{(3,2)} & c_1^{(3,3)} & 0 & 0 & 0 \\ 0 & 0 & 0 & 0 & c_2^{(1,1)} & c_2^{(1,2)} & c_2^{(1,3)} \\ 0 & 0 & 0 & 0 & c_2^{(2,1)} & c_2^{(2,2)} & c_2^{(2,3)} \\ 0 & 0 & 0 & 0 & c_2^{(3,1)} & c_2^{(3,2)} & c_2^{(3,3)} \end{bmatrix} \tag{5-44}$$

where $c_k^{(i,j)}$ represents the compoenent at the *i*th row and *j*th column in a matrix $\mathbf{c}_k$, defined by equation (5-45).

$$\mathbf{c}_k = \begin{bmatrix} a_k^{(1,1)} & a_k^{(1,2)} & a_k^{(1,3)} \\ a_k^{(2,1)} & a_k^{(2,2)} & a_k^{(2,3)} \\ a_k^{(3,1)} & a_k^{(3,2)} & a_k^{(3,3)} \end{bmatrix} \begin{bmatrix} b_k^{(1,1)} & b_k^{(1,2)} & b_k^{(1,3)} \\ b_k^{(2,1)} & b_k^{(2,2)} & b_k^{(2,3)} \\ b_k^{(3,1)} & b_k^{(3,2)} & b_k^{(3,3)} \end{bmatrix} \tag{5-45}$$

Each component of matrices $\mathbf{a}_k$ and $\mathbf{b}_k$ is calculated as

$$a_k^{(1,1)} = -\frac{\|\vec{\phi}_k\| - 2\tan\frac{\|\vec{\phi}_k\|}{2}}{2\|\vec{\phi}_k\|^2 \tan\frac{\|\vec{\phi}_k\|}{2}} \left(2\phi_k^{(1,1)} w_k^{(1,1)} + \phi_k^{(2,1)} w_k^{(2,1)} + \phi_k^{(3,1)} w_k^{(3,1)}\right) \tag{5-46}$$

$$a_k^{(1,2)} = \frac{w_k^{(3,1)}}{2} - \frac{\phi_k^{(1,1)} w_k^{(2,1)}}{\|\vec{\phi}_k\|^2} \left(\frac{\|\vec{\phi}_k\|}{2\tan\frac{\|\vec{\phi}_k\|}{2}} - 1\right) \tag{5-47}$$

$$a_k^{(1,3)} = -\frac{w_k^{(2,1)}}{2} - \frac{\phi_k^{(1,1)} w_k^{(3,1)}}{\|\vec{\phi}_k\|^2} \left(\frac{\|\vec{\phi}_k\|}{2\tan\frac{\|\vec{\phi}_k\|}{2}} - 1\right) \tag{5-48}$$

$$a_k^{(2,1)} = -\frac{w_k^{(3,1)}}{2} - \frac{\phi_k^{(2,1)} w_k^{(1,1)}}{\|\vec{\phi}_k\|^2} \left(\frac{\|\vec{\phi}_k\|}{2\tan\frac{\|\vec{\phi}_k\|}{2}} - 1\right) \tag{5-49}$$

$$a_k^{(2,2)} = -\frac{\|\vec{\phi}_k\| - 2\tan\frac{\|\vec{\phi}_k\|}{2}}{2\|\vec{\phi}_k\|^2 \tan\frac{\|\vec{\phi}_k\|}{2}} \left(\phi_k^{(1,1)} w_k^{(1,1)} + 2\phi_k^{(2,1)} w_k^{(2,1)} + \phi_k^{(3,1)} w_k^{(3,1)}\right) \tag{5-50}$$

$$a_k^{(2,3)} = \frac{w_k^{(1,1)}}{2} - \frac{\phi_k^{(2,1)} w_k^{(3,1)}}{\left\|\vec{\phi}_k\right\|^2}\left(\frac{\left\|\vec{\phi}_k\right\|}{2\tan\frac{\left\|\vec{\phi}_k\right\|}{2}} - 1\right) \tag{5-51}$$

$$a_k^{(3,1)} = \frac{w_k^{(2,1)}}{2} - \frac{\phi_k^{(3,1)} w_k^{(1,1)}}{\left\|\vec{\phi}_k\right\|^2}\left(\frac{\left\|\vec{\phi}_k\right\|}{2\tan\frac{\left\|\vec{\phi}_k\right\|}{2}} - 1\right) \tag{5-52}$$

$$a_k^{(3,2)} = -\frac{w_k^{(1,1)}}{2} - \frac{\phi_k^{(3,1)} w_k^{(2,1)}}{\left\|\vec{\phi}_k\right\|^2}\left(\frac{\left\|\vec{\phi}_k\right\|}{2\tan\frac{\left\|\vec{\phi}_k\right\|}{2}} - 1\right) \tag{5-53}$$

$$a_k^{(3,3)} = -\frac{\left\|\vec{\phi}_k\right\| - 2\tan\frac{\left\|\vec{\phi}_k\right\|}{2}}{2\left\|\vec{\phi}_k\right\|^2 \tan\frac{\left\|\vec{\phi}_k\right\|}{2}}\left(\phi_k^{(1,1)} w_k^{(1,1)} + \phi_k^{(2,1)} w_k^{(2,1)} + 2\phi_k^{(3,1)} w_k^{(3,1)}\right) \tag{5-54}$$

$$b_k^{(1,1)} = \frac{\left\|\vec{\phi}_k\right\|}{2\tan\frac{\left\|\vec{\phi}_k\right\|}{2}} + \left(\phi_k^{(1,1)}\right)^2\left(\frac{1}{\left\|\vec{\phi}_k\right\|^2} - \frac{1}{2\left\|\vec{\phi}_k\right\|\tan\frac{\left\|\vec{\phi}_k\right\|}{2}}\right) \tag{5-55}$$

$$b_k^{(1,2)} = \phi_k^{(1,1)}\phi_k^{(2,1)}\left(\frac{1}{\left\|\vec{\phi}_k\right\|^2} - \frac{1}{2\left\|\vec{\phi}_k\right\|\tan\frac{\left\|\vec{\phi}_k\right\|}{2}}\right) + \frac{\phi_k^{(3,1)}}{2} \tag{5-56}$$

$$b_k^{(1,3)} = \phi_k^{(1,1)}\phi_k^{(3,1)}\left(\frac{1}{\left\|\vec{\phi}_k\right\|^2} - \frac{1}{2\left\|\vec{\phi}_k\right\|\tan\frac{\left\|\vec{\phi}_k\right\|}{2}}\right) - \frac{\phi_k^{(2,1)}}{2} \tag{5-57}$$

$$b_k^{(2,1)} = \phi_k^{(1,1)}\phi_k^{(2,1)}\left(\frac{1}{\left\|\vec{\phi}_k\right\|^2} - \frac{1}{2\left\|\vec{\phi}_k\right\|\tan\frac{\left\|\vec{\phi}_k\right\|}{2}}\right) - \frac{\phi_k^{(3,1)}}{2} \tag{5-58}$$

$$b_k^{(2,2)} = \frac{\left\|\vec{\phi}_k\right\|}{2\tan\frac{\left\|\vec{\phi}_k\right\|}{2}} + \left(\phi_k^{(2,1)}\right)^2\left(\frac{1}{\left\|\vec{\phi}_k\right\|^2} - \frac{1}{2\left\|\vec{\phi}_k\right\|\tan\frac{\left\|\vec{\phi}_k\right\|}{2}}\right) \tag{5-59}$$

$$b_k^{(2,3)} = \phi_k^{(2,1)}\phi_k^{(3,1)}\left(\frac{1}{\left\|\vec{\phi}_k\right\|^2} - \frac{1}{2\left\|\vec{\phi}_k\right\|\tan\frac{\left\|\vec{\phi}_k\right\|}{2}}\right) + \frac{\phi_k^{(1,1)}}{2} \tag{5-60}$$

$$b_k^{(3,1)} = \phi_k^{(1,1)}\phi_k^{(3,1)}\left(\frac{1}{\left\|\vec{\phi}_k\right\|^2} - \frac{1}{2\left\|\vec{\phi}_k\right\|\tan\frac{\left\|\vec{\phi}_k\right\|}{2}}\right) + \frac{\phi_k^{(2,1)}}{2} \tag{5-61}$$

$$b_k^{(3,2)} = \phi_k^{(2,1)}\phi_k^{(3,1)}\left(\frac{1}{\left\|\vec{\phi}_k\right\|^2} - \frac{1}{2\left\|\vec{\phi}_k\right\|\tan\frac{\left\|\vec{\phi}_k\right\|}{2}}\right) - \frac{\phi_k^{(1,1)}}{2} \tag{5-62}$$

$$b_k^{(3,3)} = \frac{\left\|\vec{\phi}_k\right\|}{2\tan\frac{\left\|\vec{\phi}_k\right\|}{2}} + \left(\phi_k^{(3,1)}\right)^2\left(\frac{1}{\left\|\vec{\phi}_k\right\|^2} - \frac{1}{2\left\|\vec{\phi}_k\right\|\tan\frac{\left\|\vec{\phi}_k\right\|}{2}}\right) \tag{5-63}$$

where $\phi_k^{(i,1)}$ and $w_k^{(i,1)}$ denote the *i*th compoenent of vectors $\vec{\phi}_k$ and $\vec{w}_k$, respectively. $\vec{w}_k$ is the local moment vector of the *k*th node, described as

$$\vec{w}_k = \begin{bmatrix} F_e^{(3k-1,1)} \\ F_e^{(3k,1)} \\ F_e^{(3k+1,1)} \end{bmatrix} \tag{5-64}$$

where $F_e^{(i,1)}$ is the *i*th component of $\vec{F}_e$. If the vector norm of $\vec{\phi}_k$ is 0, $\mathbf{a}_k$ and $\mathbf{b}_k$ are determined using equations (5-65) and (5-66), respectively.

$$\mathbf{a}_k\left(\left\|\vec{\phi}_k\right\| = 0\right) = \frac{1}{2}\begin{bmatrix} 0 & w_k^{(3,1)} & -w_k^{(2,1)} \\ -w_k^{(3,1)} & 0 & w_k^{(1,1)} \\ w_k^{(2,1)} & -w_k^{(1,1)} & 0 \end{bmatrix} \tag{5-65}$$

$$\mathbf{b}_k\left(\left\|\vec{\phi}_k\right\| = 0\right) = \mathbf{I}_3 \tag{5-66}$$

$\mathbf{K}_2$ is defined as

$$\mathbf{K}_2 = \mathbf{K}_{2,1} + \mathbf{K}_{2,2} + \mathbf{K}_{2,3} \tag{5-67}$$

where matrices $\mathbf{K}_{2,1}$, $\mathbf{K}_{2,2}$, and $\mathbf{K}_{2,3}$ are determined using equations (5-68), (5-69), and (5-70), respectively.

$$\mathbf{K}_{2,1} = \frac{\mathrm{F}_{\mathrm{T}_1}^{(1,1)}}{\mathcal{L}} \begin{bmatrix} \mathbf{I}_3 - \vec{r}_{\mathrm{x}} \times \vec{r}_{\mathrm{x}}{}^{\mathrm{T}} & \mathbf{0}_3 & -\mathbf{I}_3 + \vec{r}_{\mathrm{x}} \times \vec{r}_{\mathrm{x}}{}^{\mathrm{T}} & \mathbf{0}_3 \\ \mathbf{0}_3 & \mathbf{0}_3 & \mathbf{0}_3 & \mathbf{0}_3 \\ -\mathbf{I}_3 + \vec{r}_{\mathrm{x}} \times \vec{r}_{\mathrm{x}}{}^{\mathrm{T}} & \mathbf{0}_3 & \mathbf{I}_3 - \vec{r}_{\mathrm{x}} \times \vec{r}_{\mathrm{x}}{}^{\mathrm{T}} & \mathbf{0}_3 \\ \mathbf{0}_3 & \mathbf{0}_3 & \mathbf{0}_3 & \mathbf{0}_3 \end{bmatrix} \tag{5-68}$$

$$\mathbf{K}_{2,2} = -\begin{bmatrix} \boldsymbol{\mathcal{R}}_{\mathrm{r}} & \mathbf{0}_3 & \boldsymbol{\mathcal{R}}_{\mathrm{r}} & \mathbf{0}_3 \\ \mathbf{0}_3 & \mathbf{0}_3 & \mathbf{0}_3 & \mathbf{0}_3 \\ \boldsymbol{\mathcal{R}}_{\mathrm{r}} & \mathbf{0}_3 & \boldsymbol{\mathcal{R}}_{\mathrm{r}} & \mathbf{0}_3 \\ \mathbf{0}_3 & \mathbf{0}_3 & \mathbf{0}_3 & \mathbf{0}_3 \end{bmatrix}^{\mathrm{T}} \mathbf{P} \begin{bmatrix} -\boldsymbol{\mathcal{A}}_1{}^{\mathrm{T}} \\ -\boldsymbol{\mathcal{A}}_2{}^{\mathrm{T}} \\ \boldsymbol{\mathcal{A}}_1{}^{\mathrm{T}} \\ -\boldsymbol{\mathcal{A}}_3{}^{\mathrm{T}} \end{bmatrix}^{\mathrm{T}} \begin{bmatrix} \boldsymbol{\mathcal{R}}_{\mathrm{r}} & \mathbf{0}_3 & \boldsymbol{\mathcal{R}}_{\mathrm{r}} & \mathbf{0}_3 \\ \mathbf{0}_3 & \mathbf{0}_3 & \mathbf{0}_3 & \mathbf{0}_3 \\ \boldsymbol{\mathcal{R}}_{\mathrm{r}} & \mathbf{0}_3 & \boldsymbol{\mathcal{R}}_{\mathrm{r}} & \mathbf{0}_3 \\ \mathbf{0}_3 & \mathbf{0}_3 & \mathbf{0}_3 & \mathbf{0}_3 \end{bmatrix} \tag{5-69}$$

$$\mathbf{K}_{2,3} = \begin{bmatrix} \boldsymbol{\mathcal{R}}_{\mathrm{r}} & \mathbf{0}_3 & \boldsymbol{\mathcal{R}}_{\mathrm{r}} & \mathbf{0}_3 \\ \mathbf{0}_3 & \mathbf{0}_3 & \mathbf{0}_3 & \mathbf{0}_3 \\ \boldsymbol{\mathcal{R}}_{\mathrm{r}} & \mathbf{0}_3 & \boldsymbol{\mathcal{R}}_{\mathrm{r}} & \mathbf{0}_3 \\ \mathbf{0}_3 & \mathbf{0}_3 & \mathbf{0}_3 & \mathbf{0}_3 \end{bmatrix}^{\mathrm{T}} \begin{bmatrix} -\boldsymbol{\mathcal{A}}_1{}^{\mathrm{T}} \\ -\boldsymbol{\mathcal{A}}_2{}^{\mathrm{T}} \\ \boldsymbol{\mathcal{A}}_1{}^{\mathrm{T}} \\ -\boldsymbol{\mathcal{A}}_3{}^{\mathrm{T}} \end{bmatrix} \begin{bmatrix} 0 \\ \chi_1 \\ \chi_2 \end{bmatrix} \begin{bmatrix} -\vec{r}_{\mathrm{x}}{}^{\mathrm{T}} & \mathbf{0}_{1\times 3} & \vec{r}_{\mathrm{x}}{}^{\mathrm{T}} & \mathbf{0}_{1\times 3} \end{bmatrix} \tag{5-70}$$

Here, $\mathrm{F}_{\mathrm{T}_1}^{(\mathrm{i},1)}$ is the *i*th component of $\vec{\mathrm{F}}_{\mathrm{T}_1}$, calculated as

$$\vec{\mathrm{F}}_{\mathrm{T}_1} = \mathbf{B}_{\mathrm{T}_1} \vec{\mathrm{F}}_{\mathrm{e}} \tag{5-71}$$

and $\mathbf{P}$ is described as

$$\mathbf{P} = \begin{bmatrix} \mathbf{J}_1 \\ \mathbf{J}_2 \\ \mathbf{J}_3 \\ \mathbf{J}_4 \end{bmatrix} \tag{5-72}$$

where $\mathbf{J}_{\mathrm{i}}$ is expressed as

$$\mathbf{J}_{\mathrm{i}} = \begin{bmatrix} 0 & -\psi^{(3\mathrm{i},1)} & \psi^{(3\mathrm{i}-1,1)} \\ \psi^{(3\mathrm{i},1)} & 0 & -\psi^{(3\mathrm{i}-2,1)} \\ -\psi^{(3\mathrm{i}-1,1)} & \psi^{(3\mathrm{i}-2,1)} & 0 \end{bmatrix} \tag{5-73}$$

and $\psi^{(\mathrm{i},1)}$ is the *i*th component of $\vec{\psi}$, determined using equation (5-74).

$$\vec{\psi} = \begin{bmatrix} \boldsymbol{\mathcal{A}}_1{}^{\mathrm{T}} & \boldsymbol{\mathcal{A}}_2{}^{\mathrm{T}} + \mathbf{I}_3 & -\boldsymbol{\mathcal{A}}_1{}^{\mathrm{T}} & \boldsymbol{\mathcal{A}}_3{}^{\mathrm{T}} \\ \boldsymbol{\mathcal{A}}_1{}^{\mathrm{T}} & \boldsymbol{\mathcal{A}}_2{}^{\mathrm{T}} & -\boldsymbol{\mathcal{A}}_1{}^{\mathrm{T}} & \boldsymbol{\mathcal{A}}_3{}^{\mathrm{T}} + \mathbf{I}_3 \end{bmatrix}^{\mathrm{T}} \begin{bmatrix} \mathrm{F}_{\mathrm{T}_1}^{(2,1)} \\ \mathrm{F}_{\mathrm{T}_1}^{(3,1)} \\ \mathrm{F}_{\mathrm{T}_1}^{(4,1)} \\ \mathrm{F}_{\mathrm{T}_1}^{(5,1)} \\ \mathrm{F}_{\mathrm{T}_1}^{(6,1)} \\ \mathrm{F}_{\mathrm{T}_1}^{(7,1)} \end{bmatrix} \tag{5-74}$$

Also, χ_1 and χ_2 are defined by equations (5-75) and (5-76), respectively.

$$\chi_1 = \frac{\mathcal{S}_0}{\mathcal{L}}\left(\mathrm{F}_{\mathrm{T}_1}^{(2,1)} + \mathrm{F}_{\mathrm{T}_1}^{(5,1)}\right) + \frac{1}{\mathcal{L}}\left(\mathrm{F}_{\mathrm{T}_1}^{(3,1)} + \mathrm{F}_{\mathrm{T}_1}^{(6,1)}\right) \tag{5-75}$$

$$\chi_2 = \frac{1}{\mathcal{L}}\left(\mathrm{F}_{\mathrm{T}_1}^{(4,1)} + \mathrm{F}_{\mathrm{T}_1}^{(7,1)}\right) \tag{5-76}$$

Table 5-1. Geometric and mechanical properties of bulge and non-4-way junction. These properties have the following values that are independent of base sequences. In this study, the standard deviation values of all properties and coupling coefficients are set to zero.

Properties	Units	Bulge	Non-4-way junction
T_x	nm	1.55	2.25
T_y	nm	0.00	0.00
T_z	nm	0.00	0.00
$R_{x,1}$	°	0.00	0.00
$R_{x,2}$	°	0.00	0.00
$R_{y,1}$	°	0.00	0.00
$R_{y,2}$	°	0.00	0.00
$R_{z,1}$	°	0.00	-17.43
$R_{z,2}$	°	0.00	-17.43
S	pN	700.00	2500.00
Y_y	pN	10.00	780.00
Y_z	pN	10.00	780.00
C	$pN \cdot nm^2$	10.00	350.00
B_y	$pN \cdot nm^2$	5.00	300.00
B_z	$pN \cdot nm^2$	5.00	300.00
G	-	0.00	0.00

5.3. Modeling of single-stranded DNA

Unlike other structural motifs, ssDNA has unique mechanical characteristics that depend on the end-to-end distance (d_{EE}) and the contour length (L_c). The end-to-end distance of ssDNA is very short when its contour length is long, whereas ssDNA with a short contour length has an end-to-end distance comparable to the equilibrated length and exhibits significant mechanical stiffness. The end-to-end distance of ssDNA is expressed in relation to the contour length as

$$d_{EE} = \gamma L_c \sqrt{\frac{5}{14} - \frac{3L_c}{28P_{L,B}} + \frac{1}{7}\sqrt{\left(\frac{5}{2} - \frac{3L_c}{4P_{L,B}^{s}}\right)^2 + 14}} \tag{5-77}$$

where $P_{L,B}^{s}$ is the bending persistence length of ssDNA with a value of 0.67 [nm] under an ionized solution with Mg^{2+} concentration of 10 [mM][50], and γ is the correction factor with a value of 2, which was previously reported as the most appropriate[29].

The mechanical behavior of ssDNA is described by the freely-jointed-chain model, represented as

$$\frac{d_{EE}}{L_c} = \left(\coth \eta F_S - \frac{1}{\eta F_S}\right)\left(1 + \frac{F_S}{K}\right) \tag{5-78}$$

where η is defined as

$$\eta = \frac{2P_{L,B}^{s}}{k_B T_a} \tag{5-79}$$

and F_S, k_B, and T_a indicate the stretching force, Boltzmann's constant, and absolute temperature, respectively. K is set to be 710 [pN] with Mg^{2+} concentration of 10 [mM]. The stretching rigidity is obtained by performing the partial derivative

of F_S with respect to d_{EE}/L_c, as given by equation (5-80), which represents the relationship between S and F_S.

$$S = \frac{\partial F_S}{\partial (d_{EE}/L_c)} = \frac{K}{\left\{\coth \eta F_S - \frac{1}{\eta F_S} + \frac{K}{\eta {F_S}^2} - \eta K(\coth^2 \eta F_S - 1)\right\}} \tag{5-80}$$

By utilizing equations (5-78) and (5-80), we examine the correlation between S and d_{EE}/L_c, and formulate an appriximate stretching rigidity ($\mathcal{S}$) that characterizes this relationship. The definition of $\mathcal{S}$ are given in equations (5-81), (5-82), and (5-83), which are used for convenience in the finite element modeling (Figure 5-1).

$$\mathcal{S} = S^H \qquad \left(\frac{d_{EE}}{L_c} \geq 1.2\right) \tag{5-81}$$

$$\mathcal{S} = \left(S^H - S^L\right)\frac{5d_{EE}}{2L_c} - 2S^H + 3S^L \qquad \left(0.8 \leq \frac{d_{EE}}{L_c} < 1.2\right) \tag{5-82}$$

$$\mathcal{S} = S^L \qquad \left(\frac{d_{EE}}{L_c} < 0.8\right) \tag{5-83}$$

Here, S^H and S^L are set to be 710 [pN] and 8 [pN], respectively. Other primary rigidities, including the shearing, bending, and twisting ones, are determined to be 10 [pN] or 10 [pN·nm^2], and all coupling coefficients are set to be 0.

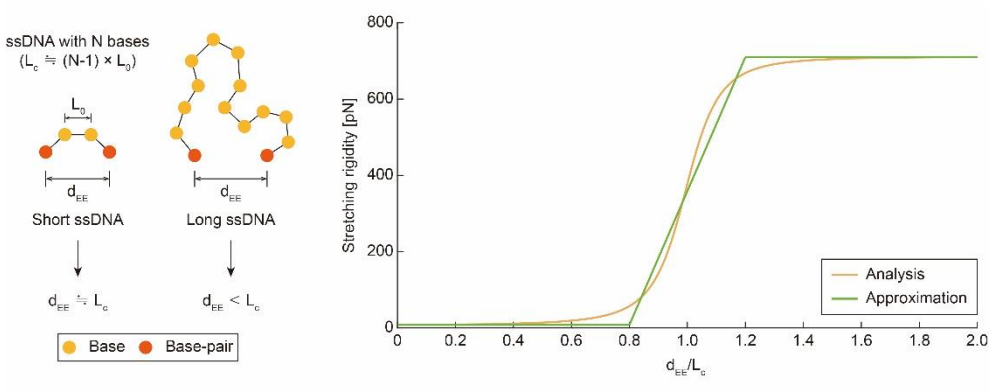

Figure 5-1. Modeling of ssDNA. While the contour length and the end-to-end distance of short ssDNA are similar, the end-to-end distance of long ssDNA is shorter than its contour length. The stretchging rigidity of ssDNA is determined by considering the end-to-end distance over the contour length.

5.4. Modeling of electrostatic interaction

DNA has a negatively charged backbone, resulting in electrostatic repulsive forces between DNA helices in DNA nanostructures. To describe the interaction between two base-pairs separated by a distance ξ, we employ a Debye-Hückel potential (U_{DH}). This potential is defined as

$$U_{DH} = \frac{{Q_e}^2}{4\pi\varepsilon\xi} e^{-\frac{\xi}{L_{DH}}} \tag{5-84}$$

where ε is the permittivity of water (2.76×10^{-2} [e^2/pN·nm^2]), and Q_e denotes the effective charge, calculated using equation (5-85) with the molar concentration of Mg^{2+} ($w_{Mg^{2+}}$), as described in the previous reported study[29].

$$Q_e = 0.01 w_{Mg^{2+}} + 0.5 \tag{5-85}$$

L_{DH} indicates the Debye length, which is calculated as

$$L_{DH} = \sqrt{\frac{\varepsilon k_B T_a}{2 N_A e^2 I_s}} \tag{5-86}$$

where k_B, T_a, and N_A refer to the Boltzmann's constant, the absolute temperature, and Avogadro's number, respectively. I_s represents the ionic strength calculated as

$$I_s = \frac{1}{2}\sum_i w_i {q_i}^2 \tag{5-87}$$

where w_i and q_i denote the molar concentration and the charge number of the *i*th ion, respectively.

When two base-pair nodes exert electrostatic repulsive forces on each other ($\xi <$

ξ_c, where ξ_c is the specified cutoff distance), a finite element truss model is generated to describe the electrostatic interaction between the nodes. It is important to note that only translational forces are applied to this element without rotational moments. The one-dimensional force and stiffness matrix for the ξ-axis connecting the two nodes are calculated as follows. The force (F_ξ) is obtained by differentiating U_{DH} with respect to ξ using equation (5-88).

$$F_\xi = \frac{dU_{DH}}{d\xi} = -\frac{Q^2(L_{DH}+\xi)}{4\pi\varepsilon L_{DH}\xi^2} e^{-\frac{\xi}{L_{DH}}} \tag{5-88}$$

If the distance between two nodes changes from ξ_1 to ξ_2 during the incremental time step, the Green-Lagrange strain (ϵ) and the second Piola-Kirchhoff stress (σ_{PK}) given to the model are

$$\epsilon = \frac{{\xi_2}^2 - {\xi_1}^2}{2{\xi_1}^2} \tag{5-89}$$

$$\sigma_{PK} = \frac{\xi_1 F_{\xi_2}}{\xi_2 A_{DH}} \tag{5-90}$$

where A_{DH} is a virtual area of the electrostatic element. Then, the stiffness matrix of the element is defined by equation (5-91).

$$K_\xi = \frac{{\xi_2}^2}{{\xi_1}^3}\left(\frac{\partial\sigma_{PK}}{\partial\xi_2}\right)\left(\frac{\partial\xi_2}{\partial\epsilon}\right)A_{DH}\bigg|_{\xi_2=\xi} = \frac{Q^2\left(3{L_{DH}}^2 + 3L_{DH}\xi + \xi^2\right)}{4\pi\varepsilon {L_{DH}}^2\xi^3} e^{-\frac{\xi}{L_{DH}}} \tag{5-91}$$

The internal force vector ($\vec{F}_{ES}$) and the stiffness matrix ($\mathbf{K}_{ES}$) of the electrostatic element in the global coordinate are calculated as

$$\vec{F}_{ES} = \frac{F_\xi}{\xi}\begin{bmatrix} \vec{p}_1 - \vec{p}_2 \\ \mathbf{O}_{3\times1} \\ \vec{p}_2 - \vec{p}_1 \\ \mathbf{O}_{3\times1} \end{bmatrix} \tag{5-92}$$

$$\mathbf{K}_{\mathrm{ES}} = \begin{bmatrix} \mathbf{A} & \mathbf{O}_{3\times3} & -\mathbf{A} & \mathbf{O}_{3\times3} \\ \mathbf{O}_{3\times3} & \mathbf{O}_{3\times3} & \mathbf{O}_{3\times3} & \mathbf{O}_{3\times3} \\ -\mathbf{A} & \mathbf{O}_{3\times3} & \mathbf{A} & \mathbf{O}_{3\times3} \\ \mathbf{O}_{3\times3} & \mathbf{O}_{3\times3} & \mathbf{O}_{3\times3} & \mathbf{O}_{3\times3} \end{bmatrix} \tag{5-93}$$

where $\vec{\mathrm{p}}_1$ and $\vec{\mathrm{p}}_2$ are the position vectors of the first and second nodes, $\mathbf{O}_{\mathrm{m}\times\mathrm{n}}$ is an m-by-n zero matrix, and $\mathbf{A}$ is a matrix obtained using equation (5-94).

$$\mathbf{A} = \frac{\mathrm{K}_\xi}{\xi}(\vec{\mathrm{p}}_2 - \vec{\mathrm{p}}_1) \cdot (\vec{\mathrm{p}}_2 - \vec{\mathrm{p}}_1)^{\mathrm{T}} + \frac{\mathrm{F}_\xi}{\xi}\mathbf{I}_3 \tag{5-94}$$

Here, $\mathbf{I}_3$ is a 3-by-3 identity matrix.

5.5. Control of elements over incremental steps

During structural analysis, the geometric and mechanical properties ($\vec{P}^t$) of structural elements have valus at incremental step t as the step changes from t_0 to t_1. These values are calculated using linear interpolation, as shown in equation (5-95).

$$\vec{P}^t = \vec{P}^{t_0} + \alpha^t\left(\vec{P}^{t_1} - \vec{P}^{t_0}\right) \tag{5-95}$$

Here, α^t is an interpolation coefficient of structural elements defined as

$$\alpha^t = \left(\frac{t - t_0}{t_1 - t_o}\right)^{n_\alpha} \tag{5-96}$$

where n_α is a positive number (Figure 5-2A).

Electrostatic elements are effective in describing electrostatic repulsions between DNA helices. However, computational time can significantly increase if all the electrostatic elements between two nodes that are less than the cutoff distance are generated. Therefore, we control the number of electrostatic elements at incremental step t using a coefficient (β^t) as

$$N_e{}^t = \beta^t M_e{}^t \tag{5-97}$$

$$\beta^t = \left(\frac{t - t_0}{t_1 - t_o}\right)^{n_\beta} \tag{5-98}$$

where $N_e{}^t$ corresponds to the number of electrostatic elements that are generated, $M_e{}^t$ indicates the total number of them with two nodes located within the set cutoff distance, and n_β is a non-negative number (Figure 5-2B).

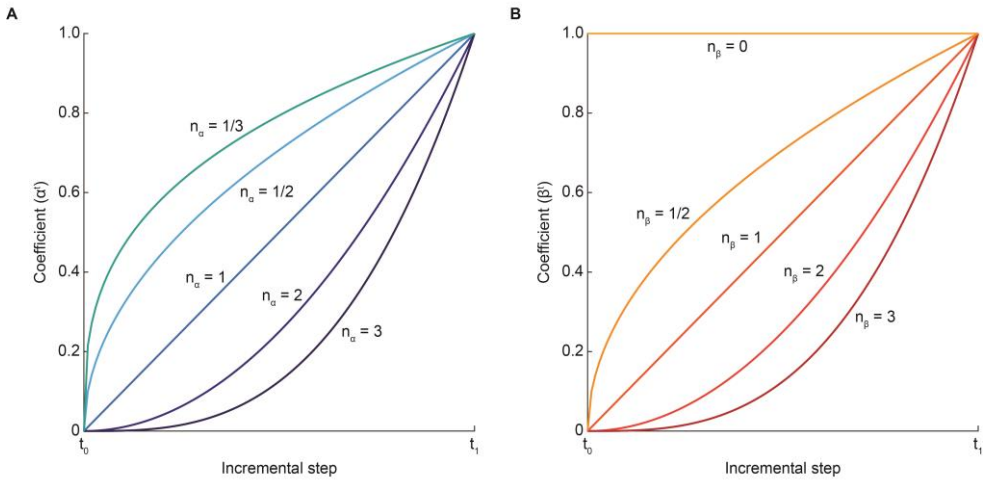

Figure 5-2. Controlling structural and electrostatic elements using analysis coefficients. (A) Coefficients for structural elements. (B) Coefficients for electrostatic elements.

5.6. Iterative solution method

When the incremental step changes from t to $t+\Delta t$, the structure is nonlinearly analyzed using the following basic equation as

$$\vec{F}_n\left(\vec{U}_i^{t+\Delta t}\right) = \vec{R}^{t+\Delta t}\left(\vec{U}_i^{t+\Delta t}\right) - \vec{F}^{t+\Delta t}\left(\vec{U}_i^{t+\Delta t}\right) = 0 \tag{5-99}$$

where $\vec{U}_i^{t+\Delta t}$ is the displacement vector at time of $t+\Delta t$ and iteration of i, and $\vec{R}^{t+\Delta t}$ and $\vec{F}^{t+\Delta t}$ are the externally applied external and internal force vectors at time of $t+\Delta t$, respectively. Here, we employ Newton-Raphson iterations[51] to solve equation (5-99) for multiple degrees of freedom. By using a Taylor series expansion, the total force vector ($\vec{F}_n$) can be rewritten as

$$\vec{F}_n\left(\vec{U}_i^{t+\Delta t}\right) = \vec{F}_n\left(\vec{U}_{i-1}^{t+\Delta t}\right) + \left[\frac{\partial \vec{F}_n}{\partial \vec{U}}\right]_{\vec{U}_{i-1}^{t+\Delta t}} \left(\vec{U}_i^{t+\Delta t} - \vec{U}_{i-1}^{t+\Delta t}\right) \tag{5-100}$$

when the higher-order terms are neglected. Then, we obtain

$$\left[\frac{\partial \vec{F}_n}{\partial \vec{U}}\right]_{\vec{U}_{i-1}^{t+\Delta t}} \left(\vec{U}_i^{t+\Delta t} - \vec{U}_{i-1}^{t+\Delta t}\right) = \vec{R}^{t+\Delta t} - \vec{F}_{i-1}^{t+\Delta t} \tag{5-101}$$

under the assumption that $\vec{R}$ is independent of the structural deformation. As a result, equation (5-101) is arranged for calculating the increment in displacements, as shown in equation (5-102).

$$\mathbf{K}_{i-1}^{t+\Delta t}\Delta\vec{U}_i = \vec{R}^{t+\Delta t} - \vec{F}_{i-1}^{t+\Delta t} \tag{5-102}$$

Here, the tangent stiffness matrix, $\mathbf{K}_{i-1}^{t+\Delta t}$, is defined in equation (5-103).

$$\mathbf{K}_{i-1}^{t+\Delta t} = \left[\frac{\partial \vec{F}_n}{\partial \vec{U}}\right]_{\vec{U}_{i-1}^{t+\Delta t}} \tag{5-103}$$

The displacement vector is updated as

$$\vec{U}_i^{t+\Delta t} = \vec{U}_{i-1}^{t+\Delta t} + \Delta\vec{U}_i \tag{5-104}$$

with the initial conditions given by equations (5-105), (5-106), and (5-107).

$$\mathbf{K}_0^{t+\Delta t} = \mathbf{K}^t \tag{5-105}$$

$$\vec{F}_0^{t+\Delta t} = \vec{F}^t \tag{5-106}$$

$$\vec{U}_0^{t+\Delta t} = \vec{U}^t \tag{5-107}$$

The iteration procedure continues until the convergence criteria are satisfied. These criteria, which include tolerances for displacement (ϵ_D), force (ϵ_F), and energy (ϵ_E), are defined in equations (5-108), (5-109), and (5-110).

$$\left\|\Delta\vec{U}_i\right\| \leq \epsilon_D \left\|\vec{U}_i^{t+\Delta t}\right\| \tag{5-108}$$

$$\left\|\vec{R}^{t+\Delta t} - \vec{F}_i^{t+\Delta t}\right\| \leq \epsilon_F \left\|\vec{R}^{t+\Delta t} - \vec{F}^t\right\| \tag{5-109}$$

$$\Delta\vec{U}_i \cdot \left(\vec{R}^{t+\Delta t} - \vec{F}_{i-1}^{t+\Delta t}\right) \leq \epsilon_E \left\{\Delta\vec{U}_1 \cdot \left(\vec{R}^{t+\Delta t} - \vec{F}^t\right)\right\} \tag{5-110}$$

6. Predicting final equilibrium shapes of DNA nanostructures

6.1. Abstract

The efficiency of the proposed computational procedure is demonstrated by performing structural analysis and predicting the final equilibrium shapes of various-shaped DNA nanostructures. Initially, the procedure classifies structural motifs and generates DEFCONFs for multi-helical DNA origami structures. From these configurations, finite element structural analysis successfully predicts their final equilibrium shapes. Representative examples, including wireframe and topologically closed circular structures, are chosen to demonstrate the effectiveness of the proposed procedure in resolving computational difficulties during structural analysis from lattice-based configurations. In cases where structural analysis from lattice-based configurations diverges, the proposed procedure successfully obtains final equilibrium shapes. Furthermore, for reconfigurable structures where local structural motifs are altered by adding DNA strands and the global shape is consequently changed, we confirm that the proposed procedure predicts the equilibrium shapes with changing structural motifs without computational difficulties. Hence, it is confirmed that our computational procedure can be effectively used to predict the structural equilibrium shapes of a variety of DNA nanostructures.

6.2. Setting parameters for structural analysis

In this study, we set the simulation parameters as follows for structural analysis. The displacement, force, and energy tolerance values denoted as ϵ_D, ϵ_F, and ϵ_E in equations (5-108), (5-109), and (5-110), are set to be 1, 10^{-3}, and 10^{-6}, respectively. The Debye-Hückel potential is employed to describe electrostatic replusions between DNA helices, using a cutoff distance of 1.2 [nm], a temperature of 300 [K], and an ion concentration of 20 [mM] for Mg^{2+}. Under the ion concentration, we set the contour length and the persistence length of a single-stranded DNA as 0.67 [nm/base] and 0.74 [nm], respectively, which were values previously reported[49]. Additionally, the multipliers n_α and n_β for coefficients of structural and electrostatic elements specifed in equations (5-96) and (5-98) are set to have values of 1 and 2, respectively.

6.3. Multi-helical structures

In order to evalutate the efficacy of our proposed method, we first conduct a structural analysis of multi-helical DNA origami structures that were previously reported. An examined block-shaped structure (Block1)[19], containing 15120 bases with a 6-by-10 helix cross-section, is found to be composed of 1065 dsDNAs (with 6495 regulars), 227 nicks, and 419 4-way junctions through the rough structural motif classification procedure (Figure 6-1A). When the positions and orientations of base-pairs, as well as the connectivity between bases, are initially provided, it is confirmed that its DSTBCONF is consistent with the provided lattice-based configuration. It is because all base-pairs on a three-dimensional lattice are either stacked or connected via Holliday junctions, resulting in a single substructure with no partitioning (Figure 6-1B). On the other hand, the DSTBCONF is generated in which 1065 dsDNAs (regarded as substructures) are well distributed in three-dimensional space when only the connectivity between bases is available (Figure 6-1C). The implementation of coarse-grained Brownian dynamics simulation on the DSTBCONFs reveals that the structure ultimately comprises structrual motifs inlcuding 1065 dsDNA, 167 stacked nicks, 838 junction nicks, 838 double junctions, and 60 open nicks, resulting in DEFCONFs. Considering the types of structural motifs present, finite element models are built for the DEFCONFs. Consequently, final equilibrium shapes are successfully predicted by the finite element structural analysis from the models, which are in agreement with the previously reported shape. It is observed that the final equilibrium shapes resulting from the DEFCONFs remains consistent regardless of the initial inputs: one where the positions and orientations of base-pairs, and the connectivity between bases are provided, and the other where only the base connectivity is given (Figure 6-1D).

Furthermore, we apply the proposed procedure into various-shaped DNA origami block structures, each of which has a different cross-section composed of 16-by-4 (Block2), 10-by-6 (Block3), 8-by-8 (Block4), 4-by-16 (Block5), 3-by-20 (Block6), and 2-by-30 (Block7) helices, respectively. The number of bases and DNA strands in them ranges from 15120 to 16128 and from 215 to 273, respectively. All

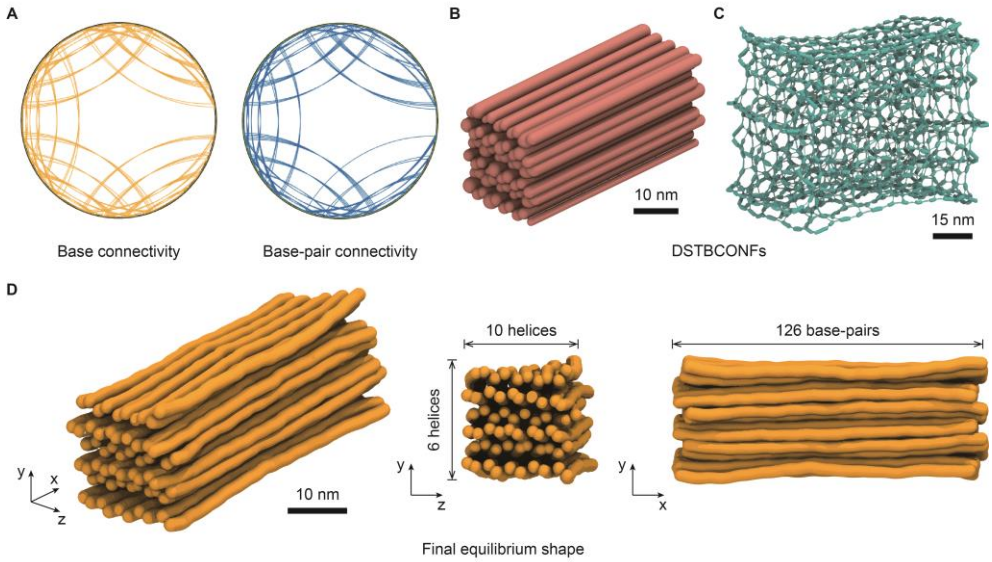

Figure 6-1. Structural analysis of DNA origami bloack-shaped structures. (A) The connectivity between bases and that between base-pairs of Block1. Covalent and complementray bonds between bases are represented by orange and green lines, respectively, in base connectivity. Also, structural motifs between base-pairs are denoted by individual lines, where yellow, green, purple, red, and blue lines indicate regular, bulge, nick, ssDNA, and junction among them, respectively, in the base-pair connectivity (B) The DSTBCONF when the positions and orientations of base-pairs as well as the connectivity between bases are initially provided. (C) The DSTBCONF when only the connectivity between bases is provided. (D) The final equilibrium shape predicted by finite element structural analysis. (E) Predicted final equilibrium shapes related to Block2, Block3, Block4, Block5, Block6, and Block7. They also follow the same analysis approach as Block1.

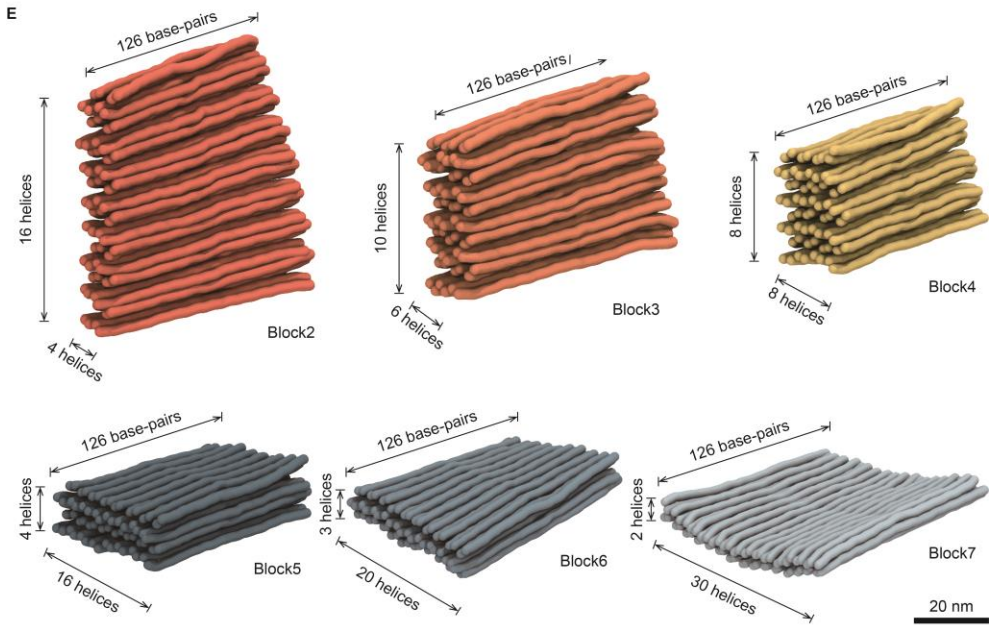

Figure 6-1 (Continued)

of them are confirmed to be composed of only dsDNAs, nicks, and junctions among structural motifs with the number of each motif ranging from 985 to 1160, 215 to 273, and 385 to 448, respectively. From the coarse-grained Brownian dynamics modelings and simulations, nick and junction among them are clssified as either stacked nick or open nick, and either double junction, single junction, or junction nick, respectively, resulting in generation of DEFCONFs. Structural prediction of the structures are successfully performed from their DEFCONFs (Figure 6-1E). Detailed structural motifs comprising the block structures are represented in Table 6-1.

Structural analysis is performed for several DNA origami structures, which are designed to have various bending angles by controlling curvatures through insertion and deletion of base-pairs in each helix[4]. The structure whose expected bending angle is 90 [˚] (Protractor-90) is composed of 15132 bases, 208 DNA strands, and structural motifs including 1006 dsDNAs (6560 regulars), 208 nicks, and 399 junctions (Figure 6-2A). Unlike block structures whose final equilibrium shape is al-

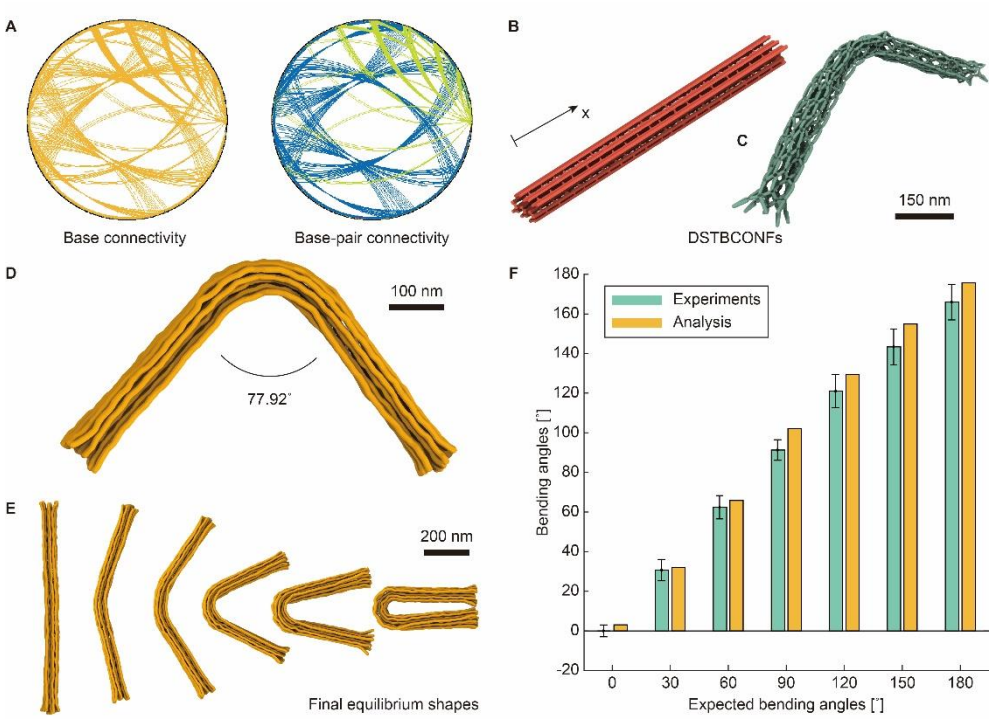

Figure 6-2. Structural analysis of DNA origami deformed structures. (A) The connectivity between bases and that between base-pairs of Protractor-90. In the base connectivity, orange and green lines represent covalent and complementary bonds between bases, respectively. Also, yellow, green, purple, red, and blue lines indicate regular, bulge, nick, ssDNA, and junction among structural motifs, respectively, in the base-pair connectivity. (B) The DSTBCONF of Protractor-90 generated when the positions and orientations of base-pairs as well as the connectiviy between bases are initially provided. (C) The DSTBCONF of Protractor-90 generated when the only the connectivity between bases is provided. (D) The final equilibrium shape of Protractor-90 predicted by finite element structural analysis. (E) Predicted final equilibrium shapes of other bent structures (Protractor-0, Protractor-30, Protractor-60, Protractor-120, Protractor-150, and Protractor-180). (F) Comparison between analyzed bending angles and experimental results.

most straight, its DSTBCONF generated considering both the connectivity between

bases and the positions and orientations of base-pairs differs greatly from that generated when only the connectivity between bases is provided. When the positions and orientations of base-pairs are also considered, the lattice-based structure becomes a single substructure without any parititon, so the DSTBCONF is same as the lattice-based straight one (Figure 6-2B). However, when only the connectivity of bases is available, a total of 1006 dsDNAs are well distributed in three-dimesnsional space. This has the effect of controlling the length of helices through insertion and deletion of base-pairs. As a result, the DSTBCONF is bent, which is close to the final equilibrium shape (Figure 6-2C). Through the coarse-grained Brownian dynamics simulations, it is confirmed that the structure is ultimately composed of structural motifs including 6560 regulars, 190 stacked nicks, 798 junction nicks, 798 double junctions, and 18 open nicks, and the DEFCONFs are obtained. Due to the specific experimental setup, where the base-pairs located at the structure's bottom are attached to the transmission electron microscopy (TEM) floor for observation, we impose limitations on the vertical displacement of the corresponding nodes in the finite element analysis. As a result, the finite element structural analysis from the DEFCONFs successfully predicts the consistent final equilibrium shape with the bending angle of 102.08 [˚] (Figure 6-2D). Other structures (Protractor-0, Protractor-30, Protractor-60, Protractor-120, Protractor-150, and Protractor-180) whose expected bending angles are 0 [˚], 30 [˚], 60 [˚], 120 [˚], 150 [˚], and 180 [˚], respectively, are also analyzed with the proposed procedure (Figure 6-2E). While the analysis predicts a slightly larger bending angle than observed in the experiments[4], the overall agreement is considered good (Figure 6-2F). Detailed structural motifs consisting of bent structures are represented in Table 6-1.

We apply the proposed procedure to various-shaped multi-helical DNA nanostructures including gear-[4], A-[25], S-[25], robot-[25], and spiral-shaped[4] structures, and successfully obtain their final equilibrium shapes. Through this, we confirm the proposed procedure can be used to perform structural analysis of various-shaped DNA nanostructures (Figure 6-3).

Table 6-1. The number of structural motifs of multi-helical DNA nanostructures.

Models	Regular	dsDNA	Bulge	ssDNA	Stcaked nick
Block1	6495	1065	0	0	167
Block2	7035	1029	0	0	153
Block3	6575	985	0	0	155
Block4	6916	1148	0	0	196
Block5	6895	1169	0	0	209
Block6	6504	1056	0	0	172
Block7	6523	1037	0	0	191
Protractor-0	6554	1006	0	0	190
Protractor-30	6554	1006	0	0	190
Protractor-60	6554	1006	0	0	190
Protractor-90	6560	1006	0	0	190
Protractor-120	6554	1006	0	0	190
Protractor-150	6557	1006	0	0	190
Protractor-180	6578	1006	0	0	190

Models	Juntion nick	Double junction	Single junction	Open nick
Block1	838	838	0	60
Block2	812	782	15	64
Block3	770	770	0	60
Block4	888	888	0	64
Block5	896	896	0	64
Block6	824	824	0	60
Block7	786	786	0	60
Protractor-0	798	798	0	18
Protractor-30	798	798	0	18
Protractor-60	798	798	0	18
Protractor-90	798	798	0	18
Protractor-120	798	798	0	18
Protractor-150	798	798	0	18
Protractor-180	798	798	0	18

Figure 6-3. Predicted final equilibrium shapes of various-shaped multi-helical nanostructures. (A) A gear-shaped structure with bending angle of 90 [˚]. (B) A gear-shaped structure with bending angle of 180 [˚]. (C) A A-shaped structure. (D) A S-shaped structure. (E) A robot-shaped structure. (F)-(H) Sprial-shaped structures.

6.4. Wireframe structures

Wireframe structures are representative examples that frequently exhibit nonconvergence when predicting their final shapes from lattice-based designs. These structures are generally designed on a three-dimensional lattice, where wireframe edges are positioned parallel and connected to each other thorugh stretched bonds. Since the on-lattice configuration of each wireframe structure is distant from its final shape, the wireframe edges must undergo significant rigid-body-like motions. However, these motions are impeded by electrostatic repulsive forces between DNA helices, preventing them from passing through one another. Consequently, the wireframe structure is liable to become trapped in a local energy minimum state during structural analysis.

To illustrate this point and demonstrate the effectiveness of the proposed computational procedure, we perform structural analysis for an icosahedron-shaped wireframe design obtained from TALOS (Three-dimensional, Algorithmically-generated Library of DNA Origami Shapes)[22]. The structure has 30 wireframe edges of honeycomb-pleated six-helix bundles, each of which is 84-base-pair long, 30660 bases, and 361 DNA strands. It is composed of various structural motifs including 1621 dsDNAs (13499 regulars), 60 bulges, 361 nicks, and 600 junctions, which are identified through the classification procedure. Notably, the bulges are stretched bonds that connect the wireframe edges (Figure 6-4A).

When the positions and orientations of base-pairs are provided as well as the connectivity between bases, each wireframe edge and several stretched bonds between two wireframe edges is considered as a vertex and an edge, respectively. That is, the structure is converted to 30 substructures and 30 edges. We obtain the DSTBCONF that wireframe edges are spatially distributed in three-dimensional space considering connections between them (Figure 6-4B).

If only the connectivity between bases is available, then each dsDNA and structural motif connecting two dsDNAs are represented as a vertex an an edge, respectively, resulting in 1621 vertices and 1021 edges. The whole network, comprising the vertices and edges, is segmented into 30 subnetworks, each of which

contains approximately 54 vertices and 91 edges. Due to the uniformity and regularity of wireframe edges, this structure shows significant similarity between its partitioned substructures and partitioned subnetworks, which respectively consider the positional relationship of base-pairs and the connectivity between dsDNAs. It is demonstrated by a Pearson correlation coefficient of 0.97 between indices of substructures and subnetworks, which contain bases, respectively. Our approach generates the DSTBCONF with well distributed dsDNAs (Figures 6-4C and 6-4D).

Through coarse-grained Brownian dynamics modeling and simulaiton, we confirm that the structure is comprised of 1621 dsDNAs, 60 bulges, 241 stacked nicks, 1200 junction nicks, 1200 double junctions, and 120 open nicks, and obtain the DEFCONF, which is then converted into a finite element model. Finally, finite element analysis for the model successfully predicts its final equilibrium shape, in contrast to the structural analysis performed directly from its lattice-based configuration that leads to divergence as wireframe edges become obstructed due to complexly crossed pathways (Figures 6-4E and 6-4F).

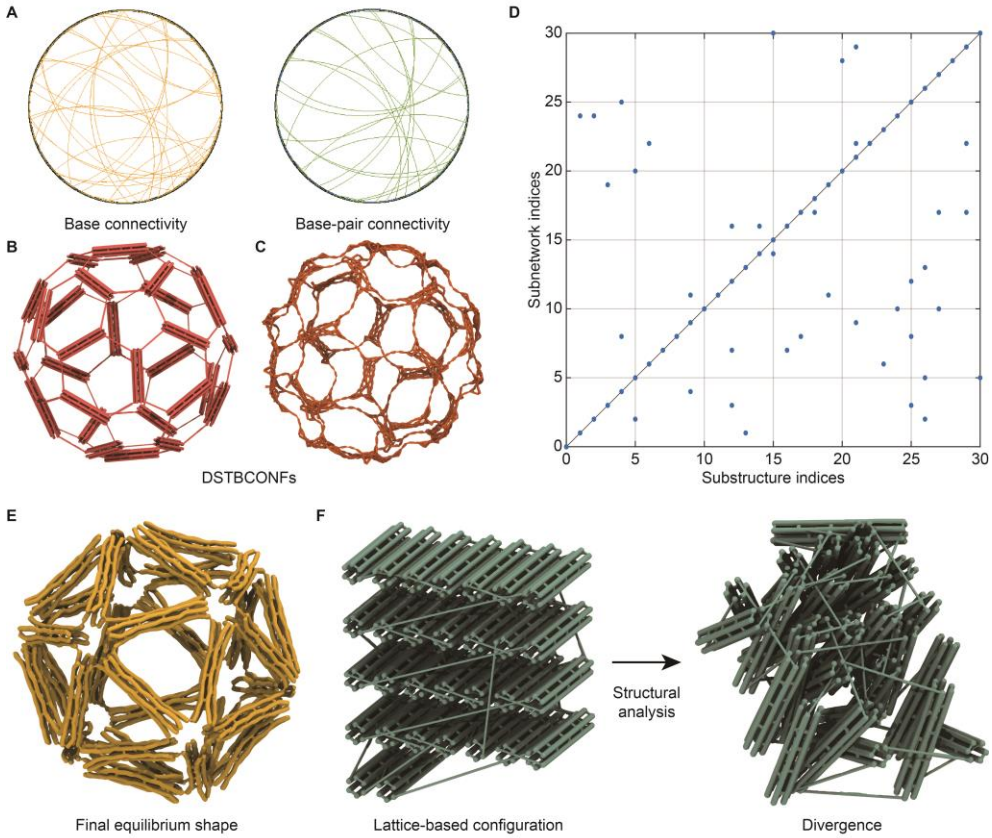

Figure 6-4. Structural analysis of an icoshaedron-shaped DNA wireframe structure. (A) The connectivity between bases and that between base-pairs. In the connectivity between bases, orange and green lines represent covalent and complementray bonds between bases, respectively. Structural motifs between base-pairs are denoted by individual lines, where yellow, green, purple, red, and blue lines indicate regular, bulge, nick, ssDNA, and junction, respectively. (B) The DSTBCONF when the positions and orientations of base-pairs as well as the connectivity between bases are initially provided. (C) The DSTBCONF when only the connectivity between bases is provided. (D) Correlation between substructures in Figure 6-4B and subnetworks in Figure 6-4C with the Pearson correlation coefficient of 0.97. (E) The final equilibrium shape predicted by finite element structural analysis. (F) Divergence of structural analysis from its lattice-based configuration.

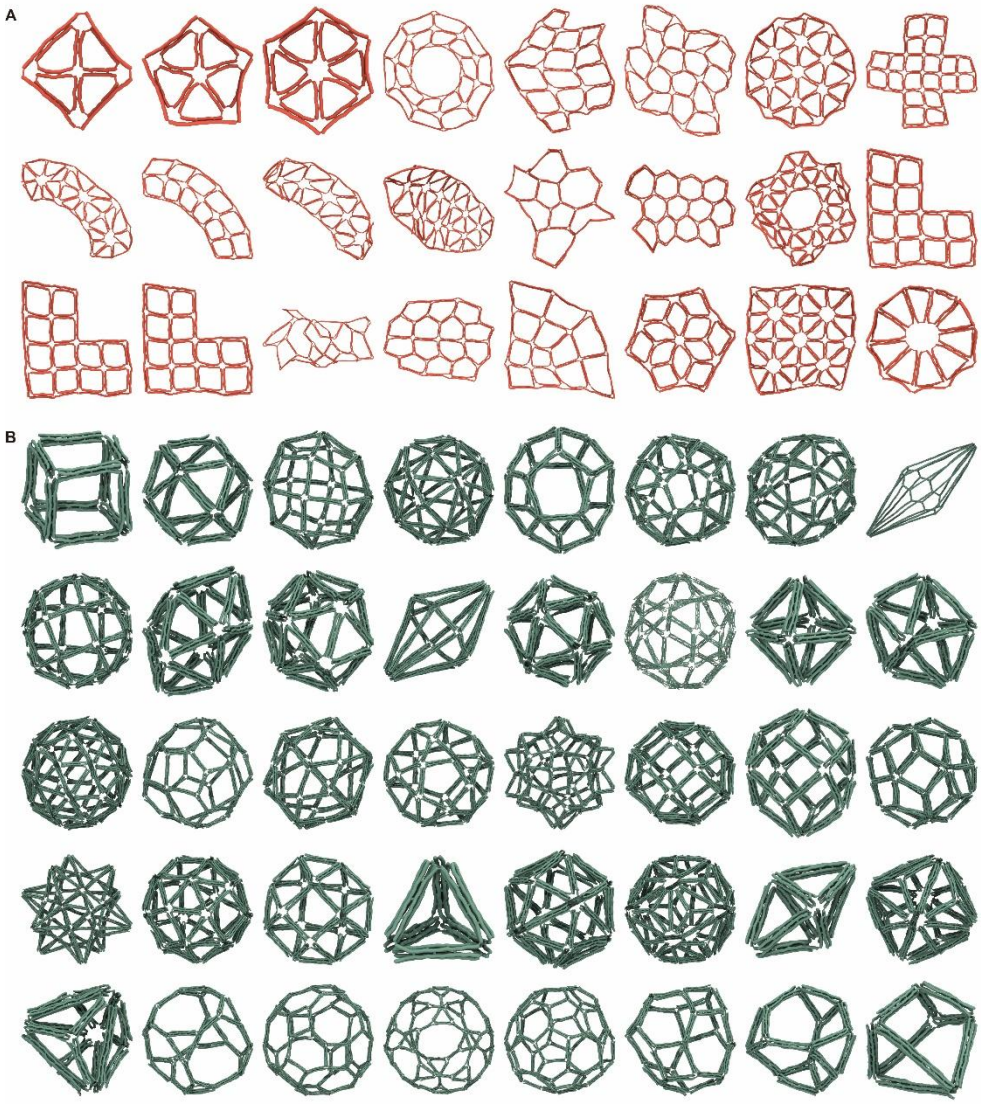

Figure 6-5. Structural analysis of DNA wireframe structures. (A) Predicted final equilibrium shapes of two-dimensional wireframes. (B) Predicted final equilibrium shapes of three-dimensional wireframes.

We apply the proposed proceudre to a total of 24 two-dimensional and 40 three-dimensional wireframe structures including the icosahedron analyzed above. These structures are obtained from PERDIX (Programmed Eulerian Routing for DNA Design using X-overs)[23] and TALOS[22], and have two-helix bundled 42-base-pair

long edges and honeycomb-pleated six-helix bundled 84-base-pair long edges, respectively. While all structural analyses from their lattice-based configurationss diverge by trapping unstable states (Figure A-2 in Appendix A.7), our procedure is successful to obtain their final equilibrium shapes (Figure 6-5).

In addition, we design tetrahedron, octahedron, and icoshahedron wireframes with bent inward or outward edges by inserting or deleting base-pairs in DNA helices. Using the proposed procedure, we obtain their final equilibrium shapes without any computational difficulty (Figure 6-6A). Experiments conducted on octahedron structures with straight, bent inward, and bent outward edges confiirm the successful realization of nonstraight wireframe structures (Figure 6-6B). Figure A-3 (in Appendix A.8), Appendix A.9, and Figure A-4 (in Appendix A.10) provide detailed descriptions of the lattice-based designs for the wireframe edges, the exprimental method, and the experimental results, respectively.

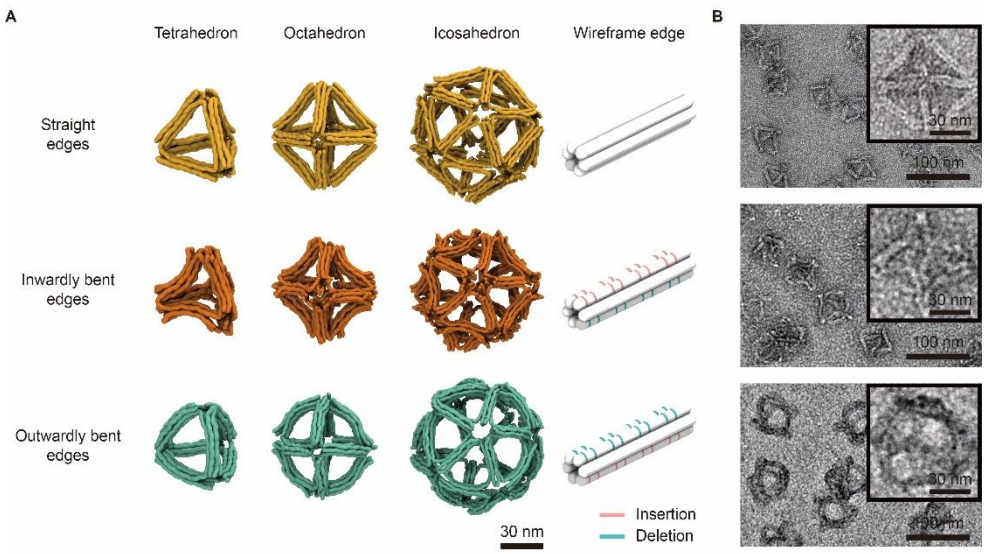

Figure 6-6. Structural analysis of DNA wireframes with nonstraight wireframe edges. (A) Predicted final equilibrium shapes of tetrahedron, octahedron, and icosahedron wireframes with straight or bent edges. (B) TEM images of octahedron wireframes with straight, inwardly bent, and outwardly bent edges.

6.5. Topologically closed structures

Topologically closed circular DNA structures designed on a three-dimensional lattice are arbitrarily cut and flattened onto a plane, which results in artificially stretched end-to-end bonds. Stretched bonds passing through the structure causes a compressive force to be exerted on it and gradually shrink towards an equilibrium bond length during structural analysis. The structural instabillity and buckling of DNA helices often occur during structural analysis, leading to a significant deterioration in the convergence of the solution procedure aimed at predicting the equilibrium shape.

The proposed procedure can effective solve the computational difficulty. The main idea is changing the buckling-inducing compressive force to tensile force by partitioning the structure into several segments. When the positions and orientations of base-pairs as well as the connectivity between bases are provided, it is important to determine the number of substructures to ensure computational efficiency in structural anlaysis of circular structures. To find an optimer number of substructures, we perform structural analysis with varying numbers of substructures. If the initially provided configuration is divdied into two substructures, structural analysis leads to divergence as each substructure needs to be deformed too much. Structural analysis conveges if three or more than three substructures are considered. Using three substructures requires substatantial deformation and increases analysis time, while using more substructures leads to a longer time for generating the DSTBCONF. Ultimately, partitioning into four substructures is found to be the most efficient chocie for computational time (Figures 6-7A and 6-7B). On the other hand, if only the connectivity between bases is provided, the number of substructures is same as that of dsDNAs among structural motifs. The DSTBCONF is generated in close proximity to a circular shape. (Figure 6-7C).

We perform structural analysis from the DEFCONFs of ten topologically closed circular structures including rings[8,14], tubes[9,11], a Möbius strip[6], spheres[7], and a vaselike structure[7], and obtain their final equilibrium shapes. Through this, it is confirmed that the proposed procedure can effectively circumvent the computational

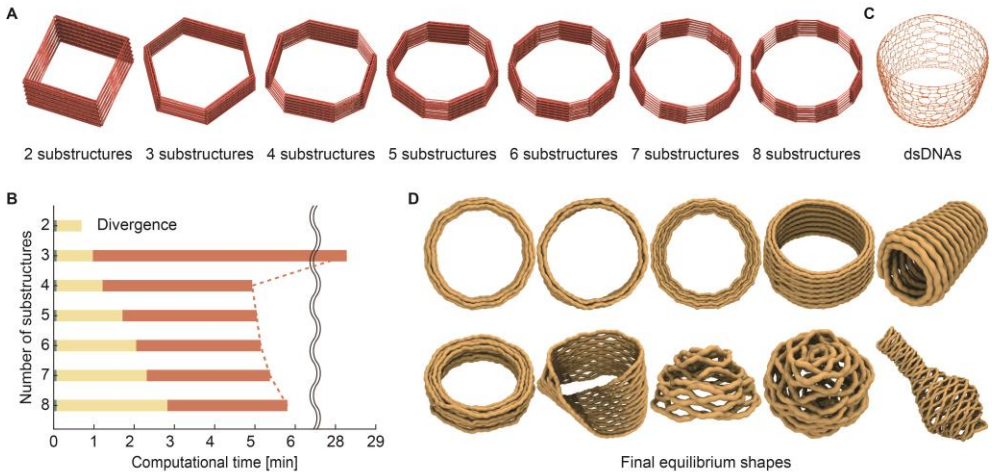

Figure 6-7. Structural analysis of topologically closed circular structures. (A) DSTBCONFs with respect to the number of substructures when the positions and orientations of base-pairs as well as the connectivity between bases are provided. (B) Computational time required in structural analysis with respect to the number of substructures. Green, yellow, and orange indicate the computational time required for partitioning the structure into substructures, generating the DSTBCONF, and performing structural analysis. The computation is implemented using MATLAB version R2019a (MathWorks) on a single PC (Intel Xeon CPU E5-2660 v4 @ 2.00 GHz). (C) A DSTBCONF generated when only the connectivity between bases is provided. (D) Predicted final equilibrium shapes of ten circular structures.

diffculty in structrual analysis from lattice-based configurations of circular structures (Figure 6-7D).

6.6. Reconfiguration of DNA nanostructures

DNA structural motifs in a lattice-based configuration are classified depending on the relative positioning of base-pairs. For example, if two base-pairs are positioned next to each other within a helix, the structural motif connecting them is classified as regular, stacked nick, or junction nick. In constrat, when two base-pairs are adjacent to each other in neighboring helices, the structural motif connecting them is identified as a junction-type motif such as double junction or single junction. However, the 4-way double junction has two closed isomers in a positively charged solution with metal cations, and its conformation depends on the mechanical energy of surrounding DNA strands. Thus, even though the conventional classificiation method of structural motifs is effective for the majority of DNA nanostructures, it is not accurate for structures that especially utilize isomers of 4-way double junctions.

To demonstrate this, we perform structural analysis of previously reported DNA array structures[52]. When a DNA strand is inserted into ssDNA around the 4-way double junction, this ssDNA is converted into one dsDNA and two stacked nicks. Then, since dsDNA prefers a straight configuration, the inserted DNA strand consequently changes the confomation of the 4-way double junction (Figure 6-8).

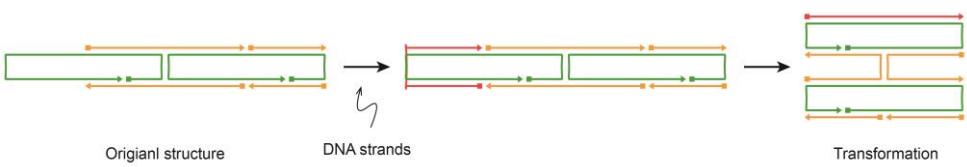

Figure 6-8. Conformational change of 4-way double junction. In a positively charged solution, 4-way double junction has two isomers, which is determined by the mechanical energy of surrounding DNA strands. That is, change of surrounding strands leads to occur the confomational transform of 4-way double junction.

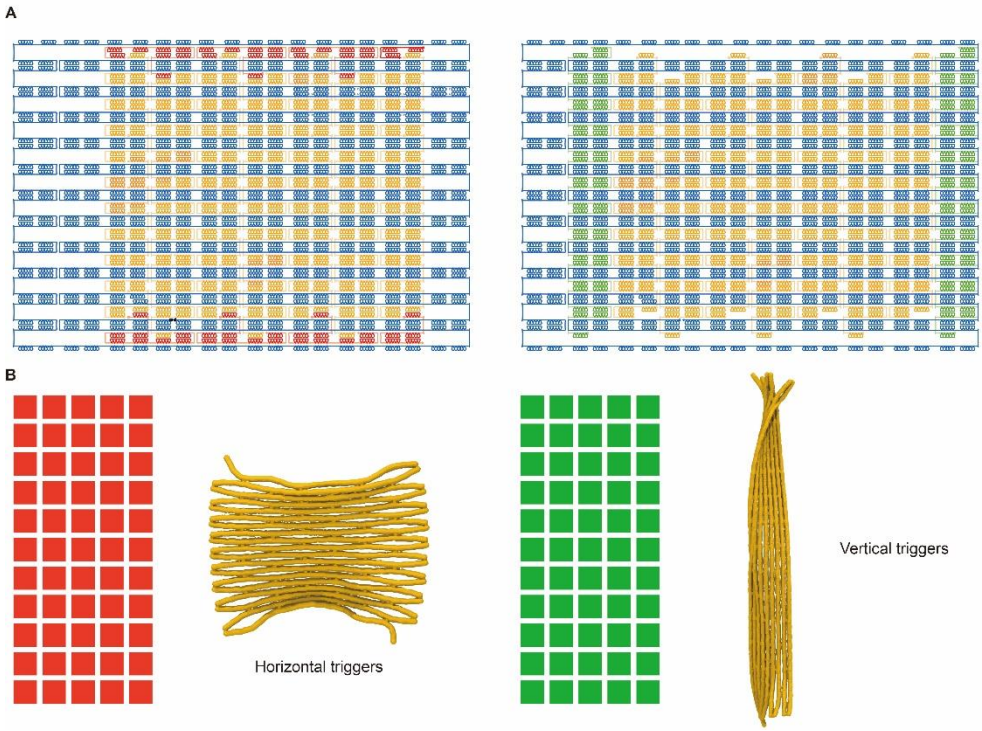

Figure 6-9. Predicted final equilibrium shapes dependent of DNA trigger types. (A) Designs of DNA array structures with horizontal triggers and vertical triggers inserted. Horizontal triggers do not change structural motifs within the reference array structure, while vertical triggers occur the change of structural motifs. Horizontal and vertical triggers are represented by red and green DNA strands, respectively. (B) Predicted final equilibrium shapes. Depending on how and where DNA trigger strands are inserted, the structural shape changes.

Using the design principle, the two geometries are generated by inserting DNA strands with a function of horizontal triggers and those with a function of vertical triggers to a reference array structure. Horizontal triggers do not change any of structural motif constituting the reference structure. That is, they do not cause the conformational change of the reference structure. However, vertical triggers convert ssDNAs within the reference structure to dsDNAs, resulting in a change in the shape

of the structure (Figure 6-9A).

We predict the final equilibrium shapes of the structure with horizontal triggers and that with vertical triggers, using the proposed procedure. It is confirmed that the proposed procedure successfully the final equilibrium shapes, which are consistent with experimental results[51]. Through this, we demonstrate that the proposed procedure is effective for structural analysis with conformational change of structural motifs (Figure 6-9B).

6.7. Structural details at the base-pair level

To demonstrate the accuracy of structural predictions more quantitatively through the proposed computational procedure, we analyze the geometric properties of stracked motifs (regular, stacked nick, and junction nick) and crossover motifs (double junction, single junction, and open nick) in the DNA origami block-shaped structures shown in Figure 6-1. Subsequently, these geometric properties are compared with the results obtained from all molecular dynamics simulations in Cha-

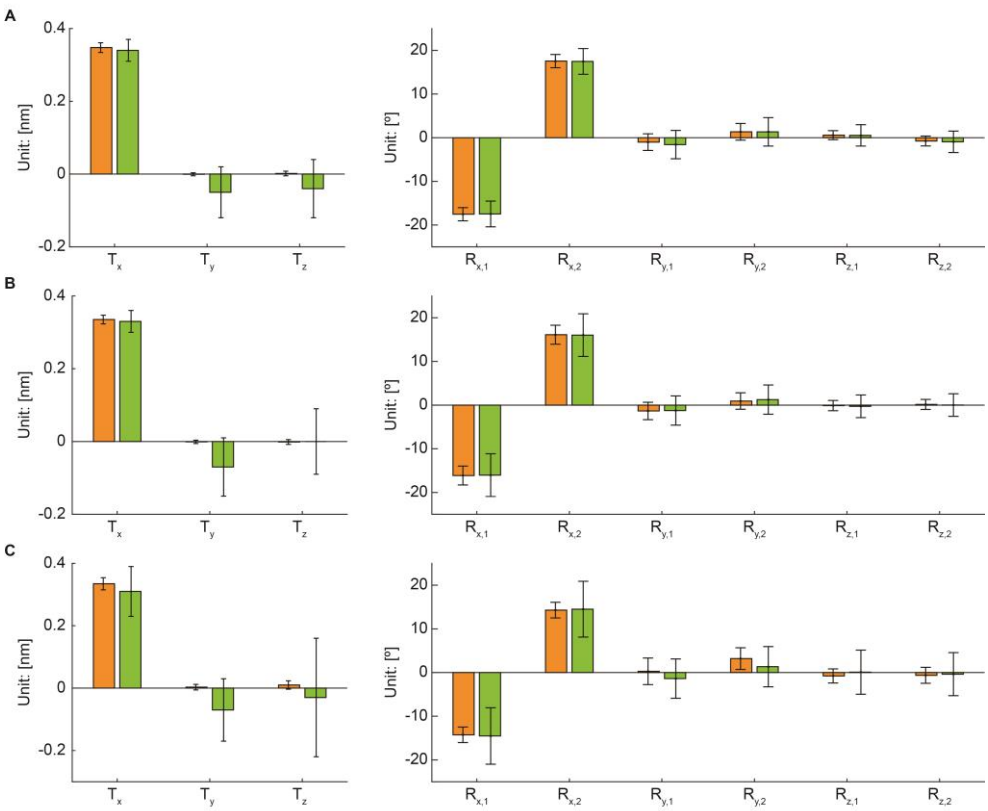

Figure 6-10. Geometric properties of local structural motifs within DNA origami block-shaped structures. Orange and green colors represent results from the proposed computational procedures and those from the molecular dynamics simulations, respectively. (A) Regular. (B) Stacked nick. (C) Junction nick. (D) Double junction. (E) Single junction. (F) Open nick.

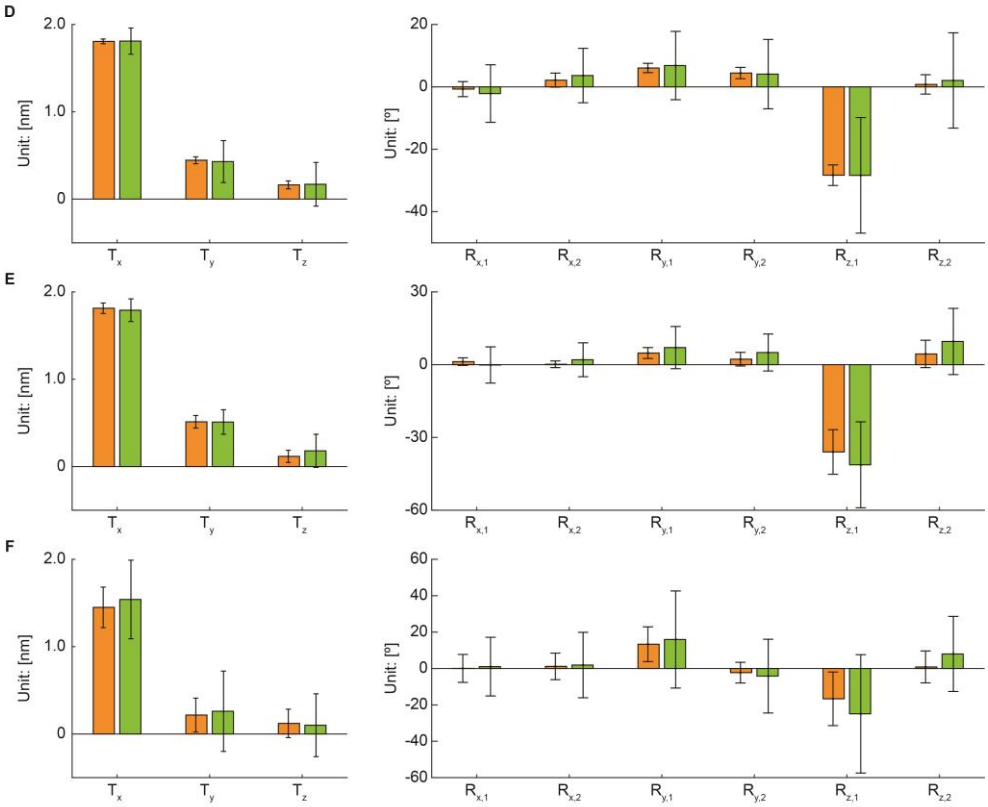

Figure 6-10 (Continued)

pter 2. The comparison reveals a good agreement between our results and those of molecular dynamics simulations (Figure 6-10).

6.8. Dependence on initial lattice-based configurations

When the positions and orientations of base-pairs, as well as the connectivity between bases, are initially provided, this computational procedure generates a DSTBCONF based on the initial lattice-based configuration (described in Chapter 3). However, if two designs have the same connectivity between bases, even though they have different initial lattice-based configurations, this computational procedure eventually predicts the same final equilibrium shape despite generating different DSTBCONF. To demonstrate this, we modify the lattice-based design of an icosahedron wireframe structure with wireframe edges composed of 84 base-pair long six-helix bundles, which is obtained from TALOS[22]. The original and modified designs are partitioned into 30 substructures and 33 substructures, respectively, and the substructures are well distributed. As a result of finite element structural analysis, we obtain the well predicted icosahedron structures with good agreement for both cases (Figure 6-11A). Additionally, the lattice-based design of a topologically closed circular structure with a cross-section composed of six helices is modified. The original and modified designs generate four and 11 substructures, respectively, all of which are well distributed without overlapping. Finite element structural analysis provides a reliable prediction of perperly formed circular structures, displaying notable similarity in both cases (Figure 6-11B). Note that this is irrelevant when only the connectivity between bases is provided.

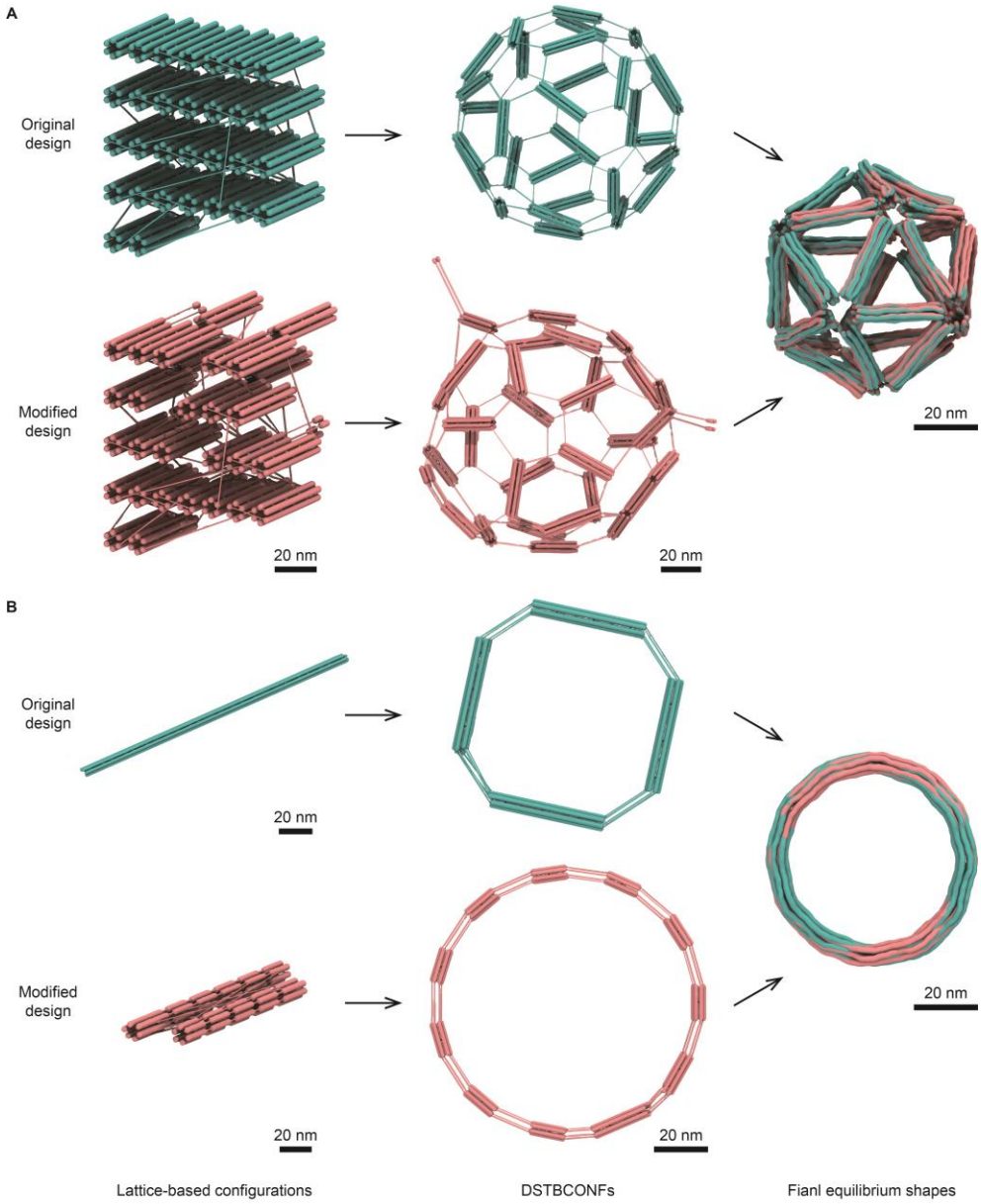

Figure 6-11. Dependence on initial lattice-based configurations. (A) Wireframe icosahedrons. (B) Circular structures. Despite differences in the DSTBCONFs resulting from these lattice-based designs, the computational procedure accurately predicts the final equilibrium shapes of both the icosahedron and circular structures.

7. Analyzing mechanical and dynamic properties of DNA nanostructures

7.1. Abstract

We introduce a method for analyzing the mechanical and dynamic properties of DNA nanostructures. We assume that a DNA bundle structure behaves similarly to a homogeneous Euler-Bernoulli beam. By analyzing the natural frequency and bending mode shape obtained through normal mode analysis, we derive the overall bending rigidity, which is then converted into the bending persistence length. We apply this method to DNA nanotubes with various shapes and observe that the calculated persistence lengths align well with previously reported values. Additionally, we examine the dynamic characteristics of DNA nanostructures with different shapes using normal mode analysis. This involves analyzing the root-mean-squared fluctuations of base-pairs that constitute the structures. Through these, we confirm that the proposed computational procedure not only predicts the final equilibrium shapes but also enables the analysis of the mechanical and dynamic properties of DNA nanostructures.

7.2. Methods

Normal mode analysis is performed to analyze the bending persistence lengths of DNA nanotubes and the root-mean-squared fluctuation of base-pairs constituting DNA nanostructures. In normal mode analysis, the generalized eigenproblem is described as

$$\mathbf{K}_{\mathrm{G}} = \mathbf{M}_{\mathrm{G}} \boldsymbol{\Upsilon} \boldsymbol{\Lambda} \tag{7-1}$$

where $\mathbf{K}_{\mathrm{G}}$ is the global stiffness matrix in which global structural and electrostatic stiffness matrices are assembled. These matrices are calculated as equations (5-43) and (5-93), respectively. $\mathbf{M}_{\mathrm{G}}$ denotes the total mass matrix described as

$$\mathbf{M}_{\mathrm{G}} = \begin{bmatrix} \mathbf{M}_1^{\mathrm{e}} & \mathbf{O}_6 & \cdots & \mathbf{O}_6 \\ \mathbf{O}_6 & \mathbf{M}_2^{\mathrm{e}} & \cdots & \mathbf{O}_6 \\ \vdots & \vdots & \ddots & \vdots \\ \mathbf{O}_6 & \mathbf{O}_6 & \cdots & \mathbf{M}_{\mathrm{N_n}}^{\mathrm{e}} \end{bmatrix} \tag{7-2}$$

where $\mathbf{O}_6$ is a 6-by-by zero matrix, and $\mathbf{M}_{\mathrm{k}}$ is the element-based local mass matrix of the *k*th base-pair among all $\mathrm{N_n}$ base-pairs, defined as equation (7-3).

$$\mathbf{M}_{\mathrm{k}} = \begin{bmatrix} \mathrm{n_k m_k^e} & 0 & 0 & 0 & 0 & 0 \\ 0 & \mathrm{n_k m_k^e} & 0 & 0 & 0 & 0 \\ 0 & 0 & \mathrm{n_k m_k^e} & 0 & 0 & 0 \\ 0 & 0 & 0 & 0 & 0 & 0 \\ 0 & 0 & 0 & 0 & 0 & 0 \\ 0 & 0 & 0 & 0 & 0 & 0 \end{bmatrix} \tag{7-3}$$

Here, $\mathrm{n_k}$ represents the number of elements associated with the *k*th base-pair, and $\mathrm{m_k^e}$ indicates the nodal mass obtained by summing the masses of all atoms constituting the *k*th base-pair. Using the Krylov-Schur algorithm[53], we obtain eigenvalue ($\boldsymbol{\Lambda}$) and eigenvector ($\boldsymbol{\Upsilon}$) matrices for $\mathrm{N_m}$ modes, described as

$$\mathbf{\Lambda} = \begin{bmatrix} \lambda_1 & 0 & \cdots & 0 \\ 0 & \lambda_2 & \cdots & 0 \\ \vdots & \vdots & \ddots & \vdots \\ 0 & 0 & \cdots & \lambda_{N_m} \end{bmatrix} \tag{7-4}$$

$$\mathbf{\Upsilon} = \begin{bmatrix} \vec{\Upsilon}_1 & \vec{\Upsilon}_2 & \cdots & \vec{\Upsilon}_{N_m} \end{bmatrix} \tag{7-5}$$

$$\vec{\Upsilon}_i = \begin{bmatrix} \vec{\upsilon}_{i,1}{}^T & \vec{\upsilon}_{i,2}{}^T & \cdots & \vec{\upsilon}_{i,N_n}{}^T \end{bmatrix}^T \tag{7-6}$$

where λ_i and $\vec{\Upsilon}_i$ are the eigenvalue and eigenvector corresponding to the *i*th mode, respectively, and $\vec{\upsilon}_{i,k}$ is a 6-by-1 eigenvector of the *k*th node corresponding to the *i*th mode. Here, N_m is set to be 200, which is appropriate, as previously reported[54]. The eigenvectors are orthogonal to the stiffness matrix and orthonormal to the mass matrix, described as

$$\vec{\Upsilon}_i{}^T \mathbf{K}_G \vec{\Upsilon}_j = \delta_{ij}\lambda_i \tag{7-7}$$

$$\vec{\Upsilon}_i{}^T \mathbf{M}_G \vec{\Upsilon}_j = \delta_{ij} \tag{7-8}$$

where δ_{ij} is the Kronecker delta, which has a value of 1 if i and j are equal, and 0 otherwise.

Under assumption that a DNA nanotube behaves like a homogeneous Euler-Bernoulli beam with the bending rigidity about the y-axis (B_y), its behavior is determined by equation (7-9).

$$B_y \frac{d^4 y(x)}{dx^4} - \frac{\lambda}{L_c} y(x) \sum_{k=1}^{N_n} m_k^e = 0 \tag{7-9}$$

Here, displacements parallel and transverse to the beam axis are represented by x and y, respectively. L_c denotes the contour length of the beam, and λ indicates the eigenvalue, related to the natural frequency ω as described in equation (7-10).

$$\lambda = \omega^2 \tag{7-10}$$

Equation (7-9) has a general solution as

$$y(x) = A_1 e^{-\Im\beta x} + A_2 e^{\Im\beta x} + A_3 e^{-\beta x} + A_4 e^{\beta x} \tag{7-11}$$

where A_1, A_2, A_3, and A_4 are constants, and $\Im$ and β represent an imaginary number ($\sqrt{-1}$) and the wavenumber, respectively. Here, the free-free boundary condition is applied, which is described by equation (7-12).

$$\cosh L_c\beta \cos L_c\beta = 1 \tag{7-12}$$

By applying the boundary condition, we obtain various numerical values of $L_c\beta$, such as 4.733 (corresponding to the first bending mode), 7.853 (corresponding to the second bending mode), 10.996 (corresponding to the third bending mode), and so on. Consequently, the bending rigidity B_y of the beam is derived as

$$B_y = \frac{{\omega_{y,k}}^2}{L_c\beta^4}\sum_{k=1}^{N_n} m_k^e = \frac{{\omega_{y,k}}^2 {L_c}^3}{(L_c\beta)^4}\sum_{k=1}^{N_n} m_k^e \tag{7-13}$$

where $\omega_{y,k}$ represents the natural frequency in the kth bending mode related to the bending about the y-axis. In this study, we specifically analyze the first bending mode with $L_c\beta$ having a value of 4.733 and $\omega_{y,1}$.

Likewise, the bending rigidity about the z-axis (B_z) is calculated as

$$B_z = \frac{{\omega_{z,1}}^2 {L_c}^3}{4.733^4}\sum_{k=1}^{N_n} m_k^e \tag{7-14}$$

where $\omega_{z,1}$ represents the natural frequency in the first bending mode related to the bending about the z-axis. Then, the equivalent bending rigidity (B) is obtained by calculating the harmonic average of the two bending rigidities (B_y and B_z), as shown in equation (2-28). Finally, the bending persistence length ($P_{L,B}$) is analyzed using the relation as

$$P_{L,B} = \frac{B}{k_B T_a} \tag{7-15}$$

where k_B is Boltzmann's constant and T_a is the absolute temperature.

The fluctuation vector ($\vec{\Delta}_{F,k}$) of the *k*th base-pair is calculated as equation (7-16).

$$\vec{\Delta}_{F,k} = \sum_{i=1}^{N_m} \sqrt{\frac{k_B T_a}{\lambda_i}} \vec{\upsilon}_{i,k} \tag{7-16}$$

Then, the root-mean-squared fluctuation ($\Delta_{R,k}$) of the *k*th base-pair is derived as equation (7-17).

$$\Delta_{R,k} = \sqrt{\langle \vec{\Delta}_{F,k} \cdot \vec{\Delta}_{F,k} \rangle} = \sqrt{k_B T_a \sum_{i=1}^{N_m} \frac{\vec{\upsilon}_{i,k} \cdot \vec{\upsilon}_{i,k}}{\lambda_i}} \tag{7-17}$$

7.3. Bending persistence length

We inverstigate the bending persistence lengths of DNA nanotubes with various-shaped cross-sections. These nanotubes are classified into two types: tile-shaped structure, in which N helices are primarily connected by single junctions (*N*HT), and origami structures, where double junctions are the dominant local structural motifs connecting N helices (*N*HB). The nanotubes examined in this study are 6HT, 8HT, 10HT, 4HB, 6HB, and 10HB, as previously reported[13,55].

To analyze their bending properties, we perform normal mode analysis on the nanotubes' first bending modes after predicting their final equilibirum shapes (Figure 7-1A). Our results confirm the previous findings that an increase in the number of helices composing a structure corresponds to an increase in its persistence length[13,55]. Furthermore, we observe that the analyzed persistence lengths align well with the previously reported values[13,55] (Figure 7-1B).

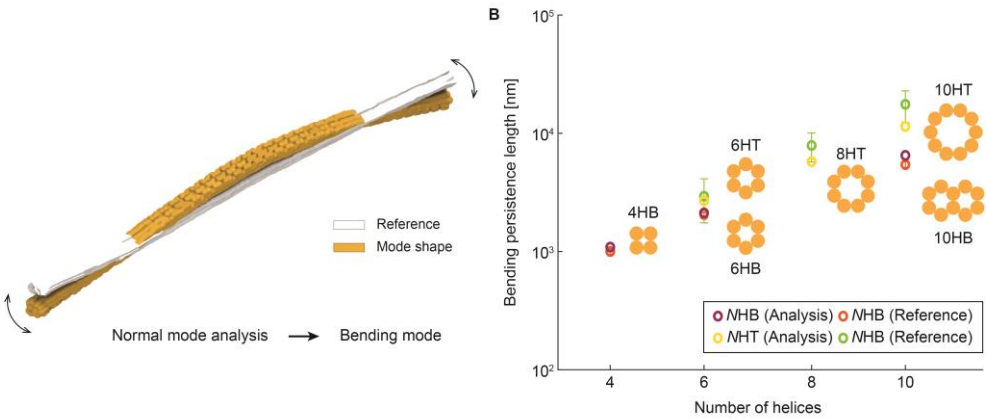

Figure 7-1. Analysis of bending persistence lengths of DNA nanotubes. (A) Analysis of bending persistence length using normal mode analysis. (B) Comparison between analyzed values and previously reported ones. Purple and yellow dots indicate analyzed values of *N*HB and *N*HT, respectively, while reported values are denoted by orange and green dots.

7.4. Root-mean-squared fluctuation

Through the application of normal mode analysis, we examine the root-mean-squared fluctuations of base-pairs within various-shaped DNA nanostructures, including block-shaped, wireframe, and circular DNA nanostructures (Figure 7-2). In general, base-pairs located outside the structures demonstrate greater fluctuations compared to those situated inside[25]. Wireframe structures, specifically, exhibit larger fluctuations in base-pairs at the wireframe vertices compared to those at the wireframe edges[30]. This phenomenon occurs because base-pairs with fewer covalent bonds connected to them have higher dynamic freedom.

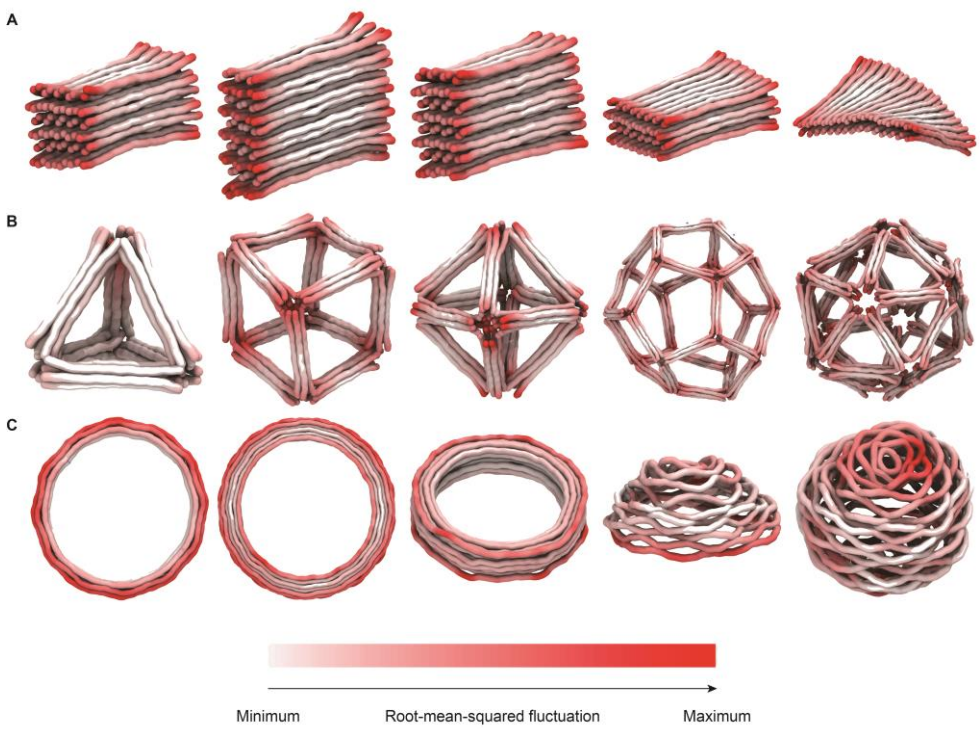

Figure 7-2. Root-mean-squared fluctuations of base-pairs in DNA nanostructures. (A) Block-shaed structures. (B) Wireframe structures. (C) Circular structures. A higher fluctuation is observed in base-pairs with a smaller number of covalent bonds.

8. Conclusion

The convential procedure of analyzing DNA nanostructures from initial configurations designed on a clearly defined three-dimensional lattice faces several computational difficulties. When attempting to design free-form DNA structures on a lattice, DNA bases must be forcibely constrained to the prepositioned lattice, causing the initially designed lattice-based configurations to often become unnatural. As a result, these lattice-based configurations exhibit artifically stretched bonds between bases or incorrect definitions of DNA structural motifs (connecting two DNA base-pairs), which are determined by considering the positional relationship between the base-pairs. This leads to computational structural analysis from the lattice-based configurations diverging or inappropriately predicting their final equilibirum shapes.

In this study, we propose a computational procedure that addresses the computational difficulties associated with the conventional approach. To achieve this, we first gain an understanding of the overall DNA structural motifs that constitute DNA nanostructures, along with their geometric and mechanical properties. We perform all-atom molecular dynamics simulations on DNA helices and DNA bundle structures with various shapes and base sequences, classifying DNA structural motifs accordingly. From the equilibrated trajectories, we define the positions and orientations of base-pairs as well as the orientations of structural motifs. Subsequently, we analyze the sequence-dependent geometric and mechanical properties of each structural motif. This understanding serves as the basis for subsequent coarse-grained Brownian dynamics modeling (to provide detailed classification of structural motifs) and finite element modeling (for structural analysis).

Next, we introduce a design method that utilizes the connectivity between bases instead of the conventional lattice-based design. By analyzing the connectivity between bases, which represents the base topology in a DNA nanostructure, we roughly classify the structural motifs that constitute the DNA nanostructure. The

roughly classified structural motifs include regular (a fundamental component of dsDNA), bulge, ssDNA, nick, and N-way junction. Using these structural motifs, we generate a DSTBCONF based on the provided information, where substructures are evenly distributed in three-dimensional space. If the connectivity between bases, as well as the positions and orientations of base-pairs (located on the lattice), are provided, we define substructures as adjacent base-pairs. On the other hand, if only the connectivity between bases is provided, substructures are defined as dsDNA. By applying attractive and repulsive forces to the substructures, they are consequently well distributed, resulting in the generation of the DSTBCONF.

To perform a detailed classification of structural motifs, we utilize coarse-grained Brownian dynamics modeling on the DSTBCONF. Within the roughly classified structural motifs, the nick motif is further categorized as either stacked nick or open nick, depending on the stacking state of the two connected base-pairs. Additionally, the N-way junction motif is subdivided into 4-way junction or non-4-way junction, based on the involvement of four base-pairs. Moreover, the 4-way junction motif is divided into 4-way double junction and 4-way single junction, depending on whether four or five DNA strands are participating. Lastly, the 4-way double junction and 4-way single junction motifs are further distinguished as two junction nicks and two double junctions, and two junction nicks and one single junction, respectively. Throughout the modeling process, the structural motifs, including dsDNA, stacked nick, junction nick, double junction, single junction, open nick, non-4-way junction, bulge, and ssDNA, are represented using two-node-beam elements with clearly defined orientations of nodes and elements. As the coarse-grained Brownian dynamics simulation progresses, the structural state achieves stability and convergence while preserving the integrity of the structural motifs. This detailed classification procedure enables us to obtain a DEFCONF in which the positions, orientations of base-pairs, and types of structural motifs are precisely determined.

For structural analysis, the DEFCONF is converted into a finite element model that includes structural elements describing various structural motifs such as regular,

stacked nick, junction nick, double junction, single junction, open nick, non-4-way junction, bulge, and ssDNA. Additionally, electrostatic elements are incorporated to represent the electrostatic repulsion between negatively charged DNA helices in an ionic solution. To demonstrate the practical application of our computational procedure, we carry out finite element structural analysis on the converted configurations, which exhibit various shapes. As a result, we successfully obtain their final equilibrium shapes. Furthermore, using finite element structural analysis and normal mode analysis, we examine the overall mechanical and dynamic properties of various-shaped DNA nanostructures. This analysis includes assessing the bending persistence lengths and the root-mean-squared fluctuations of base-pairs. Our results show good agreement with previously reported findings. This process confirms that our computational procedure can predict equilibrium shapes and expand the design possibilities for DNA nanostructures in structural analysis. Thus, our computational procedure proves to be effective and versatile for studying DNA nanostructures. Although in this study, finite element structural analysis is conducted using atom-level properties obtained from all-atom molecular dynamics simulations, it also suggests the potential for structural analysis through passive modification of properties, which can be utilized in parameterization studies of local elements.

We expect that our computational procedure will provide more detailed and accurate insights into structured DNA assemblies in the field of structural DNA nanotechnology, thereby facilitating a more efficient design-analysis-validation process. Furthermore, we envision that the proposed computational procedure could be further advanced through machine-learning-based studies for predicting the connectivity between bases from the base sequences of DNA strands that comprise DNA nanostructures, for promptly generating structural configurations, and so on. Lastly, we anticipate that this computational procedure would also be applied to the analysis of the attachment effect of proteins or gold nanoparticles on DNA origami structures.

A. Appendix

A.1. Mathematical notation

▶ Matrix

1) A matrix represents a rectangular array.
2) An m-by-n matrix is a matrix with m rows and n columns.
3) In this main text, matrices are symbolized using boldface.
4) For example,

$$\mathbf{A} = \begin{bmatrix} a_{11} & a_{12} & \cdots & a_{1n} \\ a_{21} & a_{22} & \cdots & a_{2n} \\ \vdots & \vdots & \ddots & \vdots \\ a_{m1} & a_{m2} & \cdots & a_{mn} \end{bmatrix} \tag{A-1}$$

▶ Vector

1) A vector includes a column vector and a row vector, which are matrices with a single column and a single row, respectively.
2) In this main text, column vectors are used exclusively, and represented by an arrow pointing to the right above their names.
3) For example,

$$\vec{u} = \begin{bmatrix} u_1 \\ u_2 \\ \vdots \\ u_m \end{bmatrix} \tag{A-2}$$

▶ Operations

1) Transpose of a matrix $\mathbf{A}$: $\mathbf{A}^T$
   A. It switches the row and column components of $\mathbf{A}$.
   B. The component located in the *i*th row and *j*th column of $\mathbf{A}^T$ corresponds to the component in the *j*th row and *i*th column of $\mathbf{A}$.

C. Vector transpose follows the same rules as matrix transpose. That is, transposing a column vector results in a row vector, and reciprocally for a row vector.

2) Matrix multiplication

A. If $\mathbf{A}$ and $\mathbf{B}$ are p-by-q and q-by-r matrices, respectively, as follows.

$$\mathbf{A} = \begin{bmatrix} a_{11} & a_{12} & \cdots & a_{1q} \\ a_{21} & a_{22} & \cdots & a_{2q} \\ \vdots & \vdots & \ddots & \vdots \\ a_{p1} & a_{p2} & \cdots & a_{pq} \end{bmatrix} \tag{A-3}$$

$$\mathbf{B} = \begin{bmatrix} b_{11} & b_{12} & \cdots & b_{1r} \\ b_{21} & b_{22} & \cdots & b_{2r} \\ \vdots & \vdots & \ddots & \vdots \\ b_{q1} & b_{q2} & \cdots & b_{qr} \end{bmatrix} \tag{A-4}$$

B. The *i*th row and *j*th column component of their matrix multiplication ($\mathbf{AB}$) is calculated as: $[\mathbf{AB}]^{(i,j)} = a_{i1}b_{1j} + a_{i2}b_{2j} + \cdots + a_{iq}b_{qj}$

C. The multiplied matrix ($\mathbf{AB}$) becomes the p-by-r matrix.

3) Inverse of a matrix $\mathbf{A}$: $\mathbf{A}^{-1}$

A. If $\mathbf{A}$ is a non-singular n-by-n matrix, an inverse matrix of $\mathbf{A}$ exists, satisfying $\mathbf{AA}^{-1} = \mathbf{A}^{-1}\mathbf{A} = \mathbf{I}_n$ where $\mathbf{I}_n$ is an n-by-n identity matrix.

B. The *i*th row and *j*th column component of $\mathbf{A}^{-1}$ is calculated as

$$[\mathbf{A}^{-1}]^{(I,j)} = \frac{(-1)^{i+j}\mathbf{M}_{ji}}{\det(\mathbf{A})} \tag{A-5}$$

where $\det(\mathbf{A})$ and $\mathbf{M}_{ji}$ denote the determinant and the (j, i)-minor of $\mathbf{A}$, respectively.

4) Norm of a vector $\vec{u}$: $\|\vec{u}\|$

A. In this main context, it entirely represents the Euclidean norm of the vector $\vec{u} = [u_1 \quad u_2 \quad \cdots \quad u_m]^T$, which is defined as: $\|\vec{u}\| = \sqrt{{u_i}^2 + {u_2}^2 + \cdots + {u_m}^2}$

5) Dot product of two vectors $\vec{u}$ and $\vec{v}$: $\vec{u} \cdot \vec{v}$

A. The dot product of two vectors $\vec{u} = [u_1 \quad u_2 \quad \cdots \quad u_m]^T$ and $\vec{v} = [v_1 \quad v_2 \quad \cdots \quad v_m]^T$ is defined as: $\vec{u} \cdot \vec{v} = u_1 v_1 + u_2 v_2 + \cdots + u_m v_m$

6) Cross product of two vectors $\vec{u}$ and $\vec{v}$: $\vec{u} \times \vec{v}$

A. The cross product of two 3-by-1 vectors $\vec{u} = [u_1 \quad u_2 \quad u_3]^T$ and $\vec{v} = [v_1 \quad v_2 \quad v_3]^T$ is calculated as a follow.

$$\vec{u} \times \vec{v} = \begin{bmatrix} u_2 v_3 - u_3 v_2 \\ u_3 v_1 - u_1 v_3 \\ u_1 v_2 - u_2 v_1 \end{bmatrix} \tag{A-6}$$

7) Tensor product of two vectors $\vec{u}$ and $\vec{v}$: $\vec{u} \otimes \vec{v}$

A. The tensor product of two column vectors $\vec{u}$ and $\vec{v}$ is defined as: $\vec{u} \otimes \vec{v} = \vec{u}\vec{v}^T$

B. When considering the vectors $\vec{u}$ (m-by-1) and $\vec{v}$ (n-by-1), their tensor product generates an m-by-n matrix.

8) Capital-sigma notation: $\sum$

A. It represents summation of similar terms.

B. It is defined as

$$\sum_{k=p}^{q} a_k = a_p + a_{p+1} + a_{p+2} + \cdots + a_{q-1} + a_q \tag{A-7}$$

where k is the index of summation, and p and q are the lower and upper bounds of summation, respectively. Here, both p and q must be integers, with the additional requirement that p is less than or equal to q.

C. Occasionally, the index and bounds of summation can be omitted, particularly when it is understood that the lower and upper bounds of summation correspond to 1 and the total number of a_k, respectively. Also, instead of using the traditional bounds, an arbitrary logical condition may be employed.

A.2. Base sequences of DNA bundle structures

To analyze the sequence-dependent geometric and mechanical properties of junction nick, double junction, single junction, and open nick among structural motifs, we perform all-atom molecular dynamics simulations on a total of 13 DNA bundle structures composed of six helices. These structures are illustrated schematically in Figure 2-2 and named as follows: 6-helix-bundle-1.1, 6-helix-bundle-1.2, 6-helix-bundle-1.3, 6-helix-bundle-1.4, 6-helix-bundle-2, 6-helix-bundle-3, 6-helix-bundle-4, 6-helix-bundle-5, 6-helix-bundle-6, 6-helix-bundle-7, 6-helix-bundle-8, 6-helix-bundle-9, and 6-helix-bundle-10. The base sequences of these structures are provided in detail in Table A-1.

Table A-1. Overall sequence of DNA bundle structures.

Models	Identifier of strands	Base sequences
6-helix-bundle-1.1	1	AGCGATAACGACCAACAGCGAGAACGGATGTGCAACCACACCGCTGTGGAGCGGAAGGTCTGA
	2	TTCACTTTATCGCTTCGCATG
	3	TGGTCGTGGGATGGCTTTGTT
	4	GCTTAAGAGCGACCTCGCTGT
	5	AATTGCATCCGTTCGCTTCTT
	6	TTGCACAGCCTAGCTATGCCG
	7	GGCGCGTTTGTAGAGGTGTGG
	8	CTAAGGTCCACAGCGCTCGTA
	9	TTCCGCTGCCATACATTGTCC
	10	CGAATGGGGGTAGGTCAGACC
	11	CCTACCCTCTCAAATACGAGCTCTACAACGCGGGCAAGAAGCGGTCGCTCCGGGTCCATGCGA
	12	GACCCGGTAGGGTTAACCCTC
	13	GCCCGCGTTGCTGAAAAACCG
	14	TTTGAGACGAGAGAACGTTCT
	15	GGGGTAGAACCCTACTTAAGCGGTCCGGTCAGCAAACGCGCCTCACCCATCTCTCGCCATTCG
	16	ATCCTAATTTCACTCTACCCC
	17	AAAGTGCAAGCACACCGGACC
	18	AAAATCCCTTTCGATGGGTGA
	19	ATTATTGAGAACGTTCGAAAGCACAATGCGGTTTTTGTGCTTGTGTGGGGAGGGTTAGTGAAA
	20	CCCACACCCCGCTGGTATGTA

Table A-1 (Continued)

Models	Identifier of strands	Base sequences
6-helix-bundle-1.1	21	CATTGTGATCCTTTATTGCTA
	22	CAATAATCTCGGGGCTTGGAC
	23	TTAGGATAACAAAGCAGCGGGGCACTTTCGGCATAAAAGGATGGATTTTGGACAATCCCCGAG
	24	GTCCAAGGTATGGCACCTTAGTAGCAATGCTAGGCTGCAATTTACATACCCATCCCAAGTGAA
6-helix-bundle-1.2	1	TGCGATAACGACCAACAGCGAGAACGGATGTGCAACCACACCGCTGTGGAGCGGAAGGTCTGC
	2	TTCACTTTATCGCAGCGCATG
	3	TGGTCGTGGGATGGCTTTGTT
	4	GCTTAAGAGCGACCTCGCTGT
	5	AATTGCATCCGTTCGCTTCTT
	6	TTGCACAGCCTAGCTATGCCG
	7	GGCGCGTTTGTAGAGGTGTGG
	8	CTAAGGTCCACAGCGCTCGTA
	9	TTCCGCTGCCATACATTGTCC
	10	CGAATGGGGGTAGCGCAGACC
	11	GCTACCCTCTCAAATACGAGCTCTACAACGCGGGCAAGAAGCGGTCGCTCCGGGTCCATGCGC
	12	GACCCGGTAGGGTTAACCCTC
	13	GCCCGCGTTGCTGAAAAACCG
	14	TTTGAGACGAGAGAACGTTCT
	15	GGGGTAGAACCCTACTTAAGCGGTCCGGTCAGCAAACGCGCCTCACCCATCTCTCGCCATTCG

Table A-1 (Continued)

Models	Identifier of strands	Base sequences
6-helix-bundle-1.2	16	ATCCTACTTTCACTCTACCCC
	17	AAAGTGCAAGCACACCGGACC
	18	AAAATCCCTTTCGATGGGTGA
	19	CTTATTGAGAACGTTCGAAAGCACAATGCGGTTTTTG TGCTTGTGTGGGGAGGGTTAGTGAAA
	20	CCCACACCCCGCTGGTATGTA
	21	CATTGTGATCCTTTATTGCTA
	22	CAATAAGCTCGGGGCTTGGAC
	23	GTAGGATAACAAAGCAGCGGGGCACTTTCGGCATAA AAGGATGGATTTTGGACAATCCCCGAG
	24	GTCCAAGGTATGGCACCTTAGTAGCAATGCTAGGCTG CAATTTACATACCCATCCCAAGTGAA
6-helix-bundle-1.3	1	TGCGATAACGACCAACAGCGAGAACGGATGTGCAAC CACACCGCTGTGGAGCGGAAGGTCTGC
	2	TTCACTTTATCGCACCGCATG
	3	TGGTCGTGGGATGGCTTTGTT
	4	GCTTAAGAGCGACCTCGCTGT
	5	AATTGCATCCGTTCGCTTCTT
	6	TTGCACAGCCTAGCTATGCCG
	7	GGCGCGTTTGTAGAGGTGTGG
	8	CTAAGGTCCACAGCGCTCGTA
	9	TTCCGCTGCCATACATTGTCC
	10	CGAATGGGGGTAGTGCAGACC

Table A-1 (Continued)

Models	Identifier of strands	Base sequences
6-helix-bundle-1.3	11	ACTACCCTCTCAAATACGAGCTCTACAACGCGGGCAAGAAGCGGTCGCTCCGGGTCCATGCGG
	12	GACCCGGTAGGGTTAACCCTC
	13	GCCCGCGTTGCTGAAAAACCG
	14	TTTGAGACGAGAGAACGTTCT
	15	GGGGTAGAACCCTACTTAAGCGGTCCGGTCAGCAAACGCGCCTCACCCATCTCTCGCCATTCG
	16	ATCCTACATTCACTCTACCCC
	17	AAAGTGCAAGCACACCGGACC
	18	AAAATCCCTTTCGATGGGTGA
	19	CTTATTGAGAACGTTCGAAAGCACAATGCGGTTTTTGTGCTTGTGTGGGGAGGGTTAGTGAAT
	20	CCCACACCCCGCTGGTATGTA
	21	CATTGTGATCCTTTATTGCTA
	22	CAATAAGATCGGGGCTTGGAC
	23	GTAGGATAACAAAGCAGCGGGGCACTTTCGGCATAAAAGGATGGATTTTGGACAATCCCCGAT
	24	GTCCAAGGTATGGCACCTTAGTAGCAATGCTAGGCTGCAATTTACATACCCATCCCAAGTGAA
6-helix-bundle-1.4	1	TGCGATAACGACCAACAGCGAGAACGGATGTGCAACCACACCGCTGTGGAGCGGAAGGTCTGT
	2	TTCACTTTATCGCAACGCATG
	3	TGGTCGTGGGATGGCTTTGTT
	4	GCTTAAGAGCGACCTCGCTGT
	5	AATTGCATCCGTTCGCTTCTT

Table A-1 (Continued)

Models	Identifier of strands	Base sequences
6-helix-bundle-1.4	6	TTGCACAGCCTAGCTATGCCG
	7	GGCGCGTTTGTAGAGGTGTGG
	8	CTAAGGTCCACAGCGCTCGTA
	9	TTCCGCTGCCATACATTGTCC
	10	CGAATGGGGGTAGTACAGACC
	11	ACTACCCTCTCAAATACGAGCTCTACAACGCGGGCAAGAAGCGGTCGCTCCGGGTCCATGCGT
	12	GACCCGGTAGGGTTAACCCTC
	13	GCCCGCGTTGCTGAAAAACCG
	14	TTTGAGACGAGAGAACGTTCT
	15	GGGGTAGAACCCTACTTAAGCGGTCCGGTCAGCAAACGCGCCTCACCCATCTCTCGCCATTCG
	16	ATCCTACCTTCACTCTACCCC
	17	AAAGTGCAAGCACACCGGACC
	18	AAAATCCCTTTCGATGGGTGA
	19	CTTATTGAGAACGTTCGAAAGCACAATGCGGTTTTTGTGCTTGTGTGGGGAGGGTTAGTGAAG
	20	CCCACACCCCGCTGGTATGTA
	21	CATTGTGATCCTTTATTGCTA
	22	CAATAAGGTCGGGGCTTGGAC
	23	GTAGGATAACAAAGCAGCGGGGCACTTTCGGCATAAAAGGATGGATTTTGGACAATCCCCGAC
	24	GTCCAAGGTATGGCACCTTAGTAGCAATGCTAGGCTGCAATTTACATACCCATCCCAAGTGAA

Table A-1 (Continued)

Models	Identifier of strands	Base sequences
6-helix-bundle-2	1	AGATAGACGGTTTTTCGCCCTATGACGTTGGAGTCCACGTTCATTAATAGTGGACTGTTGTTC
	2	AAAACCGTCTATCTTAACAAGAGTCCACTATTAAA
	3	AGGGCGACATTAAAGAACGTG
	4	GACTCCAACGTCATCAACGTG
	5	GAACGTGGCGTCAAAGGGCGA
	6	AGTCCACTATTAATGGGGCGA
	7	GAACAACCCTATCA
	8	TGATAGGCGGTTTTTCGCCCTTTGACGCTGGAGTTCACGTTCTTTAATGGTGGACGCTTGTTC
	9	GAACAAG
	10	TCCCGCTTTTTGGCCGTCCAC
	11	CTTGCACCTGAGGTAACTCCA
	12	GAACAAGAGTCCACAAAACCG
	13	GCTATCTGCCAAAAAGCGGGAAACTGCAACCTCAGGTGCAAGAAATTATGTGGACTCTTGTTC
	14	AGATAGCGAACAAGAGTCCAC
	15	TGCAGTTGAACGTGGACTCCA
	16	ATAATTTAGGGCGAAAAACCG
	17	TGATAGACGGTTTTTCGCCCTTTGACGTTGGAGTCCACGTTCTTTAATAGTGGACTCTTGTTC
	18	TGCAGTTTCCCGCTTATTAAA
	19	ATAATTTCTTGCACACGTCAA
	20	CTTGTTCTCTATCA

Table A-1 (Continued)

Models	Identifier of strands	Base sequences
6-helix-bundle-2	21	ACTATCTGCCAAAAAGCGGGAAACTGCAACGTCAGGTGCAAGAAATTATCACCTGAGAACAAG
	22	TTTTGGCAGATAGT
	23	CTGACGTGACTCCAACGTCAA
	24	TCAGGTGTAAACCGTCTATCA
	25	TGATAGACGGTTTATCGCCCCTTGACGTTGGAGTCCACGTTGTTTAATAGTGGACTCTTGTTA
6-helix-bundle-3	1	TGATAGACGGTTTTTCGCCCTTTGACGTTGGAGTCCACGTTCTTTAATAGTGGACTCTTGTTC
	2	AAAACCGTCTATCATAACAAGTCTATCA
	3	AGGGCGATATTAAAGAACGTG
	4	GACTCCAACGTCAACAACGTG
	5	GAACGTGACGTCAAAGGGCGA
	6	AGTCCACAAAACCGAGTCCACTATTAAAGGGGCGA
	7	TCTATCAGAACAAGTCTATCA
	8	TGATAGACGGTTTTTCGCCCTTTGACGTTGGAGTGCACGTTCTTTAATAGTGGACTCTTGTTC
	9	GAACAAGTCTATCAGAACAAGAGTCCAC
	10	AGGGCGAAAAACCGAGTCCAC
	11	GAACGTGGACTCCGCACTCCA
	12	TGATAGACGGTTTTTCGCCCTTTGACGTCGGAGTCCACGTTCTTTAATAGTGGACTCTTGTTC
	13	ACGTCAAGAACGTGGACTCCA
	14	TATTAAAAGGGCGAAAAACCGAGTCCACTAAACCG

Table A-1 (Continued)

Models	Identifier of strands	Base sequences
6-helix-bundle-3	15	GAACAAGTCTATCAGAACAAG
	16	TGATAGACGGTTTTTCGCCCTTTGACGTTGGAGTCCACGTTCTTTAATAGTGGACTCTTGTTC
	17	ACGTCAAAGGGCGATATTAAA
	18	TATTAAAGAACGTGACGTCAA
	19	TGATAGACGGTTTTTCGCCCTTTGACGTCGGAGTCCACGTTCTTTAATAGTGGACTCTTGTTC
	20	AAAACCGAGTCCACTATTAAA
	21	GACTCCGGACTCCAACGTCAA
	22	TGATAGACGGTTTATCGCCCCTTGACGTTGGAGTCCACGTTGTTTAATAGTGGACTCTTGTTA
6-helix-bundle-4	1	TGATAGACGG
	2	AGACGTACGAACCGTTTCCCTACCGTCTATCACCGTCTATCA
	3	TGATAGACGGTTTTTCGCCCT
	4	ATCGAGGGGAATTTCAACTAAACCGTCTATCAAGGGCGAAAA
	5	TGATAGACGGTTTTTCGCCCT
	6	GGCACACTTGGTTCTGTTGGCGCGGCGGACTCAGGGCGAAAA
	7	GAGTCCGCCGCTCGTCCGAAC
	8	ATCCGTGAACCCACGGTCGTACCTTTTGGAGCGTTCGGACGA
	9	GCTCCAAAAGG
	10	TAAAATACGTTCGTACGTCT

Table A-1 (Continued)

Models	Identifier of strands	Base sequences
6-helix-bundle-4	11	TCTGTCGATGTAATTATGTCCTCCCCTCGATAGGGAAACGGT
	12	CGTGTATAGCATCGATAGCTCCAAGTGTGCCTTAGTTGAAAT
	13	TGCGCGAAGTCGCGCTCCCCCGTTCACGGATGCCAACAGAAC
	14	TACGACCGTGG
	15	GTTGGAGATGCTCTCAGTTGAACATCGACAGAACGTATTTTA
	16	AAGGAACGGAAGTTCTGCCACTGCTATACACGGGACATAATT
	17	CCGGAGTTAACATAGTGAAGCGACTTCGCGCAGAGCTATCGA
	18	TTACTCGGCTCGGTAGCCGTAACAGATGCCTTGGGGGAGCGC
	19	AAGGCATCTGT
	20	CTTGTTTGTTCATCTCCAAC
	21	CAGCGTGGCGATAAGACTGGCTCCGTTCCTTTCAACTGAGAG
	22	ACGGGGGTTTACCTGAAGGGTTTAACTCCGGGTGGCAGAACT
	23	GGATTTCTAATGTACTACGCAAGCCGAGTAAGCTTCACTATG
	24	TACGGCTACCG
	25	TCAGGTGTTATCCCTAGTTCATCGCCACGCTGAACAAACAAG

Table A-1 (Continued)

Models	Identifier of strands	Base sequences
6-helix-bundle-4	26	TACTAGTGGACGCGTACCATATAAACCCCCGTGCCAGTCTTA
	27	TGGGTATGGACAACGTGGTCAATTAGAAATCCACCCTTCAGG
	28	GGAGTTAACATTGTTAGCGATCAACGAGGAGCTGCGTAGTAC
	29	GCTCCTCGTTG
	30	TAACACCTGA
	31	TCCACTAGTATGAACTAGGGA
	32	TCCATACCCATATGGTACGCG
	33	TGTTAACTCCTGACCACGTTG
	34	ATCGCTAACAA
6-helix-bundle-5	1	TAAGCTCTATGTTTATGATCTATTGATGTCCCTGAGGCTGCAATTTATGTAATGAGACAGTATTCGCGGTAAGTCCTAGTGCAA
	2	GAGCTTATATGTTATCAACCA
	3	ATTCGAGATACAAAAAACATA
	4	CCACAACGGGCTGTTACTTATCTATATAAGATCATTACTAGA
	5	CCTTTATAGGGACTTCAGGGACATCAATAGCCGATGATGAAG
	6	CAAATATTGCAGCCCCGACGTTAAATACTAATACTTTCCGGA
	7	CATAAATAGGCAATAAGCGATATATTCGTCCGTCTAATAGCC

Table A-1 (Continued)

Models	Identifier of strands	Base sequences
6-helix-bundle-5	8	AGCGCCATTTTTTTGAATCTTCGCAGGAATTACTCCTCATTA
	9	TCGGCCGACCCATAATGAATGCAACAGAATACTGTTGTCATA
	10	CTCAATTTTGCACTAGGACTTACCGCGAAATTAACCACCCCG
	11	TGGCGGTATTTTTGTATCTCGAAT
	12	AACGTGATCCTGAATGGCGCTTATGACAGAGTAATGTATTTAACGTCGGAGTCCCTGTAGTTATCTAGTATTCAGTGTTTACTCTTACATAAAGGGGCTATTAGTATTATCCTGCGAAGATTCAAAAAGGTGAGCCAACTCGGCCGATCCGGAAAGACGGACTTCAAAGCTACGTGACGACGGTTGTGGGTCCGTA
	13	TAACTACGTAAGAGACGTAGCTTTGAAGGACTACTAAAAAGA
	14	CGGGAGCTTCAGGATCACGTT
	15	CCGACCACGTCGTCTAAACACTGAAAATACCGCCATACGGAC
	16	ACAAAATCCTCATAATAAGCTCCCGTGAGTGT
	17	TCTGCAAATTTTGTACACTCA
	18	GCCCAAGAGTTGGCTCACCATTATGAGGGGTATCGGAACGGT
	19	TGGTTGAACAGCCCTGGTCGGCTTCATCAGTAGTCCGAATATATCGCTTTATGGGTCTTGGGCCGGGGTGCGATACCTTGCAGA
	20	AATTGAGACCGTTCGTTAATTTCTGTTGCATTCATATTGCCTATATTTGTCTTTTTATCGGCTTATATAGATAAGTATAACATA

Table A-1 (Continued)

Models	Identifier of strands	Base sequences
6-helix-bundle-6	1	TAAGCTATATGTTTATGATCTATTGATCTCCCTGAACGTCGGATTTATCTAATGAGACAGTATTCGCGGTAAGTCCTAGTGCAA
	2	AGCTTATATGTTATCAACCA
	3	CAGTACGAAGGTCCAAACATA
	4	CCACAACGGGCTGTTACTTATCTATATAAGATCATTAAAGGT
	5	CCTTTATTATGAGTTCAGGGAGATCAATAGCCGATGATGAAG
	6	CAAATATCCGACGTCTTTCCAATATCCTTAATACTTTCCGGA
	7	ATAAATAGGCAATAAGCGATATATTCGTCCGTCTAATAGC
	8	GCACTCATTTTTTTGAATCTTCGCAGGATATTAATCTCATTA
	9	CGGCCGACCCATAATGAATGCAACAGAATACTGTGATAAC
	10	CTCAATTTTGCACTAGGACTTACCGCGAAATTAACCACCCCG
	11	TGGCGGTATTTTACCTTCGTACTG
	12	TAGTAGAGGTGACGTGAGTGCCGTTATCATTAATAAGGATATTGGAAAGACTCATAGGCCTCGACCTTTAGGCAGTGTTTACTCTTACATAAAGGCGCTATTAGTATTATCCTGCGAAGATTCAAAAAGGTGAGCCAACTCGGCCGATCCGGAAAGACGGACTTCAAAGCTACCTGACGACGGTTGTGGATCCGTA
	13	GAGGCCGTAAGAGAGGTAGCTTTGAAGGACTACTAAAAAG

Table A-1 (Continued)

Models	Identifier of strands	Base sequences
6-helix-bundle-6	14	CACGGGAGCCGTCACCTCTACTA
	15	CGACGACGTCGTCTAAACACTGAAAATACCGCCATACGGA
	16	ACAAAATCCTCATAATAAGCTCCCGTGGGTGT
	17	TGTGCAAATTTTGTACAC
	18	CCCAAGAGTTGGCTCACCATTATGAGGGGTATCGGAACGG
	19	TGGTTGAACAGCCCTCGTCGGCTTCATCAGTAGTCCGAATATATCGCTTTATGGGTCTTGGGTCGGGGTGCGATACCTTGCACA
	20	AATTGAGGCCGTTCGTTAATTTCTGTTGCATTCATATTGCCTATATTTGTCTTTTTATCGGCTTATATAGATAAGTATAACATA
6-helix-bundle-7	1	TAAGGGATATGTTTATGATCTATTGATCTCCCTGAACGTCGGATTTGTTTAATGAGACAGTATTCGCGGTAAGTCCTAGTGCAA
	2	CTTATATGTTATCAACCA
	3	CAGTACGAAGGTCCAAACATA
	4	CCACAACGGGCTGTTACTTATCTATATAAGATCATTAAAGGT
	5	CCTTTATTATGAGTTCAGGGAGATCAATAGCCGATGATGAAG
	6	CAAATATCCGACGTCTTTCCAATATCCTTAATACTTTCCGGA
	7	AAATAGGCAATAAGCGATATATTCGTCCGTCTAATA
	8	GCACTCATTTTTTTGAATCTTCGCAGGATATTAATCTCATTA

Table A-1 (Continued)

Models	Identifier of strands	Base sequences
6-helix-bundle-7	9	GCCGACCCATAATGAATGCAACAGAATACTGTGATA
	10	CTCAATTTTGCACTAGGACTTACCGCGAAATTAACCACCCCG
	11	TGGCGGTATTTTACCTTCGTACTG
	12	TAGTAGAGGTGACGTGAGTGCTTATATCATTAATAAGGATATTGGAAAGACTCATAGGCCGTCACCTTTAGGCAGTGTTTACTCTTACATAAAGGACATATTAGTATTATCCTGCGAAGATTCAAAAAGGTGAGCCAACTCGGCATTTCCGGAAAGACGGACTTCAAAGCTACCTGACGACGGTTGTGGGGTCGTA
	13	GGCCGTAAGAGAGGTAGCTTTGAAGGACTACTAAAA
	14	CGGGAGCCGTCACCTCTACTA
	15	ACGACGTCGTCTAAACACTGAAAATACCGCCATACG
	16	ACAAAATCCTCATAATAAGCTCCCGGATGTGT
	17	TGTGCAAATTTTGTACAC
	18	CAAGAGTTGGCTCACCATTATGAGGGGTATCGGAAC
	19	TGGTTGAACAGCCCTCGTGTCCTTCATCAGTAGTCCGAATATATCGCTTTATGGGTCTTGTATCGGGGTGCGATACCTTGCACA
	20	AATTGAGACAGTTCGTTAATTTCTGTTGCATTCATATTGCCTATATTTGCCATTTTATCGGCTTATATAGATAAGTATAACATA
6-helix-bundle-8	1	TAAGAAATGTGTTTATGATCTATTGATCTCCCTGAACGTCGGATTTACGCTATGAGACAGTATTCGCGGTAAGTCCTAGTGCAA
	2	CTTATATGTTATCAACCA
	3	CAGTACGAAGGTCCAAACA

Table A-1 (Continued)

Models	Identifier of strands	Base sequences
6-helix-bundle-8	4	ACAACGGGCTGTTACTTATCTATATAAGATCATTAAAG
	5	TTTATTATGAGTTCAGGGAGATCAATAGCCGATGATGA
	6	AATATCCGACGTCTTTCCAATATCCTTAATACTTTCCG
	7	AAATAGGCAATAAGCGATATATTCGTCCGTCTAATA
	8	ACTCATTTTTTTGAATCTTCGCAGGATATTAATCTCAT
	9	GCCGACCCATAATGAATGCAACAGAATACTGTGATA
	10	CAATTTTGCACTAGGACTTACCGCGAAATTAACCACCC
	11	TGGCGGTATTTTACCTTCGTACTG
	12	TAGTAGAGGTGACGTGAGTCATTCTATCATTAATAAGGATATTGGAAAGACTCATAGGCCGCGTTCTTTAGGCAGTGTTTACTCTTACATAAAGACAGTATTAGTATTATCCTGCGAAGATTCAAAAAGGTGAGCCAACTCGGCCGGGTCGGAAAGACGGACTTCAAAGCTACCTGACGACGGTTGTATATACGTA
	13	GGCCGTAAGAGAGGTAGCTTTGAAGGACTACTAAAA
	14	GGAGCCGTCACCTCTACTA
	15	ACGACGTCGTCTAAACACTGAAAATACCGCCATACG
	16	ACAAAATCCTCATAATAAGCTCCGTATAGTGT
	17	TGTGCAAATTTTGTACAC
	18	CAAGAGTTGGCTCACCATTATGAGGGGTATCGGAAC
	19	TGGTTGAACAGCCCTCGTGATTATCATCAGTAGTCCGAATATATCGCTTTATGGGTCTTGAACGGGGGTGCGATACCTTGCACA

Table A-1 (Continued)

Models	Identifier of strands	Base sequences
6-helix-bundle-8	20	AATTGAAAGAGTTCGTTAATTTCTGTTGCATTCATATTGCCTATATTTCGGGTTTTATCGGCTTATATAGATAAGTATAACATA
6-helix-bundle-9	1	AATGCTACTACTATTAGTAGAATTGATGCCACCTTTTCAGCTCGCGCCCCAAATGAAAATATAGCT
	2	AGCTATATGAGCTTCAAAGCGAACCAGACCGTGCTGTAAATATGCAACTAAAGCAAATGTGGGGCGCGAGCTGATTCAAATAACTCCAACAGGTCATAGAGCTGTCTGGAAGTTTCATGTTTGACGCATCAATTCTACTAATTAAGAAGAGTACCTTTAATTGAGGTCAAACAGTTGATTCCCAATTCTGCTAGCATT
	3	TTGATAAGCTCCTTGATTGCATCAAAAAGATAGTAGGAACGAGTAGATTTATCCATGTTTTTTGCGGATGGCTGGATTAGGGAAGCCCGAAAGACAAAGGTGCATTAGATACATTTCGTACGGTTAATTGCTGAATCTGGGAAGCAATCGCGTTTTAATTCTTTCATTGTCAATAACCTGTTTATGTTTTAGCTCAAC
	4	AAACAGGTTATTGACCATTTGCGAAATGTATCTAATGGTCAAACTAAATCTACTCGTTCGCAGAAT
	5	TGGGAATCAACTGTTACATGGAATGAAACTTCCAGACACCGTACTTTAGTTGCATATTTAAAACAT
	6	GTTGAGCTACAGCACCAGATTCAGCAATTAAGCTCTAAGCCATCCGCAAAAATGACCTCTTATCAA
	7	AAGGAGCAATTAAAGGTACTCTCTAATCCTGACCTGTTGGAGTTTGCTTCCGGTCTGGTTCGCTTT
	8	GAAGCTCGAATTAAAACGCGATATTTGAAGTCTTTCGGGCTTCCTCTTAATCTTTTTGATGCAATC
6-helix-bundle-10	1	AATGCTACTACTATTAGTAGAATTGATGCCACCTTTTCAGCTCGCGCCCCAAATGAAAATATAGCT

Table A-1 (Continued)

Models	Identifier of strands	Base sequences
6-helix-bundle-10	2	AGCTATACGAGCTTCAAAGCGAACCAGACGTGCTGTAATATGCAACTAAAGGCAAATGGTGGGGCGCGAGCTGCTTCAAATAACTCCAACAGGTCTAGAGCTTCTGGAAGTTTTCATGTTTGACCGCATCAATTCTACTGATTAAGAAGAGTACCTTTAATGAGGTCATACAGTTGATTCCCAATTCTGCGTAGCATT
	3	TTGATAATGCTCCTTGATTGCATCAAAAAAATAGTAGAACGAGTAGATTTATCCATGTATTTTGCGGATGGCTAGGATTAGGGAAGCCCGAAAGAAAAAGGTGATTAGATACATTTCTACGGTGTAATTGCTGAATCTGCGGAAGCAATCGCGTTTTAATTTTTTCATTTCAATAACCTGTTTTGTTTTAAGCTCAAC
	4	AAACAGGTTATTGACCATTTGCGAAATGTATCTAATGGTCAAACTAAATCTACTCGTTCGCAGAAT
	5	TGGGAATCAACTGTTACATGGAATGAAAACTTCCAGACACCGTACTTTAGTTGCATATTTAAAACA
	6	GTTGAGCTACAGCACCAGATTCAGCAATTAAGCTCTAAGCCATCCGCAAAAATGACCTCTTATCAA
	7	AAGGAGCAATTAAAGGTACTCTCTAATCCTGACCTGTTGGAGTTTGCTTCCGGTCTGGTTCGCTTT
	8	GAAGCTCGAATTAAAACGCGATATTTGAAGTCTTTCGGGCTTCCTCTTAATCTTTTTGATGCAATC

A.3. All-atom model systems

All-atom model systems are constructed for a total of 39 sets, comprising ten DNA helices for regular, 16 for stacked nick, and 13 DNA bundle structures for junction nick, double junction, single junction, and open nick. The box dimensions and the number of water and ion molecules for each system are listed in Table A-2. Each system is assigned a label, including Regular (AA/TT), Regular (AC/GT), Regular (AG/CT), Regular (AT/AT), Regular (CA/TG), Regular (CC/GG), Regular (CG/CG), Regular (GA/TC), Regular (GC/GC), Regular (TA/TA), Stacked nick (AA/TnT), Stacked nick (AC/GnT), Stacked nick (AG/CnT), Stacked nick (AT/AnT), Stacked nick (CA/TnG), Stacked nick (CC/GnG), Stacked nick (CG/CnG), Stacked nick (CT/AnG), Stacked nick (GA/TnC), Stacked nick (GC/GnC), Stacked nick (GG/CnC), Stacked nick (GT/AnC), Stacked nick (TA/TnA), Stacked nick (TC/GnA), Stacked nick (TG/CnA), Stacked nick (TT/AnA), 6-helix-bundle-1.1, 6-helix-bundle-1.2, 6-helix-bundle-1.3, 6-helix-bundle-1.4, 6-helix-bundle-2, 6-helix-bundle-3, 6-helix-bundle-4, 6-helix-bundle-5, 6-helix-bundle-6, 6-helix-bundle-7, 6-helix-bundle-8, 6-helix-bundle-9, or 6-helix-bundle-10.

Table A-2. Box dimensions and total number of water and ion molecules for 39 all-atom model systems.

Models	Box dimensions [nm]			Number		
	x	y	z	Water	Mg^{2+}	Cl^{-}
Regular (AA/TT)	17.76	5.39	5.37	14595	46	10
Regular (AC/GT)	17.76	5.39	5.37	14597	46	10
Regular (AG/CT)	17.76	5.39	5.37	14596	46	10
Regular (AT/AT)	17.76	5.39	5.37	14595	46	10
Regular (CA/TG)	17.76	5.39	5.37	14595	46	10
Regular (CC/GG)	17.76	5.39	5.37	14597	46	10
Regular (CG/CG)	17.76	5.39	5.37	14597	46	10
Regular (GA/TC)	17.76	5.39	5.37	14597	46	10
Regular (GC/GC)	17.76	5.39	5.37	14598	46	10
Regular (TA/TA)	17.76	5.39	5.37	14594	46	10
Stacked nick (AA/TnT)	17.76	5.39	5.37	14596	46	11
Stacked nick (AC/GnT)	17.76	5.39	5.37	14598	46	11
Stacked nick (AG/CnT)	17.76	5.39	5.37	14597	46	11
Stacked nick (AT/AnT)	17.76	5.39	5.37	14596	46	11
Stacked nick (CA/TnG)	17.76	5.39	5.37	14597	46	11
Stacked nick (CC/GnG)	17.76	5.39	5.37	14600	46	11
Stacked nick (CG/CnG)	17.76	5.39	5.37	14598	46	11
Stacked nick (CT/AnG)	17.76	5.39	5.37	14598	46	11
Stacked nick (GA/TnC)	17.76	5.39	5.37	14592	46	11
Stacked nick (GC/GnC)	17.76	5.39	5.37	14598	46	11
Stacked nick (GG/CnC)	17.76	5.39	5.37	14597	46	11

Table A-2 (Continued)

Models	Box dimensions [nm]			Number		
	x	y	z	Water	Mg^{2+}	Cl^{-}
Stacked nick (GT/AnC)	17.76	5.39	5.37	14596	46	11
Stacked nick (TA/TnA)	17.76	5.39	5.37	14595	46	11
Stacked nick (TC/GnA)	17.76	5.39	5.37	14598	46	11
Stacked nick (TG/CnA)	17.76	5.39	5.37	14596	46	11
Stacked nick (TT/AnA)	17.76	5.39	5.37	14596	46	11
6-helix-bundle-1.1	24.90	9.89	9.29	58832	387	42
6-helix-bundle-1.2	24.90	9.89	9.29	58831	387	42
6-helix-bundle-1.3	24.90	9.89	9.29	58828	387	42
6-helix-bundle-1.4	24.90	9.89	9.29	58826	387	42
6-helix-bundle-2	24.90	9.89	9.29	59016	387	43
6-helix-bundle-3	24.90	9.89	9.29	58999	388	42
6-helix-bundle-4	32.04	16.64	5.62	72795	513	52
6-helix-bundle-5	32.04	9.89	9.47	75203	521	54
6-helix-bundle-6	32.04	10.02	9.70	75316	515	55
6-helix-bundle-7	32.04	9.89	9.46	75702	503	55
6-helix-bundle-8	32.04	9.89	9.60	76155	491	54
6-helix-bundle-9	24.90	9.89	9.29	58766	413	42
6-helix-bundle-10	24.90	9.89	9.29	58735	413	42

A.4. Geometric properties of DNA structural motifs

We investigate the sequence-dependent geometric properties (T_x, T_y, T_z, $R_{x,1}$, $R_{x,2}$, $R_{y,1}$, $R_{y,2}$, $R_{z,1}$, and $R_{z,2}$) of regular and stacked nick thorugh all-atom molecular dynamics simulations of DNA helices. The results are summarized in Table A-3 for the regular motifs and Table A-4 for the stacked nick motifs. Additionally, we analyze the geometric properties of junction nick, double junction, single junction, and open nick using all-atom molecular dynamics simulations of DNA bundle structures, which are presented in Tables A-5, A-9, A-10, and A-11, respectively.

For the stacked motifs, inlcuding the regular, stacked nick, and junction nick motifs, 3DNA[31,32] defines six geometric parameters: shift, slide, rise, tilt, roll, and twist. These parameters correspond to $-T_z$, T_y, T_x, $R_{z,1} - R_{z,2}$, $R_{y,2} - R_{y,1}$, and $R_{x,2} - R_{x,1}$, respectively. The sequence-dependent 3DNA parameters for the regular, stacked nick, and junction nick motifs are provided in Tables A-6, A-7, and A-8, respectively.

In all the tables mentioned, μ and σ represent the mean and standard deviation values, respectively.

Table A-3. Sequence-dependent geometric properties of regular.

Properties		Units	AA/TT	AC/GT	AG/CT	AT/AT	CA/TG
μ	T_x	nm	0.33	0.34	0.35	0.32	0.33
	T_y	nm	-0.04	-0.08	-0.10	-0.09	-0.03
	T_z	nm	-0.04	-0.03	0.01	0.00	-0.08
	$R_{x,1}$	°	-17.92	-17.25	-16.00	-16.00	-16.05
	$R_{x,2}$	°	17.92	17.25	16.00	16.00	16.05
	$R_{y,1}$	°	-0.27	0.27	-0.92	0.43	-4.25
	$R_{y,2}$	°	-0.16	-0.19	1.14	-0.49	3.91
	$R_{z,1}$	°	1.33	-0.17	-0.84	0.29	0.62
	$R_{z,2}$	°	-1.34	0.27	0.52	-0.15	-1.72
σ	T_x	nm	0.03	0.03	0.03	0.03	0.03
	T_y	nm	0.06	0.05	0.06	0.04	0.06
	T_z	nm	0.07	0.07	0.07	0.06	0.09
	$R_{x,1}$	°	2.44	2.39	2.84	1.85	2.97
	$R_{x,2}$	°	2.44	2.39	2.84	1.85	2.97
	$R_{y,1}$	°	2.44	2.53	2.64	2.32	3.19
	$R_{y,2}$	°	2.40	2.58	2.79	2.33	3.29
	$R_{z,1}$	°	1.97	2.10	2.31	1.92	2.70
	$R_{z,2}$	°	2.03	2.04	2.13	1.91	2.62
Properties		Units	CC/GG	CG/CG	GA/TC	GC/GC	TA/TA
μ	T_x	nm	0.36	0.33	0.34	0.34	0.34
	T_y	nm	-0.10	-0.01	-0.01	-0.04	0.01
	T_z	nm	0.00	-0.03	-0.07	-0.03	-0.11
	$R_{x,1}$	°	-17.29	-16.41	-19.41	-19.62	-18.67
	$R_{x,2}$	°	17.29	16.41	19.41	19.62	18.67
	$R_{y,1}$	°	-2.27	-4.48	-1.13	-0.22	-2.99
	$R_{y,2}$	°	1.95	4.26	0.78	-0.05	2.31
	$R_{z,1}$	°	0.75	0.13	0.87	0.81	1.57
	$R_{z,2}$	°	-1.37	-1.35	-1.16	-0.82	-2.36
σ	T_x	nm	0.03	0.04	0.03	0.03	0.03
	T_y	nm	0.08	0.06	0.07	0.05	0.07
	T_z	nm	0.07	0.09	0.07	0.06	0.08
	$R_{x,1}$	°	2.74	3.66	2.42	2.06	2.54
	$R_{x,2}$	°	2.74	3.66	2.42	2.06	2.54

Table A-3 (Continued)

Properties		Units	CC/GG	CG/CG	GA/TC	GC/GC	TA/TA
σ	$R_{y,1}$	°	2.62	3.18	2.59	2.48	3.39
	$R_{y,2}$	°	2.62	3.22	2.62	2.48	3.49
	$R_{z,1}$	°	2.34	2.82	2.39	2.08	2.62
	$R_{z,2}$	°	2.34	2.79	2.37	2.09	2.57

Table A-4. Sequence-dependent geometric properties of stacked nick.

Properties		Units	AA/TnT	AC/GnT	AG/CnT	AT/AnT	CA/TnG	CC/GnG
μ	T_x	nm	0.32	0.33	0.32	0.32	0.32	0.35
	T_y	nm	-0.06	-0.09	-0.09	-0.09	-0.07	-0.14
	T_z	nm	0.01	-0.05	0.00	-0.02	0.06	0.02
	$R_{x,1}$	°	-16.30	-18.50	-15.72	-15.65	-13.10	-15.92
	$R_{x,2}$	°	16.30	18.50	15.72	15.65	13.10	15.92
	$R_{y,1}$	°	-0.12	0.61	-1.13	0.91	-4.41	-2.07
	$R_{y,2}$	°	0.54	-0.35	1.55	-0.86	4.46	2.46
	$R_{z,1}$	°	-1.48	-0.71	-1.65	-0.08	-0.63	-1.72
	$R_{z,2}$	°	1.47	0.90	1.31	0.35	-0.24	1.15
σ	T_x	nm	0.03	0.03	0.03	0.03	0.04	0.03
	T_y	nm	0.07	0.06	0.08	0.05	0.06	0.07
	T_z	nm	0.07	0.07	0.08	0.06	0.09	0.09
	$R_{x,1}$	°	4.90	3.24	4.02	2.86	5.75	4.00
	$R_{x,2}$	°	4.90	3.24	4.02	2.86	5.75	4.00
	$R_{y,1}$	°	2.84	2.49	2.67	2.46	3.46	2.91
	$R_{y,2}$	°	2.81	2.59	2.72	2.45	3.46	2.94
	$R_{z,1}$	°	2.22	2.20	2.39	2.05	2.79	2.59
	$R_{z,2}$	°	2.20	2.06	2.31	2.06	2.76	2.52
Properties		Units	CG/CnG	CT/AnG	GA/TnC	GC/GnC	GG/CnC	GT/AnC
μ	T_x	nm	0.32	0.32	0.33	0.34	0.34	0.32
	T_y	nm	-0.02	-0.10	-0.05	-0.04	-0.11	-0.08
	T_z	nm	-0.01	0.01	0.03	-0.05	-0.01	0.03
	$R_{x,1}$	°	-15.03	-14.04	-17.98	-20.41	-15.94	-14.88
	$R_{x,2}$	°	15.03	14.04	17.98	20.41	15.94	14.88
	$R_{y,1}$	°	-2.76	-0.72	-0.59	0.57	-1.71	0.07
	$R_{y,2}$	°	2.61	0.50	0.66	-0.76	1.52	-0.22
	$R_{z,1}$	°	0.17	0.64	-0.33	0.69	0.43	0.52
	$R_{z,2}$	°	-0.82	-0.76	0.30	-0.44	-0.85	-0.38
σ	T_x	nm	0.04	0.03	0.03	0.03	0.04	0.03
	T_y	nm	0.08	0.08	0.09	0.05	0.11	0.08
	T_z	nm	0.10	0.10	0.08	0.06	0.08	0.08
	$R_{x,1}$	°	5.37	4.46	5.88	2.68	3.83	4.48
	$R_{x,2}$	°	5.37	4.46	5.88	2.68	3.83	4.48

Table A-4 (Continued)

Properties		Units	CG/CnG	CT/AnG	GA/TnC	GC/GnC	GG/CnC	GT/AnC
σ	$R_{y,1}$	°	3.15	2.73	3.34	2.48	2.88	2.81
	$R_{y,2}$	°	3.10	2.64	3.30	2.55	2.87	2.81
	$R_{z,1}$	°	2.91	2.34	2.43	2.22	2.47	2.21
	$R_{z,2}$	°	3.00	2.46	2.47	2.13	2.49	2.23

Properties		Units	TA/TnA	TC/GnA	TG/CnA	TT/AnA
μ	T_x	nm	0.32	0.34	0.32	0.32
	T_y	nm	-0.04	-0.04	-0.04	-0.07
	T_z	nm	0.03	-0.03	-0.03	-0.02
	$R_{x,1}$	°	-14.17	-19.41	-13.82	-15.74
	$R_{x,2}$	°	14.17	19.41	13.82	15.74
	$R_{y,1}$	°	-3.71	-0.88	-3.56	-0.25
	$R_{y,2}$	°	3.84	0.75	3.50	0.02
	$R_{z,1}$	°	-0.94	0.20	-0.37	0.74
	$R_{z,2}$	°	0.20	-0.42	-0.40	-0.73
σ	T_x	nm	0.03	0.03	0.04	0.03
	T_y	nm	0.08	0.09	0.07	0.07
	T_z	nm	0.09	0.08	0.11	0.08
	$R_{x,1}$	°	5.12	3.71	5.21	4.17
	$R_{x,2}$	°	5.12	3.71	5.21	4.17
	$R_{y,1}$	°	3.77	2.75	3.11	2.67
	$R_{y,2}$	°	3.76	2.83	3.14	2.64
	$R_{z,1}$	°	2.72	2.55	2.89	2.30
	$R_{z,2}$	°	2.72	2.49	2.92	2.35

Table A-5. Sequence-dependent geometric properties of junction nick.

Properties		Units	AA/TnT	AC/GnT	AG/CnT	AT/AnT	CA/TnG	CC/GnG
μ	T_x	nm	0.32	0.29	0.33	0.31	0.31	0.33
	T_y	nm	-0.07	-0.03	-0.10	-0.08	-0.05	-0.13
	T_z	nm	0.02	-0.01	-0.02	-0.01	0.03	-0.01
	$R_{x,1}$	°	-13.81	-14.38	-13.67	-13.04	-13.47	-14.75
	$R_{x,2}$	°	13.82	14.38	13.68	13.03	13.48	14.76
	$R_{y,1}$	°	-0.06	-0.69	-0.26	-0.06	-3.67	-1.83
	$R_{y,2}$	°	0.60	0.06	0.71	0.02	4.03	1.58
	$R_{z,1}$	°	-1.36	0.82	-1.49	0.21	0.28	0.53
	$R_{z,2}$	°	1.28	-0.42	1.44	-0.20	-0.99	-0.81
σ	T_x	nm	0.05	0.15	0.06	0.03	0.09	0.07
	T_y	nm	0.08	0.12	0.10	0.06	0.10	0.08
	T_z	nm	0.09	0.11	0.13	0.07	0.13	0.17
	$R_{x,1}$	°	7.17	7.94	4.97	3.38	7.48	6.66
	$R_{x,2}$	°	7.11	7.95	4.95	3.38	7.49	6.66
	$R_{y,1}$	°	3.25	5.20	3.69	2.46	5.24	3.90
	$R_{y,2}$	°	3.63	7.88	3.13	2.46	5.65	4.38
	$R_{z,1}$	°	4.36	10.62	3.73	2.25	7.70	3.52
	$R_{z,2}$	°	4.03	8.80	4.18	2.25	7.15	2.98
Properties		Units	CG/CnG	CT/AnG	GA/TnC	GC/GnC	GG/CnC	GT/AnC
μ	T_x	nm	0.31	0.32	0.31	0.25	0.36	0.32
	T_y	nm	-0.06	-0.09	-0.05	-0.06	-0.14	-0.07
	T_z	nm	-0.04	-0.01	-0.04	-0.25	0.01	-0.03
	$R_{x,1}$	°	-13.18	-14.07	-15.20	-16.03	-19.43	-14.46
	$R_{x,2}$	°	13.20	14.07	15.19	16.04	19.43	14.46
	$R_{y,1}$	°	-3.42	-0.82	-0.58	0.27	-2.37	-1.48
	$R_{y,2}$	°	3.20	0.40	0.89	-0.31	2.09	1.21
	$R_{z,1}$	°	0.35	1.32	-0.86	0.51	0.08	0.85
	$R_{z,2}$	°	-1.01	-1.52	0.89	-0.54	-1.09	-1.14
σ	T_x	nm	0.04	0.06	0.09	0.15	0.09	0.03
	T_y	nm	0.07	0.09	0.13	0.16	0.11	0.05
	T_z	nm	0.10	0.10	0.19	0.53	0.12	0.08
	$R_{x,1}$	°	7.08	7.44	6.33	5.13	6.78	3.68
	$R_{x,2}$	°	7.06	7.42	6.32	5.12	6.81	3.67

Table A-5 (Continued)

Properties		Units	CG/CnG	CT/AnG	GA/TnC	GC/GnC	GG/CnC	GT/AnC
σ	$R_{y,1}$	°	3.29	6.89	4.28	4.09	6.27	2.78
	$R_{y,2}$	°	3.51	6.03	3.88	4.21	5.23	2.71
	$R_{z,1}$	°	2.98	8.54	3.69	4.10	3.69	2.26
	$R_{z,2}$	°	2.82	9.14	4.04	3.98	5.11	2.35

Properties		Units	TA/TnA	TC/GnA	TG/CnA	TT/AnA
μ	T_x	nm	0.32	0.29	0.32	0.32
	T_y	nm	-0.07	-0.02	-0.06	-0.09
	T_z	nm	-0.01	-0.01	-0.04	-0.01
	$R_{x,1}$	°	-14.28	-14.12	-14.07	-14.49
	$R_{x,2}$	°	14.29	14.13	14.07	14.49
	$R_{y,1}$	°	-3.10	-0.40	-3.24	-0.60
	$R_{y,2}$	°	3.05	0.32	3.28	0.34
	$R_{z,1}$	°	-0.17	0.16	-0.64	1.09
	$R_{z,2}$	°	-0.47	-0.30	-0.09	-1.14
σ	T_x	nm	0.04	0.10	0.04	0.03
	T_y	nm	0.09	0.14	0.06	0.07
	T_z	nm	0.12	0.20	0.09	0.08
	$R_{x,1}$	°	5.20	8.22	4.58	5.62
	$R_{x,2}$	°	5.19	8.22	4.59	5.61
	$R_{y,1}$	°	3.95	4.67	3.28	2.92
	$R_{y,2}$	°	3.99	4.49	3.29	2.89
	$R_{z,1}$	°	3.13	4.79	2.73	2.51
	$R_{z,2}$	°	3.10	4.94	2.71	2.58

Table A-6. Sequence-dependent 3DNA parameters of regular.

Parameters		Units	AA/TT	AC/GT	AG/CT	AT/AT	CA/TG
μ	Shift	nm	0.04	0.03	-0.01	0.00	0.08
	Slide	nm	-0.04	-0.08	-0.10	-0.09	-0.03
	Rise	nm	0.33	0.34	0.35	0.32	0.33
	Tilt	°	2.68	-0.45	-1.36	0.44	2.34
	Roll	°	0.11	-0.46	2.06	-0.92	8.16
	Twist	°	35.83	34.51	32.00	32.00	32.11
σ	Shift	nm	0.07	0.07	0.07	0.06	0.09
	Slide	nm	0.06	0.05	0.06	0.04	0.06
	Rise	nm	0.03	0.03	0.03	0.03	0.03
	Tilt	°	3.93	4.07	4.38	3.77	5.25
	Roll	°	4.80	5.07	5.40	4.62	6.43
	Twist	°	4.87	4.77	5.68	3.70	5.95
Parameters		Units	CC/GG	CG/CG	GA/TC	GC/GC	TA/TA
μ	Shift	nm	0.00	0.03	0.07	0.03	0.11
	Slide	nm	-0.10	-0.01	-0.01	-0.04	0.01
	Rise	nm	0.36	0.33	0.34	0.34	0.34
	Tilt	°	2.12	1.48	2.03	1.62	3.93
	Roll	°	4.22	8.74	1.91	0.17	5.30
	Twist	°	34.59	32.83	38.81	39.24	37.33
σ	Shift	nm	0.07	0.09	0.07	0.06	0.08
	Slide	nm	0.08	0.06	0.07	0.05	0.07
	Rise	nm	0.03	0.04	0.03	0.03	0.03
	Tilt	°	4.62	5.53	4.68	4.09	5.08
	Roll	°	5.19	6.34	5.15	4.91	6.83
	Twist	°	5.49	7.32	4.84	4.12	5.07

Table A-7. Sequence-dependent 3DNA parameters of stacked nick.

Parameters		Units	AA/TnT	AC/GnT	AG/CnT	AT/AnT	CA/TnG	CC/GnG
μ	Shift	nm	-0.01	0.05	0.00	0.02	-0.06	-0.02
	Slide	nm	-0.06	-0.09	-0.09	-0.09	-0.07	-0.14
	Rise	nm	0.32	0.33	0.32	0.32	0.32	0.35
	Tilt	°	-2.95	-1.61	-2.97	-0.43	-0.38	-2.87
	Roll	°	0.66	-0.96	2.68	-1.77	8.87	4.53
	Twist	°	32.60	37.00	31.44	31.29	26.19	31.84
σ	Shift	nm	0.07	0.07	0.08	0.06	0.09	0.09
	Slide	nm	0.07	0.06	0.08	0.05	0.06	0.07
	Rise	nm	0.03	0.03	0.03	0.03	0.04	0.03
	Tilt	°	4.35	4.18	4.64	4.05	5.48	5.05
	Roll	°	5.61	5.04	5.35	4.88	6.89	5.81
	Twist	°	9.80	6.48	8.05	5.73	11.49	7.99
Parameters		Units	CG/CnG	CT/AnG	GA/TnC	GC/GnC	GG/CnC	GT/AnC
μ	Shift	nm	0.01	-0.01	-0.03	0.05	0.01	-0.03
	Slide	nm	-0.02	-0.10	-0.05	-0.04	-0.11	-0.08
	Rise	nm	0.32	0.32	0.33	0.34	0.34	0.32
	Tilt	°	0.99	1.40	-0.62	1.13	1.29	0.89
	Roll	°	5.37	1.22	1.25	-1.33	3.23	-0.29
	Twist	°	30.06	28.08	35.96	40.82	31.87	29.76
σ	Shift	nm	0.10	0.10	0.08	0.06	0.08	0.08
	Slide	n	0.08	0.08	0.09	0.05	0.11	0.08
	Rise	nm	0.04	0.03	0.03	0.03	0.04	0.03
	Tilt	°	5.84	4.74	4.80	4.26	4.89	4.38
	Roll	°	6.19	5.33	6.59	4.97	5.70	5.59
	Twist	°	10.75	8.91	11.76	5.37	7.66	8.96
Parameters		Units	TA/TnA	TC/GnA	TG/CnA	TT/AnA		
μ	Shift	nm	-0.03	0.03	0.03	0.02		
	Slide	nm	-0.04	-0.04	-0.04	-0.07		
	Rise	nm	0.32	0.34	0.32	0.32		
	Tilt	°	-1.14	0.62	0.04	1.47		
	Roll	°	7.55	1.63	7.05	0.28		
	Twist	°	28.34	38.82	27.63	31.48		
σ	Shift	nm	0.09	0.08	0.11	0.08		
	Slide	nm	0.08	0.09	0.07	0.07		
	Rise	nm	0.03	0.03	0.04	0.03		

Table A-7 (Continued)

Parameters		Units	TA/TnA	TC/GnA	TG/CnA	TT/AnA
σ	Tilt	°	5.36	4.96	5.76	4.59
	Roll	°	7.49	5.51	6.21	5.27
	Twiat	°	10.25	7.42	10.41	8.33

Table A-8. Sequence-dependent 3DNA parameters of junction nick.

Parameters		Units	AA/TnT	AC/GnT	AG/CnT	AT/AnT	CA/TnG	CC/GnG
μ	Shift	nm	-0.02	0.01	0.02	0.01	-0.03	0.00
	Slide	nm	-0.07	-0.03	-0.10	-0.08	-0.05	-0.13
	Rise	nm	0.32	0.29	0.33	0.31	0.31	0.33
	Tilt	°	-2.65	1.24	-2.95	0.41	1.23	1.35
	Roll	°	0.65	0.76	0.96	0.09	7.68	3.42
	Twist	°	27.67	28.75	27.35	26.04	26.96	29.54
σ	Shift	nm	0.09	0.11	0.13	0.07	0.13	0.17
	Slide	nm	0.08	0.12	0.10	0.06	0.10	0.08
	Rise	nm	0.05	0.15	0.06	0.03	0.09	0.07
	Tilt	°	8.18	19.21	7.86	4.48	14.62	6.29
	Roll	°	6.66	11.59	6.65	4.89	8.76	8.16
	Twist	°	14.31	15.77	9.92	6.76	15.09	13.32
Parameters		Units	CG/CnG	CT/AnG	GA/TnC	GC/GnC	GG/CnC	GT/AnC
μ	Shift	nm	0.04	0.01	0.04	0.25	-0.01	0.03
	Slide	nm	-0.06	-0.09	-0.05	-0.06	-0.14	-0.07
	Rise	nm	0.31	0.32	0.31	0.25	0.36	0.32
	Tilt	°	1.38	2.82	-1.76	1.06	1.17	2.00
	Roll	°	6.62	1.22	1.46	-0.60	4.53	2.66
	Twist	°	26.39	28.13	30.40	32.05	38.85	28.91
σ	Shift	nm	0.10	0.10	0.19	0.53	0.11	0.08
	Slide	nm	0.07	0.09	0.13	0.16	0.11	0.05
	Rise	nm	0.04	0.06	0.09	0.15	0.09	0.03
	Tilt	°	5.69	17.11	7.66	7.92	8.38	4.55
	Roll	°	6.74	10.59	8.10	8.26	11.49	5.44
	Twist	°	14.14	14.81	12.63	10.24	13.61	7.35
Parameters		Units	TA/TnA	TC/GnA	TG/CnA	TT/AnA		
μ	Shift	nm	0.01	0.01	0.04	0.01		
	Slide	nm	-0.07	-0.02	-0.06	-0.09		
	Rise	nm	0.32	0.29	0.32	0.32		
	Tilt	°	0.29	0.46	-0.54	2.24		
	Roll	°	6.17	0.74	6.49	0.93		
	Twist	°	28.59	28.25	28.15	28.98		
σ	Shift	nm	0.12	0.20	0.09	0.08		
	Slide	nm	0.09	0.14	0.06	0.07		
	Rise	nm	0.04	0.10	0.04	0.03		

Table A-8 (Continued)

Parameters		Units	TA/TnA	TC/GnA	TG/CnA	TT/AnA
σ	Tilt	°	6.15	9.70	5.38	5.03
	Roll	°	7.88	9.05	6.52	5.78
	Twiat	°	10.38	16.42	9.16	11.22

Table A-9. Sequence-dependent geometric properties of double junction.

Properties		Units	AA||TT	AC||GT	AG||CT	AT||AT	CA||TG	CC||GG
μ	T_x	nm	1.78	1.80	1.81	1.83	1.80	1.80
	T_y	nm	0.49	0.40	0.42	0.35	0.43	0.49
	T_z	nm	0.17	0.22	0.24	0.15	0.13	0.18
	$R_{x,1}$	°	-0.58	-0.37	-0.01	-4.58	3.26	-4.30
	$R_{x,2}$	°	1.97	2.52	0.93	3.01	-1.15	6.73
	$R_{y,1}$	°	5.30	9.88	7.03	5.53	5.66	8.84
	$R_{y,2}$	°	5.76	4.56	8.01	4.49	0.92	3.48
	$R_{z,1}$	°	-33.97	-20.96	-28.20	-25.27	-32.10	-33.07
	$R_{z,2}$	°	3.73	-4.28	2.34	4.16	5.94	3.06
σ	T_x	nm	0.21	0.14	0.09	0.20	0.13	0.12
	T_y	nm	0.15	0.12	0.14	0.33	0.19	0.16
	T_z	nm	0.29	0.21	0.18	0.30	0.25	0.19
	$R_{x,1}$	°	9.96	10.03	6.68	8.93	9.97	7.61
	$R_{x,2}$	°	8.66	7.65	5.77	11.80	8.93	6.57
	$R_{y,1}$	°	10.59	11.02	7.46	8.50	15.52	9.91
	$R_{y,2}$	°	13.13	7.37	6.84	17.84	6.86	7.63
	$R_{z,1}$	°	16.92	12.34	19.44	15.94	17.26	17.72
	$R_{z,2}$	°	16.56	10.36	15.43	19.52	12.47	12.62
Properties		Units	CG||CG	CT||AG	GA||TC	GC||GC	GG||CC	GT||AC
μ	T_x	nm	1.81	1.88	1.75	1.75	1.78	1.85
	T_y	nm	0.41	0.37	0.44	0.47	0.46	0.37
	T_z	nm	0.22	0.08	0.24	0.21	0.21	0.19
	$R_{x,1}$	°	-3.56	-4.30	1.02	0.54	1.93	1.10
	$R_{x,2}$	°	5.13	5.94	1.94	-0.20	-0.46	1.00
	$R_{y,1}$	°	7.20	6.38	8.59	9.76	6.74	6.17
	$R_{y,2}$	°	6.98	0.36	6.17	1.55	5.69	4.47
	$R_{z,1}$	°	-26.17	-28.56	-24.72	-32.46	-30.17	-25.81
	$R_{z,2}$	°	1.21	6.91	-3.01	4.98	2.47	3.64
σ	T_x	nm	0.13	0.14	0.18	0.18	0.14	0.09
	T_y	nm	0.16	0.20	0.34	0.48	0.31	0.22
	T_z	nm	0.19	0.21	0.28	0.29	0.28	0.29
	$R_{x,1}$	°	7.20	6.52	8.98	10.83	8.93	7.11
	$R_{x,2}$	°	7.25	6.04	8.02	10.46	8.63	6.65

Table A-9 (Continued)

Properties		Units	CG‖CG	CT‖AG	GA‖TC	GC‖GC	GG‖CC	GT‖AC
σ	$R_{y,1}$	°	9.81	9.04	12.58	11.24	11.22	13.47
	$R_{y,2}$	°	8.71	9.97	10.82	16.99	13.10	8.53
	$R_{z,1}$	°	15.47	15.41	21.89	28.69	17.71	20.16
	$R_{z,2}$	°	15.81	12.15	16.04	20.06	13.01	11.63

Properties		Units	TA‖TA	TC‖GA	TG‖CA	TT‖AA
μ	T_x	nm	1.80	1.82	1.81	1.85
	T_y	nm	0.43	0.46	0.48	0.45
	T_z	nm	0.15	0.09	0.16	0.08
	$R_{x,1}$	°	-4.33	-8.38	-5.73	-6.05
	$R_{x,2}$	°	6.27	9.66	7.76	6.63
	$R_{y,1}$	°	6.86	5.92	5.15	4.04
	$R_{y,2}$	°	3.71	0.31	6.72	1.95
	$R_{z,1}$	°	-27.34	-23.40	-33.82	-28.73
	$R_{z,2}$	°	0.74	-4.19	4.20	1.57
σ	T_x	nm	0.09	0.11	0.24	0.09
	T_y	nm	0.19	0.12	0.25	0.18
	T_z	nm	0.22	0.19	0.27	0.19
	$R_{x,1}$	°	7.77	7.62	10.14	8.39
	$R_{x,2}$	°	7.22	7.01	9.06	7.62
	$R_{y,1}$	°	10.19	8.71	12.23	8.42
	$R_{y,2}$	°	8.05	9.46	12.68	7.15
	$R_{z,1}$	°	17.69	13.86	18.02	15.52
	$R_{z,2}$	°	14.32	14.41	16.50	14.39

Table A-10. Sequence-dependent geometric properties of single junction.

Properties		Units	AA|TT	AC|GT	AG|CT	AT|AT	CA|TG	CC|GG
μ	T_x	nm	1.76	1.78	1.59	1.88	1.87	1.84
	T_y	nm	0.55	0.56	0.44	0.50	0.45	0.40
	T_z	nm	0.21	0.16	0.25	0.00	0.10	0.31
	$R_{x,1}$	°	-0.24	0.13	2.23	-2.96	1.64	4.74
	$R_{x,2}$	°	2.42	1.74	-0.94	2.42	0.56	-1.85
	$R_{y,1}$	°	7.25	5.54	5.17	0.03	5.26	12.38
	$R_{y,2}$	°	6.23	4.23	8.57	2.19	1.33	6.88
	$R_{z,1}$	°	-41.39	-53.08	-48.48	-46.70	-33.10	-17.67
	$R_{z,2}$	°	6.98	18.32	18.35	17.00	6.39	-6.99
σ	T_x	nm	0.11	0.11	0.20	0.09	0.12	0.09
	T_y	nm	0.14	0.10	0.16	0.12	0.15	0.19
	T_z	nm	0.18	0.18	0.18	0.20	0.22	0.14
	$R_{x,1}$	°	5.25	5.54	6.73	6.46	7.05	6.62
	$R_{x,2}$	°	5.30	4.87	7.29	5.69	6.35	6.41
	$R_{y,1}$	°	7.60	7.85	9.28	7.43	9.97	7.40
	$R_{y,2}$	°	7.37	6.25	7.41	6.88	7.92	7.37
	$R_{z,1}$	°	13.98	6.08	7.02	7.35	13.84	18.11
	$R_{z,2}$	°	8.71	5.78	8.70	9.18	9.63	9.66
Properties		Units	CG|CG	CT|AG	GA|TC	GC|GC	GG|CC	GT|AC
μ	T_x	nm	1.86	1.87	1.75	1.74	1.83	1.72
	T_y	nm	0.40	0.44	0.58	0.61	0.51	0.55
	T_z	nm	0.25	0.10	0.27	0.19	0.22	0.11
	$R_{x,1}$	°	5.74	0.77	0.76	0.75	-1.45	-12.65
	$R_{x,2}$	°	-3.65	0.65	4.50	2.24	1.81	13.62
	$R_{y,1}$	°	8.90	4.11	13.92	7.95	4.61	8.88
	$R_{y,2}$	°	6.01	2.65	3.68	4.01	7.96	6.35
	$R_{z,1}$	°	-21.33	-32.29	-47.79	-50.08	-48.93	-55.19
	$R_{z,2}$	°	-2.54	6.02	11.84	11.77	18.15	19.69
σ	T_x	nm	0.10	0.14	0.10	0.08	0.12	0.06
	T_y	nm	0.16	0.14	0.09	0.07	0.12	0.08
	T_z	nm	0.18	0.20	0.16	0.14	0.17	0.14
	$R_{x,1}$	°	5.65	5.85	5.46	5.11	5.91	6.31
	$R_{x,2}$	°	5.28	5.86	4.75	4.85	6.79	5.72

Table A-10 (Continued)

Properties		Units	CG|CG	CT|AG	GA|TC	GC|GC	GG|CC	GT|AC
σ	$R_{y,1}$	°	6.31	7.51	7.43	7.37	8.94	7.67
	$R_{y,2}$	°	7.91	8.25	6.55	6.29	6.80	6.04
	$R_{z,1}$	°	15.52	17.28	5.73	5.75	6.01	6.63
	$R_{z,2}$	°	10.67	16.01	6.43	5.69	8.00	5.70

Properties		Units	TA|TA	TC|GA	TG|CA	TT|AA
μ	T_x	nm	1.81	1.74	1.71	1.82
	T_y	nm	0.54	0.61	0.55	0.51
	T_z	nm	0.22	0.09	0.27	0.10
	$R_{x,1}$	°	2.00	-6.60	1.98	1.54
	$R_{x,2}$	°	-0.32	7.32	0.82	1.05
	$R_{y,1}$	°	6.36	4.18	9.14	9.00
	$R_{y,2}$	°	7.44	5.09	8.07	-1.30
	$R_{z,1}$	°	-28.71	-56.91	-42.44	-37.15
	$R_{z,2}$	°	-4.13	18.50	7.38	5.95
σ	T_x	nm	0.08	0.10	0.10	0.11
	T_y	nm	0.11	0.07	0.13	0.14
	T_z	nm	0.16	0.15	0.18	0.17
	$R_{x,1}$	°	6.26	6.43	6.72	6.49
	$R_{x,2}$	°	5.58	5.01	6.04	6.61
	$R_{y,1}$	°	6.59	10.59	7.91	8.08
	$R_{y,2}$	°	6.50	6.71	9.10	6.10
	$R_{z,1}$	°	16.44	8.51	25.58	19.11
	$R_{z,2}$	°	14.26	8.18	19.46	14.20

Table A-11. Sequence-dependent geometric properties of open nick.

Properties		Units	AA/TnT	AC/GnT	AG/CnT	AT/AnT	CA/TnG	CC/GnG
μ	T_x	nm	1.60	1.69	1.43	1.01	1.35	1.83
	T_y	nm	0.09	0.09	0.21	0.14	0.08	0.55
	T_z	nm	0.16	-0.05	0.02	0.06	0.39	-0.14
	$R_{x,1}$	°	6.41	1.58	4.23	-7.44	17.72	-19.20
	$R_{x,2}$	°	-4.12	0.38	3.73	7.78	-17.61	12.63
	$R_{y,1}$	°	13.00	3.72	3.42	21.32	36.86	-9.09
	$R_{y,2}$	°	-0.56	-7.32	-10.50	3.37	6.47	7.71
	$R_{z,1}$	°	-14.07	-11.22	-18.21	-24.81	-17.20	-46.09
	$R_{z,2}$	°	7.93	5.50	9.77	15.26	12.86	9.83
σ	T_x	nm	0.21	0.14	0.44	0.64	0.55	0.11
	T_y	nm	0.35	0.36	0.44	0.57	0.69	0.10
	T_z	nm	0.42	0.37	0.42	0.56	0.32	0.17
	$R_{x,1}$	°	13.92	8.60	8.92	23.46	18.22	6.28
	$R_{x,2}$	°	14.52	9.02	8.73	20.12	34.74	5.90
	$R_{y,1}$	°	19.78	16.36	23.71	44.89	42.12	9.34
	$R_{y,2}$	°	13.40	12.40	18.87	38.29	16.99	6.91
	$R_{z,1}$	°	22.47	20.92	40.21	27.54	56.31	9.76
	$R_{z,2}$	°	13.50	13.27	11.45	33.03	15.52	6.42
Properties		Units	CG/CnG	CT/AnG	GA/TnC	GC/GnC	GG/CnC	GT/AnC
μ	T_x	nm	1.66	1.58	1.69	1.52	1.38	1.54
	T_y	nm	0.21	0.58	0.24	0.52	0.28	0.54
	T_z	nm	0.17	0.03	0.38	-0.01	0.03	0.15
	$R_{x,1}$	°	1.13	-6.74	18.55	-1.27	-2.09	6.92
	$R_{x,2}$	°	-3.27	12.04	-17.93	12.80	10.54	1.09
	$R_{y,1}$	°	16.61	14.10	33.13	20.21	19.61	16.15
	$R_{y,2}$	°	-4.26	-3.10	-6.53	-10.50	-19.84	-5.52
	$R_{z,1}$	°	1.33	-56.74	-3.77	-53.13	-10.57	-50.61
	$R_{z,2}$	°	-15.31	17.70	-17.14	17.67	4.89	12.47
σ	T_x	nm	0.18	0.20	0.12	0.33	0.51	0.21
	T_y	nm	0.17	0.11	0.18	0.18	0.43	0.16
	T_z	nm	0.23	0.21	0.19	0.26	0.26	0.25
	$R_{x,1}$	°	6.22	9.54	7.49	10.82	10.12	7.54
	$R_{x,2}$	°	6.15	7.80	5.81	9.82	9.79	6.78

Table A-11 (Continued)

Properties		Units	CG/CnG	CT/AnG	GA/TnC	GC/GnC	GG/CnC	GT/AnC
σ	$R_{y,1}$	°	12.39	12.30	7.82	14.15	21.85	14.59
	$R_{y,2}$	°	10.25	9.41	10.46	17.75	12.87	6.90
	$R_{z,1}$	°	13.90	9.02	10.05	10.22	40.62	6.48
	$R_{z,2}$	°	10.72	10.73	9.37	15.14	9.64	9.24

Properties		Units	TA/TnA	TC/GnA	TG/CnA	TT/AnA
μ	T_x	nm	1.69	1.89	1.52	1.27
	T_y	nm	0.41	0.28	-0.06	0.04
	T_z	nm	0.01	0.08	0.14	0.25
	$R_{x,1}$	°	-0.05	-1.03	1.33	-3.53
	$R_{x,2}$	°	0.19	4.32	-3.17	10.04
	$R_{y,1}$	°	6.62	11.83	18.12	30.34
	$R_{y,2}$	°	-5.46	-5.17	-4.31	-1.25
	$R_{z,1}$	°	-26.39	-31.24	-7.95	-29.78
	$R_{z,2}$	°	-0.89	14.27	7.63	25.83
σ	T_x	nm	0.26	0.15	0.66	0.70
	T_y	nm	0.29	0.33	0.78	0.63
	T_z	nm	0.28	0.23	0.41	0.43
	$R_{x,1}$	°	11.16	8.57	10.68	30.11
	$R_{x,2}$	°	9.61	7.82	29.81	19.56
	$R_{y,1}$	°	15.34	10.64	47.24	21.89
	$R_{y,2}$	°	12.96	8.29	15.07	46.05
	$R_{z,1}$	°	19.48	15.49	43.52	23.35
	$R_{z,2}$	°	18.17	10.11	18.52	39.22

A.5. Mechanical properties of DNA structural motifs

The mechanical properties include six primary rigidities (S, Y_y, Y_z, C, B_y, and B_z) and 15 coupling coefficients ($G_{s_1 s_2}$) between geoemtric parameters s_1 and s_2. Here, s_1 and s_2 can be any of T_x, T_y, T_z, R_x ($R_{x,2} - R_{x,1}$), R_y ($R_{y,2} - R_{y,1}$), and R_z ($R_{z,2} - R_{z,1}$). We analyze the mechanical properties using the geometric properties obtained from all-atom molecular dynamics simulations under the quasi-harmonic approximation[33]. Additionally, the equivalent shearing and bending rigidities (Y and B) are calculated using the harmonic average of the two shearing rigidities (Y_y and Y_z) and the two bending rigidities (B_y and B_z), respectively.

Table A-12 through Table A-17 present the sequence-dependent mechanical properties of various structural motifs, including regular, stacked nick, junction nick, double junction, single junction, and open nick, respectively. In all the tables, the mean (μ) and standard deviation (σ) values for the mechanical properties are denoted accordingly.

Table A-12. Sequence-dependent mechanical properties of regular.

Properties		Units	AA/TT	AC/GT	AG/CT	AT/AT	CA/TG
μ	S	pN	2478.77	2552.04	1924.88	2576.91	1607.52
	Y_y	pN	757.56	794.47	762.50	873.78	568.04
	Y_z	pN	467.82	355.26	513.36	412.58	246.55
	Y	pN	576.12	489.67	611.24	558.21	342.69
	C	$pN \cdot nm^2$	304.05	261.70	307.40	368.39	199.74
	B_y	$pN \cdot nm^2$	209.39	223.69	208.85	247.15	148.72
	B_z	$pN \cdot nm^2$	366.73	327.08	354.36	329.87	231.64
	B	$pN \cdot nm^2$	265.52	264.72	261.56	281.37	179.83
	$G_{T_xT_y}$	pN	218.26	573.78	218.89	558.40	215.92
	$G_{T_xT_z}$	pN	139.46	-31.85	-134.56	-2.76	20.16
	$G_{T_xR_x}$	pN·nm	-190.58	-208.93	-152.03	-120.34	-214.46
	$G_{T_xR_y}$	pN·nm	-22.67	179.40	22.82	184.77	-83.07
	$G_{T_xR_z}$	pN·nm	-358.33	-51.90	310.70	7.99	54.72
	$G_{T_yT_z}$	pN	234.96	33.51	-60.38	26.95	106.42
	$G_{T_yR_x}$	pN·nm	-209.58	-87.84	-221.47	-108.07	-91.46
	$G_{T_yR_y}$	pN·nm	-60.03	37.84	-28.23	-20.59	53.03
	$G_{T_yR_z}$	pN·nm	22.18	72.33	-10.43	-4.98	11.21
	$G_{T_zR_x}$	pN·nm	52.99	-16.99	-155.08	13.84	-57.06
	$G_{T_zR_y}$	pN·nm	-9.67	-32.60	-93.66	-32.00	-12.46
	$G_{T_zR_z}$	pN·nm	-7.44	-41.11	-89.17	12.07	-101.62
	$G_{R_xR_y}$	$pN \cdot nm^2$	31.03	52.42	4.61	48.24	53.16
	$G_{R_xR_z}$	$pN \cdot nm^2$	46.32	-55.36	-36.97	-9.45	21.16
	$G_{R_yR_z}$	$pN \cdot nm^2$	19.57	-34.51	-17.96	-5.15	-8.59
σ	S	pN	213.31	237.65	179.41	247.71	168.70
	Y_y	pN	65.19	73.98	71.07	83.99	59.61

Table A-12 (Continued)

Properties		Units	AA/TT	AC/GT	AG/CT	AT/AT	CA/TG
σ	Y_z	pN	40.26	33.08	47.85	39.66	25.87
	Y	pN	36.42	34.56	41.66	40.38	27.72
	C	pN·nm^2	26.17	24.37	28.65	35.41	20.96
	B_y	pN·nm^2	18.02	20.83	19.47	23.76	15.61
	B_z	pN·nm^2	31.56	30.46	33.03	31.71	24.31
	B	pN·nm^2	16.91	17.90	17.86	19.40	13.90
	$G_{T_xT_y}$	pN	18.78	53.43	20.40	53.68	22.66
	$G_{T_xT_z}$	pN	12.00	2.97	12.54	0.27	2.12
	$G_{T_xR_x}$	pN·nm	16.40	19.46	14.17	11.57	22.51
	$G_{T_xR_y}$	pN·nm	1.95	16.71	2.13	17.76	8.72
	$G_{T_xR_z}$	pN·nm	30.84	4.83	28.96	0.77	5.74
	$G_{T_yT_z}$	pN	20.22	3.12	5.63	2.59	11.17
	$G_{T_yR_x}$	pN·nm	18.04	8.18	20.64	10.39	9.60
	$G_{T_yR_y}$	pN·nm	5.17	3.52	2.63	1.98	5.57
	$G_{T_yR_z}$	pN·nm	1.91	6.74	0.97	0.48	1.18
	$G_{T_zR_x}$	pN·nm	4.56	1.58	14.45	1.33	5.99
	$G_{T_zR_y}$	pN·nm	0.83	3.04	8.73	3.08	1.31
	$G_{T_zR_z}$	pN·nm	0.64	3.83	8.31	1.16	10.66
	$G_{R_xR_y}$	pN·nm^2	2.67	4.88	0.43	4.64	5.58
	$G_{R_xR_z}$	pN·nm^2	3.99	5.16	3.45	0.91	2.22
	$G_{R_yR_z}$	pN·nm^2	1.68	3.21	1.67	0.49	0.90
Properties		Units	CC/GG	CG/CG	GA/TC	GC/GC	TA/TA
μ	S	pN	2256.28	1565.25	2552.07	2845.26	1752.81
	Y_y	pN	389.11	548.99	492.47	746.83	657.10
	Y_z	pN	400.14	301.55	398.73	502.37	407.66

Table A-12 (Continued)

Properties		Units	CC/GG	CG/CG	GA/TC	GC/GC	TA/TA
μ	Y	pN	392.90	386.75	439.05	598.47	501.86
	C	pN·nm^2	249.71	135.71	282.68	330.19	394.26
	B_y	pN·nm^2	205.60	132.27	202.62	236.02	164.08
	B_z	pN·nm^2	376.85	231.57	345.29	327.51	223.91
	B	pN·nm^2	264.98	167.39	254.40	273.25	188.86
	$G_{T_xT_y}$	pN	382.09	241.31	239.71	595.11	163.77
	$G_{T_xT_z}$	pN	-111.96	-3.20	160.99	17.95	-96.98
	$G_{T_xR_x}$	pN·nm	-237.44	-240.41	-167.19	-255.62	-214.05
	$G_{T_xR_y}$	pN·nm	18.41	-82.69	1.99	251.75	-78.79
	$G_{T_xR_z}$	pN·nm	424.14	41.29	-408.49	-27.76	97.60
	$G_{T_yT_z}$	pN	-19.15	91.92	203.51	132.28	217.54
	$G_{T_yR_x}$	pN·nm	-136.16	-90.13	-155.69	-97.94	-222.29
	$G_{T_yR_y}$	pN·nm	22.70	32.39	-17.94	89.26	38.41
	$G_{T_yR_z}$	pN·nm	22.39	3.25	68.19	18.42	-27.22
	$G_{T_zR_x}$	pN·nm	-71.40	-28.45	-90.34	-53.22	15.07
	$G_{T_zR_y}$	pN·nm	-43.35	-8.11	-1.28	-17.33	-24.35
	$G_{T_zR_z}$	pN·nm	-152.04	-147.10	-82.48	-123.97	-71.25
	$G_{R_xR_y}$	pN·nm^2	31.22	30.53	67.58	31.14	93.86
	$G_{R_xR_z}$	pN·nm^2	-11.27	2.14	-8.65	-16.42	40.28
	$G_{R_yR_z}$	pN·nm^2	15.43	-0.72	-13.39	3.32	8.07
σ	S	pN	231.67	180.20	220.10	233.55	153.89
	Y_y	pN	39.95	63.20	42.47	61.30	57.69
	Y_z	pN	41.09	34.72	34.39	41.24	35.79
	Y	pN	29.05	33.45	27.04	35.95	32.39
	C	pN·nm^2	25.64	15.62	24.38	27.10	34.61

Table A-12 (Continued)

Properties		Units	CC/GG	CG/CG	GA/TC	GC/GC	TA/TA
σ	B_y	pN·nm^2	21.11	15.23	17.47	19.37	14.41
	B_z	pN·nm^2	38.69	26.66	29.78	26.88	19.66
	B	pN·nm^2	20.43	14.20	16.18	16.23	12.01
	$G_{T_xT_y}$	pN	39.23	27.78	20.67	48.85	14.38
	$G_{T_xT_z}$	pN	11.50	0.37	13.88	1.47	8.51
	$G_{T_xR_x}$	pN·nm	24.38	27.68	14.42	20.98	18.79
	$G_{T_xR_y}$	pN·nm	1.89	9.52	0.17	20.66	6.92
	$G_{T_xR_z}$	pN·nm	43.55	4.75	35.23	2.28	8.57
	$G_{T_yT_z}$	pN	1.97	10.58	17.55	10.86	19.10
	$G_{T_yR_x}$	pN·nm	13.98	10.38	13.43	8.04	19.52
	$G_{T_yR_y}$	pN·nm	2.33	3.73	1.55	7.33	3.37
	$G_{T_yR_z}$	pN·nm	2.30	0.37	5.88	1.51	2.39
	$G_{T_zR_x}$	pN·nm	7.33	3.27	7.79	4.37	1.32
	$G_{T_zR_y}$	pN·nm	4.45	0.93	0.11	1.42	2.14
	$G_{T_zR_z}$	pN·nm	15.61	16.93	7.11	10.18	6.26
	$G_{R_xR_y}$	pN·nm^2	3.21	3.52	5.83	2.56	8.24
	$G_{R_xR_z}$	pN·nm^2	1.16	0.25	0.75	1.35	3.54
	$G_{R_yR_z}$	pN·nm^2	1.58	0.08	1.15	0.27	0.71

Table A-13. Sequence-dependent mechanical properties of stacked nick.

Properties		Units	AA/TnT	AC/GnT	AG/CnT	AT/AnT
μ	S	pN	2247.09	2393.12	2025.26	2622.91
	Y_y	pN	407.53	486.27	283.91	614.45
	Y_z	pN	348.89	407.81	286.28	395.82
	Y	pN	374.29	440.87	283.40	479.37
	C	pN·nm^2	96.40	151.83	98.47	173.39
	B_y	pN·nm^2	181.18	238.60	180.12	222.20
	B_z	pN·nm^2	316.28	303.97	307.73	288.12
	B	pN·nm^2	229.46	266.12	225.75	249.53
	$G_{T_xT_y}$	pN	183.62	407.04	239.59	415.57
	$G_{T_xT_z}$	pN	-153.97	-128.85	-143.69	0.83
	$G_{T_xR_x}$	pN·nm	-194.50	-153.25	-180.87	-86.89
	$G_{T_xR_y}$	pN·nm	-14.42	251.52	-30.57	195.74
	$G_{T_xR_z}$	pN·nm	393.28	48.41	374.22	102.86
	$G_{T_yT_z}$	pN	-92.61	45.32	-20.20	51.49
	$G_{T_yR_x}$	pN·nm	-116.10	-66.09	-58.42	-42.17
	$G_{T_yR_y}$	pN·nm	-8.24	79.65	-8.19	19.20
	$G_{T_yR_z}$	pN·nm	35.88	47.78	62.93	56.90
	$G_{T_zR_x}$	pN·nm	45.85	79.87	26.27	85.22
	$G_{T_zR_y}$	pN·nm	-71.07	-3.88	-36.40	-30.27
	$G_{T_zR_z}$	pN·nm	-59.24	-54.77	-81.90	11.20
	$G_{R_xR_y}$	pN·nm^2	30.71	14.39	20.44	30.59
	$G_{R_xR_z}$	pN·nm^2	-37.34	-18.78	-45.07	8.90
	$G_{R_yR_z}$	pN·nm^2	-9.24	-33.52	-19.31	14.29
σ	S	pN	218.11	251.32	220.90	265.97
	Y_y	pN	39.56	51.07	30.97	62.31
	Y_z	pN	33.86	42.83	31.22	40.14
	Y	pN	25.75	33.69	22.58	35.63
	C	pN·nm^2	9.36	15.94	10.74	17.58
	B_y	pN·nm^2	17.59	25.06	19.65	22.53
	B_z	pN·nm^2	30.70	31.92	33.57	29.22
	B	pN·nm^2	16.43	20.24	18.29	18.28
	$G_{T_xT_y}$	pN	17.82	42.75	26.13	42.14

Table A-13 (Continued)

Properties		Units	AA/TnT	AC/GnT	AG/CnT	AT/AnT
	$G_{T_xT_z}$	pN	14.94	13.53	15.67	0.08
	$G_{T_xR_x}$	pN·nm	18.88	16.09	19.73	8.81
	$G_{T_xR_y}$	pN·nm	1.40	26.41	3.33	19.85
	$G_{T_xR_z}$	pN·nm	38.17	5.08	40.82	10.43
	$G_{T_yT_z}$	pN	8.99	4.76	2.20	5.22
	$G_{T_yR_x}$	pN·nm	11.27	6.94	6.37	4.28
	$G_{T_yR_y}$	pN·nm	0.80	8.36	0.89	1.95
	$G_{T_yR_z}$	pN·nm	3.48	5.02	6.86	5.77
	$G_{T_zR_x}$	pN·nm	4.45	8.39	2.87	8.64
	$G_{T_zR_y}$	pN·nm	6.90	0.41	3.97	3.07
	$G_{T_zR_z}$	pN·nm	5.75	5.75	8.93	1.14
	$G_{R_xR_y}$	pN·nm^2	2.98	1.51	2.23	3.10
	$G_{R_xR_z}$	pN·nm^2	3.62	1.97	4.92	0.90
	$G_{R_yR_z}$	pN·nm^2	0.90	3.52	2.11	1.45
Properties		Units	CA/TnG	CC/GnG	CG/CnG	CT/AnG
	S	pN	1438.83	1917.97	1537.21	1906.00
	Y_y	pN	493.45	455.92	348.00	493.35
	Y_z	pN	260.21	389.02	246.67	368.90
	Y	pN	338.86	417.98	285.82	418.89
	C	pN·nm^2	72.33	175.66	78.53	166.91
	B_y	pN·nm^2	134.58	180.84	133.11	181.72
	B_z	pN·nm^2	190.24	301.55	195.60	297.12
	B	pN·nm^2	156.61	225.05	157.10	223.84
μ	$G_{T_xT_y}$	pN	93.61	75.21	108.36	126.52
	$G_{T_xT_z}$	pN	4.49	59.43	-36.91	36.97
	$G_{T_xR_x}$	pN·nm	-148.76	-109.20	-163.19	-127.33
	$G_{T_xR_y}$	pN·nm	-63.18	16.03	-60.64	-35.90
	$G_{T_xR_z}$	pN·nm	19.76	-240.02	52.95	-230.73
	$G_{T_yT_z}$	pN	-26.25	-83.32	47.88	76.91
	$G_{T_yR_x}$	pN·nm	-51.73	-115.94	-53.55	-111.35
	$G_{T_yR_y}$	pN·nm	44.74	44.08	16.09	-18.23

Table A-13 (Continued)

Properties		Units	CA/TnG	CC/GnG	CG/CnG	CT/AnG
μ	$G_{T_yR_z}$	pN·nm	74.29	129.92	67.93	81.14
	$G_{T_zR_x}$	pN·nm	48.70	152.76	53.12	136.74
	$G_{T_zR_y}$	pN·nm	-27.02	-0.38	1.88	-8.70
	$G_{T_zR_z}$	pN·nm	-73.51	-113.37	-90.91	-24.11
	$G_{R_xR_y}$	pN·nm^2	30.33	30.38	19.31	21.39
	$G_{R_xR_z}$	pN·nm^2	-25.46	-45.08	-28.32	21.43
	$G_{R_yR_z}$	pN·nm^2	6.87	-5.10	13.30	41.13
σ	S	pN	160.58	194.27	204.03	232.52
	Y_y	pN	55.07	46.18	46.19	60.18
	Y_z	pN	29.04	39.40	32.74	45.00
	Y	pN	28.56	30.42	27.92	37.22
	C	pN·nm^2	8.07	17.79	10.42	20.36
	B_y	pN·nm^2	15.02	18.32	17.67	22.17
	B_z	pN·nm^2	21.23	30.54	25.96	36.25
	B	pN·nm^2	12.84	16.82	15.38	20.22
	$G_{T_xT_y}$	pN	10.45	7.62	14.38	15.43
	$G_{T_xT_z}$	pN	0.50	6.02	4.90	4.51
	$G_{T_xR_x}$	pN·nm	16.60	11.06	21.66	15.53
	$G_{T_xR_y}$	pN·nm	7.05	1.62	8.05	4.38
	$G_{T_xR_z}$	pN·nm	2.21	24.31	7.03	28.15
	$G_{T_yT_z}$	pN	2.93	8.44	6.35	9.38
	$G_{T_yR_x}$	pN·nm	5.77	11.74	7.11	13.58
	$G_{T_yR_y}$	pN·nm	4.99	4.47	2.13	2.22
	$G_{T_yR_z}$	pN·nm	8.29	13.16	9.02	9.90
	$G_{T_zR_x}$	pN·nm	5.44	15.47	7.05	16.68
	$G_{T_zR_y}$	pN·nm	3.02	0.04	0.25	1.06
	$G_{T_zR_z}$	pN·nm	8.20	11.48	12.07	2.94
	$G_{R_xR_y}$	pN·nm^2	3.39	3.08	2.56	2.61
	$G_{R_xR_z}$	pN·nm^2	2.84	4.57	3.76	2.61
	$G_{R_yR_z}$	pN·nm^2	0.77	0.52	1.77	5.02

Table A-13 (Continued)

Properties		Units	GA/TnC	GC/GnC	GG/CnC	GT/AnC
μ	S	pN	2342.68	2644.01	2066.73	2362.62
	Y_y	pN	329.48	671.79	200.92	425.65
	Y_z	pN	352.84	545.63	298.73	422.54
	Y	pN	339.24	600.36	237.95	420.02
	C	pN·nm^2	97.55	183.65	118.36	144.75
	B_y	pN·nm^2	150.99	238.44	169.88	218.31
	B_z	pN·nm^2	300.55	303.56	318.12	280.27
	B	pN·nm^2	200.34	266.18	219.06	243.71
	$G_{T_xT_y}$	pN	256.77	517.21	305.96	354.12
	$G_{T_xT_z}$	pN	-157.29	-75.29	-72.28	85.35
	$G_{T_xR_x}$	pN·nm	-190.73	-196.61	-160.67	-104.96
	$G_{T_xR_y}$	pN·nm	52.09	308.12	38.22	163.33
	$G_{T_xR_z}$	pN·nm	432.60	75.72	429.28	123.16
	$G_{T_yT_z}$	pN	-74.15	52.72	31.38	48.91
	$G_{T_yR_x}$	pN·nm	-106.27	-48.49	-53.32	-107.22
	$G_{T_yR_y}$	pN·nm	30.95	101.53	22.59	12.33
	$G_{T_yR_z}$	pN·nm	64.90	58.36	54.95	64.22
	$G_{T_zR_x}$	pN·nm	89.88	10.89	47.47	109.61
	$G_{T_zR_y}$	pN·nm	-21.09	-32.83	-21.24	-41.91
	$G_{T_zR_z}$	pN·nm	-88.24	-121.87	-74.93	2.24
	$G_{R_xR_y}$	pN·nm^2	27.74	-9.41	12.46	44.72
	$G_{R_xR_z}$	pN·nm^2	-40.39	-21.13	-36.00	19.79
	$G_{R_yR_z}$	pN·nm^2	22.19	-5.08	17.67	46.79
σ	S	pN	263.10	226.55	296.86	303.82
	Y_y	pN	37.00	57.56	28.86	54.73
	Y_z	pN	39.63	46.75	42.91	54.34
	Y	pN	27.16	36.87	25.44	39.71
	C	pN·nm^2	10.96	15.74	17.00	18.61
	B_y	pN·nm^2	16.96	20.43	24.40	28.07
	B_z	pN·nm^2	33.75	26.01	45.69	36.04
	B	pN·nm^2	16.83	16.56	23.78	22.64
	$G_{T_xT_y}$	pN	28.84	44.32	43.95	45.54

Table A-13 (Continued)

Properties		Units	GA/TnC	GC/GnC	GG/CnC	GT/AnC
σ	$G_{T_xT_z}$	pN	17.66	6.45	10.38	10.98
	$G_{T_xR_x}$	pN·nm	21.42	16.85	23.08	13.50
	$G_{T_xR_y}$	pN·nm	5.85	26.40	5.49	21.00
	$G_{T_xR_z}$	pN·nm	48.58	6.49	61.66	15.84
	$G_{T_yT_z}$	pN	8.33	4.52	4.51	6.29
	$G_{T_yR_x}$	pN·nm	11.94	4.16	7.66	13.79
	$G_{T_yR_y}$	pN·nm	3.48	8.70	3.24	1.59
	$G_{T_yR_z}$	pN·nm	7.29	5.00	7.89	8.26
	$G_{T_zR_x}$	pN·nm	10.09	0.93	6.82	14.09
	$G_{T_zR_y}$	pN·nm	2.37	2.81	3.05	5.39
	$G_{T_zR_z}$	pN·nm	9.91	10.44	10.76	0.29
	$G_{R_xR_y}$	pN·nm^2	3.12	0.81	1.79	5.75
	$G_{R_xR_z}$	pN·nm^2	4.54	1.81	5.17	2.54
	$G_{R_yR_z}$	pN·nm^2	2.49	0.44	2.54	6.02
Properties		Units	TA/TnA	TC/GnA	TG/CnA	TT/AnA
μ	S	pN	1564.99	2110.50	1490.25	2044.54
	Y_y	pN	410.97	342.44	427.38	492.72
	Y_z	pN	195.35	352.50	199.17	430.30
	Y	pN	263.69	345.76	270.09	456.54
	C	pN·nm^2	105.23	169.53	83.01	154.21
	B_y	pN·nm^2	137.88	185.42	146.69	184.38
	B_z	pN·nm^2	179.29	294.03	183.68	283.23
	B	pN·nm^2	154.95	226.27	161.55	222.34
	$G_{T_xT_y}$	pN	90.32	140.86	93.52	20.80
	$G_{T_xT_z}$	pN	23.29	101.93	27.79	61.64
	$G_{T_xR_x}$	pN·nm	-117.16	-135.46	-138.40	-112.65
	$G_{T_xR_y}$	pN·nm	-81.61	-15.72	-110.41	-15.55
	$G_{T_xR_z}$	pN·nm	23.06	-298.38	50.43	-246.16
	$G_{T_yT_z}$	pN	-0.98	47.65	37.96	107.10
	$G_{T_yR_x}$	pN·nm	-105.04	-117.38	-70.64	-112.45
	$G_{T_yR_y}$	pN·nm	50.30	18.09	29.43	-39.36

Table A-13 (Continued)

Properties		Units	TA/TnA	TC/GnA	TG/CnA	TT/AnA
μ	$G_{T_yR_z}$	pN·nm	47.59	82.80	59.84	96.72
	$G_{T_zR_x}$	pN·nm	29.54	69.91	38.86	113.77
	$G_{T_zR_y}$	pN·nm	-3.99	29.36	-7.00	-22.86
	$G_{T_zR_z}$	pN·nm	-41.10	-64.43	-65.35	9.65
	$G_{R_xR_y}$	pN·nm^2	45.79	43.07	27.55	30.64
	$G_{R_xR_z}$	pN·nm^2	-11.51	-10.29	-13.37	12.33
	$G_{R_yR_z}$	pN·nm^2	8.07	-6.05	4.43	16.63
σ	S	pN	149.76	214.21	183.11	197.15
	Y_y	pN	39.33	34.76	52.51	47.51
	Y_z	pN	18.69	35.78	24.47	41.49
	Y	pN	19.17	25.34	25.69	32.03
	C	pN·nm^2	10.07	17.21	10.20	14.87
	B_y	pN·nm^2	13.19	18.82	18.02	17.78
	B_z	pN·nm^2	17.16	29.84	22.57	27.31
	B	pN·nm^2	10.75	17.00	14.39	15.63
	$G_{T_xT_y}$	pN	8.64	14.30	11.49	2.01
	$G_{T_xT_z}$	pN	2.23	10.35	3.41	5.94
	$G_{T_xR_x}$	pN·nm	11.21	13.75	17.01	10.86
	$G_{T_xR_y}$	pN·nm	7.81	1.60	13.57	1.50
	$G_{T_xR_z}$	pN·nm	2.21	30.29	6.20	23.74
	$G_{T_yT_z}$	pN	0.09	4.84	4.66	10.33
	$G_{T_yR_x}$	pN·nm	10.05	11.91	8.68	10.84
	$G_{T_yR_y}$	pN·nm	4.81	1.84	3.62	3.80
	$G_{T_yR_z}$	pN·nm	4.55	8.40	7.35	9.33
	$G_{T_zR_x}$	pN·nm	2.83	7.10	4.78	10.97
	$G_{T_zR_y}$	pN·nm	0.38	2.98	0.86	2.20
	$G_{T_zR_z}$	pN·nm	3.93	6.54	8.03	0.93
	$G_{R_xR_y}$	pN·nm^2	4.38	4.37	3.39	2.95
	$G_{R_xR_z}$	pN·nm^2	1.10	1.04	1.64	1.19
	$G_{R_yR_z}$	pN·nm^2	0.77	0.61	0.54	1.60

Table A-14. Sequence-dependent mechanical properties of junction nick.

Properties		Units	AA/TnT	AC/GnT	AG/CnT	AT/AnT
μ	S	pN	2195.22	2230.92	2070.55	2599.10
	Y_y	pN	823.15	913.39	631.01	956.47
	Y_z	pN	587.13	455.27	501.62	430.24
	Y	pN	637.77	559.68	531.00	566.85
	C	pN·nm^2	255.05	194.77	220.41	249.24
	B_y	pN·nm^2	211.86	206.41	222.26	246.50
	B_z	pN·nm^2	307.16	227.46	310.52	273.07
	B	pN·nm^2	243.15	202.78	251.16	255.51
	$G_{T_xT_y}$	pN	85.66	489.05	138.27	472.45
	$G_{T_xT_z}$	pN	-121.18	-96.47	-88.14	-11.93
	$G_{T_xR_x}$	pN·nm	-128.30	-113.49	-124.02	-97.78
	$G_{T_xR_y}$	pN·nm	-3.04	163.88	-11.59	146.61
	$G_{T_xR_z}$	pN·nm	339.21	-35.78	319.36	-6.78
	$G_{T_yT_z}$	pN	-47.25	-3.62	-52.21	-9.59
	$G_{T_yR_x}$	pN·nm	-225.71	-63.71	-146.97	-97.43
	$G_{T_yR_y}$	pN·nm	-26.47	30.19	-12.71	-30.83
	$G_{T_yR_z}$	pN·nm	-18.50	21.99	-4.84	-7.05
	$G_{T_zR_x}$	pN·nm	-18.09	21.42	-26.24	2.70
	$G_{T_zR_y}$	pN·nm	-23.76	7.67	-41.81	-2.31
	$G_{T_zR_z}$	pN·nm	-45.13	4.88	-48.93	2.10
	$G_{R_xR_y}$	pN·nm^2	24.92	9.96	13.19	31.69
	$G_{R_xR_z}$	pN·nm^2	-22.52	-21.23	-15.83	-1.30
	$G_{R_yR_z}$	pN·nm^2	-7.92	-33.26	-21.17	-7.42
σ	S	pN	441.00	865.37	454.29	368.19
	Y_y	pN	345.57	470.67	208.88	351.38
	Y_z	pN	226.62	193.81	152.84	105.35
	Y	pN	213.70	215.11	136.01	132.90
	C	pN·nm^2	138.75	103.33	85.98	89.67
	B_y	pN·nm^2	53.46	75.88	47.73	43.45
	B_z	pN·nm^2	73.09	88.70	84.66	46.21
	B	pN·nm^2	47.28	64.33	46.37	32.93
	$G_{T_xT_y}$	pN	95.10	205.99	98.52	160.53

Table A-14 (Continued)

Properties		Units	AA/TnT	AC/GnT	AG/CnT	AT/AnT
σ	$G_{T_xT_z}$	pN	91.04	101.63	115.13	45.92
	$G_{T_xR_x}$	pN·nm	53.36	69.56	61.27	45.17
	$G_{T_xR_y}$	pN·nm	49.24	95.64	53.44	61.08
	$G_{T_xR_z}$	pN·nm	130.60	66.56	130.53	60.25
	$G_{T_yT_z}$	pN	84.96	77.54	77.35	88.78
	$G_{T_yR_x}$	pN·nm	137.55	81.48	79.52	83.08
	$G_{T_yR_y}$	pN·nm	50.93	41.80	38.11	46.89
	$G_{T_yR_z}$	pN·nm	77.70	63.53	66.08	47.48
	$G_{T_zR_x}$	pN·nm	71.04	76.03	71.63	54.11
	$G_{T_zR_y}$	pN·nm	32.42	35.70	46.63	35.54
	$G_{T_zR_z}$	pN·nm	37.42	22.39	45.80	23.94
	$G_{R_xR_y}$	pN·nm^2	20.82	20.36	19.54	24.04
	$G_{R_xR_z}$	pN·nm^2	22.52	19.41	28.17	18.27
	$G_{R_yR_z}$	pN·nm^2	13.23	19.87	19.79	18.02
Properties		Units	CA/TnG	CC/GnG	CG/CnG	CT/AnG
μ	S	pN	1447.67	2074.95	1456.52	2089.43
	Y_y	pN	697.52	614.53	636.25	716.99
	Y_z	pN	360.82	547.96	409.95	507.96
	Y	pN	447.46	536.61	477.14	560.38
	C	pN·nm^2	192.65	201.41	190.83	287.07
	B_y	pN·nm^2	160.54	198.07	162.39	220.37
	B_z	pN·nm^2	199.80	318.19	208.45	314.75
	B	pN·nm^2	172.99	237.00	180.40	250.91
	$G_{T_xT_y}$	pN	56.59	130.93	52.29	152.55
	$G_{T_xT_z}$	pN	-15.99	26.06	60.69	48.40
	$G_{T_xR_x}$	pN·nm	-118.60	-157.58	-122.68	-132.59
	$G_{T_xR_y}$	pN·nm	-82.15	-29.85	-69.66	-19.25
	$G_{T_xR_z}$	pN·nm	-10.86	-322.28	-0.12	-304.12
	$G_{T_yT_z}$	pN	-22.69	14.77	-44.39	51.07
	$G_{T_yR_x}$	pN·nm	-115.70	-104.78	-120.34	-198.56
	$G_{T_yR_y}$	pN·nm	16.44	21.10	-16.23	-6.24

Table A-14 (Continued)

Properties		Units	CA/TnG	CC/GnG	CG/CnG	CT/AnG
μ	$G_{T_yR_z}$	pN·nm	0.26	5.54	-15.45	13.89
	$G_{T_zR_x}$	pN·nm	19.70	55.97	9.72	90.51
	$G_{T_zR_y}$	pN·nm	-2.87	3.62	-4.00	40.63
	$G_{T_zR_z}$	pN·nm	-60.52	-93.97	-71.46	-45.92
	$G_{R_xR_y}$	pN·nm^2	27.91	16.48	28.37	13.09
	$G_{R_xR_z}$	pN·nm^2	-10.43	1.41	10.48	21.93
	$G_{R_yR_z}$	pN·nm^2	-3.48	-16.76	-5.97	25.90
σ	S	pN	360.64	500.29	274.90	541.00
	Y_y	pN	260.55	244.56	180.45	271.73
	Y_z	pN	132.54	234.00	136.56	142.98
	Y	pN	137.85	185.12	121.99	150.07
	C	pN·nm^2	88.65	84.46	70.02	112.86
	B_y	pN·nm^2	38.06	54.66	28.03	52.82
	B_z	pN·nm^2	45.56	62.97	34.92	87.45
	B	pN·nm^2	31.31	47.61	22.98	50.28
	$G_{T_xT_y}$	pN	102.76	120.20	91.06	93.57
	$G_{T_xT_z}$	pN	60.66	121.65	73.88	85.63
	$G_{T_xR_x}$	pN·nm	54.41	80.77	34.68	56.21
	$G_{T_xR_y}$	pN·nm	53.64	61.81	59.47	56.07
	$G_{T_xR_z}$	pN·nm	33.25	135.66	48.77	130.08
	$G_{T_yT_z}$	pN	77.30	105.31	75.48	99.91
	$G_{T_yR_x}$	pN·nm	73.69	99.70	62.36	80.25
	$G_{T_yR_y}$	pN·nm	32.02	33.79	29.86	38.02
	$G_{T_yR_z}$	pN·nm	58.33	75.05	37.91	59.12
	$G_{T_zR_x}$	pN·nm	45.22	79.41	46.52	80.67
	$G_{T_zR_y}$	pN·nm	24.22	39.09	26.55	46.86
	$G_{T_zR_z}$	pN·nm	37.80	51.87	27.80	39.91
	$G_{R_xR_y}$	pN·nm^2	18.56	21.44	13.64	18.71
	$G_{R_xR_z}$	pN·nm^2	23.53	37.56	18.72	30.44
	$G_{R_yR_z}$	pN·nm^2	12.60	17.76	10.33	18.38

Table A-14 (Continued)

Properties		Units	GA/TnC	GC/GnC	GG/CnC	GT/AnC
μ	S	pN	2300.87	2082.32	1997.23	2541.77
	Y_y	pN	830.94	755.62	593.98	925.42
	Y_z	pN	482.96	605.17	457.39	407.23
	Y	pN	571.16	628.37	477.96	551.52
	C	pN·nm^2	243.84	298.14	244.43	233.42
	B_y	pN·nm^2	201.95	297.10	180.77	205.32
	B_z	pN·nm^2	299.08	309.30	299.06	276.78
	B	pN·nm^2	237.17	280.02	220.21	233.31
	$G_{T_xT_y}$	pN	102.52	445.31	100.38	561.21
	$G_{T_xT_z}$	pN	-164.36	8.61	-79.30	67.67
	$G_{T_xR_x}$	pN·nm	-148.56	-169.65	-113.65	-154.90
	$G_{T_xR_y}$	pN·nm	-5.29	186.39	-10.47	92.24
	$G_{T_xR_z}$	pN·nm	371.45	1.66	303.05	53.09
	$G_{T_yT_z}$	pN	-66.36	19.91	-25.68	-16.46
	$G_{T_yR_x}$	pN·nm	-217.52	-143.03	-78.82	-92.48
	$G_{T_yR_y}$	pN·nm	17.89	78.63	37.62	4.87
	$G_{T_yR_z}$	pN·nm	-26.14	-11.69	-37.25	-34.57
	$G_{T_zR_x}$	pN·nm	-12.45	-25.98	-46.56	-4.27
	$G_{T_zR_y}$	pN·nm	-6.46	12.44	-22.35	1.17
	$G_{T_zR_z}$	pN·nm	-75.63	-86.94	-93.59	-32.77
	$G_{R_xR_y}$	pN·nm^2	39.01	0.27	12.10	34.59
	$G_{R_xR_z}$	pN·nm^2	-9.84	14.25	11.14	26.54
	$G_{R_yR_z}$	pN·nm^2	17.06	-7.55	8.51	26.21
σ	S	pN	576.03	1019.25	409.07	294.14
	Y_y	pN	516.05	352.28	343.12	200.68
	Y_z	pN	156.73	168.33	134.43	106.45
	Y	pN	201.80	192.17	166.20	112.67
	C	pN·nm^2	92.63	117.14	79.24	64.24
	B_y	pN·nm^2	37.33	138.70	40.81	29.75
	B_z	pN·nm^2	60.46	115.50	67.77	42.31
	B	pN·nm^2	33.97	99.70	38.58	25.55
	$G_{T_xT_y}$	pN	122.27	248.30	140.91	98.16

Table A-14 (Continued)

Properties		Units	GA/TnC	GC/GnC	GG/CnC	GT/AnC
σ	$G_{T_xT_z}$	pN	112.50	61.98	107.94	81.75
	$G_{T_xR_x}$	pN·nm	63.49	88.53	55.83	52.09
	$G_{T_xR_y}$	pN·nm	58.77	117.34	109.34	77.60
	$G_{T_xR_z}$	pN·nm	131.47	53.49	186.10	65.68
	$G_{T_yT_z}$	pN	124.41	99.84	122.69	107.31
	$G_{T_yR_x}$	pN·nm	120.20	104.24	177.39	72.89
	$G_{T_yR_y}$	pN·nm	74.73	54.75	36.15	58.00
	$G_{T_yR_z}$	pN·nm	70.71	48.79	89.57	23.00
	$G_{T_zR_x}$	pN·nm	60.67	75.28	118.78	69.04
	$G_{T_zR_y}$	pN·nm	42.08	36.24	47.11	41.05
	$G_{T_zR_z}$	pN·nm	34.89	31.95	52.38	31.88
	$G_{R_xR_y}$	pN·nm^2	28.45	22.25	24.37	33.86
	$G_{R_xR_z}$	pN·nm^2	38.16	29.93	39.17	21.98
	$G_{R_yR_z}$	pN·nm^2	15.69	26.58	16.22	13.35
Properties		Units	TA/TnA	TC/GnA	TG/CnA	TT/AnA
μ	S	pN	1469.22	2130.40	1486.14	2218.12
	Y_y	pN	713.66	643.31	674.46	768.67
	Y_z	pN	343.46	463.40	356.06	550.67
	Y	pN	436.53	507.03	438.29	607.21
	C	pN·nm^2	247.48	221.32	195.24	257.87
	B_y	pN·nm^2	149.89	192.88	153.60	216.17
	B_z	pN·nm^2	190.19	259.95	206.44	293.67
	B	pN·nm^2	165.19	210.31	173.42	243.84
	$G_{T_xT_y}$	pN	45.79	135.04	84.41	49.48
	$G_{T_xT_z}$	pN	-10.04	86.96	17.51	89.87
	$G_{T_xR_x}$	pN·nm	-104.93	-130.55	-134.52	-137.58
	$G_{T_xR_y}$	pN·nm	-64.99	8.27	-65.64	-27.89
	$G_{T_xR_z}$	pN·nm	13.35	-325.98	17.34	-319.72
	$G_{T_yT_z}$	pN	35.33	42.40	2.87	72.69
	$G_{T_yR_x}$	pN·nm	-169.46	-187.00	-121.57	-236.94
	$G_{T_yR_y}$	pN·nm	34.37	7.72	25.06	-22.48

Table A-14 (Continued)

Properties		Units	TA/TnA	TC/GnA	TG/CnA	TT/AnA
μ	$G_{T_yR_z}$	pN·nm	1.59	6.05	0.75	20.79
	$G_{T_zR_x}$	pN·nm	13.15	34.73	0.35	34.69
	$G_{T_zR_y}$	pN·nm	-4.04	19.82	14.07	30.69
	$G_{T_zR_z}$	pN·nm	-47.75	-57.94	-64.50	-39.95
	$G_{R_xR_y}$	pN·nm^2	46.20	25.76	27.95	27.29
	$G_{R_xR_z}$	pN·nm^2	0.85	8.84	9.75	22.02
	$G_{R_yR_z}$	pN·nm^2	-0.29	-23.91	-0.75	16.04
σ	S	pN	265.25	782.31	238.01	403.66
	Y_y	pN	271.40	248.26	272.07	258.47
	Y_z	pN	130.59	150.99	108.77	153.68
	Y	pN	141.87	146.39	125.16	151.77
	C	pN·nm^2	88.39	101.02	74.59	112.06
	B_y	pN·nm^2	26.55	52.64	28.47	42.77
	B_z	pN·nm^2	28.52	96.62	29.39	55.02
	B	pN·nm^2	20.41	54.70	22.23	35.42
	$G_{T_xT_y}$	pN	89.59	99.60	101.83	131.90
	$G_{T_xT_z}$	pN	103.25	104.52	54.23	59.62
	$G_{T_xR_x}$	pN·nm	49.10	73.88	29.94	45.59
	$G_{T_xR_y}$	pN·nm	34.48	52.34	35.80	58.68
	$G_{T_xR_z}$	pN·nm	49.08	188.09	38.83	99.88
	$G_{T_yT_z}$	pN	171.66	70.32	63.11	86.19
	$G_{T_yR_x}$	pN·nm	95.12	109.61	68.52	116.36
	$G_{T_yR_y}$	pN·nm	36.91	32.29	31.68	46.81
	$G_{T_yR_z}$	pN·nm	47.08	57.49	43.21	65.32
	$G_{T_zR_x}$	pN·nm	49.80	79.71	60.83	64.48
	$G_{T_zR_y}$	pN·nm	29.40	48.08	25.60	35.86
	$G_{T_zR_z}$	pN·nm	25.75	46.56	30.02	35.11
	$G_{R_xR_y}$	pN·nm^2	21.96	29.93	16.05	19.35
	$G_{R_xR_z}$	pN·nm^2	26.52	28.65	16.73	25.44
	$G_{R_yR_z}$	pN·nm^2	11.37	21.21	12.26	16.49

Table A-15. Sequence-dependent mechanical properties of double junction.

Properties		Units	AA||TT	AC||GT	AG||CT	AT||AT
μ	S	pN	3456.93	4412.75	3739.70	4590.27
	Y_y	pN	1314.94	1438.34	1229.64	1269.53
	Y_z	pN	511.69	771.54	602.51	610.94
	Y	pN	697.47	979.10	781.51	781.23
	C	pN·nm^2	426.47	468.10	422.26	451.38
	B_y	pN·nm^2	389.64	466.59	432.40	426.03
	B_z	pN·nm^2	463.41	621.35	608.94	620.87
	B	pN·nm^2	397.87	501.11	466.74	465.56
	$G_{T_xT_y}$	pN	1050.19	1321.15	888.98	994.96
	$G_{T_xT_z}$	pN	395.20	781.93	665.46	508.09
	$G_{T_xR_x}$	pN·nm	41.53	133.62	27.83	25.52
	$G_{T_xR_y}$	pN·nm	89.22	-30.75	55.66	70.86
	$G_{T_xR_z}$	pN·nm	-439.85	-1014.43	-854.43	-902.54
	$G_{T_yT_z}$	pN	191.03	291.89	191.74	160.27
	$G_{T_yR_x}$	pN·nm	25.18	46.30	8.33	34.15
	$G_{T_yR_y}$	pN·nm	-20.96	-26.33	-36.68	46.56
	$G_{T_yR_z}$	pN·nm	-145.43	-406.33	-231.91	-278.55
	$G_{T_zR_x}$	pN·nm	125.28	150.96	112.93	128.26
	$G_{T_zR_y}$	pN·nm	6.48	79.24	28.79	54.47
	$G_{T_zR_z}$	pN·nm	-60.94	-191.83	-175.87	-103.41
	$G_{R_xR_y}$	pN·nm^2	-20.34	19.57	-10.25	4.75
	$G_{R_xR_z}$	pN·nm^2	10.01	-11.21	0.09	0.18
	$G_{R_yR_z}$	pN·nm^2	-35.75	12.92	-18.90	-27.02
σ	S	pN	1452.91	1843.47	2043.13	2499.36
	Y_y	pN	506.82	256.92	289.20	491.45
	Y_z	pN	149.32	208.23	190.76	184.22
	Y	pN	189.40	193.87	191.57	216.49
	C	pN·nm^2	101.30	101.12	92.62	121.70
	B_y	pN·nm^2	111.54	105.10	162.40	156.76
	B_z	pN·nm^2	217.36	337.27	357.86	396.33
	B	pN·nm^2	123.16	152.38	176.56	181.08
	$G_{T_xT_y}$	pN	515.44	530.50	343.48	580.18

Table A-15 (Continued)

Properties		Units	AA||TT	AC||GT	AG||CT	AT||AT
σ	$G_{T_xT_z}$	pN	251.93	444.45	404.23	389.43
	$G_{T_xR_x}$	pN·nm	153.91	113.40	146.01	134.07
	$G_{T_xR_y}$	pN·nm	228.86	148.38	113.32	143.19
	$G_{T_xR_z}$	pN·nm	384.82	725.60	808.64	814.69
	$G_{T_yT_z}$	pN	122.04	116.47	98.44	128.86
	$G_{T_yR_x}$	pN·nm	104.83	58.37	54.18	82.98
	$G_{T_yR_y}$	pN·nm	105.18	104.40	69.04	91.47
	$G_{T_yR_z}$	pN·nm	169.15	252.40	202.15	233.85
	$G_{T_zR_x}$	pN·nm	55.49	55.41	44.08	53.70
	$G_{T_zR_y}$	pN·nm	51.36	68.12	38.41	71.66
	$G_{T_zR_z}$	pN·nm	69.18	185.88	143.44	112.01
	$G_{R_xR_y}$	pN·nm^2	50.85	31.64	24.17	42.33
	$G_{R_xR_z}$	pN·nm^2	61.57	39.51	59.12	46.02
	$G_{R_yR_z}$	pN·nm^2	72.07	104.54	46.23	33.64
Properties		Units	CA||TG	CC||GG	CG||CG	CT||AG
μ	S	pN	2498.80	3464.00	3250.62	4108.40
	Y_y	pN	1175.55	1808.96	1291.74	1303.96
	Y_z	pN	516.59	780.45	685.33	713.20
	Y	pN	666.12	1031.83	854.20	863.29
	C	pN·nm^2	328.79	442.34	389.81	438.30
	B_y	pN·nm^2	314.70	423.95	429.60	395.02
	B_z	pN·nm^2	374.55	515.19	496.65	474.09
	B	pN·nm^2	315.98	434.41	435.65	405.30
	$G_{T_xT_y}$	pN	598.05	1302.07	1008.64	884.19
	$G_{T_xT_z}$	pN	392.26	663.63	654.15	598.76
	$G_{T_xR_x}$	pN·nm	57.74	135.46	131.75	140.76
	$G_{T_xR_y}$	pN·nm	-51.63	-106.21	-72.13	-118.29
	$G_{T_xR_z}$	pN·nm	-260.14	-544.41	-608.87	-699.51
	$G_{T_yT_z}$	pN	215.05	377.32	291.40	236.31
	$G_{T_yR_x}$	pN·nm	15.27	138.69	96.40	52.27
	$G_{T_yR_y}$	pN·nm	-70.80	-54.16	-54.66	-22.98

Table A-15 (Continued)

Properties		Units	CA||TG	CC||GG	CG||CG	CT||AG
μ	$G_{T_yR_z}$	pN·nm	-85.92	-299.68	-194.18	-138.46
	$G_{T_zR_x}$	pN·nm	94.90	202.40	135.75	168.22
	$G_{T_zR_y}$	pN·nm	-10.08	-19.70	-31.72	-42.27
	$G_{T_zR_z}$	pN·nm	-55.46	-116.47	-124.14	-126.38
	$G_{R_xR_y}$	pN·nm^2	-7.80	6.46	-16.30	-22.25
	$G_{R_xR_z}$	pN·nm^2	-3.29	-19.84	-17.36	-31.60
	$G_{R_yR_z}$	pN·nm^2	15.30	-2.42	10.65	-9.97
σ	S	pN	1464.21	1714.97	1377.01	1798.51
	Y_y	pN	554.81	664.78	352.99	486.30
	Y_z	pN	183.57	269.08	227.06	259.08
	Y	pN	226.38	305.05	223.14	265.71
	C	pN·nm^2	113.46	86.65	93.79	78.14
	B_y	pN·nm^2	114.48	131.46	109.47	114.82
	B_z	pN·nm^2	226.96	339.87	301.92	331.37
	B	pN·nm^2	123.46	161.48	146.90	149.60
	$G_{T_xT_y}$	pN	352.30	651.75	377.32	309.31
	$G_{T_xT_z}$	pN	310.37	348.05	329.73	495.57
	$G_{T_xR_x}$	pN·nm	153.98	89.23	108.64	135.13
	$G_{T_xR_y}$	pN·nm	87.55	168.62	189.92	247.77
	$G_{T_xR_z}$	pN·nm	597.38	682.27	600.42	681.14
	$G_{T_yT_z}$	pN	189.15	185.18	118.62	86.72
	$G_{T_yR_x}$	pN·nm	46.14	115.63	76.45	88.51
	$G_{T_yR_y}$	pN·nm	65.65	110.67	88.13	84.62
	$G_{T_yR_z}$	pN·nm	160.95	277.04	193.77	174.80
	$G_{T_zR_x}$	pN·nm	40.51	66.08	35.99	46.75
	$G_{T_zR_y}$	pN·nm	61.51	53.43	55.80	82.40
	$G_{T_zR_z}$	pN·nm	96.48	151.48	100.95	161.81
	$G_{R_xR_y}$	pN·nm^2	30.23	32.19	42.94	43.67
	$G_{R_xR_z}$	pN·nm^2	50.74	56.20	46.69	66.93
	$G_{R_yR_z}$	pN·nm^2	37.38	46.08	56.71	65.33

Table A-15 (Continued)

Properties		Units	GA||TC	GC||GC	GG||CC	GT||AC
μ	S	pN	2756.67	1934.72	3451.36	4277.55
	Y_y	pN	1147.74	1390.63	1483.46	1330.23
	Y_z	pN	518.09	454.94	564.61	593.91
	Y	pN	670.70	643.69	765.08	767.02
	C	pN·nm^2	372.74	352.16	396.72	393.42
	B_y	pN·nm^2	396.90	309.33	409.20	399.83
	B_z	pN·nm^2	384.76	337.57	485.71	493.06
	B	pN·nm^2	360.23	300.25	408.98	406.54
	$G_{T_xT_y}$	pN	908.64	769.55	1126.10	1019.27
	$G_{T_xT_z}$	pN	474.78	284.01	554.76	578.12
	$G_{T_xR_x}$	pN·nm	-8.09	30.91	42.62	21.22
	$G_{T_xR_y}$	pN·nm	-17.22	-78.46	0.55	11.05
	$G_{T_xR_z}$	pN·nm	-359.91	-116.94	-474.35	-562.53
	$G_{T_yT_z}$	pN	240.99	184.38	237.78	250.07
	$G_{T_yR_x}$	pN·nm	46.68	60.39	47.20	35.84
	$G_{T_yR_y}$	pN·nm	-30.57	-86.86	-37.32	-10.41
	$G_{T_yR_z}$	pN·nm	-169.23	-33.45	-154.23	-187.16
	$G_{T_zR_x}$	pN·nm	59.62	93.23	73.25	93.76
	$G_{T_zR_y}$	pN·nm	10.47	16.60	14.82	50.73
	$G_{T_zR_z}$	pN·nm	-77.48	-37.97	-103.86	-124.59
	$G_{R_xR_y}$	pN·nm^2	8.50	18.63	-5.48	15.70
	$G_{R_xR_z}$	pN·nm^2	7.48	0.64	-24.47	-21.43
	$G_{R_yR_z}$	pN·nm^2	-4.95	-27.72	-23.00	-17.32
σ	S	pN	1414.26	1162.72	1952.68	1911.05
	Y_y	pN	485.86	671.02	621.60	551.67
	Y_z	pN	174.18	145.28	248.42	232.10
	Y	pN	210.10	203.09	287.77	260.72
	C	pN·nm^2	85.27	134.38	96.51	76.48
	B_y	pN·nm^2	138.83	89.23	137.37	152.44
	B_z	pN·nm^2	204.99	183.50	261.28	240.65
	B	pN·nm^2	133.95	102.71	146.79	146.99
	$G_{T_xT_y}$	pN	475.71	442.59	546.72	559.97

Table A-15 (Continued)

Properties		Units	GA||TC	GC||GC	GG||CC	GT||AC
σ	$G_{T_xT_z}$	pN	352.55	226.04	401.49	527.42
	$G_{T_xR_x}$	pN·nm	132.17	130.90	113.47	133.62
	$G_{T_xR_y}$	pN·nm	133.73	127.01	206.85	226.05
	$G_{T_xR_z}$	pN·nm	481.95	481.74	524.83	706.55
	$G_{T_yT_z}$	pN	141.85	166.43	197.90	200.75
	$G_{T_yR_x}$	pN·nm	70.31	111.04	118.18	75.26
	$G_{T_yR_y}$	pN·nm	83.08	76.92	131.43	92.68
	$G_{T_yR_z}$	pN·nm	163.73	265.89	206.47	220.77
	$G_{T_zR_x}$	pN·nm	69.62	100.31	74.07	69.50
	$G_{T_zR_y}$	pN·nm	62.35	86.53	59.60	71.45
	$G_{T_zR_z}$	pN·nm	88.07	102.85	103.02	115.47
	$G_{R_xR_y}$	pN·nm^2	41.78	40.34	49.81	40.23
	$G_{R_xR_z}$	pN·nm^2	42.75	59.64	70.81	44.05
	$G_{R_yR_z}$	pN·nm^2	57.72	36.23	61.95	62.07
Properties		Units	TA||TA	TC||GA	TG||CA	TT||AA
μ	S	pN	3707.03	5046.92	3699.01	4331.94
	Y_y	pN	1184.73	1794.25	1292.45	1441.90
	Y_z	pN	631.59	811.04	542.52	691.46
	Y	pN	782.47	1088.29	725.40	891.59
	C	pN·nm^2	437.86	461.26	386.87	445.50
	B_y	pN·nm^2	413.15	439.42	355.37	422.84
	B_z	pN·nm^2	590.67	777.84	504.02	599.13
	B	pN·nm^2	448.30	524.44	387.39	462.32
	$G_{T_xT_y}$	pN	890.67	1638.50	1172.22	1166.04
	$G_{T_xT_z}$	pN	520.58	659.62	502.18	511.41
	$G_{T_xR_x}$	pN·nm	119.64	182.92	148.27	95.45
	$G_{T_xR_y}$	pN·nm	-65.76	-47.27	20.46	30.18
	$G_{T_xR_z}$	pN·nm	-759.82	-1277.93	-607.48	-745.79
	$G_{T_yT_z}$	pN	254.48	346.31	226.25	228.25
	$G_{T_yR_x}$	pN·nm	77.32	107.15	67.88	85.19
	$G_{T_yR_y}$	pN·nm	-30.72	56.92	8.32	25.12

Table A-15 (Continued)

Properties		Units	TA||TA	TC||GA	TG||CA	TT||AA
μ	$G_{T_yR_z}$	pN·nm	-225.96	-434.01	-229.69	-295.91
	$G_{T_zR_x}$	pN·nm	129.53	175.94	124.13	144.55
	$G_{T_zR_y}$	pN·nm	-23.42	-5.65	-7.34	16.43
	$G_{T_zR_z}$	pN·nm	-83.51	-149.31	-69.95	-83.95
	$G_{R_xR_y}$	pN·nm^2	3.07	24.78	-12.47	14.16
	$G_{R_xR_z}$	pN·nm^2	3.17	-17.70	7.00	-1.76
	$G_{R_yR_z}$	pN·nm^2	-18.43	-29.69	-38.57	-35.68
σ	S	pN	1790.24	2240.80	2095.43	1984.23
	Y_y	pN	355.98	500.15	487.93	491.17
	Y_z	pN	218.06	195.06	175.17	192.64
	Y	pN	216.28	218.35	206.66	219.53
	C	pN·nm^2	80.06	82.41	123.45	87.11
	B_y	pN·nm^2	139.96	101.21	123.21	118.20
	B_z	pN·nm^2	339.11	452.05	358.07	341.71
	B	pN·nm^2	162.24	160.72	151.58	153.90
	$G_{T_xT_y}$	pN	499.48	884.87	607.78	577.64
	$G_{T_xT_z}$	pN	370.44	421.40	281.54	365.66
	$G_{T_xR_x}$	pN·nm	139.77	151.49	135.46	97.48
	$G_{T_xR_y}$	pN·nm	192.57	166.74	162.94	209.03
	$G_{T_xR_z}$	pN·nm	633.56	977.02	753.12	700.32
	$G_{T_yT_z}$	pN	110.22	184.71	108.59	114.59
	$G_{T_yR_x}$	pN·nm	87.09	77.58	72.30	84.71
	$G_{T_yR_y}$	pN·nm	69.83	89.26	74.30	97.63
	$G_{T_yR_z}$	pN·nm	167.21	321.96	207.13	228.11
	$G_{T_zR_x}$	pN·nm	59.32	77.49	59.10	65.09
	$G_{T_zR_y}$	pN·nm	57.68	100.69	64.65	48.21
	$G_{T_zR_z}$	pN·nm	98.32	168.24	84.26	123.59
	$G_{R_xR_y}$	pN·nm^2	41.34	42.03	42.52	38.58
	$G_{R_xR_z}$	pN·nm^2	69.51	92.33	47.80	56.53
	$G_{R_yR_z}$	pN·nm^2	59.24	71.42	38.88	59.46

Table A-16. Sequence-dependent mechanical properties of single junction.

Properties		Units	AA|TT	AC|GT	AG|CT	AT|AT
μ	S	pN	2317.71	1592.49	1585.48	1954.40
	Y_y	pN	1356.71	1459.28	1544.07	1316.81
	Y_z	pN	485.59	420.39	504.54	380.50
	Y	pN	687.70	642.42	756.26	586.12
	C	pN·nm^2	380.88	335.81	319.95	324.86
	B_y	pN·nm^2	325.21	266.72	243.46	247.81
	B_z	pN·nm^2	236.85	316.47	356.06	230.30
	B	pN·nm^2	262.17	287.95	283.58	235.80
	$G_{T_xT_y}$	pN	835.29	893.40	1000.11	998.22
	$G_{T_xT_z}$	pN	435.12	338.40	442.50	240.92
	$G_{T_xR_x}$	pN·nm	-20.26	49.77	49.04	37.80
	$G_{T_xR_y}$	pN·nm	63.91	-102.87	-67.17	-6.18
	$G_{T_xR_z}$	pN·nm	-0.25	190.42	70.11	-16.36
	$G_{T_yT_z}$	pN	161.41	78.10	151.08	85.05
	$G_{T_yR_x}$	pN·nm	27.22	-28.92	106.64	58.62
	$G_{T_yR_y}$	pN·nm	25.83	-27.22	-43.96	33.88
	$G_{T_yR_z}$	pN·nm	-37.77	80.42	-137.97	36.72
	$G_{T_zR_x}$	pN·nm	101.60	114.62	41.20	112.22
	$G_{T_zR_y}$	pN·nm	22.42	21.18	45.60	1.74
	$G_{T_zR_z}$	pN·nm	39.76	64.22	-4.75	38.93
	$G_{R_xR_y}$	pN·nm^2	8.29	17.93	15.32	-0.10
	$G_{R_xR_z}$	pN·nm^2	21.11	-14.59	-38.02	-16.21
	$G_{R_yR_z}$	pN·nm^2	-30.70	-14.59	-4.69	-5.93
σ	S	pN	314.81	222.43	115.71	192.13
	Y_y	pN	437.18	211.64	170.71	164.81
	Y_z	pN	131.95	112.40	51.40	55.29
	Y	pN	163.36	136.91	61.52	69.11
	C	pN·nm^2	64.71	15.31	88.33	51.46
	B_y	pN·nm^2	45.70	35.75	63.18	27.45
	B_z	pN·nm^2	115.17	18.70	19.41	42.77
	B	pN·nm^2	79.94	22.74	47.62	27.12
	$G_{T_xT_y}$	pN	235.57	185.85	68.00	105.19

Table A-16 (Continued)

Properties		Units	AA|TT	AC|GT	AG|CT	AT|AT
σ	$G_{T_xT_z}$	pN	268.34	100.74	119.13	82.96
	$G_{T_xR_x}$	pN·nm	60.90	57.37	2.96	28.82
	$G_{T_xR_y}$	pN·nm	64.47	20.58	11.39	65.67
	$G_{T_xR_z}$	pN·nm	99.88	110.90	94.79	46.69
	$G_{T_yT_z}$	pN	134.50	75.95	92.58	94.16
	$G_{T_yR_x}$	pN·nm	72.68	42.52	13.65	38.53
	$G_{T_yR_y}$	pN·nm	36.67	17.68	25.25	58.48
	$G_{T_yR_z}$	pN·nm	102.41	4.75	70.71	108.04
	$G_{T_zR_x}$	pN·nm	41.67	4.98	45.17	35.77
	$G_{T_zR_y}$	pN·nm	25.56	13.16	32.14	18.17
	$G_{T_zR_z}$	pN·nm	42.32	8.44	14.48	20.86
	$G_{R_xR_y}$	pN·nm^2	29.29	40.53	23.65	15.43
	$G_{R_xR_z}$	pN·nm^2	19.70	11.06	5.61	36.75
	$G_{R_yR_z}$	pN·nm^2	48.68	7.30	8.76	20.62
Properties		Units	CA|TG	CC|GG	CG|CG	CT|AG
μ	S	pN	1523.45	4543.50	2236.64	2537.98
	Y_y	pN	983.83	1653.93	1234.10	1389.65
	Y_z	pN	304.35	1048.78	538.01	491.88
	Y	pN	461.43	1190.13	724.28	695.20
	C	pN·nm^2	316.49	335.45	297.59	361.19
	B_y	pN·nm^2	269.93	375.58	397.47	306.42
	B_z	pN·nm^2	181.32	504.85	195.36	323.69
	B	pN·nm^2	210.05	396.57	254.98	299.64
	$G_{T_xT_y}$	pN	700.22	1684.91	1110.57	1104.15
	$G_{T_xT_z}$	pN	166.99	1245.60	401.52	195.24
	$G_{T_xR_x}$	pN·nm	-106.92	83.77	-55.31	49.59
	$G_{T_xR_y}$	pN·nm	99.16	-105.92	-33.80	40.45
	$G_{T_xR_z}$	pN·nm	-37.92	-741.52	-219.75	-112.23
	$G_{T_yT_z}$	pN	-70.98	490.44	76.05	72.73
	$G_{T_yR_x}$	pN·nm	-100.98	10.43	2.20	-27.74
	$G_{T_yR_y}$	pN·nm	89.28	-144.03	-29.51	65.13

Table A-16 (Continued)

Properties		Units	CA|TG	CC|GG	CG|CG	CT|AG
μ	$G_{T_yR_z}$	pN·nm	-121.37	-467.10	-143.12	-80.48
	$G_{T_zR_x}$	pN·nm	114.21	67.74	48.13	99.06
	$G_{T_zR_y}$	pN·nm	23.46	-33.68	-31.70	4.21
	$G_{T_zR_z}$	pN·nm	7.81	-255.51	-22.11	-6.27
	$G_{R_xR_y}$	pN·nm^2	-36.67	-16.79	-31.75	-12.64
	$G_{R_xR_z}$	pN·nm^2	21.79	5.12	21.15	5.16
	$G_{R_yR_z}$	pN·nm^2	-7.16	25.51	-11.78	-8.13
σ	S	pN	290.58	2810.00	641.68	723.02
	Y_y	pN	178.99	626.83	249.84	442.24
	Y_z	pN	18.65	603.83	206.91	159.30
	Y	pN	30.88	488.97	208.19	193.54
	C	pN·nm^2	52.91	146.91	32.06	94.60
	B_y	pN·nm^2	45.93	192.50	45.22	57.69
	B_z	pN·nm^2	57.25	365.50	98.13	135.78
	B	pN·nm^2	46.44	185.65	84.14	77.03
	$G_{T_xT_y}$	pN	142.18	743.14	286.35	229.66
	$G_{T_xT_z}$	pN	22.27	991.19	216.31	145.37
	$G_{T_xR_x}$	pN·nm	127.17	28.44	57.42	58.06
	$G_{T_xR_y}$	pN·nm	134.35	152.55	136.87	103.48
	$G_{T_xR_z}$	pN·nm	171.23	665.33	245.81	430.67
	$G_{T_yT_z}$	pN	49.67	283.38	50.74	216.64
	$G_{T_yR_x}$	pN·nm	42.69	152.49	89.59	43.22
	$G_{T_yR_y}$	pN·nm	47.36	85.67	90.14	69.93
	$G_{T_yR_z}$	pN·nm	58.70	276.79	108.68	235.91
	$G_{T_zR_x}$	pN·nm	41.69	77.61	67.53	68.23
	$G_{T_zR_y}$	pN·nm	21.00	60.05	38.49	64.09
	$G_{T_zR_z}$	pN·nm	24.52	277.41	88.01	61.49
	$G_{R_xR_y}$	pN·nm^2	31.76	37.84	15.93	13.05
	$G_{R_xR_z}$	pN·nm^2	25.55	49.36	8.49	16.36
	$G_{R_yR_z}$	pN·nm^2	25.05	27.70	17.76	47.85

Table A-16 (Continued)

Properties		Units	GA|TC	GC|GC	GG|CC	GT|AC
μ	S	pN	1512.61	2209.91	1196.29	3108.56
	Y_y	pN	1455.06	2576.52	1182.00	1201.73
	Y_z	pN	457.87	452.33	339.83	470.48
	Y	pN	695.80	769.43	525.86	675.80
	C	pN·nm^2	346.90	314.12	332.99	258.11
	B_y	pN·nm^2	253.98	241.58	243.87	209.22
	B_z	pN·nm^2	271.49	267.93	264.00	334.89
	B	pN·nm^2	261.71	253.93	251.32	257.33
	$G_{T_xT_y}$	pN	838.16	1504.25	771.15	476.45
	$G_{T_xT_z}$	pN	365.96	331.62	199.91	315.04
	$G_{T_xR_x}$	pN·nm	29.52	-27.41	40.01	219.84
	$G_{T_xR_y}$	pN·nm	-38.91	-181.64	-35.94	25.99
	$G_{T_xR_z}$	pN·nm	-73.33	88.93	-74.57	579.41
	$G_{T_yT_z}$	pN	237.10	356.09	114.35	164.71
	$G_{T_yR_x}$	pN·nm	-22.01	168.14	23.78	148.29
	$G_{T_yR_y}$	pN·nm	-14.31	-130.04	24.57	35.62
	$G_{T_yR_z}$	pN·nm	-3.92	115.26	61.96	69.23
	$G_{T_zR_x}$	pN·nm	108.91	49.20	53.38	141.07
	$G_{T_zR_y}$	pN·nm	-7.92	-20.54	-5.18	37.91
	$G_{T_zR_z}$	pN·nm	76.71	65.75	-26.47	71.74
	$G_{R_xR_y}$	pN·nm^2	17.37	14.31	-6.22	22.18
	$G_{R_xR_z}$	pN·nm^2	31.08	29.52	15.75	0.66
	$G_{R_yR_z}$	pN·nm^2	4.70	7.89	-46.36	-50.77
σ	S	pN	170.66	73.16	235.26	108.96
	Y_y	pN	69.15	86.71	138.62	41.78
	Y_z	pN	18.59	15.31	19.82	16.23
	Y	pN	23.27	22.58	27.84	18.26
	C	pN·nm^2	29.69	10.49	47.07	9.05
	B_y	pN·nm^2	17.15	8.20	43.54	7.34
	B_z	pN·nm^2	23.23	9.13	14.10	11.68
	B	pN·nm^2	14.38	6.14	25.13	6.60
	$G_{T_xT_y}$	pN	135.53	50.68	128.77	16.72

Table A-16 (Continued)

Properties		Units	GA|TC	GC|GC	GG|CC	GT|AC
σ	$G_{T_xT_z}$	pN	22.07	11.12	10.60	10.99
	$G_{T_xR_x}$	pN·nm	4.79	0.92	6.40	7.64
	$G_{T_xR_y}$	pN·nm	75.50	6.08	58.89	0.92
	$G_{T_xR_z}$	pN·nm	67.75	2.96	30.21	20.23
	$G_{T_yT_z}$	pN	9.65	12.04	19.80	5.77
	$G_{T_yR_x}$	pN·nm	13.41	5.68	25.43	5.15
	$G_{T_yR_y}$	pN·nm	45.83	4.40	6.64	1.26
	$G_{T_yR_z}$	pN·nm	5.19	3.92	50.42	2.42
	$G_{T_zR_x}$	pN·nm	24.96	1.67	20.92	4.94
	$G_{T_zR_y}$	pN·nm	47.48	0.70	7.10	1.34
	$G_{T_zR_z}$	pN·nm	4.25	2.22	5.69	2.51
	$G_{R_xR_y}$	pN·nm^2	30.57	0.48	13.95	0.78
	$G_{R_xR_z}$	pN·nm^2	2.90	1.00	2.71	0.02
	$G_{R_yR_z}$	pN·nm^2	9.31	0.26	8.87	1.80
Properties		Units	TA|TA	TC|GA	TG|CA	TT|AA
μ	S	pN	4150.71	1980.36	2644.30	2830.83
	Y_y	pN	1535.40	2350.77	1676.02	1771.94
	Y_z	pN	792.35	513.87	722.54	582.88
	Y	pN	1011.79	841.31	975.16	840.71
	C	pN·nm^2	362.31	346.43	392.20	302.98
	B_y	pN·nm^2	429.42	216.10	282.98	313.75
	B_z	pN·nm^2	398.56	331.02	413.69	279.96
	B	pN·nm^2	388.27	261.16	313.45	280.20
	$G_{T_xT_y}$	pN	1556.43	1231.32	1055.75	1343.03
	$G_{T_xT_z}$	pN	926.74	367.77	735.03	308.41
	$G_{T_xR_x}$	pN·nm	-36.55	97.13	167.95	40.09
	$G_{T_xR_y}$	pN·nm	-127.55	-78.90	-191.66	-187.69
	$G_{T_xR_z}$	pN·nm	-541.47	166.71	-515.09	-23.83
	$G_{T_yT_z}$	pN	379.11	119.95	300.46	135.31
	$G_{T_yR_x}$	pN·nm	91.28	156.16	105.57	49.18
	$G_{T_yR_y}$	pN·nm	-75.15	-11.86	-149.30	-69.89

Table A-16 (Continued)

Properties		Units	TA|TA	TC|GA	TG|CA	TT|AA
μ	$G_{T_yR_z}$	pN·nm	-315.26	145.03	-223.65	-57.03
	$G_{T_zR_x}$	pN·nm	51.97	122.27	58.02	64.81
	$G_{T_zR_y}$	pN·nm	-61.45	31.87	-53.61	-4.35
	$G_{T_zR_z}$	pN·nm	-80.36	77.31	-124.39	24.49
	$G_{R_xR_y}$	pN·nm^2	-32.82	9.67	-24.41	-15.46
	$G_{R_xR_z}$	pN·nm^2	63.80	59.51	19.59	43.44
	$G_{R_yR_z}$	pN·nm^2	-11.17	-27.62	2.95	-76.50
σ	S	pN	2098.90	663.99	2228.96	1048.71
	Y_y	pN	274.53	121.52	215.97	590.91
	Y_z	pN	261.22	72.41	367.36	171.06
	Y	pN	246.37	98.31	346.22	217.64
	C	pN·nm^2	107.90	20.00	136.02	70.88
	B_y	pN·nm^2	123.42	13.06	169.19	77.69
	B_z	pN·nm^2	191.20	15.73	273.52	107.35
	B	pN·nm^2	125.21	10.83	149.88	75.75
	$G_{T_xT_y}$	pN	605.87	419.48	645.08	356.39
	$G_{T_xT_z}$	pN	499.22	171.65	555.29	134.78
	$G_{T_xR_x}$	pN·nm	99.16	46.60	67.44	177.82
	$G_{T_xR_y}$	pN·nm	117.89	94.65	214.33	107.37
	$G_{T_xR_z}$	pN·nm	548.17	141.34	717.79	575.38
	$G_{T_yT_z}$	pN	134.26	44.63	147.93	145.31
	$G_{T_yR_x}$	pN·nm	27.47	31.82	34.21	100.65
	$G_{T_yR_y}$	pN·nm	68.83	60.96	80.24	31.58
	$G_{T_yR_z}$	pN·nm	222.79	7.59	400.74	274.79
	$G_{T_zR_x}$	pN·nm	6.87	5.94	74.37	41.00
	$G_{T_zR_y}$	pN·nm	31.19	38.39	63.18	22.23
	$G_{T_zR_z}$	pN·nm	149.02	6.54	228.17	78.23
	$G_{R_xR_y}$	pN·nm^2	36.94	24.64	13.62	15.68
	$G_{R_xR_z}$	pN·nm^2	54.15	14.11	23.79	45.43
	$G_{R_yR_z}$	pN·nm^2	38.64	20.32	54.86	40.30

Table A-17. Sequence-dependent mechanical properties of open nick.

Properties		Units	AA/TnT	AC/GnT	AG/CnT	AT/AnT
μ	S	pN	354.36	543.84	400.22	176.73
	Y_y	pN	119.51	119.86	168.99	69.46
	Y_z	pN	132.33	191.65	160.73	97.40
	Y	pN	120.96	141.56	155.01	75.32
	C	pN·nm^2	110.18	121.21	118.73	69.28
	B_y	pN·nm^2	133.42	146.40	138.57	52.62
	B_z	pN·nm^2	86.41	67.89	107.32	44.38
	B	pN·nm^2	102.74	92.00	118.82	44.82
	$G_{T_xT_y}$	pN	-49.01	-59.45	-18.36	13.37
	$G_{T_xT_z}$	pN	44.81	-90.14	-15.03	-2.56
	$G_{T_xR_x}$	pN·nm	-1.10	-33.30	-4.65	-3.38
	$G_{T_xR_y}$	pN·nm	-22.56	-52.28	-52.39	-17.29
	$G_{T_xR_z}$	pN·nm	-41.64	-9.94	-54.10	-18.78
	$G_{T_yT_z}$	pN	-6.28	-20.45	5.54	-8.29
	$G_{T_yR_x}$	pN·nm	16.94	27.25	28.46	8.01
	$G_{T_yR_y}$	pN·nm	4.86	16.22	26.48	7.25
	$G_{T_yR_z}$	pN·nm	-41.59	-34.39	-48.59	11.39
	$G_{T_zR_x}$	pN·nm	19.05	37.66	14.63	6.99
	$G_{T_zR_y}$	pN·nm	39.21	61.55	40.04	6.71
	$G_{T_zR_z}$	pN·nm	-16.07	-2.67	-22.14	2.79
	$G_{R_xR_y}$	pN·nm^2	8.38	27.95	15.22	2.62
	$G_{R_xR_z}$	pN·nm^2	-16.10	-4.41	-14.61	2.43
	$G_{R_yR_z}$	pN·nm^2	-8.27	-5.96	-6.98	0.29
σ	S	pN	79.93	191.25	64.90	142.43
	Y_y	pN	33.04	41.93	38.30	47.15
	Y_z	pN	34.51	31.48	78.80	53.55
	Y	pN	25.49	35.07	47.94	36.18
	C	pN·nm^2	15.23	13.17	32.25	52.57
	B_y	pN·nm^2	15.77	12.88	30.13	40.30
	B_z	pN·nm^2	23.69	11.58	14.50	22.34
	B	pN·nm^2	18.87	11.28	15.41	21.07
	$G_{T_xT_y}$	pN	17.02	5.30	32.88	31.33

Table A-17 (Continued)

Properties		Units	AA/TnT	AC/GnT	AG/CnT	AT/AnT
σ	$G_{T_xT_z}$	pN	63.43	111.98	58.34	60.30
	$G_{T_xR_x}$	pN·nm	21.99	32.18	23.93	11.54
	$G_{T_xR_y}$	pN·nm	23.75	5.09	13.94	28.60
	$G_{T_xR_z}$	pN·nm	31.63	34.97	7.59	44.31
	$G_{T_yT_z}$	pN	11.24	8.55	26.45	25.66
	$G_{T_yR_x}$	pN·nm	17.96	8.39	9.54	16.16
	$G_{T_yR_y}$	pN·nm	9.60	22.55	16.58	25.80
	$G_{T_yR_z}$	pN·nm	24.00	37.67	20.83	22.22
	$G_{T_zR_x}$	pN·nm	9.11	8.80	14.28	18.08
	$G_{T_zR_y}$	pN·nm	8.45	8.92	40.63	32.22
	$G_{T_zR_z}$	pN·nm	18.63	16.69	12.07	17.51
	$G_{R_xR_y}$	pN·nm^2	5.08	5.78	2.63	13.09
	$G_{R_xR_z}$	pN·nm^2	28.68	24.97	10.69	7.94
	$G_{R_yR_z}$	pN·nm^2	7.69	7.37	6.74	7.15
Properties		Units	CA/TnG	CC/GnG	CG/CnG	CT/AnG
μ	S	pN	852.17	1540.78	1059.25	291.40
	Y_y	pN	213.79	1752.26	390.07	774.26
	Y_z	pN	173.63	323.96	255.33	204.39
	Y	pN	179.80	546.47	305.62	322.33
	C	pN·nm^2	195.10	259.25	214.62	148.49
	B_y	pN·nm^2	112.94	172.02	249.42	107.11
	B_z	pN·nm^2	191.38	180.34	240.97	115.08
	B	pN·nm^2	135.83	175.69	242.64	110.18
	$G_{T_xT_y}$	pN	74.92	1076.04	196.36	185.48
	$G_{T_xT_z}$	pN	127.23	109.86	33.17	46.01
	$G_{T_xR_x}$	pN·nm	68.57	83.65	-108.16	83.51
	$G_{T_xR_y}$	pN·nm	-32.34	68.28	-279.78	-67.04
	$G_{T_xR_z}$	pN·nm	-173.39	162.11	-289.56	18.88
	$G_{T_yT_z}$	pN	25.00	19.17	-9.90	66.96
	$G_{T_yR_x}$	pN·nm	41.90	91.87	31.02	50.95
	$G_{T_yR_y}$	pN·nm	-24.57	53.41	-45.42	4.24

Table A-17 (Continued)

Properties		Units	CA/TnG	CC/GnG	CG/CnG	CT/AnG
μ	$G_{T_yR_z}$	pN·nm	70.96	-54.69	-90.48	72.12
	$G_{T_zR_x}$	pN·nm	58.86	86.27	8.06	54.89
	$G_{T_zR_y}$	pN·nm	-12.10	49.15	-80.59	15.04
	$G_{T_zR_z}$	pN·nm	-28.93	30.63	38.32	15.36
	$G_{R_xR_y}$	pN·nm^2	-4.90	57.12	36.70	-20.15
	$G_{R_xR_z}$	pN·nm^2	-11.14	-50.76	46.10	-39.55
	$G_{R_yR_z}$	pN·nm^2	-12.39	-18.52	-6.64	-31.03
σ	S	pN	660.95	74.19	163.06	30.01
	Y_y	pN	147.38	83.53	65.57	80.54
	Y_z	pN	52.40	15.34	29.00	21.23
	Y	pN	66.34	22.25	30.13	28.08
	C	pN·nm^2	158.41	12.26	26.12	15.28
	B_y	pN·nm^2	80.31	8.19	22.33	11.06
	B_z	pN·nm^2	154.48	8.74	36.32	11.85
	B	pN·nm^2	71.76	6.05	22.11	8.15
	$G_{T_xT_y}$	pN	148.70	52.27	148.77	19.24
	$G_{T_xT_z}$	pN	80.71	5.21	55.17	4.73
	$G_{T_xR_x}$	pN·nm	91.26	3.98	44.40	8.66
	$G_{T_xR_y}$	pN·nm	34.89	3.24	27.73	6.92
	$G_{T_xR_z}$	pN·nm	255.67	7.75	40.26	1.97
	$G_{T_yT_z}$	pN	45.17	0.91	25.58	6.92
	$G_{T_yR_x}$	pN·nm	39.58	4.37	41.77	5.26
	$G_{T_yR_y}$	pN·nm	18.34	2.55	47.41	0.44
	$G_{T_yR_z}$	pN·nm	75.57	2.59	29.71	7.42
	$G_{T_zR_x}$	pN·nm	42.10	4.15	30.40	5.67
	$G_{T_zR_y}$	pN·nm	20.12	2.32	31.20	1.56
	$G_{T_zR_z}$	pN·nm	25.22	1.46	40.62	1.60
	$G_{R_xR_y}$	pN·nm^2	3.17	2.74	6.04	2.07
	$G_{R_xR_z}$	pN·nm^2	29.95	2.39	9.09	4.08
	$G_{R_yR_z}$	pN·nm^2	13.65	0.89	18.85	3.21

Table A-17 (Continued)

Properties		Units	GA/TnC	GC/GnC	GG/CnC	GT/AnC
μ	S	pN	735.91	86.90	124.27	307.54
	Y_y	pN	264.68	223.44	300.19	423.33
	Y_z	pN	237.65	117.65	158.51	216.63
	Y	pN	249.75	152.10	199.02	284.42
	C	pN·nm^2	187.69	85.91	82.24	175.77
	B_y	pN·nm^2	229.75	42.18	95.83	204.75
	B_z	pN·nm^2	131.85	90.94	113.18	208.35
	B	pN·nm^2	167.16	57.00	99.17	204.94
	$G_{T_xT_y}$	pN	56.30	3.31	-71.69	48.68
	$G_{T_xT_z}$	pN	32.27	14.53	-14.78	75.44
	$G_{T_xR_x}$	pN·nm	-26.55	-8.37	-4.52	35.42
	$G_{T_xR_y}$	pN·nm	-153.14	-12.67	-14.38	-124.94
	$G_{T_xR_z}$	pN·nm	-104.64	-34.38	-39.83	-28.97
	$G_{T_yT_z}$	pN	-18.74	-16.52	-7.72	94.98
	$G_{T_yR_x}$	pN·nm	55.05	5.09	33.00	-26.13
	$G_{T_yR_y}$	pN·nm	-48.40	3.29	72.83	-76.43
	$G_{T_yR_z}$	pN·nm	-14.11	-4.05	-117.48	90.03
	$G_{T_zR_x}$	pN·nm	-11.52	17.41	48.84	71.13
	$G_{T_zR_y}$	pN·nm	-67.97	-15.83	24.99	52.43
	$G_{T_zR_z}$	pN·nm	-11.69	0.55	-16.87	-30.70
	$G_{R_xR_y}$	pN·nm^2	56.52	-1.22	28.75	34.19
	$G_{R_xR_z}$	pN·nm^2	6.78	-35.79	-26.72	-41.02
	$G_{R_yR_z}$	pN·nm^2	-23.21	0.68	-20.48	-32.25
σ	S	pN	50.94	14.59	34.79	36.60
	Y_y	pN	18.38	37.33	84.99	50.37
	Y_z	pN	16.47	19.66	44.97	25.39
	Y	pN	12.43	19.50	45.92	24.93
	C	pN·nm^2	13.06	14.37	23.30	20.53
	B_y	pN·nm^2	16.01	6.99	26.97	24.12
	B_z	pN·nm^2	9.17	15.24	32.22	24.60
	B	pN·nm^2	8.52	7.32	22.60	17.57
	$G_{T_xT_y}$	pN	3.87	0.56	20.28	5.72

Table A-17 (Continued)

Properties		Units	GA/TnC	GC/GnC	GG/CnC	GT/AnC
σ	$G_{T_xT_z}$	pN	2.23	2.43	4.16	8.91
	$G_{T_xR_x}$	pN·nm	1.85	1.38	1.27	4.18
	$G_{T_xR_y}$	pN·nm	10.57	2.10	4.13	14.55
	$G_{T_xR_z}$	pN·nm	7.29	5.78	11.21	3.41
	$G_{T_yT_z}$	pN	1.30	2.75	2.19	11.24
	$G_{T_yR_x}$	pN·nm	3.78	0.86	9.28	3.08
	$G_{T_yR_y}$	pN·nm	3.42	0.54	20.55	9.10
	$G_{T_yR_z}$	pN·nm	0.99	0.67	33.14	10.61
	$G_{T_zR_x}$	pN·nm	0.80	2.86	13.71	8.42
	$G_{T_zR_y}$	pN·nm	4.77	2.66	6.98	6.21
	$G_{T_zR_z}$	pN·nm	0.82	0.09	4.75	3.58
	$G_{R_xR_y}$	pN·nm^2	3.93	0.20	8.12	4.03
	$G_{R_xR_z}$	pN·nm^2	0.47	5.87	7.55	4.78
	$G_{R_yR_z}$	pN·nm^2	1.60	0.11	5.78	3.82
Properties		Units	TA/TnA	TC/GnA	TG/CnA	TT/AnA
μ	S	pN	619.64	947.18	207.52	155.51
	Y_y	pN	198.01	762.70	118.57	85.85
	Y_z	pN	197.77	273.15	107.03	108.32
	Y	pN	188.03	397.67	109.11	88.50
	C	pN·nm^2	160.46	148.08	88.09	70.22
	B_y	pN·nm^2	152.10	179.63	88.17	56.33
	B_z	pN·nm^2	138.35	168.43	85.69	62.46
	B	pN·nm^2	140.85	169.87	80.70	55.85
	$G_{T_xT_y}$	pN	106.50	446.16	25.94	24.11
	$G_{T_xT_z}$	pN	15.66	182.06	21.78	34.13
	$G_{T_xR_x}$	pN·nm	9.17	60.11	14.45	20.09
	$G_{T_xR_y}$	pN·nm	-73.87	-130.97	-52.24	-34.16
	$G_{T_xR_z}$	pN·nm	-39.70	95.54	-49.90	-13.36
	$G_{T_yT_z}$	pN	3.17	84.15	12.66	15.42
	$G_{T_yR_x}$	pN·nm	19.14	55.78	-3.50	7.64
	$G_{T_yR_y}$	pN·nm	-7.14	-26.00	-23.98	-2.53

Table A-17 (Continued)

Properties		Units	TA/TnA	TC/GnA	TG/CnA	TT/AnA
μ	$G_{T_yR_z}$	pN·nm	-25.65	5.37	-56.54	15.03
	$G_{T_zR_x}$	pN·nm	38.26	71.00	34.61	13.40
	$G_{T_zR_y}$	pN·nm	13.59	-6.68	13.96	-4.44
	$G_{T_zR_z}$	pN·nm	-5.17	-28.94	5.89	6.05
	$G_{R_xR_y}$	pN·nm^2	6.71	-10.51	13.67	-3.22
	$G_{R_xR_z}$	pN·nm^2	-23.23	-50.12	-15.37	-17.53
	$G_{R_yR_z}$	pN·nm^2	-13.10	-33.94	-2.24	3.38
σ	S	pN	188.94	159.78	137.48	138.88
	Y_y	pN	70.73	101.14	31.02	35.16
	Y_z	pN	48.78	61.92	24.59	45.33
	Y	pN	46.49	69.68	20.70	30.52
	C	pN·nm^2	48.91	9.23	54.39	37.54
	B_y	pN·nm^2	32.65	36.96	61.20	41.13
	B_z	pN·nm^2	35.58	34.37	40.22	38.81
	B	pN·nm^2	25.64	26.63	36.44	27.91
	$G_{T_xT_y}$	pN	101.25	37.73	62.53	32.15
	$G_{T_xT_z}$	pN	61.84	118.59	30.25	32.22
	$G_{T_xR_x}$	pN·nm	32.33	28.13	11.38	30.54
	$G_{T_xR_y}$	pN·nm	36.98	57.79	55.65	32.06
	$G_{T_xR_z}$	pN·nm	101.07	22.53	54.01	24.97
	$G_{T_yT_z}$	pN	23.33	36.76	4.58	31.23
	$G_{T_yR_x}$	pN·nm	24.55	29.70	3.79	19.77
	$G_{T_yR_y}$	pN·nm	12.13	36.67	16.84	8.01
	$G_{T_yR_z}$	pN·nm	44.88	60.45	30.88	20.33
	$G_{T_zR_x}$	pN·nm	26.72	14.45	21.51	21.32
	$G_{T_zR_y}$	pN·nm	32.19	46.82	17.73	13.77
	$G_{T_zR_z}$	pN·nm	31.10	2.43	7.89	16.12
	$G_{R_xR_y}$	pN·nm^2	11.74	10.95	12.42	12.00
	$G_{R_xR_z}$	pN·nm^2	22.00	17.28	9.30	15.07
	$G_{R_yR_z}$	pN·nm^2	25.86	26.19	8.92	15.73

A.6. Connectivity between DNA bases

Figure A-1 demonstrates the connectivity between DNA bases that constitute the lattice-based design shown in Figure 3-1. The first, second, third, fourth, and fifth columns in the base connectivity correspond to the current base identifier, the identifier of the base covalently bonded to the current base in the 5'-direction, the identifier of the base covalently bonded to the current base in the 3'-direction, the identifier of the complementary base, and the base sequence of the current base, respectively.

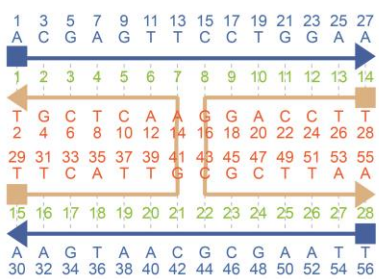

1	-1	3	2	DA
2	4	-1	1	DT
3	1	5	4	DC
4	6	2	3	DG
5	3	7	6	DG
6	8	4	5	DC
7	5	9	8	DA
8	10	6	7	DT
9	7	11	10	DG
10	12	8	9	DC
11	9	13	12	DT
12	14	10	11	DA
13	11	15	14	DT
14	41	12	13	DA
15	13	17	16	DC
16	18	43	15	DG
17	15	19	18	DC
18	20	16	17	DG
19	17	21	20	DT
20	22	18	19	DA
21	19	23	22	DG
22	24	20	21	DC
23	21	25	24	DG
24	26	22	23	DC
25	23	27	26	DA
26	28	24	25	DT
27	25	-1	28	DA
28	-1	26	27	DT
⋮				

⋮				
29	-1	31	30	DT
30	32	-1	29	DA
31	29	33	32	DT
32	34	30	31	DA
33	31	35	34	DC
34	36	32	33	DG
35	33	37	36	DA
36	38	34	35	DT
37	35	39	38	DT
38	40	36	37	DA
39	37	41	40	DT
40	42	38	39	DA
41	39	14	42	DG
42	44	40	41	DC
43	16	45	44	DC
44	46	42	43	DG
45	43	47	46	DG
46	48	44	45	DC
47	45	49	48	DC
48	50	46	47	DG
49	47	51	50	DT
50	52	48	49	DA
51	49	53	52	DT
52	54	50	51	DA
53	51	55	54	DA
54	56	52	53	DT
55	53	-1	56	DA
56	-1	54	55	DT

Figure A-1. Connectivity between DNA bases. The lattice-based design is composed of 56 bases, and its base connectivity is expressed by a 56-by-5 matrix.

A.7. Structural analysis from on-lattice designs (wireframes)

The lattice-based designs (represented in Figure 6-5) for wireframe structures obtained from PERDIX[23] and TALOS[22] contain complicated and artifically stretched bonds between base-pairs. When performing structural analyses directly on these designs, they deviate into unstable states, as shown in Figure A-2.

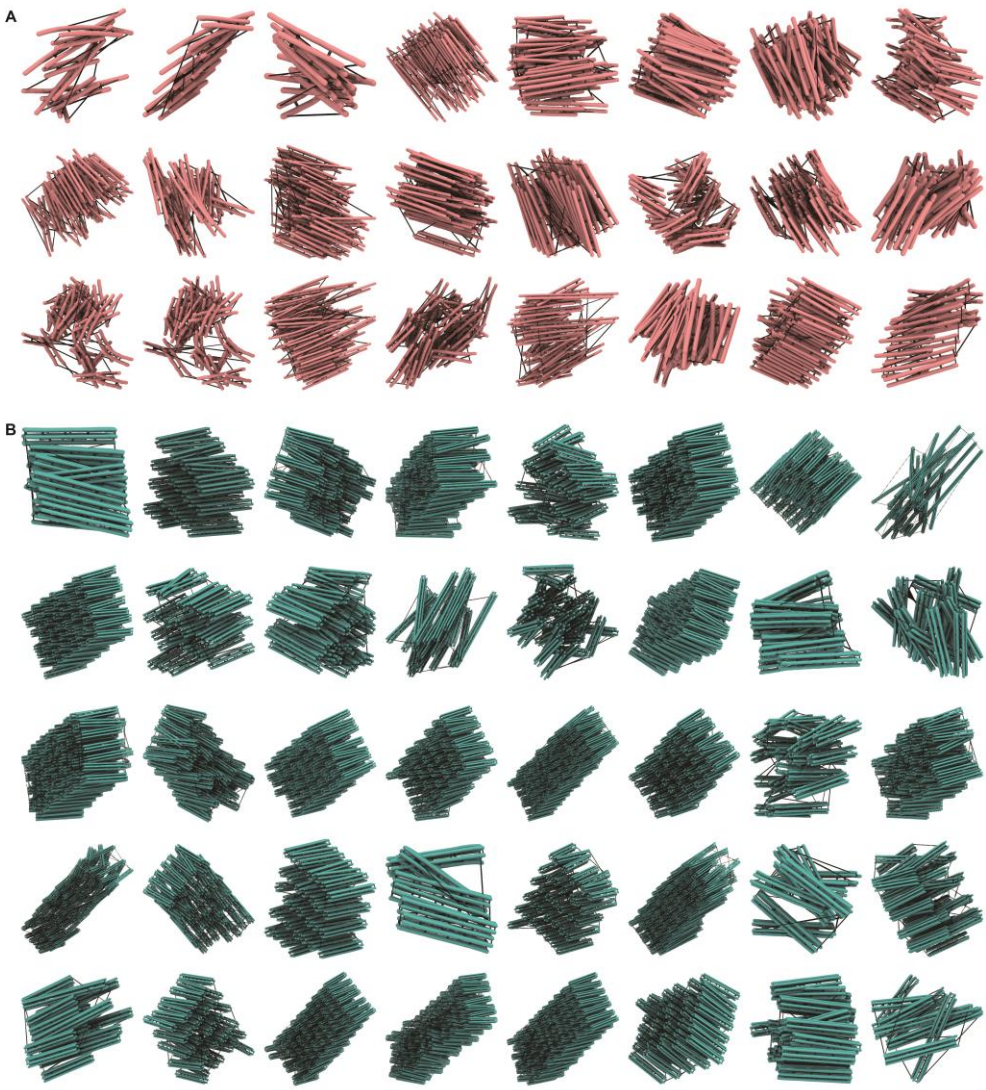

Figure A-2. Divergence of structural analysis from on-lattice designs of wireframe structures. (A) PERDIX wireframes, (B) TALOS wireframes.

A.8. Lattice-based designs of deformed wireframe edges

To achieve inward and outward bends in wireframe edges, we modify the reference wireframe designs obtained from TALOS[22] by inserting or deleting base-pairs in DNA helices. The manipulation of the number of base-pairs controls the structural strain energy, ultimately causing structural deformation[4]. Figure A-3 provides visual representations of the lattice-based desings of straight, inwardly bent, and outwardly bent wireframe edges.

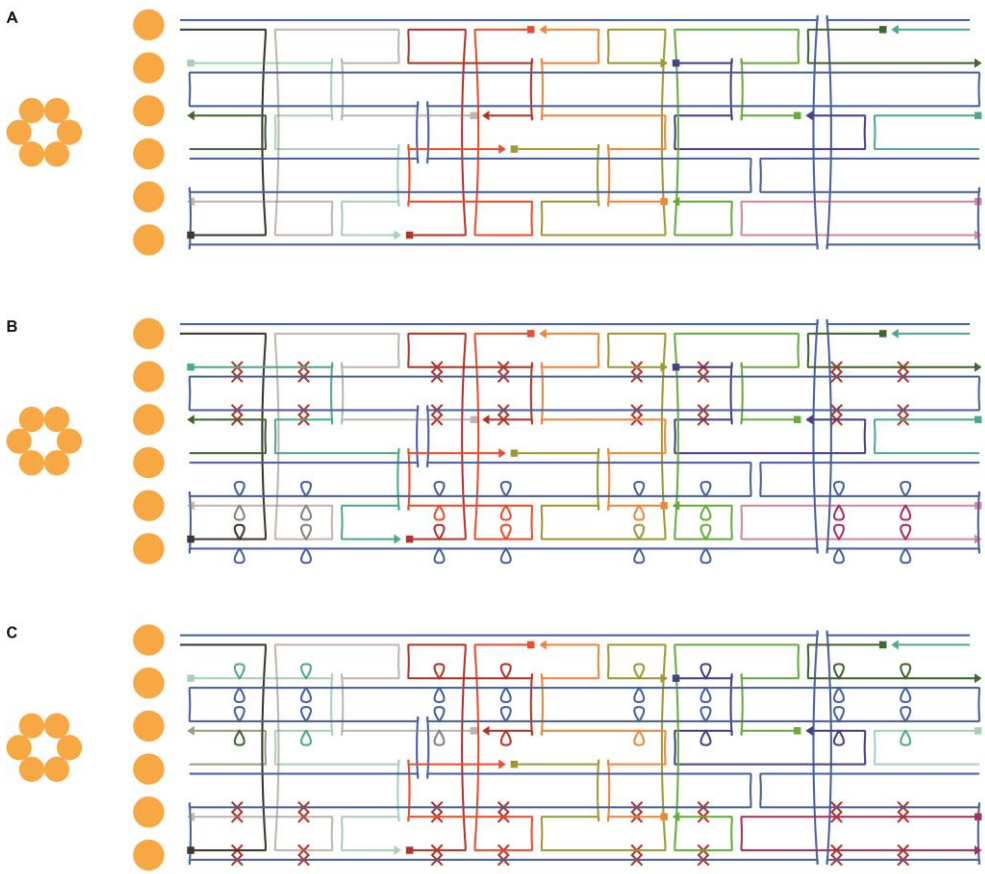

Figure A-3. Lattice-based designs for wireframe edges. (A) A straight wireframe edge, (B) An inwardly bent wireframe edge, (C) An outwardly bent wireframe edge.

A.9. Experimental method for octahedron wireframes

Integrated DNA Technologies provides the M13 bacteriopharge scaffold DNA (p7560) directly for DNA origami assembly. Bioneer Corporation supplies stale DNA oligonucleotides necessary for wireframe octahedrons in nuclease-free water at a concentration of 100 [μM]. To obtain an equimolar staple mix, equal volumes of each staple are combined. 10×Tris-acetate-EDTA (TAE), $MgCl_2$, and NaCl are procured from Sigma-Aldrich. The sample preparation involved mixing staple strands with the scaffold at a final concentration of 20 [nM] in a 5-fold molar excess (100 [nm]) in folding buffer (1×TAE, $MgCl_2$ of 10 [mM] and NaCl of 100 [mM]) with a total volume of 50 [μL]. The solution undergoes a slow annealing process from 95 [°C] to 25 [°C] overnight in a T100 Thermocycler (Bio-Rad) following a specific temperature process: 95 [°C] for 5 [min], 85 [°C] to 70 [°C] at 1 [°C] per 5 [min], 70 [°C] to 30 [°C] at 1 [°C] per 30 [min], and 30 [°C] to 25 [°C] at 1 [°C] per 10 [min].

For the purification of folded DNA origami samples and removal of excess staples, buffer exchanges are performed using centrifugal filter units with 100 [kDa] MWCO membranes. The membranes are first rinsed with a $MgCl_2$ solution of 5 [mM] and then subjected to centrifuation at 5000 [rcf] for 5 [min] at 20 [°C]. The samples (100 [μL]) and folding buffer (400 [μL]) are centrifuged for 10 [min] at 10000 [rcf] and subsequently recovered by inverting the filter and spinning for 3 [min] at 10000 [rcf]. The concentration of the origami samples post-filtration is approximately 10 [nM], determined using a NanoDrop One UV spectrometer (Thermo Fisher Scientific).

For TEM imaging, the purified samples are adsorbed onto glow-discharged TEM grids and then stained with a 2 [%] aqueous uranyl acetate solution containing NaOH of 50 [mM] for 40 [s]. Negative stained TEM images are captured using a JEOL JEM-2100Plus operated at 200 [kV].

A.10. Experimental results for octahedron wireframes

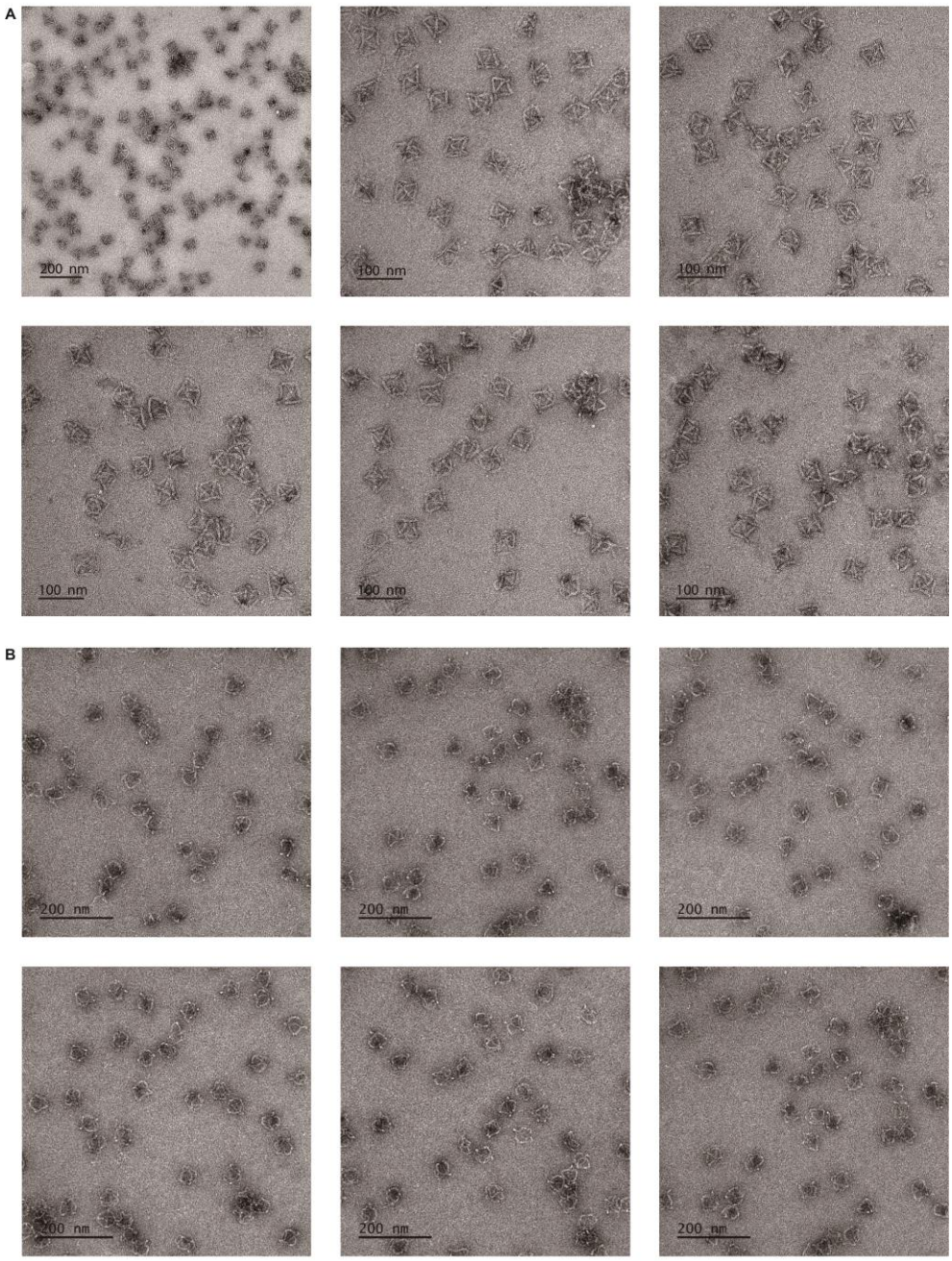

Figure A-4. TEM images for octahedron wireframes. (A) Octahedron wireframes with straight edges, (B) Octahedron wireframes with inwardly bent edges, (C) Octahedron wireframes with outwardly bent edges.

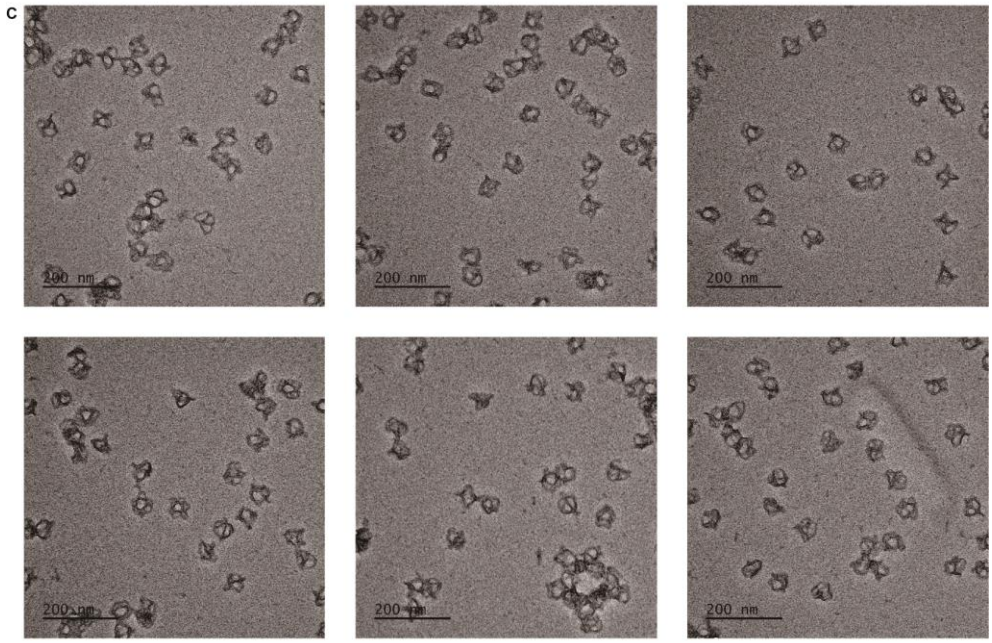

Figure A-4 (Continued)

Bibliography

1 Seeman, N. C. Nucleic acid junctions and lattices. *J. Theor. Biol*., **99**, 237–247 (1982).

2 Seeman, N. C. Nanomaterials bsed on DNA. *Annu. Rev. Biochem.*, **79**, 65–87 (2010).

3 Rothemund, P. W. Folding DNA to create nanoscale shapes and patterns. *Nature*, **440**, 297–302 (2006).

4 Dietz, H., Douglas, S. M. & Shih, W. M. Folding DNA into twisted and curved nanoscale shapes. *Science*, **325**, 725–730 (2009).

5 Douglas, S. M., Dietz, H., Liedl, T., Högberg, B., Graf, F. & Shih, W. M. Self-assembly of DNA into nanoscale three-dimensional shapes. *Nature*, **459**, 414–418 (2009).

6 Han, D., Pal, S., Liu, Y. & Yan, H. Folding and cutting DNA into reconfigurable topological nanostructures. *Nat. Nanotechnol.*, **5**, 712–717 (2010).

7 Han, D., Pal, S., Nangreave, J., Deng, Z., Liu, Y. & Yan, H. DNA origami with complex curvatures in three-dimensional space. *Science*, **332**, 342–346 (2011).

8 Lin, C., Perrault, S. D., Kwak, M., Graf, F. & Shih, W. M. Purification of DNA-origami nanostructures by rate-zonal centrifugation. *Nucleic Acids Res.*, **41**, No. e40 (2013).

9 Ponnuswamy, N., Bastings, M. M., Nathwani, B., Ryu, J. H., Chou, L. Y., Vinther, M., Li, W. A., Anastassacos, F. M., Mooney, D. J. & Shih, W. M. Oligolysine-based coating protects DNA nanostructures from low-salt denaturation and nuclease degradation. *Nat. Commun.*, **8**, 15654 (2017).

10 Lee, C., Lee, J. Y. & Kim, D.-N. Polymorphic design of DNA origami structures through mechanical control of modular components. *Nat. Commun.*, **8**, 2067 (2017).

11 Ketterer, P., Ananth, A. N., Laman Trip, D. S., Mishra, A., ertosin, E., Ganji, M., van der Torre, J., Onck, P., Dietz, H. & Dekker, C. DNA origami

scaffold for studying intrinsically disordered proteins of the nuclear pore complex. *Nat. Commun.*, **9**, 902 (2018).

12 Kim, Y.-J., Lee, C., Lee, J. G. & Kim, D.-N. Configurational design of mechanical perturbation for fine control of twisted DNA origami structures. *ACS Nano*, **13**, 6348–6355 (2019).

13 Lee, C., Kim, K. S., Kim, Y.-J., Lee, J. Y. & Kim, D.-N. Tailoring the mechanical stiffness of DNA nanostructures using engineered defects. *ACS Nano*, **13**, 8329–8336 (2019).

14 Bian, X., Zhang, Z., Xiong, Q., De Camilli, P. D. & Lin, C. A programmable DNA-origami platform for studying lipid transfer between bilayers. *Nat. Chem. Biol.*, **15**, 830–837 (2019).

15 Kim, Y.-J., Park, J., Lee, J. Y. & Kim, D.-N. Programming ultrasensitive threshold response through chemomechanical instability. *Nat. Commun.*, **12**, 5177 (2021).

16 Birac, J. J., Sherman, W. B., Kopatsch, J., Constantinou, P. E. & Seeman, N. C. Architecture with GIDEON, a program for design in structural DNA nanotechnology. *J. Mol. Graphics Modell.*, **25**, 470–480 (2006).

17 Andersen, E. S., Dong, M., Nielsen, M. M., Jahn, K., Lind-Thomsen, A., Mamdouh, W., Gothelf, K. V., Besenbacher, F. & Kjems, J. DNA origami design of dolphin-shaped structures with flexible tails. *ACS Nano*, **2**, 1213–1218 (2008).

18 Williams, S., Lund, K., Lin, C., Wonka, P., Lindsay, S. & Yan, H. Tiamat: a three-dimensional editing tool for complex DNA structures. *DNA Computing*, Springer: Berlin, 2008, Vol. 5347, pp 90–101.

19 Douglas, S. M., Marblestone, A. H., Teerapittayanon, S., Vazquez, A., Church, G. M. & Shih, W. M. Rapid prototyping of 3D DNA-origami shapes with caDNAno. *Nucleic Acids Res.*, **37**, 5001–5006 (2009).

20 Veneziano, R., Ratanalert, S., Zhang, K., Zhang, F., Yan, H., Chiu, W. & Bathe, M. Designer nanoscale DNA assemblies programmed from the top down. *Science*, **352**, 1534–1534 (2016).

21 Jun, H., Zhang, F., Shepherd, T., Ratanalert, S., Qi, X., Yan, H. & Bathe, M. Autonomously designed free-form 2D DNA origami. *Sci. Adv.*, **5**, No. eaav0655 (2019).

22 Jun, H., Shepherd, T. R., Zhang, K., Bricker, W. P., Li, S., Chiu, W. & Bathe, M. Automated sequence design of 3D polyhedral wireframe DNA origami with honeycomb edges. *ACS Nano*, **13**, 2083–2093 (2019).

23 Jun, H., Wang, X., Bricker, W. P. & Bathe, M. Automated sequence design of 2D wireframe DNA origami with honeycomb edges. *Nat. Commun.*, **10**, 5419 (2019).

24 Castro, C. E., Kilchherr, F., Kim, D.-N., Shiao, E. L., Wauer, T., Wortmann, P., Bathe, M. & Dietz, H. A Primer to scaffolded DNA origami. *Nat. Methods*, **8**, 221–229 (2011).

25 Kim, D.-N., Kilchherr, F., Dietz, H. & Bathe, M. Quantitative prediction of 3D solution shape and flexibility of nucleic acid nanostructures. *Nucleic Acids Res.*, **40**, 2862–2868 (2012).

26 Pan, K., Kim, D.-N., Zhang, F., Adendorff, M. R., Yan, H. & Bathe, M. Lattice-free prediction of three-dimensional structure of programmed DNA assemblies. *Nat. Commun.*, **5**, 5578 (2014).

27 Ouldridge, T. E., Louis, A. A. & Doye, J. P. K. Structural, mechanical, and thermodynamic properties of a coarse-grained DNA model. *J. Chem. Phys.*, **134**, No. 085101 (2011).

28 Maffeo, C. & Aksimentiev, A. MrDNA: a multi-resolution model for predicting the structure and dynamics of DNA systems. *Nucleic Acids Res.*, **48**, 5135–5146 (2020).

29 Lee, J. Y., Lee, J. G., Yun, G., Lee, C., Kim, Y.-J., Kim, K. S., Kim, T. H. & Kim, D.-N. Rapid computational analysis of DNA origami assemblies at near-atomic resolution. *ACS Nano*, **15**, 1002–1015 (2021).

30 Lee, J. G., Kim, K. S., Lee, J. Y. & Kim, D.-N. Predicting the free-form shape of structured DNA assemblies from their lattice-based design blueprint. *ACS nano*, **16**, 4289–4297 (2022).

31 Lu, X. J. & Olson, W. K. 3DNA: a software package for the analysis, rebuilding and visualization of three-dimensional nucleic acid structures. *Nucleic Acids Res.*, **31**, 5108–5121 (2003).

32 Lu, X. J. & Olson, W. K. 3DNA: a versatile, integrated software system for the analysis, rebuilding and visualization of three-dimensional nucleic-acid structures. *Nat. Protocols*, **3**, 1213–1227 (2008).

33 Lee, J. Y., Kim, Y.-J., Lee, C., Lee, J. G., Yagyu, H., Tabata, O. & Kim, D.-N. Investigating the sequence-dependent mechanical properties of DNA nicks for applications in twisted DNA nanostructure design. *Nucleic Acids Res.*, **47**, 93−102 (2019).

34 Phillips, J. C., Braun, R., Wang, W., Gumbart, J., Tajkhorshid, E., Villa, E., Chipot, C., Skeel, R. D., Kale, L. & Schulten, K. Scalable molecular dynamics with NAMD. *J. Comput. Chem.*, **26**, 1781–1802 (2005).

35 Ivan, I., Dans, P. D., Noy, A., Pérez, A., Faustino, I., Hospital, A., Walther, J., Andrio, P., Goñi, R., Balaceanu, A. & Portella, G. Parmbsc1: a refined force field for DNA simulations. *Nat. Methods*, **13**, 55–58 (2016).

36 Dans, P. D., Ivan, I., Hospital, A., Portella, G., González, C. & Orozco, M. How accurate are accurate force-fields for B-DNA?. *Nucleic Acids Res.*, **45**, 4217–4230 (2017).

37 Jorgensen, W. L., Chandrasekhar, J., Madura, J. D., Impey, R. W. & Klein, M. L. Comparison of simple potential functions for simulating liquid water. *J. Chem. Phys.*, **79**, 926–935 (1983).

38 Essmann, U., Perera, L., Berkowitz, M. L., Darden, T., Lee, H. & Pedersen, L. G. A smooth particle mesh ewald method. *J. Chem. Phys.*, **103**, 8577–8593 (1995).

39 Feller, S. E., Zhang, Y. H., Pastor, R. W. & Brooks, B. R. Constant pressure molecular dynamics simulation: The langevin piston method. *J. Chem. Phys.*, **103**, 4613–4621 (1995).

40 Gore, J., Bryant, Z., Nollmann, M., Le, M. U., Cozzarelli, N. R. & Bustamante, C. DNA overwinds when stretched. *Nature*, **442**, 836–839 (2006).

41 Gross, P., Laurens, N., Oddershede, L. B., Bockelmann, U., Peterman, E. J. G. & Wuite, G. J. L. Quantifying how DNA stretches, melts and changes twist under tension. *Nat. Phys.*, **7**, 731–736 (2011).

42 Lankas, F., Sponer, J., Langowski, J. & Cheatham, T. E. DNA basepair step deformability inferred from molecular dynamics simulations. *Biophys. J.*, **85**, 2872–2883 (2003).

43 Marin-Gonzalez, A., Vilhena, J. G., Perez, R. & Moreno-Herrero, F. Understanding the mechanical response of double-stranded DNA and RNA under constant stretching forces using all-atom molecular dynamics. *Proc. Natl. Acad. Sci. U.S.A.*, **114**, 7049–7054 (2017).

44 Liebl, K., Drsata, T., Lankas, F., Lipfert, J. & Zacharias, M. Explaining the striking difference in twist-stretch coupling between DNA and RNA: A comparative molecular dynamics analysis. *Nucleic Acids Res.*, **43**, 10143–10156 (2015).

45 Fruchterman, T. M. & Reingold, E. M. Graph drawing by force-directed placement. *Software: Practice and experience*, **21**, 1129-1164 (1991).

46 Wang, W., Nocka, L. M., Wiemann, B. Z., Hinckley, D. M., Mukerji, L., Starr, F. W. Holliday junction thermodynamics and structure: coarse-grained simulations and experiments. *Sci. Rep.*, **6**, No. 22863 (2016).

47 Lukacs, G. L., Haggie, P., Seksek, O., Lechardeur, D., Freedman, N. & Verkman, A. S. Size-dependent DNA mobility in cytoplasm and nucleus. *J. Biol. Chem.*, **275**, 1625-1629 (2000).

48 Smith, D. E., Perkins, T. T. & Chu, S. Dynamical scaling of DNA diffusion coefficients. *Macromolecules*, **29**, 1372-1373 (1996).

49 Einstein, A. *Investigations on the theory of the brownian movement*. Courier Corporation (1956).

50 Bosco, A., Camunas-Soler, J. & Ritort, F. Elastic properties and secondary structure formation of single-stranded DNA at monovalent and divalent salt conditions. *Nucleic Acids Res.*, **42**, 2064-2074 (2013).

51 Bathe, K.-J. *Finite Element Procedures*. (2014).

52 Song, J., Li, Z., Wang, P., Meyer, T., Mao, C. & Ke, Y., Reconfiguration of DNA molecular arrays driven by information relay. *Science*, **357**, p.eaan3377 (2017).

53 Stewart, G. W. A Krylov-Schur algorithm for large eigenproblems. *SIAM J. Matrix Anal. Appl.*, **23**, 601-614 (2002).

54 Kim, D.–N., Nguyen, C.–T. & Bathe, M. Conformational dynamics of supramolecular protein assemblies. *J. Struct. Biol.*, **173**, 261-270 (2011).

55 Schiffels, D., Liedl, T. & Fygenson, D. K. Nanoscale structure and microscale stiffness of DNA nanotubes. *ACS Nano*, **7**, 6700-6710 (2013).

Abstract in Korean

DNA 나노기술 분야에서, DNA는 유전물질로 사용되기 보다는, 특정한 형상과 기능을 가지는 DNA 나노구조물을 제작하기 위한 공학적인 소재로 활용되고 있다. 구조화된 DNA 조립체는, DNA의 주요 특성인 염기상보성을 고려한 자기조립의 활용 및 DNA 가닥을 정렬하고 연결하는 편의성 때문에, 기본적으로 잘 정의된 3차원 격자 위에서 설계된다. 하지만, 이러한 설계 전략은 3차원의 DNA 나노구조물을 하나 또는 여러 개의 하위 구조로 임의로 분할한 다음, 이미 위치가 정해진 격자 위에 배열 및 연결하는 과정이 요구된다. 이 과정에서, 설계된 구조물 내부에는 염기 사이를 서로 연결하는 결합이 자연스럽지 않게 인장되거나, DNA 가닥의 잘못된 배열로 인해 DNA 구조모티프가 잘못 분류되기도 한다. 결과적으로, 격자 기반의 형상에서 시작하는 전산구조해석은 비수렴 또는 부적절한 최종 평형 형상을 예측하는 등 전산상의 어려움에 직면할 수 있다.

본 연구에서는, 염기 사이의 연결성을 이용하여 DNA 나노구조물을 설계하고, 최종 평형 형상을 정확하게 예측하기 위한 전산해석과정을 제시한다. 우선, 전원자 분자동역학 시뮬레이션을 이용한 염기서열에 따른 기하학적 및 역학적 특성 분석 및 이를 통해 DNA 나노구조물을 구성하는 DNA 구조모티프를 이해한다. 다음으로, 우리는 연결성 기반의 설계로부터, 해당 구조물을 구성하는 DNA 구조모티프의 대략적인 분류 및 구성요소를 3차원 공간에 잘 분배시킨 초기 형상을 설립한다. 설립된 초기 형상에 대해서 축소화된 브라우니안 동역학 모델링 및 시뮬레이션을

수행함으로써, DNA 구조모티프를 더욱 상세하게 분류한다. 마지막으로, 이렇게 잘 정의된 형상에 대해서, 각 구조모티프의 고유한 구조적 특성을 묘사하는 구조 요소와 음전하를 띤 DNA 가닥 사이의 정전기적 반발력을 묘사하는 정전기 요소를 통합하는 유한요소모델을 개발한다. 유한요소해석을 통해 다양한 형상의 DNA 나노구조물의 최종 평형 형상을 성공적으로 예측한다. 또한, 정상 모드 분석을 통해 DNA 나노구조물의 역학적 및 동적 특성을 분석한다. 우리는 본 연구에서 제안한 포괄적인 전산 과정이 구조화된 핵산 조립체의 설계-해석-검증 프로세스를 상당히 가속화 및 크게 향상시킬 것으로 기대한다.

주요어: DNA 나노기술, 전산해석, 멀티스케일 모델링, 분자동역학 시뮬레이션, 브라우니안 동역학, 유한요소해석

학 번: 2016-27382